MAGNETIC RECORDS OF EXTREME GEOLOGICAL EVENTS

EDITED BY: Eric Font, Alexandra Abrajevitch and Fabio Florindo
PUBLISHED IN: Frontiers in Earth Science

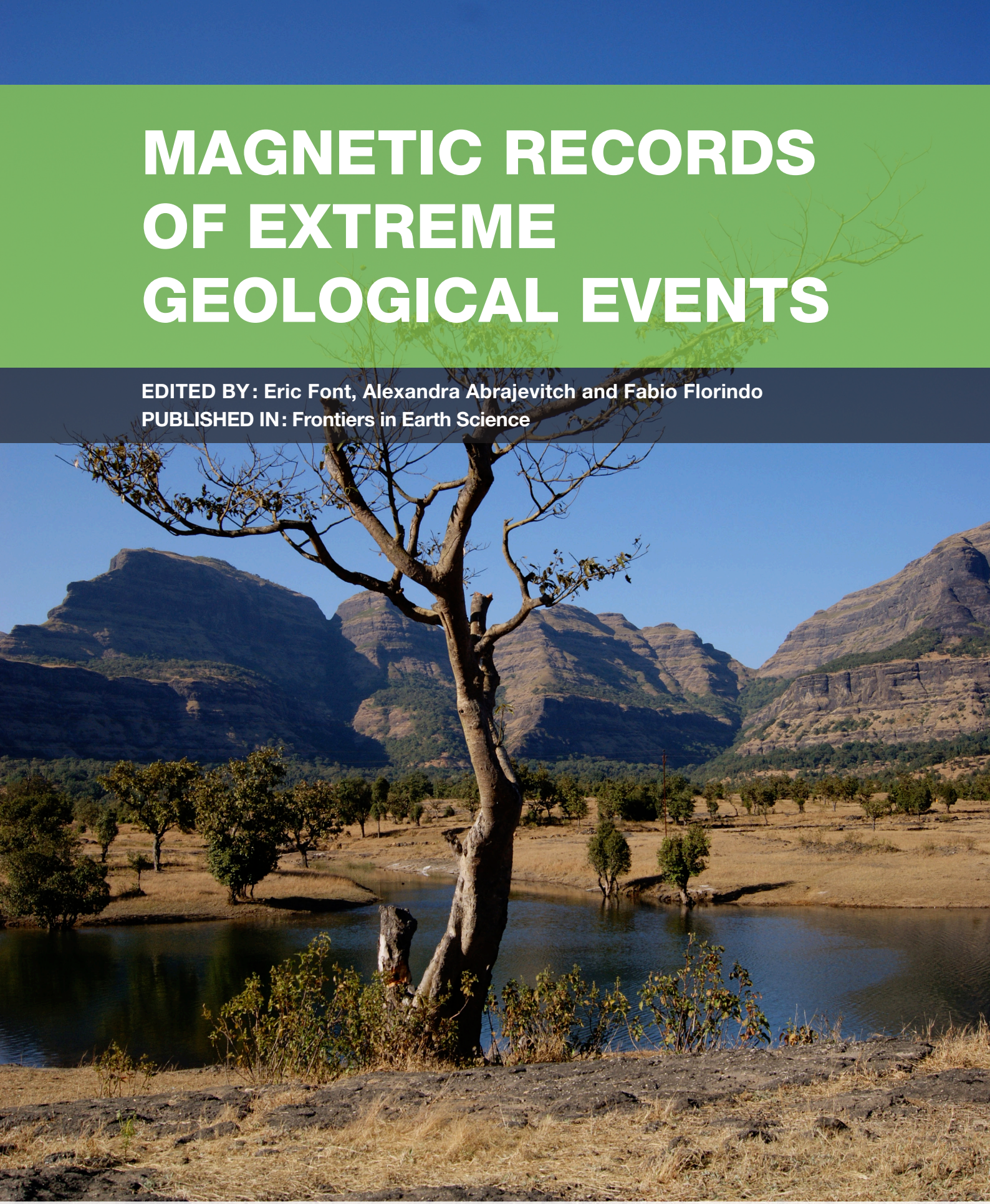

frontiers Research Topics

frontiers

ISSN 1664-8714
ISBN 978-2-88945-170-8
DOI 10.3389/978-2-88945-170-8

About Frontiers

Frontiers is more than just an open-access publisher of scholarly articles: it is a pioneering approach to the world of academia, radically improving the way scholarly research is managed. The grand vision of Frontiers is a world where all people have an equal opportunity to seek, share and generate knowledge. Frontiers provides immediate and permanent online open access to all its publications, but this alone is not enough to realize our grand goals.

Frontiers Journal Series

The Frontiers Journal Series is a multi-tier and interdisciplinary set of open-access, online journals, promising a paradigm shift from the current review, selection and dissemination processes in academic publishing. All Frontiers journals are driven by researchers for researchers; therefore, they constitute a service to the scholarly community. At the same time, the Frontiers Journal Series operates on a revolutionary invention, the tiered publishing system, initially addressing specific communities of scholars, and gradually climbing up to broader public understanding, thus serving the interests of the lay society, too.

Dedication to Quality

Each Frontiers article is a landmark of the highest quality, thanks to genuinely collaborative interactions between authors and review editors, who include some of the world's best academicians. Research must be certified by peers before entering a stream of knowledge that may eventually reach the public - and shape society; therefore, Frontiers only applies the most rigorous and unbiased reviews.
Frontiers revolutionizes research publishing by freely delivering the most outstanding research, evaluated with no bias from both the academic and social point of view.
By applying the most advanced information technologies, Frontiers is catapulting scholarly publishing into a new generation.

What are Frontiers Research Topics?

Frontiers Research Topics are very popular trademarks of the Frontiers Journals Series: they are collections of at least ten articles, all centered on a particular subject. With their unique mix of varied contributions from Original Research to Review Articles, Frontiers Research Topics unify the most influential researchers, the latest key findings and historical advances in a hot research area! Find out more on how to host your own Frontiers Research Topic or contribute to one as an author by contacting the Frontiers Editorial Office: **researchtopics@frontiersin.org**

MAGNETIC RECORDS OF EXTREME GEOLOGICAL EVENTS

Topic Editors:
Eric Font, Universidade de Lisboa, Portugal
Alexandra Abrajevitch, Russian Academy of Sciences, Russia
Fabio Florindo, Istituto Nazionale di Geofisica e Vulcanologia, Italy

The Deccan Magmatic Province, India.
Courtesy by Thierry Adatte

Recent advances in environmental magnetism offer the opportunity to link the magnetic signature of marine and continental rocks to the paleoenvironmental and paleoclimatic settings that controlled their formation or deposition, as well as to post-depositional events, such as diagenesis, that can alter their primary signature. This Research Topic assembles studies that used state of the art rock magnetic techniques to unravel the causes and effects of catastrophic geological events, including tsunami, meteorite impacts, Archean oxygenation event, geomagnetic reversals, and global climate changes linked to large volcanic eruptions.

Citation: Font, E., Abrajevitch, A., Florindo, F., eds. (2017). Magnetic Records of Extreme Geological Events. Lausanne: Frontiers Media. doi: 10.3389/978-2-88945-170-8

Table of Contents

frontiers in Earth Science

EDITORIAL
published: 08 November 2016
doi: 10.3389/feart.2016.00094

Editorial: Magnetic Records of Extreme Geological Events

Eric Font[1]*, *Alexandra Abrajevitch*[2] *and Fabio Florindo*[3]

[1] *Faculdade de Ciências, Instituto Dom Luís, Universidade de Lisboa, Lisboa, Portugal,* [2] *Institute of Tectonics and Geophysics, Russian Academy of Sciences, Khabarovsk, Russia,* [3] *Istituto Nazionale di Geofisica e Vulcanologia, Rome, Italy*

Keywords: magnetism, geology, extreme events, geosciences, earth sciences

The Editorial on the Research Topic

Magnetic Records of Extreme Geological Events

The normal evolution of the Earth has been punctuated in the past by sudden, dramatic events. Changes in the Earth's rotational speed, asteroid impacts, violent volcanic eruptions, earthquakes, tsunami, and extreme climatic events have periodically caused changes in the environment, which often harmed dominant life forms, but also triggered rapid biotic evolution by opening up many new ecological niches. Changes in sedimentation patterns and redox conditions that accompany catastrophic events affect accumulation, formation and alteration of magnetic minerals in rocks, and thus leave evidence in the geologic record. This E-Book is derived from the *Frontiers in Geomagnetism and Paleomagnetism* Research Topic entitled "Magnetic Records of Extreme Geological Events." Nine contributions included in this book adopt very different approaches to answer the varied and complex research challenges related to the study of the past catastrophic events.

Two contributions to this Research Topic discuss high energy fluvial events. Building on their previous extensive experience in studies of historical high-energy flooding events in the region, Wassmer et al. present reconstruction of the flooding characteristics during the 4220 BP paleo-tsunami event in North Sumatra. In addition to classical sedimentological analysis, the authors used the Anisotropy of Magnetic Susceptibility (AMS) technique to assess flow direction that prevailed during sediment emplacement. Information gathered about orientation, energy and flow patterns over the coastal plain have demonstrated similar behavior of the 4220 BP and the historical 2004 tsunami events. The possibility of using rock magnetic techniques for dating high energy fluvial events is discussed by Muxworthy et al. The authors used unblocking temperatures of viscous remanent magnetization (VRM) in erratics associated with three large flood events to estimate the timing of block rotations. Their findings suggest that the VRM dating method works the best for recent events (<2–3 ka) where the ambient temperature history can be constrained, while age estimates of older events have greater uncertainty.

The next two contributions to this Research Topic are broadly related to understanding geologic signatures of asteroid impacts. In their original research article, Kubo et al. investigated the cause of the anomalously strong natural remanent magnetization observed in shocked granitic rocks in the crystalline core of the Vredefort crater—the largest and oldest (2023 ± 4 Ma) known terrestrial impact structure. The authors found that coarse magnetite grains are subdivided by hematite lamellae creating striped magnetic domains, and attributed the strong remanence primarily to this unusual domain structure, which formed as the result of post-impact high-temperature metamorphic alteration of shock-strained magnetic grains. Later terrestrial lightning strikes on the partially oxidized magnetite may have also intensified the remanence. In the mini-review article, Font and Abrajevitch discussed two competitive explanations, volcanism vs. asteroid impact, for the decrease in magnetic susceptibility values in the sediments just below the Cretaceous-Paleogene

OPEN ACCESS

Edited and reviewed by:
Kenneth Philip Kodama, Lehigh University, USA

***Correspondence:**
Eric Font
font_eric@hotmail.com

Specialty section:
This article was submitted to Geomagnetism and Paleomagnetism, a section of the journal Frontiers in Earth Science

Received: *27 September 2016*
Accepted: *19 October 2016*
Published: *08 November 2016*

Citation:
Font E, Abrajevitch A and Florindo F (2016) Editorial: Magnetic Records of Extreme Geological Events. Front. Earth Sci. 4:94. doi: 10.3389/feart.2016.00094

boundary. Based on environmental proxy records from two reference sections, Bidart (France) and Gubbio (Italy), the authors suggested that the evidence for dissolution of ferrimagnetic minerals accompanied with the presence of akaganeite, an unusual mineral phase in marine sediments, is best explained by an ocean acidification and aerosol deposition event linked to the Deccan Phase-2 volcanism.

Another two contributions to this Research Topic are related to studies of geomagnetic reversals. In addition to their use for dating and correlation, high resolution records of the transitional field behavior provide key constraints on the working of the geodynamo. In their original research article, Soler-Arechalde et al. presented a record of the Matuyama-Brunhes geomagnetic reversal obtained from the tephra-paleosol sedimentary sequence of Tlaxcala (Central Mexico). The authors demonstrated the primary origin of the magnetic remanence and suggested that paleosol sequences can provide good high resolution records of the geomagnetic magnetic field during geomagnetic reversals. In the following Perspective article, Pacca et al. analyzed the geomagnetic reversal frequency rates over the past 510 Myr and noted that the reversal frequency correlates with the Earth's rotation changes, as well as with the $\delta^{18}O$ oscillations, which reflect the glacial and interglacial periods. The authors hypothesized that the $\delta^{18}O$ oscillations it can be used as a possible indicator to explain the length of day variations and the associated changes in the geodynamo regime.

The last contributions to this Research Topic are broadly related to oxygenation events in the Earth history. Carlut et al. presented a study of the Late Archean Boolgeeda Banded Iron Formation (Western Australia), the association of which with free oxygen derived from oxygenic photosynthesis has long been recognized. The authors report the presence of two distinct populations of magnetite characterized by different Verwey transition temperatures, within a 2 m thick sedimentary section. They argue that secondary silicon-rich magnetite characterized by the low Verwey transition temperature can be linked to biological activity, and may thus be a potential biomarker.

Based on the presence of hematite, taken as the evidence for high oxygen fugacity during formation of the 780 Ma old subduction-associated rocks that are now outcropping in the Arabic peninsula, Macouin et al. hypothesize that the Neoproterozoic Oxygenation Event may have been triggered by multi-million years oxic volcanic emissions during a protracted period at the end of the Neoproterozoic when continents were assembled in the Rodinia supercontinent. In a short commentary paper, Nédélec and Borisova questioned the primary origin of the hematite identified by Macouin et al. in the granites and argued against the contribution of the associated magmas in the Neoproterozoic Oxygenation Event. In their response, Macouin et al. provide new arguments defending the primary origin of hematite.

Collectively, the articles in this Research Topic represent an interesting range of opinions, reviews, and original studies that contribute to understanding the role of catastrophic events in the Earth history. We hope you enjoy this eclectic mix.

AUTHOR CONTRIBUTIONS

EF, AA, and FF wrote the editorial text.

Conflict of Interest Statement: The authors declare that the research was conducted in the absence of any commercial or financial relationships that could be construed as a potential conflict of interest.

frontiers in Earth Science

METHODS
published: 21 July 2015
doi: 10.3389/feart.2015.00040

Contribution of anisotropy of magnetic susceptibility (AMS) to reconstruct flooding characteristics of a 4220 BP tsunami from a thick unconsolidated structureless deposit (Banda Aceh, Sumatra)

Patrick C. Wassmer[1,2,3]*, *Christopher A. Gomez*[3], *T. Yan W. M. Iskandarsyah*[2,4], *Franck Lavigne*[1] and *Junun Sartohadi*[5]

[1] Laboratory of Physical Geography, UMR- Centre National de la Recherche Scientifique 8591, University of Paris 1, Panthéon-Sorbonne, Meudon, France, [2] Laboratoire Image, Ville, Environnement, Université de Strasbourg, UMR 7362, Strasbourg, France, [3] Department of Geography, College of Sciences, University of Canterbury, Christchurch, New Zealand, [4] Laboratorium Geologi Lingkungan dan Hidrogeologi, Fakultas Teknik Geologi, Universitas Padjadjaran, Bandung, Indonesia, [5] Faculty of Geography, Gadjah Mada University, Yogjakarta, Indonesia

OPEN ACCESS

Edited by:
Eric Font,
University of Lisbon, Portugal

Reviewed by:
Jean-Luc Bouchez,
Toulouse University, France
Hervé Regnauld,
University of Rennes 2, France

***Correspondence:**
Patrick C. Wassmer,
Laboratoire de Geographie Physique, UMR-Centre National de la Recherche Scientifique 8591, 1, Place Aristide Briand, 92195 Meudon, France
patrick.wassmer@unistra.fr

Specialty section:
This article was submitted to Geomagnetism and Paleomagnetism, a section of the journal Frontiers in Earth Science

Received: 05 May 2015
Accepted: 03 July 2015
Published: 21 July 2015

Citation:
Wassmer PC, Gomez CA, Iskandasyah TYWM, Lavigne F and Sartohadi J (2015) Contribution of anisotropy of magnetic susceptibility (AMS) to reconstruct flooding characteristics of a 4220 BP tsunami from a thick unconsolidated structureless deposit (Banda Aceh, Sumatra). Front. Earth Sci. 3:40. doi: 10.3389/feart.2015.00040

One of the main concerns of deciphering tsunami sedimentary records along seashore is to link the emplaced layers with marine high energy events. Based on a combination of morphologic features, sedimentary figures, grain size characteristics, fossils content, microfossils assemblages, geochemical elements, heavy minerals presence; it is, in principle, possible to relate the sedimentary record to a tsunami event. However, experience shows that sometimes, in reason of a lack of any visible sedimentary features, it is hard to decide between a storm and a tsunami origin. To solve this issue, the authors have used the Anisotropy of Magnetic Susceptibility technique (AMS) to characterize the sediment fabric. The validity of the method for reconstructing flow direction has been proved when applied on sediments in the aftermath of a tsunami event, for which the behavior was well-documented like the 2004 Indian Ocean Tsunami (IOT). We present herein an application of this method for a 56 cm thick paleo-deposit dated 4220 BP laying below the soil covered by the 2004 IOT at Lampuuk, SE of Banda Aceh, North Sumatra. We analyzed this homogenous deposit, lacking of any visible structure, using methods of classic sedimentology to confirm the occurrence of a high energy event. We then applied AMS technique that allowed the reconstruction of flow characteristics during sediment deposition. We show that the whole sequence was emplaced by successive uprush phases and that the local topography played a role on the re-orientation of a part of the uprush flow, creating strong reverse current. This particular behavior was reported by eyewitnesses for the 2004 IOT event.

Keywords: paleo-tsunami, flow behavior reconstruction, anisotropy of magnetic susceptibility, structureless sediment deposit, Banda Aceh

Introduction

The Anisotropy of Magnetic Susceptibility (AMS) of rocks and sediments is certainly one of the most versatile techniques in geology, as it finds usage from Archean rocks (e.g., Borradaile et al., 2012) to contemporary deposits (e.g., Wassmer et al., 2010; Wassmer and Gomez, 2011). The method, known as AMS, based on a first inference that ferromagnetic minerals realign after a rock is subject to deformation, started with the early findings of Graham (1954) on sedimentary rocks and Balsley and Buddington (1960) who proved that the AMS could detect the fabric of minerals in orthogneiss and granites. Since then the method has been recognized as an effective petrofabric tool for granites (Bouchez et al., 1990; Bouchez, 1997; Benn et al., 2001; Esmaeily et al., 2007; Njanko et al., 2010; Raposo et al., 2012). By extension, the method has also been used for other types of magma and lava emplacement, such as mid-oceanic ridges basalts for instance (Veloso et al., 2014).

As mentioned above, sedimentary rocks have also been the subjects of similar research: Graham (1954) used the AMS to evidence the deformation of sedimentary rocks of the Appalachia Mountain (Graham, 1966). The method has then been extended to a variety of sedimentary environment, either consolidated material, e.g., the non-deformed Callovo-Oxfordian argillites of the Paris Basin, France (Esteban et al., 2006), the tectonically impacted marine clays of the Crotone basin, Italy (Macri et al., 2014), deep-sea sediments transport (Housen et al., 2014); or unconsolidated material, e.g., tsunami washover deposits in Indonesia (Wassmer et al., 2010; Wassmer and Gomez, 2011) and New Zealand (Kain et al., 2014), or lake sediments in China (Dong et al., 2013).

The AMS technique reveals the fabric acquired by sediments during deposition, i.e., the statistical common organization of the grains, providing that the grains have an oblong shape. AMS is based on the induction of a magnetic field (H) applied to a small sample of undisturbed sediment. The material exposed then produces an induced magnetic field (M) from which the volumic magnetic susceptibility can be calculated ($M = k.H$). This volumic magnetic susceptibility can vary along different orientations of the inductor magnetic field H, depending on the various magnetic minerals present in the sample. The induced magnetic field of the sample can be measured from different directions, for example by spinning the sample to the signal source in all three axes. These data characterize the shape of the induced field anisotropy. If this shape is a sphere, the field is perfectly isotropic but usually the field is close to an ellipsoid figured by a long, a short, and an intermediary axis, K_{max}, K_{min}, K_{int}. For sedimentary deposits, the maximum susceptibility axis, K_{max}, generally parallel to the mean long axis of the individual particles, reflects the internal fabric of the material.

AMS Applied on the 2004 Indian Ocean Tsunami (IOT) Deposits in Banda Aceh

The research team has investigated tsunami deposits using the AMS technique at different locations worldwide, e.g., in Japan, in New Zealand (Kain et al., 2014), along the coast of Morocco, and in Indonesia near Banda Aceh (Wassmer et al., 2010; Wassmer and Gomez, 2011) and in the Sunda Strait (Paris et al., 2014).

The 2004 IOT offers a unique chance to link the flow characteristics over land with the sediment deposits. From the available sedimentary material, Wassmer et al. (2010) have (1) clearly identified tsunami sandy deposits, lying on the often-truncated ante-2004 soil; and (2) linked the sedimentary records to the flood characteristics described by numerous eyewitnesses (Lavigne et al., 2009). Despite the breadth of available data, numerous points remained unveiled, prior to the usage of AMS. Indeed, eyewitnesses agreed on the emplacement of most of the deposits by the landward flow or uprush, but traditional techniques of sediment analysis could not provide convincing corroborating evidence, and especially no recording of the precise wave orientation. Trying to solve this issue, the research team tested several methods, such as deposits peelings, resin impregnations and thin sections in order to derive a proxy of the sediment fabric, but none of these method provided conclusive results, and we therefore turned toward the AMS method to draw conclusion at the fine scale. The combination of AMS with other traditional sediment analysis techniques proved that it was possible:

1) to reconstruct the flow direction of each individual wave of the wave-train that contributed to the sedimentary signature of the event (Wassmer and Gomez, 2011);
2) to evidence that not all the waves have left perennial records, the deposit of the first wave being erased by the second and more energetic wave while the influence of the last waves, with less energy was restricted to the proximal zone Lavigne et al., 2009; Wassmer et al., 2010);
3) to estimate the sediment stock brought by each wave, sorting out the part emplaced after the turbulent front passed through and the part emplaced by the tail of the wave (unpublished data);
4) to identify the sediment sources that provided the material for the sediment recording of the event (Wassmer et al., 2007, 2010);
5) to evaluate, in a bay context, the role played by the refraction/reflexion of the waves along the surrounding shores on the incidence angle of each wave during the event (unpublished data);
6) to reconstruct the characteristics of each wave:

   i. identifying the layers emplaced during the different phases of the tsunami swash cycle of the waves, i.e., uprush, slack, or backwash (Wassmer et al., 2010);
   ii. retrieving the variations of sedimentation dynamics from base to top for each deposit interval corresponding to the material emplaced by individual waves within the wave train (ibidem);

All these studies helped us to build the knowledge necessary to tackle paleo-tsunami deposits investigation using AMS, for which both topography and flow dynamics are unknown.

Objectives

Building on this extensive broad experience, the present article aims to contribute to the research-body on AMS on unconsolidated sediments, with a central focus on the recording of the 4220 BP thick tsunami deposit near the present-day village of Lampuuk, South Banda Aceh, Sumatra (Wassmer, 2015). The AMS technique, tested, and applied on contemporary deposits will therefore prove to be efficient to characterize sediments deposited by paleo-extreme energy events, such as paleo-tsunami.

Study Material and Location

The very flat coastal plain of Lampuuk is delimited to the North and the North-West by an amphitheater-like morphology realized by the steep lowest slopes of the small mountain range ending Sumatra Island to the NW, and by the small crest line oriented SE-NW closing the plain to the NE (**Figure 1**). A 800 m large pass interrupts the amphitheater continuity at the level of Lampisang village. This particular morphology had a role in controlling the flow behavior during the 2004 tsunami event.

Investigations carried out at Lampuuk Bay in 2005, 2006, and 2007 allow identifying, below the 25 cm thick ante-2004 soil, a 56 cm thick tsunami deposit displaying the same characteristics than those of the 2004 IOT deposits. This paleo-event, that has been dated 4220 ± 40 BP (Poz. 16331) from wood debris collected at the base of the sediment layer, has never been revealed in this area before (Wassmer, 2015). This finding is most probably to be linked to tsunami deposits of the same period identified in Maldives (Mörner, 2007); in Sri Lanka (Jackson et al., 2008, 2014; Ranasinghage, 2010) and near Padang, West Sumatra (Dura et al., 2011).

Methodology

Field Sampling

The sampling of unconsolidated sediments for AMS analysis is a delicate operation. To ensure reliability of the results, the sampling must be done meticulously when dealing with soft-sediments, the fabric of unconsolidated grains being easily altered during sampling.

During the field work campaign of March 2007, the authors dug a trench for sediment sampling from the wall. The outcrop was reworked using a trowel, until the clinometer attested of perfectly vertical wall. To collect the samples, boxes with a small hole of 1 mm diameter at the bottom—to allow air to escape—were plugged horizontally in identified tsunami layers (**Figure 2**). A clinometer was used during the process, in order to keep a strict horizontality. Azimuth and plunge of the plugging axis (axis 3) of the box have been noted on the box side (permanent ink) as well as the axis 3 direction, and the two other axes of the box (1 and 2).

The removal of the box from the wall must be done with the outmost care in order to avoid any disturbance of the structure of the sample. The material, once leveled to the rim, the box is sealed with a tape in order to keep its moisture, which guarantees the best preservation of the fabric. The sampling boxes must be propped up in a hard-box and away from any shock before laboratory analysis. The time slot between sampling and laboratory measurements must be as short as possible.

Laboratory Analysis and Data Representation

Grain Size

Before analysis, organic matter was removed from the samples with hydrogen peroxide, then washed with KCl or HCl to remove the flocculating ions, and agitated in distilled water and sodium hexametaphosphate during 4–6 h. Particles of size exceeding 2000 μm were separated thanks to the help of a T-34 sieve size. From normal samples, grain size measurement was performed using a Beckman Coulter LS-230 (Range: 0.04 to 2000 μm) at the EOST Laboratory, University of Strasbourg, France.

The data are represented by cumulative grain size curves (**Figure 5**, Section Sedimentology of the 4220 BP Tsunami).

Grain size parameters were calculated: Mean grain size (μm, Trask); Sorting (ô, Folk and Ward) and Skewness (mm, Trask). Each parameter was plotted vs. depth (**Figure 4**, Section Section Description) in order to enlight the hydrodynamic characteristics variations along the tsunami event.

Anisotropy of Magnetic Susceptibility

The AMS samples were analyzed in Strasbourg using an AGICO MFK1A Kappabridge® equipped with an automatic spinner. During the spinning on each of the three axes, 64 measurements are performed and allow visualizing the anisotropy ellipsoid characterized by three susceptibility tensors, each normal to the others: K_{max}, K_{int}, and K_{min}. Data are represented by an equal angle, lower hemisphere projection of the larger principal axis (K_{max}) of the AMS tensor. On this lower hemisphere (**Figure 3**), each point is determined by the intersection of an axis passing by the center of the hemisphere and reflecting the magnetic fabric or the sediment fabric. Considering a horizontal flow, the plunge, and azimuth value of the K_{max} axis mimics the upstream imbrications of sand grains. In consequence for sample 1, with an azimuth due North and a plunge of 23° to the North the assumed direction of the flow responsible for the fabric is oriented to the South. For sample 2, with an azimuth of 232° and a 0° plunge, the K_{max} axis is horizontal and cross cuts the equatorial circle at 232° and 52° (**Figure 3**). Additional anisotropy parameters are determined by a combination of the values of the three main axis of the anisotropy ellipsoid (F or foliation parameter, L or lineation parameter, T or shape parameter, Fs or alignment parameter, q or ellipsoid shape factor). They reflect the shape of the ellipsoid and allow approaching the hydrodynamics conditions during sediment deposition (Tarling and Hrouda, 1993).

The sedimentary material of the deposit is made of almost 100% of quartz grains containing some very small individual black grains. This very weak content has been reported by Costa et al. (2015), for the same area of Lampuuk—Lhok Nga, who mentioned values ranging from 0.352 to 0.003%. The low bulk magnetic susceptibilities (76.10 to 149.95 10^{-6} SI) reflect a lack of ferromagnetic particles.

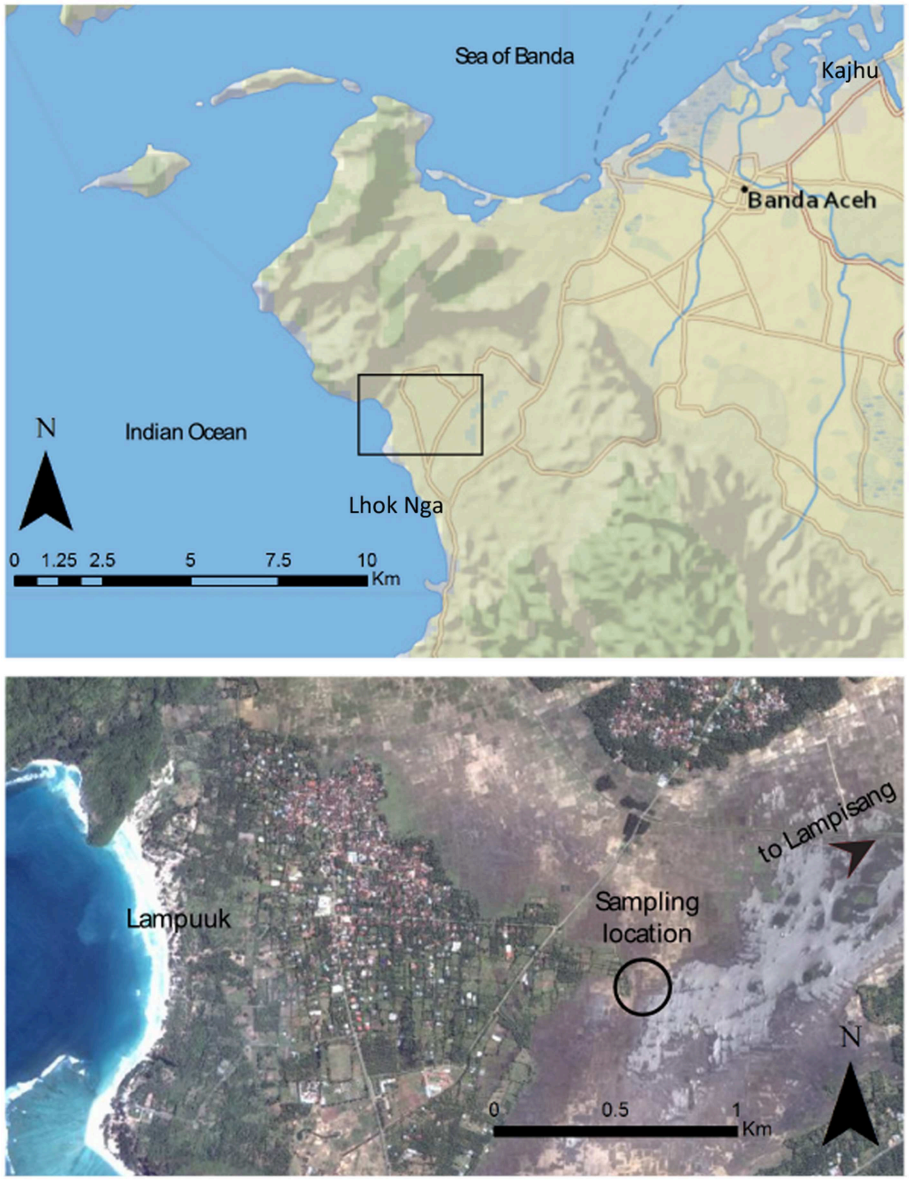

FIGURE 1 | General map of Banda Aceh area, North Sumatra, Indonesia. Black circle corresponds to investigation site.

Weaknesses of the Method

Sampling Related

a) Careful sampling is a key point for the accuracy of AMS measurement. The sampling boxes must be plugged perfectly horizontally otherwise a light tilting of the box might induce a bias in the tilting interpretation. As a horizontal plugging is sometimes hard to realize, we interpret with caution the plunge values located within the bracket 0° to 5° (**Figure 3**).

b) Sampling box size: the 20 mm.-side of the sampling boxes may constitute a limit for sampling layers thinner than 20 mm. Within a tsunami sequence, sediment layers emplaced are sometimes very thin in reason of a weak deposition or a post-depositional scouring. For fine sediments displaying a good cohesion we circumvent this issue in uncovering the surface of the thin layer and we plugged successively twice or three times in the sediment in order to fill the box. The repetition of this unconventional technique (three plugging for a single sample) five times on the same layer gave results perfectly identical.

Material Related

a) Sampling is not possible on coarse sand: unsorted material containing coarse sands or gravels cannot be sampled. If the box edge meets a granule during plugging, a perturbation of the fabric of the sample may occur.

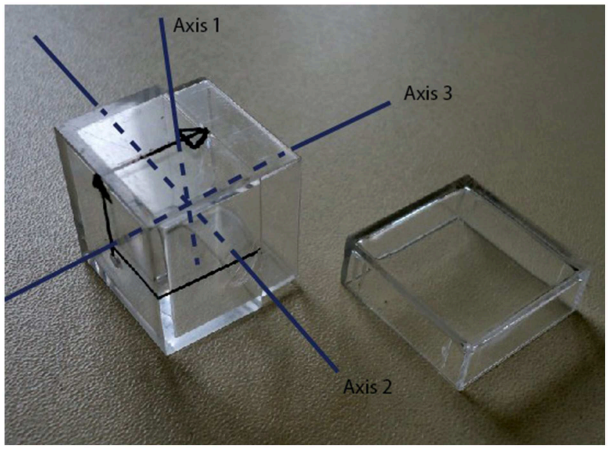

FIGURE 2 | AMS sampling box.

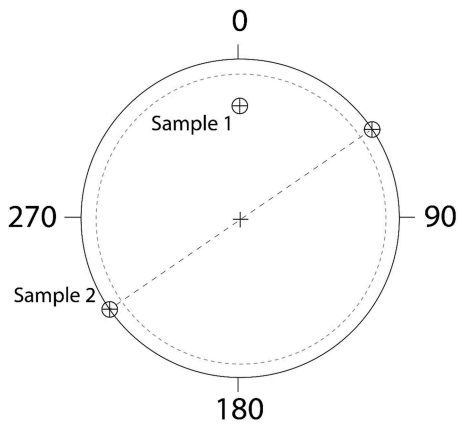

FIGURE 3 | Example of AMS data projection. The confidence zone between 0° to 5° is limited by the dashed circle.

b) Sampling on moist sediments only: In order to maintain a good cohesion of the sediments during plugging well as between sampling and analysis, sediments must be moist. In dry conditions, a water mister can be used to slowly moist the outcrop.

Interpretation Related

a) Flow direction is retrieved from the overall sediment fabric but previous research (Rusnak, 1957; Allen, 1964; Rees, 1968) show that depending on the flow velocity, the grains long axes will parallel or be normal to the flow direction prevailing during emplacement. This issue is largely developed below in Section AMS Interpretation of the Flow Direction.

Results

Section Description (Figure 4)

The deposit is made of a 56 cm thick layer of uniform medium sand, which lacks visible sediment structure and lies on a thick black paleo-soil (paleo-soil 1). At the base of the deposit, just above this paleo-soil 1, abundant pieces of broken wood were retrieved, with elongated pieces following North-South orientation. Retrieved tree trunk- and branch- splinters showed diameters ranging from 1 to 5 cm with maximum length of 30 cm. Within and above this 10–20 cm thick layer of debris, abundant in bioclasts (coral and shells) incorporated in gray muds, lays a mixed silts (57%) and medium sands (36%) unit characterized by numerous rip-up clasts of gray clay with an average size of 4–5 cm. Above this 10–20 cm basal layer, the first 28 cm are composed of homogenous structureless medium sands, brownish-pale colored with locally browner patches. The deposit color evolves vertically to light gray, gaining a yellowish color in the 10 last cm below the ante 2004 IOT soil (palaeosoil 2). The color variation is not accompanied by any visual grain size variation. Within the palaeosoil 2, the texture corresponds to sandy loam at the base evolving progressively to clay loam to the top.

Sedimentology of the 4220 BP Tsunami

The base of the section is made of silty material (mean grain size: 35 μm), very poorly sorted, and characterized by a positive skewness (very coarse skewed). Above, the mean grain size of the whole paleo-tsunami section ranges between 450 and 500 μm, and these moderately sorted medium sands represent 96–98% of the deposit. The skewness for all the section is again positive (very coarse skewed). The grain size cumulative curves of the 4220 BP deposit (**Figure 5**) show a curve shifted to silts for sample 1, at the very base. The curves for the samples 2–10 are almost perfectly superimposed and correspond to medium sands.

Sediment morphoscopy has been performed on the sands of the 4220 BP deposit and compared to the morphoscopy of the dune material which constituted the main sediment source for the 2004 event (Wassmer et al., 2007). The material of the deposit is composed almost exclusively by quartz material. The finer fraction (63–125 μm) is constituted by angular clasts. Angular clasts are present in the medium fraction (250–500 μm) but sub-angular grains dominate. The grain surfaces are mainly matted but the rounded angles are generally glossy. The coarser mode (1000–1600 μm) is represented by rounded to well-rounded grains displaying the matt surface characteristic of aeolian sands. Their most convex parts (rounded angles) are glossy. The bioclast content is very weak and only rare sponge spicules and foraminifera were identified. Compared to the potential source of the dune material, the proportion of mineral/bioclast content turns around 50–50%. The main part of the material is well-rounded and within the mineral part solely, coarse matt grains appears to be more frequent and do not display glossy convex surfaces.

Passega's CM diagram (**Figure 6**) is used to assess water flooding energy variations. The homogeneity of the processes revealed by grain size analysis is also reflected by the CM diagram that shows that the 4220 BP paleo-tsunami section was deposited by a strong energy flow under rolling and ground suspension conditions without evidence of any variations along the deposit emplacement at the exception of the silts deposited at the base.

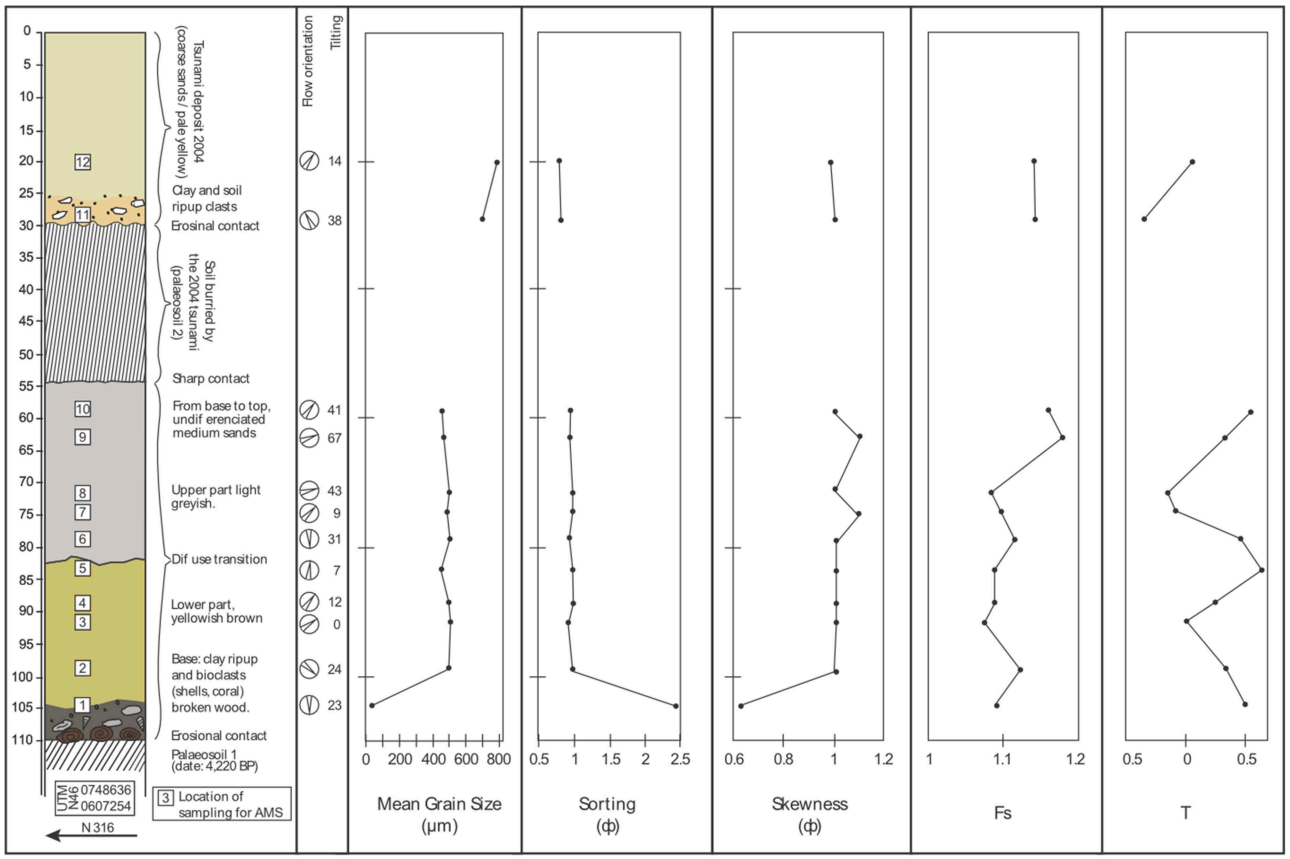

FIGURE 4 | Section description showing the emplacement of sampling boxes.

The analysis of the main physical characteristics of the deposit suggests the following conclusions:

i) The material originates from a unique and moderately-sorted sediment source, and most probably from the sand dunes located on the sea front:

ii) The material emplaced constituted exclusively by mineral sand grains underwent a strong winnowing action before deposition allowing to clear the sand dune material from its original bioclast content (50% of the dune material);

iii) The deposit reflects an apparent homogeneity of the processes from the base to the top during the emplacement of the whole 4220 BP sequence at the exception of the very base. The single and uniform transport and deposition process is reflected by the almost perfect superimposition of the grain size curves and a positive skewness from base to top of the deposit (Vijaya Lakshmi et al., 2010);

iv) The lack, within the deposited sequence, of any layer characterized by the presence of fine terrigenous material invokes a single uprush sequence.

v) The CM diagram strongly suggests that the material was deposited under high energy (**Figure 6**).

Even if these insights appear as significant for the understanding and reconstruction of the palaeo tsunami, the detailed behavior of the flow (directions, energy, and velocity variations) cannot be assessed only from the sedimentary characteristics of the deposits.

AMS Technique Contribution

Preamble

The ellipsoid shape factor $q = (K_{max}-K_{int}).(K_{max}+K_{int})/(2-K_{min})$ is an indicator of either a depositional or a tectonic fabric. A value less than 0.7 indicates a non-deformed sediment (primary fabric) while a value higher than 0.7 suggests that a tectonic activity altered the primary fabric (Hamilton and Rees, 1970). For the 4220 BP deposit, q is ranging below 0.7 with the exception of samples 8 and 9 that are slightly above this value. Hence considering that the primary fabric was not modified by post-depositional processes, the AMS approach can be used on these sediments.

Reconstruction of Flow Behavior

Interpretation of the results (**Figures 4**, **7**) allow proposing a reconstruction of the water flow behavior. From the beginning to the end of the 4220 BP event, six phases can be identified as follows (the number in brackets corresponds to sample number):

1. Uprush wave (0). The AMS was impossible to measure at the base of the deposits due to the material heterogeneity. We

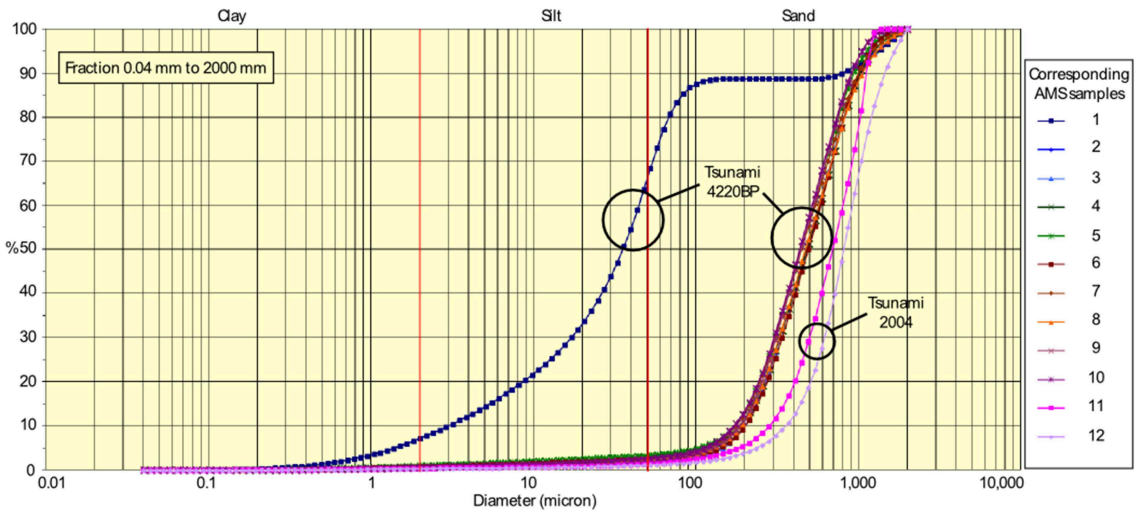

FIGURE 5 | Cumulative grain size curves for 4220 BP and 2002 tsunamis deposits.

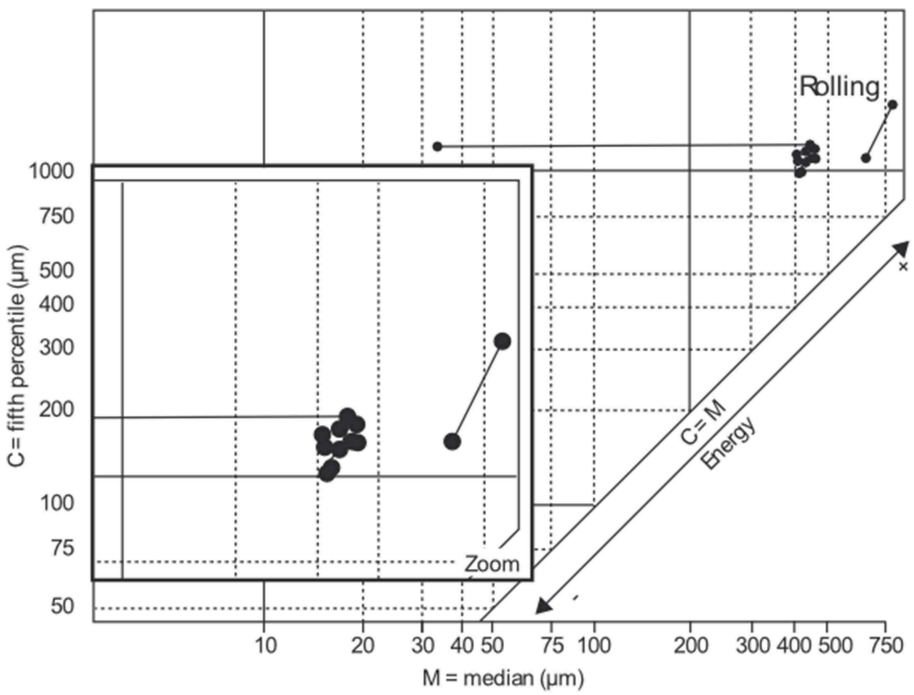

FIGURE 6 | Passega CM diagram.

assume however, from field evidence that the first wave was heading for North with an energy strong enough to bring numerous marine bioclasts and coarse sands, to break trees, and align the debris with a rough North-South orientation and to remove rip-up clasts of palaeosoil 1.

2. First backwash phase: southbound first (1), then to SE (2).
3. Slack stage or very slow motion, to SE (see ® limits of the method: rolling/tilting) no evidence of tilting (3)
4. Second uprush stage, to the NNE first (4) and then due N (5).
5. Backwash stage to the South (6).
6. Third uprush stage to the NNE (7), to the NE (8 and 9) and to the NNE (10).

If one considers the 24 cm thick soil developed from the paleo-tsunami deposit (paleo-soil 2), the sedimentary sequence emplaced by the 4220 BP event increases in thickness up to 65–70 cm. The clay loam texture of the upper part of the paleo-soil corresponds to the last slack and backwash stages,

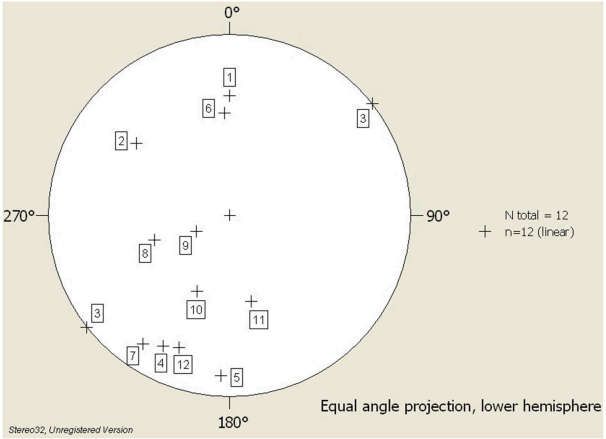

FIGURE 7 | Equal angle, lower hemisphere projection of the *Kmax* for each layer investigated: 1-10 from bottom to top of the paleo-tsunami deposit, 11 and 12 for the 2004 IOT tsunami deposit.

when the high concentration of fines in suspension resulting of the high turbulence of the water begins to settle in a laminar dominated flow. This fine material has been subject to paedogenesis processes. Bioturbation has erased the original fabric making useless an AMS approach.

Reconstructing Other Characteristics of Emplacement Processes from AMS

Besides the flow direction that constitutes the major contribution of AMS, additional parameters, calculated from the intensities of axes of the anisotropy ellipsoid, or from their logarithmic values, allow us to precise some characteristics of the emplacement process (**Figure 4**: *T*, *Fs*) The shape parameter (*T*) quantifies the relative role of lineation and foliation, i.e., indicates a deposition under the domination of settling or traction. The 4220 BP sediments have been emplaced mainly under a settling process (foliation dominant) with the exception of samples 7 and 8 where lineation dominates.

The alignment parameter (*Fs*), related to the intensity of the K_{max}, is supposed to increases with the energy of the bottom currents (de Menocal, 1986; Park et al., 2000). It can be a sensitive recorder of paleo-velocity variations (Ellwood and Ledbetter, 1977) as for the 4220 BP tsunami (**Figure 4**). During the backwash stage a slight velocity increase (1) to (2) can be noted before a velocity drop (3). The uprush is rather low (4) and (5) while the following backwash is characterized by a higher velocity. The second uprush phase, first corresponds to a rather weak flow (7) and (8) before an acceleration of the flow (9) and (10).

The angle of imbrications being larger for a turbulent flow over a rough bottom (coarse grain size) than for a turbulent flow over a smooth bottom (small grain size; Rusnak, 1957), the plunge value (**Figure 4**) is considered to be related to the velocity of the flow and to the density of the particles in the bottom traction carpet. The 4220 BP deposit displays strong tilting values ranging from 12° to 67° with the exception of three weaker values. This is consistent with a grain inertia regime at the base of the water column (Hamilton et al., 1968) and with the medium to coarse grain size of the material.

The 2004 IOT deposit is thinner than the 4220 BP deposit. The sedimentary characteristics of its base reveal the domination of traction under high velocity current during deposition. Within the upper part of the deposit foliation dominates reflecting a velocity drop accompanied by an important settling under a stable current.

Discussion

Reconstruction of Water Behavior Combining Sedimentology and AMS

If we take into account the data provided by sedimentology and AMS, it is possible to reconstruct hydrodynamic conditions that prevailed during this paleo high-energy flooding on the coastal plain of Lampuuk (**Figure 4**).

This 4220 BP event was composed of:

a) A first northward oriented uprush; the strong flow is only attested by the abundance, composition and orientation of the debris laying on the paleo-soil 1;
b) A backwash flow oriented southward (1) with low velocity currents, followed by an increasing velocity of bottom currents with settling processes (2). Water acceleration in the proximal domain has been reported frequently by eyewitnesses at the end of the backwash stage of the 2004 event.
c) A weak flow to the southeast with an equilibrium between settling and traction corresponding to the end of the backwash stage (3);
d) A drastic increasing of sediment settling during a rather low velocity uprush phase [(4) and (5)];
e) Bottom currents increasing during this backwash phase (6) dominated by settling;
f) Last uprush phase recorded: first traction dominates [(7) and (8)] with a rather weak current then settling increases strongly [(9) and (10)] under conditions of strong bottom current. This part of the deposit may come from the contribution of different pulsations, the variations in K_{max} azimuths thus reflecting wave refraction or diffraction along the bay.

Comparison with the 2004 Tsunami

The homogeneity of the 4220 BP deposit reflected by **Figure 6** can be explained by two elements of local context:

1. A unique source for the sediments: by analogy with the 2004 event, the 15 m-height sand dunes may have been shaved to the ground by the two first waves, the moderately sorted sand stock being spread on the wide flat coastal plain. The grain size distribution of sand collected on a remnant part of a dune eroded during the 2004 event, and cleared out of bioclasts (constituting around 50% of the material), almost perfectly superimposes to the grain size distribution of sediments emplaced by the 2004 tsunami (lacking of any bioclast in this area in reason of an efficient winnowing action of the turbulent waves). Moreover, the sand morphoscopy analysis from the

remnant parts of the dunes and the deposits of 2004 confirm that the sands are similar to the 4220 BP paleo-deposits. Therefore, the source of the paleo-deposit had likely similar characteristics than the 2004 event, i.e., the material mainly came from coastal sand dunes. This finding is consistent: (*i)* with the sedimentary records of the 2004 tsunami that were composed of moderately sorted sands with a mean grain size around 700–800 μm and very coarse skewed provided at 88–100% by sand from the dunes eroded on the sea front (Wassmer et al., 2007), and (*ii)* with the 2004 oral testimony of a New Zealander eyewitness who describes a huge yellowish-colored "geyser" of water and sand, higher than the dunes row, produced by the two first waves impacting and eroding the dunes (ibidem).

2. The energy of the surging waves in the investigated zone: on the eastern coast of Banda Aceh, Wassmer et al. (2010) showed that the energy of the flooding decreased landward, producing a progressive differentiation in the sedimentary signature. Near shore, in the proximal zone, the deposits are coarse and undifferentiated. In the distal zone, far inland, near the slack zone or "point of zero velocity prior to backwash flow" according to Dawson and Stewart (2007), fining upward sequences are superimposed and correspond to the record of individual successive waves. Lampuuk's palaeo tsunami site was located within the proximal zone, on the very flat coastal plain.

Huge Storm or Tsunami?

If the wood debris and the bioclasts abundance at the base of the sequence could be linked to a high-energy event, such as a catastrophic storm or a tsunami, the presence of large pieces of broken tree trunks and the clay rip-up clasts (**Figure 8**) strictly point toward a tsunami origin. The distance to the sea also calls for a tsunami hypothesis: 1.65 km at present day, this distance was probably slightly longer for thousands years ago, in reason of a local subsidence mentioned by Meltzner et al. (2006, 2010). Kawata et al. (2005) showed a co-seismic subsidence of 20 to 60 cm in Banda Aceh for the 2004 IOT, while Dura et al. (2011) state that the coastal lowlands of western Sumatra preserve an evidence of two Holocene ruptures (4200 and 3100 BP) of the Mentawai segment of the Sunda mega-thrust and that these ruptures resulted in a co-seismic subsidence of the coastline. The distance from the sea was therefore more important 4220 years BP at Lampuuk, rendering the site out of reach of the storm influence.

Additionally, the 2004 tsunami deposited coarser sands than the 4220 BP tsunami, suggesting a possible higher energy tsunami. This is also attested by the erosive basal contact with the soil and the presence of numerous rip-up clasts of soil within the sequence (**Figures 4**, **8**). One of the characteristics of tsunami deposits is the landward fining grain size of the sediments (Kortekaas and Dawson, 2007; Morton et al., 2007; Paris et al., 2007; Jankaew et al., 2008). If the 2004 and 4220 BP tsunamis emplaced at the same site material of different grain size in all likelihood from the same sea-front dunes (450–500 μm for the 4220 BP event and 700–800 μm for 2004 IOT), source, then it is reasonable to consider that when the 4220 BP tsunami took place the seashore was more distant.

FIGURE 8 | Contact paleo-soil 2 and 2004 IOT deposit showing rip-up clasts formation.

In summary, in giving access to the flow direction that prevailed during sediment emplacement, the application of AMS technique to unconsolidated sandy material related to paleo-tsunamis drastically increases our knowledge about the characteristics of such events.

The 2004 tsunami flooding orientation map was realized post-event in the same area of Lampuuk on the base of thousands measurements we performed on the orientation of elongated material laying on the ground as tree trunks, poles, fence posts (**Figure 9**). This map, which mainly reflects the behavior of the last energetic wave of the 2004 tsunami, shows a good correlation with the last recorded energetic waves of the paleo-tsunami (8, 9, and 10). The orientation of the 2004 first waves recorded (11 and 12) is well conforms to the orientation of the 4220 BP first waves (0, 4, and 5). In 2004 the first wave was followed by a receding and then, the following waves pushed inland without receding between them. At the end a strong backwash occurred. AMS data performed on the paleo-deposit show that the first wave (0) was followed by a backwash oriented first to the South (1) then to the southeast (2). This latter direction was also reported in 2004 by eyewitness that described the whirling movement of the water along the foot of the western slopes of the bay, guided by the amphitheater-like topography of the foothills (**Figure 1**), and the following receding toward southeast. The second receding (6) that is found for the paleo-event is likely due to a contrary bottom current oriented southeast initiated by the same whirling movement described in 2004 resulting from the strong impact of the second wave (34 m in this zone in 2004; Lavigne et al., 2009). The deposit emplaced by these two "apparent" backwash stages are then more related to impeded surging waves, producing a strong contrary seaward current, than actual backwash stages. This explanation is consistent with the homogeneity of the grain size and the positive skewness that otherwise would have been modified by a real backwash bringing a mixture of sandy

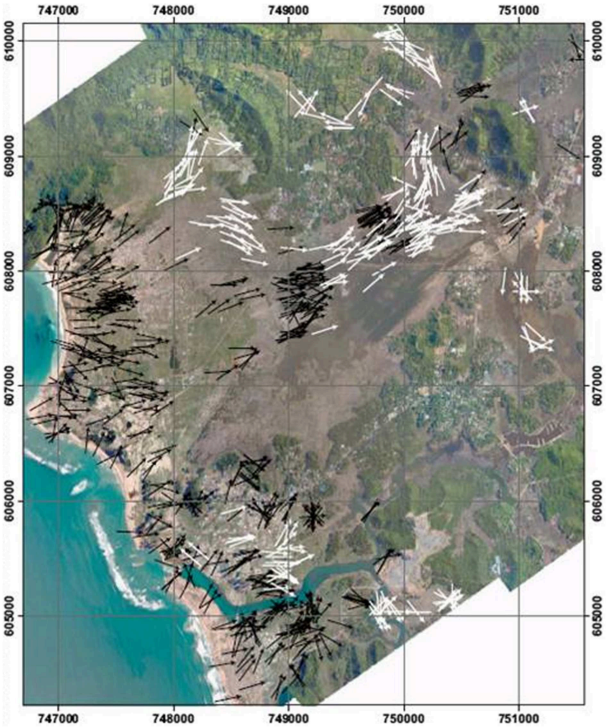

FIGURE 9 | 2004 IOT flooding directions evidenced from the orientation of elongated material laying on the ground after the event as tree trunks, poles, fence posts (from Grancher et al., 2011).

and terrigenous material. Such behavior is, in this context, site dependant.

AMS Interpretation of the Flow Direction

As presented above (section AMS) the flow direction is retrieved from the overall sediment fabric but previous research (Rusnak, 1957; Allen, 1964; Rees, 1968) show that depending on the flow velocity, the grains long axes will be parallel or normal to the flow direction prevailing during emplacement. In fact the general orientation of the long axis of the particles depends on the flow strength. For relatively strong currents (usually turbulent), the rolling and sliding of the prolate particles lead to their long-axis perpendicular to the flow direction, whereas a flow-parallel orientation dominates for weaker currents (laminar flow). Determination of the bulk orientation of the long axis of magnetic prolate particles (K_{max}) through AMS measurements leads to similar conclusions (Hamilton and Rees, 1970; Hrouda, 1982; Tarling and Hrouda, 1993). Consequently, the orientation of K_{max} is parallel to the direction of weak or laminar flow, whereas it is normal for stronger currents (Granar, 1958). This may render the flow directions evidenced by K_{max} hard to interpret.

For the present study, informations from the K_{max} were sufficiently clear (regarding the topographical context and the flooding behavior of the 2004 tsunami on the same area) to extract orientation data. In order to avoid misinterpretations in considering the flow direction as parallel to the long axis K_{max} of the susceptibility ellipsoid, several authors have shown that the pole of the magnetic foliation (K_{min}) points out the flow direction regardless of the depositional process, shingling, or rolling (Palmer et al., 1996; Ort et al., 2003; Giordano et al., 2008; Laberge et al., 2009; Willcock et al., 2014).

However, the method has several limitations, and results can't be yield from deposits modified by bioturbation and paedogenesis. The sediment records of high energy events like tsunamis along sea shore are prone to a more or less quick vegetation recovery, depending on the climate and the environmental conditions. This lead to a progressive loss of information, with soil construction, about the deposit characteristics for the upper part of the sequence deposited. This loss affected 20% of the original deposit thickness for the 4220 BP event, but we measured a loss of 14% from a 30 cm thick deposit in Kajhu area 5 years only after the 2004 IOT tsunami due to an active paedogenesis under tropical conditions).

Conclusions

The present contribution has demonstrated that the AMS technique applied to unconsolidated sediments can provide important proxies for paleo-events reconstructions, for which sedimentary signatures are preserved. In the present study, a 4220 BP tsunami deposit was clearly identified and its characteristics confirmed it to be a significant predecessor comparable to the 2004 Boxing Day tsunami. The AMS results helped the reconstruction of the flooding characteristics (orientation, energy, uprush flow patterns) and most especially the identification of at least three distinctive uprush pulsations during the paleo-event. AMS technique has contributed to show that the 4220 BP and the 2004 events behaved very similarly over the coastal plain of Lampuuk. The similarity here is most probably linked to the topographical context of the bay that controlled the uprush flow directions. Consequently, retrieved paleo-flow patterns from AMS also provided keys to unveil past-topographic features that would have disappeared.

Acknowledgments

Field work has been carried out in the frame of the Tsunarisk programme (coordinators: FL and R. Paris), funded by the French "Délégation Interministérielle pour l'Aide Post-tsunami" (DIPT). The authors are in debt to the reviewers who provided constructive comments, especially to Jean-Luc Bouchez and Hervé Regnauld, who conducted a very meticulous reading of the manuscript and contributes to significantly improve the original manuscript. We would like to express our gratitude to the editor for his prompt handling. The research has also been supported by Martine Trautmann, who helped with the sediment grain-size analysis.

References

Allen, J. R. L. (1964). Primary current lineation in the lower Old Red Sandstone (Devonian), Anglo-Welsh Basin. *Sedimentology* 3, 89–108. doi: 10.1111/j.1365-3091.1964.tb00635.x

Balsley, J. R., and Buddington, A. F. (1960). Magnetic susceptibility and fabric of some Adirondack granites and orthogneisses. *Am. J. Sci. Bradley Vol.* 258-A, 6–20.

Benn, K., Paterson, S. R., Lund, S. P., Pignotta, G. S., and Kruse, S. (2001). Magnetic fabrics in batholiths as markers of regional strains and plate kinematics: an example of the Cretaceous Mt Stuart Batholith. *Phys. Chem. Earth A* 26, 343–354. doi: 10.1016/S1464-1895(01)00064-3

Borradaile, G. J., Genviciene, I., and Charpentier, L. (2012). Magnetic fabrics in Archean granitoids, Northwestern Ontario: isolation of accessory and matrix contributions by inspection of AMS data. *Tectonophysics* 514–517, 115–122. doi: 10.1016/j.tecto.2011.10.011

Bouchez, J. L. (1997). "Granite is never isotropic: an introduction to AMS studies of granitic rocks," in *Granite: From Segregation of Melt to Emplacement Fabrics*, eds J. L. Bouchez, D. H. W. Hutton, and W. E. Stephens (Dordrecht: Kluwer Academic Pub), 95–112.

Bouchez, J. L., Gleizes, G., Djouadi, T., and Rochette, P. (1990). Microstructure and magnetic susceptibility applied to emplacement kinematics of granites: the example of the Foix pluton (French Pyrenees). *Tectonophysics* 184, 157–171. doi: 10.1016/0040-1951(90)90051-9

Costa, P. J. M., Andrade, C., Cascalho, J., Dawson, A. G., Freitas, M. C., Paris, R., et al. (2015). Onshore tsunami sediment transport mechanisms inferred from heavy mineral assemblages. *Holocene* 25, 795–809. doi: 10.1177/0959683615569322

Dawson, A. G., and Stewart, I. (2007). Tsunami deposits in the geological record. *Sediment. Geol.* 200, 166–183. doi: 10.1016/j.sedgeo.2007.01.002

de Menocal, P. (1986). *A magnetic Signature of Bottom-Current Erosion*. MS thesis, University of Rhode Island.

Dong, J., Gao, R., Wang, Y., Zhang, S., Yao, P., Chi, Z., et al. (2013). Magnetic fabric study of late holocene sediments in huangqihai lake, inner mongolia and its sedimentary significance. *Acta Geol. Sin. (Engl. Edn.)* 87, 186–196. doi: 10.1111/1755-6724.12040

Dura, T., C. M., Rubin, H. M., Kelsey, B. P., Horton, A., Hawkes, C. H., Vane, M., et al. (2011). Stratigraphic record of Holocene coseismic subsidence, Padang, West Sumatra, *J. Geophys. Res.* 116, B11306. doi: 10.1029/2011JB008205

Ellwood, B. B., and Ledbetter, M. T. (1977). Antartic bottom water fluctuations in the Vema channel: effects of velocity change on particle alignment and size. *Earth Planet. Sci. Lett.* 35, 189–198. doi: 10.1016/0012-821X(77)90121-2

Esmaeily, D., Bouchez, J. L., and Siqueira, R. (2007). Magnetic fabrics and microstructures of the Jurassic Shah-Kuh granite pluton (Lut Block, Eastern Iran) and geodynamic inference. *Tectonophysics* 439, 149–170. doi: 10.1016/j.tecto.2007.04.002

Esteban, L., Bouchez, J.-L., and Trouiller, A. (2006). The Callovo-Oxfordian argillites from the eastern Paris Basin: magnetic data and petrofabrics. *Compte Rendus Geosci.* 338, 867–881. doi: 10.1016/j.crte.2006.03.011

Giordano, G., Porreca, M., Musacchio, P., and Mattei, M. (2008). The Holocene Secce di Lazzaro phreatomagmatic succession (Stromboli, Italy): evidence of pyroclastic density current origin deduced by facies analysis and AMS flow directions. *Bull. Volcanol.* 70, 1221–1236. doi: 10.1007/s00445-008-0198-x

Graham, J. W. (1954). Magnetic susceptibility anisotropy, an unexploited petrofabric element. *Bull. Geol. Soc. Am.* 65, 1257–1258.

Graham, J. W. (1966). "Significance of magnetic anisotropy in Appalachian sedimentary rocks," in *The Earth beneath the Continents. Geophysical Monographs 10*, eds J. S. Steinhart and T. J. Smith (Washington: AGU), 627–648.

Granar, L. (1958). Magnetic measurements on Swedish varved sediments. *Arkiv foer geofysik* 3, 1–40. doi: 10.1029/2011JB008205

Grancher, D., Bar-Hen, A., Paris, R., Lavigne, F., Brunstein, D., and Wassmer, P. (2011). "Interpolation spatiale de données circulaires: application au tsunami du 26 décembre 2004," in *Tsunarisque: Le Tsunami du 26 Décembre 2004 A Aceh, Indonésie*. eds F. Lavigne and R. Paris (Paris: Publications de la Sorbonne), 49–58.

Hamilton, N., Owens, W. H., and Rees, A. I. (1968). Laboratory experiments on the production of gain orientation in shearing sand. *J. Geol.* 76, 465–472. doi: 10.1086/627344

Hamilton, N., and Rees, A. I. (1970). "The use of magnetic fabric in paleocurrent estimation," in *Paleogeophysics*, ed S. K. Runcorn (London: Academic Press), 445–464.

Housen, B. A., Novak, B., Kitamura, Y., Kanamatsu, T., and Kawamura, K. (2014). Magnetic fabric analysis as a method for determining sediment transport and deposition in deep sea sediment. *Mar. Geol.* 356, 19–30. doi: 10.1016/j.margeo.2013.12.001

Hrouda, F. (1982). Magnetic anisotropy of rocks and its application in geology and geophysics. *Geophys. Surv.* 5, 37–82. doi: 10.1007/BF01450244

Jackson, K. L., Eberli, G. P., Amelung, F., McFadden, M. A., Moore, A. L., Rankey, E. C., et al. (2014). Holocene Indian ocean tsunami history in Sri Lanka. *Geology* 42, 859–862. doi: 10.1130/G35796.1

Jackson, K. L., Eberli, G. P., Rankey, E. C., Amelung, F., and Moore, A. L. (2008). "High recurrence rate of paleotsunamis in southeastern Sri Lanka," in *Abstract Volume of the Eos Trans. AGU Fall Meeting*, (San Francisco, CA).

Jankaew, K., Atwater, B. F., Sawai, Y., Choowong, M., Charoentitirat, T., Martin, M. E., et al. (2008). Medieval forewarning of the 2004 Indian Ocean tsunami in Thailand. *Nature* 455, 1228–1231. doi: 10.1038/nature07373

Kain, C. L., Gomez, C., Hart, D. E., Wassmer, P., Goff, J., and Starheim, C. (2014). Assessing topographic controls on flow direction in whashover deposits using measurements of Magnetic Susceptibility. *Mar. Geol.* 350, 16–26. doi: 10.1016/j.margeo.2014.01.010

Kawata, Y., Tsuji, Y., Sugimoto, Y., Hayashi, H., Matsutomi, H., Okamura, Y., et al. (2005). *Comprehensive Analysis of the Damage and its Impact on Coastal Zones by the 2004 Indian Ocean Tsunami Disaster*. Report, Disaster Prevention Research Institute, University of Kyoto.

Kortekaas, S., and Dawson, A. G. (2007). Distinguishing tsunami and storm deposits: an example from Martinhal, SW Portugal. *Sediment. Geol.* 200, 208–221. doi: 10.1016/j.sedgeo.2007.01.004

Laberge, R. D., Porreca, M., Mattei, M., Giordano, G., and Cas, R. A. F. (2009). Meandering flow of a pyroclastic density current document by the anisotropy of magnetic suseptibility (AMS) in the quartz latite ignimbrite of the Pleistocene Monte Cimino volcanic centre (central Italy). *Tectonophysics* 466, 64–78. doi: 10.1016/j.tecto.2008.09.009

Lavigne, F., Paris, R., Grancher, D., Wassmer, P., Brunstein, D., Vautier, F., et al. (2009). Reconstruction of Tsunami Inland propagation on december 26th, 2004 in banda aceh, indonesia, through field investigations. *Pure Appl. Geophys.* 166, 259–281. doi: 10.1029/2011JB008205

Macri, P., Speranza, F., and Capraro, L. (2014). Magnetic fabric of Plio-Pleistocene sediments from the Crotone fore-arc basin: insights on the recent tectonic evolution of the Calabrian Arc (Italy). *J. Geodynam.* 81, 67–79. doi: 10.1016/j.jog.2014.07.002

Meltzner, A. J., Sieh, K., Abrams, M., Agnew, D. C., Hudnut, K. W., Avouac, J. P., et al. (2006). Uplift and subsidence associated with the great Aceh-Andaman earthquake of 2004. *J. Geophys. Res.* 111, B02407. doi: 10.1029/2005JB003891

Meltzner, A. J., Sieh, K., Chiang, H.-W., Shen, C.-C., Suwargadi, B. W., Natawidjaja, D. H., et al. (2010). Coral evidence for earthquake recurrence and an AD1390–1455 cluster at the south end of the 2004 Aceh–Andaman rupture. *J. Geophys. Res.* 115:B10402. doi: 10.1029/2010JB007499

Mörner, N. A. (2007). Sea level changes and tsunamis. environmental stress and migration over the seas. *Int. Asienforum.* 38, 353–374.

Morton, R. A., Gelfenbaum, G., and Jaffe, B. E. (2007). Physical criteria for distinguishing sandy tsunami and storm deposits using modern examples. *Sediment. Geol.* 200, 184–207. doi: 10.1016/j.sedgeo.2007.01.003

Njanko, T., Nedelec, A., Kwekam, M., Siqueira, R., and Esteban, L. (2010). Emplacement and deformation of the Fomopea pluton: implication for the Pan-African history of Western Cameroon. *J. Struct. Geol.* 32, 306–320. doi: 10.1016/j.jsg.2009.12.007

Ort, M. H., Orsi, G., Pappalardo, L., and Fisher, R. V. (2003). Anisotropy of magnetic susceptibility studies of depositional processes in the Campanian Ignimbrite, Italy. *Bull. Volcanol.* 65, 55–72. doi: 10.1007/s00445-002-0241-2

Palmer, H. C., Macdonald, W. D., Gromme, C. S., and Ellwood, B. B. (1996). Magnetic properties and emplacement of the Bishop Tuff, California. *Bull. Volcanol.* 58, 101–116. doi: 10.1007/s004450050129

Paris, R., Lavigne, F., Wassmer, P., and Sartohadi, J. (2007). Coastal sedimentation associated with the December 26, 2004 tsunami in Lhok Nga, west Banda Aceh (Sumatra, Indonesia). *Mar. Geol.* 238, 93–106. doi: 10.1016/j.margeo.2006.12.009

Paris, R., Wassmer, P., Lavigne, F., Belousov, A., Belousova, M., Iskandarsyah, T. Y. W. M., et al. (2014). Coupling eruption and tsunami records: the 1883 Krakatau case-study, Indonesia. *Bull. Volcanol.* 76:814. doi: 10.1007/s00445-014-0814-x

Park, C. K., Doh, S. J., Suk, D. W., and Kim, K. H. (2000). Sedimentary fabric on deep-sea sediments from KODOS area in the eastern Pacific. *Mar. Geol.* 171, 115–126. doi: 10.1016/S0025-3227(00)00107-9

Ranasinghage, P. N. (2010). *Holocene Coastal Development in Southeastern-Eastern Sri Lanka: Paleo- Depositional Environments and Paleo-Coastal Hazards*. Ph.D. thesis, Kent, Ohio, Kent State University, 437.

Raposo, M. I. B., Pressi, L. F., and de Assis Janasi, V. (2012). Magnetic fabrics and their relationship with the emplacement of the Piracaia pluton, SE Brazil. *Int, J. Earth Sci.* 101, 773–786. doi: 10.1007/s00531-011-0696-5

Rees, A. I. (1968). The production of preferred orientation in a concentrated dispersion of elongated and flattened grains. *J. Geol.* 76, 457–465. doi: 10.1086/627343

Rusnak, G. A. (1957). The orientation of sand grains under conditions of "unidirectionnal" fluid flow. *J. Geol.* 65, 384–409. doi: 10.1086/626441

Tarling, D. H., and Hrouda, F. (1993). *The Magnetic Anisotropy of Rocks*. London: Chapman & Hall. 218.

Veloso, E. E., Hayman, N. W., Anma, R., Tominaga, M., Gonzales, R. T., Yamazaki, T., et al. (2014). Magma flow directions in the sheeted dike complex at superfast spreading mid-ocean ridges. Insights from IODP Hole 1256D, Eastern Pacific. *Geochem. Geophys. Geosyst.* 15, 1283–1295. doi: 10.1002/2013GC004957

Vijaya Lakshmi, C. S., Srinivasan, P., Murthy, S. G. N., Trivedi, D., and Nair, R. R. (2010). Granularity and textural analysis as a proxy for extreme wave events in southeast coast of India. *J. Earth Syst. Sci.* 119, 297–305. doi: 10.1007/s12040-010-0023-8

Wassmer, P. (2015). *Dating of a 4220 BP Paleo-Tsunami in North Sumatra*.

Wassmer, P., Baumert, P., Lavigne, F., Paris, R., and Sartohadi, J. (2007). Sedimentary facies and transfer associated with the December 26, 2004 tsunami on the north eastern littoral of Banda Aceh (Sumatra, Indonesia) / Faciés et transferts sédimentaires associés au tsunami du 26 décembre 2004 sur le littoral au nord-est de Banda Aceh (Sumatra, Indonésie). *Geomorphologie* 4, 55–66.

Wassmer, P., and Gomez, C. (2011). Development of the AMS method for unconsolidated sediments. Application to tsunami deposits. *Geomorphol. Relief Process.* 3, 279–290. doi: 10.4000/geomorphologie.9491

Wassmer, P., Schneider, J.-L., Fonfrege, A., Lavigne, F., Paris, R., and Gomez, C. (2010). Use of Anisotropy of Magnetic Susceptibility (AMS) in the study of tsunami deposits: application to the 2004 deposits on the eastern coast of Banda Aceh, North Sumtra, Indonesia. *Mar. Geol.* 275, 255–272. doi: 10.1016/j.margeo.2010.06.007

Willcock, M. A. W., Mattei, M., Hasalova, P., Giordano, G., Cas, R. A. F., and Morelli, C. (2014). "Flow behaviour in the intra-caldera setting: an AMS study of the large (>1290 km^3) Permian Ora ignimbrite," in *The Use of Palaeomagnetism and Rock Magnetism to Understand Volcanic Processes*, Vol. 396, eds M. H. Ort, M. Porreca, and J. W. Geissman (London: Geological Society, Special Publications), 177–204. doi: 10.1144/SP396.3

Conflict of Interest Statement: The authors declare that the research was conducted in the absence of any commercial or financial relationships that could be construed as a potential conflict of interest.

frontiers in
EARTH SCIENCE

ORIGINAL RESEARCH ARTICLE
published: 23 January 2015
doi: 10.3389/feart.2015.00001

Testing the use of viscous remanent magnetisation to date flood events

Adrian R. Muxworthy[1]*, Jason Williams[1] and David Heslop[2]

[1] *Department of Earth Science and Engineering, Imperial College London, London, UK*
[2] *Research School of Earth Sciences, The Australian National University, Canberra, ACT, Australia*

Edited by:
Eric Font, University of Lisbon, Portugal

Reviewed by:
Greig A. Paterson, Chinese Academy of Sciences, China
Ann Marie Hirt, Swiss Institute of Technology Zürich, Switzerland

****Correspondence:***
Adrian R. Muxworthy, Department of Earth Science and Engineering, Imperial College London, South Kensington Campus, London, SW7 2AZ, UK
e-mail: adrian.muxworthy@imperial.ac.uk

Using erratics associated with large flood events, this paper assesses whether their viscous remanent magnetisation (VRM) can be used to date the flood events. We tested this method using flood erratics from three large events: (1) the Late Pleistocene Bonneville mega-flood in Idaho, USA, (∼14–18 ka), (2) the 1918 A.D. Mt. Katla, Iceland, eruption and associated jökulhaup (meltwater flood) at Mýrdalssandur, and (3) the Markarfljót jökulhaup due to an earlier eruption of Mt. Katla (∼2.5 ka). We measured 236 specimens, 66 of which yielded clear identifiable and measurable viscous magnetisation signals from erratics with clustered VRM directions. From the VRM unblocking temperatures, age estimates were made. The age estimate for the most recent event (Mýrdalssandur) worked well, with a median estimated age of 80 years (with individual erratic estimates distributed between 61–105 years) compared to the known age of 91 years. The ages of the other two events were over-estimated. The estimates for Markarfljót [15 ka (7–33 ka)] were based on the results of just one erratic. For the Bonneville flood the estimates were too old, however, this locality had the largest uncertainty in the ambient temperature used in the age determination; the VRM acquired is strongly dependent on the ambient temperature, the older the event the greater the uncertainty. Southern Idaho currently has hot summers, with average summer maximum temperatures of ∼31°C, but a mean annual temperature of only ∼ 9°C. It is suggested that the VRM dating method works best for recent events (<2–3 ka) where the ambient temperature history can be constrained.

Keywords: viscous remanent magnetisation, dating, flood erratic, cataclysmic event, rock magnetism

INTRODUCTION

If a magnetic-mineral bearing rock is moved or re-oriented, the magnetisation of the smaller magnetic grains slowly re-aligns to the direction of the ambient magnetic field direction due to thermal fluctuations. This secondary magnetisation is termed viscous remanent magnetisation (VRM), and is logarithmically time dependent (Dunlop, 1973, 1983). This time-dependency of the intensity of the VRM, has been applied successfully to the dating of archeological events (e.g., Heller and Markert, 1973; Borradaile, 1996, 2003; Borradaile et al., 1999), however, this same method has not been used in widely in geological studies (i.e., Borradaile, 1998; Sato et al., 2014).

The VRM dating method can be used to date any geological event that results in a significant and sudden movement/rotation of a rock, with no significant subsequent movement. One such scenario are large erratics moved during a flood, i.e., if the VRM acquired by flood erratics can be isolated it is possible to date the flood event (**Figure 1**). Another is rock-slides and cliff slumps, e.g., Borradaile (1998) used VRM dating to examine cliff-slumps on the east coast of England. The advantage of this approach over other potential methods is that the VRM is an intrinsic property of the rock and is not dependent on features like snow coverage, e.g., annual exposure rates for cosmogenic dating, nor it is dependent on the presence of any other material, e.g., organic material in the case of radiocarbon dating.

This paper presents a preliminary investigation into the use of VRM dating to determine the age of geologic events. We tested this method on two independently dated floods: (1) the Late Pleistocene Bonneville mega-flood in Idaho, USA, (∼14–18 ka), and (2) the 1918 AD Mt. Katla, in South-West Iceland, eruption and associated jökulhaup (meltwater flood) at Mýrdalssandur. We also applied this method to another Mt. Katla jökulhaup; the poorly constrained Markarfljót flood.

THEORY OF VRM DATING

The magnetisation in very small magnetic particles is uniform, and such particles are termed single-domain (SD), as the grains become larger in size the magnetisation splits up into regions of uniformity (domains) divided by very thin domain walls. These particles are termed multidomain (MD). The threshold size between SD and MD magnetic structures depends on mineralogy, grain shape etc. (Muxworthy and Williams, 2006a); however, for magnetite the threshold size is of the order 100 nm. Generally speaking, small SD grains contribute significantly to VRM, whereas MD grains do not (Williams and Muxworthy, 2006).

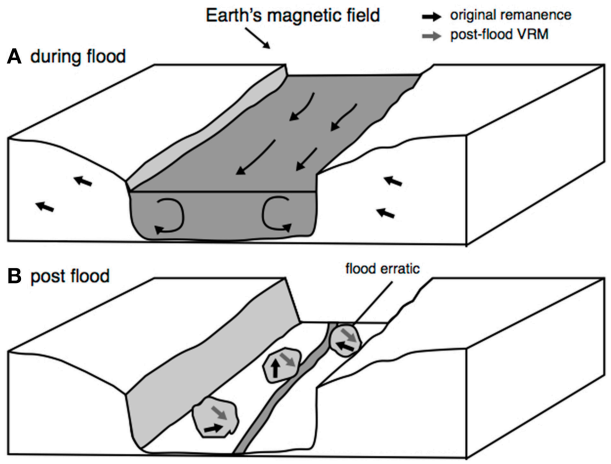

FIGURE 1 | A schematic of VRM acquisition. (A) Before the flood, the bedrock records an original remanence, e.g., a thermoremanence for a basaltic lava, aligned with an ancient magnetic field direction (this could be reversed as depicted). During the flood the bedrock is eroded from canyon walls and boulders are transported downstream. **(B)** Post-flood erratics deposited on the flood plain remain *in situ* and acquire a younger VRM parallel to the Earth's magnetic field; the original magnetisation vectors are left randomly orientated.

The theory of VRM dating is based on the thermoviscous model of Néel (1949) for magnetically ideal SD particles with uniaxial anisotropy. For an individual particle the relaxation of its magnetic moment over a given energy barrier ΔE:

$$\tau = \tau_0 \exp\left(\frac{\Delta E}{k_B T}\right) \tag{1}$$

where τ is the characteristic time for thermal activation, τ_0^{-1} is the atomic attempt frequency, k_B Boltzmann's constant and T the absolute temperature. For ideal SD particles in small external magnetic fields, like those of the Earth, whose magnetic anisotropy is controlled by a shape anisotropy, ΔE is given by $\mu_0 N M_S(T)^2 v/2$, where v the volume of the particle, μ_0 the permeability of free space, $M_S(T)$ the temperature dependent spontaneous magnetization and N the shape demagnetizing factor (Nagata, 1961).

The characteristic relaxation time τ is effectively the duration, t, of the time-frame of interest, e.g., will barriers be overcome on geological timescales or the duration of a laboratory experiment etc. Using this definition of τ, it is possible to rearrange Equation (1) to define the blocking volume (v_b), which is the critical volume of a crystal that has an equal probability of remaining fixed (blocked) for a given time t:

$$v_b = \frac{2k_B T \ln\left(t/\tau_0\right)}{\mu_0 N M_S^2(T)} \tag{2}$$

Thus, the critical blocking volume is a function of both temperature and time, i.e., a particle can become blocked at different combinations of time and temperature. For SD grains, for a geological VRM acquired in a time t_A and temperature T_A, then for a particular grain volume we can remove this VRM in a laboratory time t_L and temperature T_L using the following relationship (Pullaiah et al., 1975):

$$\frac{T_A \ln\left(t_A/\tau_0\right)}{M_S^2(T_A)} = \frac{T_L \ln\left(t_L/\tau_0\right)}{M_S^2(T_L)^2} \tag{3}$$

For dating purposes, time t_A is the VRM age, i.e., the event age to be estimated. Re-arranging Equation (3) to solve for t_A and using the standard relationship; $M_S(T) \propto (1\text{-}T/T_C)^{1/2}$ (Jiles, 1991), where T_C is the Curie temperature of a given mineral, gives:

$$t_A = t_L^{\lambda} \tau_0^{1-\lambda}$$
$$\text{where, } \lambda = \frac{T_L\left(1-(T_A/T_C)\right)}{T_A\left(1-(T_L/T_C)\right)} \tag{4}$$

In Equation (4) the parameters t_L, T_L and T_C can be measured in the laboratory, τ_0 is of the order 10^{-9} s (Moskowitz et al., 1997) and T_A can be estimated, allowing for t_A to be determined.

Some investigations of VRM (e.g., Kent, 1985; Smith and Verosub, 1994) have also assessed the VRM theory of Walton (1980) and Middleton and Schmidt (1982), which attempts to modify Equation (4) slightly to account for the effect of grain-size distributions. It is has been found that this model appears to work better than Equation (4) for long timescales, i.e, >>1 Myrs, but for shorter timescales, i.e., thousands of years, Equation (4) appears to be more applicable (Smith and Verosub, 1994).

VRM dating has been applied, albeit infrequently, to archeological investigations to yield construction ages (Heller and Markert, 1973; Borradaile and Almqvist, 2006), although not always through the direct application of Equation (4) due to the potential sources of uncertainty in this equation. For example, when determining the building dates of Roman and Medieval structures Borradaile and colleagues (Borradaile, 1996; Borradaile and Brann, 1997; Borradaile et al., 1999; Maher et al., 2000; Borradaile and Almqvist, 2006) constructed calibration curves from age-constrained buildings of the same material, allowing the relative age estimation of previously undated masonry. In this study, we consider geological events and thus such constrained calibrations are infeasible. Instead, we apply Equation (4) directly to the determination of VRM age, thereby estimating absolute, independent ages. There have been only two previous VRM-dating studies of geological processes (Borradaile, 1998; Sato et al., 2014).

GEOLOGICAL SAMPLING

Ten millimeter core samples were collected using an electric drill during fieldtrips to the USA and Iceland in the summer of 2009.

THE LAKE BONNEVILLE FLOOD

The Bonneville flood is one of the largest known geological flood events (Jarrett and Malde, 1987). It occurred when Lake Bonneville, in what is now Utah, USA, breached causing a catastrophic flood. The flood event was first identified (Malde, 1968) by the scabland topography and spectacular erosional and depositional geomorphic features in the Snake River Plain and the Snake River canyon further downstream. Discharge predictions yield

flood durations of several weeks up to ∼1 year for its 1110 km flow length (Jarrett and Malde, 1987); effectively a geologically instantaneous event. Large basaltic erratics derived from localized outcrops are littered along the Snake River canyon. Many of these erratics are several cubic meters in size, and are unlikely to have been significantly eroded or moved since they were deposited (Malde, 1968).

Using radiocarbon, U-series and aminostratigraphy dating, Oviatt et al. (1992, 1994) predicted ages between 15 and 14.5 kyr for the flood event. These studies provide the most comprehensive and best age estimate. A later palaeomagnetic investigation by Liddicoat and Coe (1997) used palaeosecular variation measurements to estimate the transgressive period of Lake Bonneville as ∼18 kyr with a span of 1000–3000 years, therefore inferring ages up to the flood event.

Three-hundred orientated cores from 45 different erratics were collected (**Table 1**). At locality one (B samples) erratics were ∼1 m^3 in size and at locality two (H samples) 1–3 m^3.

KATLA JÖKULHLAUPS

Iceland's second most active volcano, sub-glacial Katla, erupts frequently releasing catastrophic meltwater floods (jökulhlaups) (Duller et al., 2008). The caldera can be divided into three drainage sectors: Ko, So and En, that drain onto Mýrdalssandur, Sólheimasandur and Markarfljót plains (Eliasson et al., 2006). Historical records show most floods have followed along route Ko, a few have followed the So route, whereas there are only geological records of jökulhlaups from the En sector (Eliasson et al., 2006). Recurrence times are estimated as ∼58 years for Ko-type jökulhlaups and 500–800 years for En-type (Smith et al., 2002).

Orientated cores (137) from 12 basaltic erratics (size range was 0.5–1 m^3) associated with the jökulhlaup on the 12th of October 1918 were collected from the Mýrdalssandur flood plain. This was the last large Ko route jökulhlaup. On the same fieldtrip, oriented cores from three basaltic erratics (size range was ∼2 m^3) associated with an En sector flood that formed the Markarfljót canyon were collected. Estimates for the age of the Markarfljót event suggest that its age is ∼2500 years (Tómmason, 2002), however, this estimate is poorly constrained (pers. comm. Kate Smith).

EXPERIMENTAL METHODS

To avoid magnetic contamination, on collecting and orienting the samples in the field, the 10 mm cores were immediately placed in mu-metal boxes for transportation back to the Palaeomagnetic Laboratory at Imperial College London. The cores were cut and temporarily stored in a dynamic Helmholtz cage with a magnetic field <100 nT. All the measurements were conducted within 8 months of collection.

To determine the age of a VRM, it is necessary to measure t_L, T_L, and T_C (Equation 4). On heating the sample, the temperature at which the VRM demagnetizes (unblocks) is T_L. T_L was determined by continuous thermal demagnetisation with an Orion three-component low-field (<100 nT) vibrating sample magnetometer (VSM). Most samples were continually thermally demagnetised up to 250°C; this took approximately 10 min per sample. A small number of randomly selected samples were heated to 650°C. During these heating experiments t_L was measured to be 2.5 ± 0.2 s. To estimate the Curie temperature (T_C) of the remanence carrying minerals, the samples were initially demagnetised using an alternating field (AF) to erase the effect of remanence, and a low-field DC (0.5 mT) susceptibility measured as a function of temperature.

To better characterize the VRM acquisition recording process and dating fidelity of the samples, two further experiments were conducted: First, magnetic hysteresis parameters of nine unheated samples were measured using a high-field vibrating sample magnetometer. The parameters H_C (coercive force), H_{CR} (remanent coercive force), M_{RS} (saturation remanence) and M_S (saturation magnetisation) were determined and plotted on a domain state "Day" plot (Day et al., 1977). Second, we measured directly the viscosity acquisition response of 13 samples, by first AF demagnetising the samples, followed by measurement of VRM acquisition in a field of 100 A/m (∼126 μT) for 10 min.

RESULTS

THERMAL DEMAGNETISATION OF NRM

To determine the critical unblocking temperature T_L (Equation 4), the thermal demagnetisation data were plotted on orthogonal projection plots, and inflection points identified (**Figure 2**). Generally, most samples contained only two components: the characteristic remanent magnetisation (ChRM) and a secondary component associated with VRM (**Figure 2**). As all the samples were basaltic lavas, ChRM was very likely to be a thermoremanent magnetisation in origin. Where the inflection points could not be clearly identified, because either the VRM and the ChRM were closely aligned or the VRM was poorly defined, the data were rejected. For example, Bonneville sample BQ5 has a sharp inflection providing a discrete, accurate T_L selection with minimal error, while Mýrdalssandur sample YJ3 had a less distinct inflection point increasing uncertainty in T_L selection (**Figure 2**). Bonneville sample H39 (**Figure 2C**) is an example where no clear VRM was identified; such samples were not used for age estimation. If the inflection covered a range of temperatures, probably reflecting the grain-size distribution, the higher temperature was designated as T_L(**Figure 2A**).

In total 236 specimens from 34 erratics were analyzed. Nine of the erratics showed no evidence for a VRM. After removing unquantifiable cases, only 117 estimates were made. Generally, the T_L estimates for the Bonneville samples were between ∼150–210°C, from Mýrdalssandur ∼ 60–130°C, and ∼90–120°C for Markarfljót (Supplementary Material Table S1).

To confirm that the VRM had been correctly identified, the direction of the VRM was constrained using principal component analysis (Kirschvink, 1980). Individual VRM vectors for each erratic were plotted onto stereographic projections and the mean direction determined (**Figure 3**). The VRM should be approximately aligned with the current day magnetic field direction, or at least in the northern hemisphere. There will be some scatter in the VRM directions for two reasons: (1) the VRM signal is normally a minor secondary component and is subject to noise, and (2) secular variation of the geomagnetic field, means that the VRM is recording a direction that is changing significantly on the timescales of interest for the Bonneville and Markarfljót flood

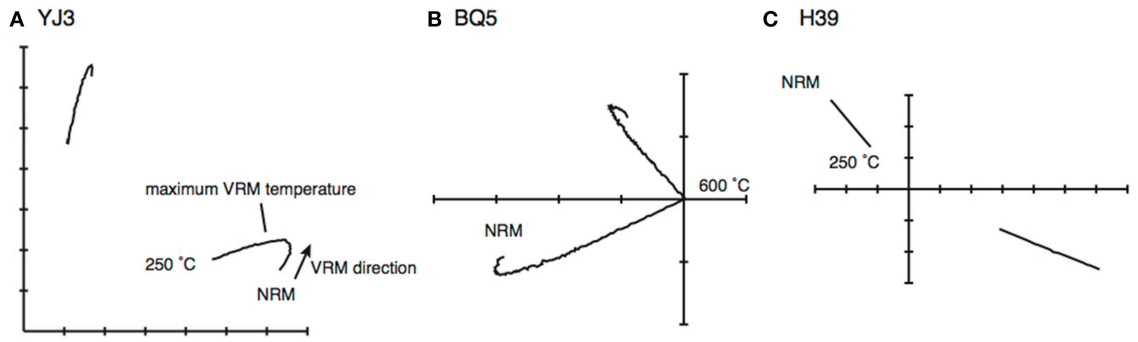

FIGURE 2 | Orthogonal plots (Zijderveld plots) of continuous thermal demagnetisation for specimens.(A) YJ3 (Mýrdalssandur), **(B)** BQ5 (Bonneville), and **(C)** H39 (Bonneville). In **(A)** the identification of the VRM is highlighted, with the maximum VRM temperature (T_L) identified. The data is measured every degree, therefore only lines are shown, not individual data points.

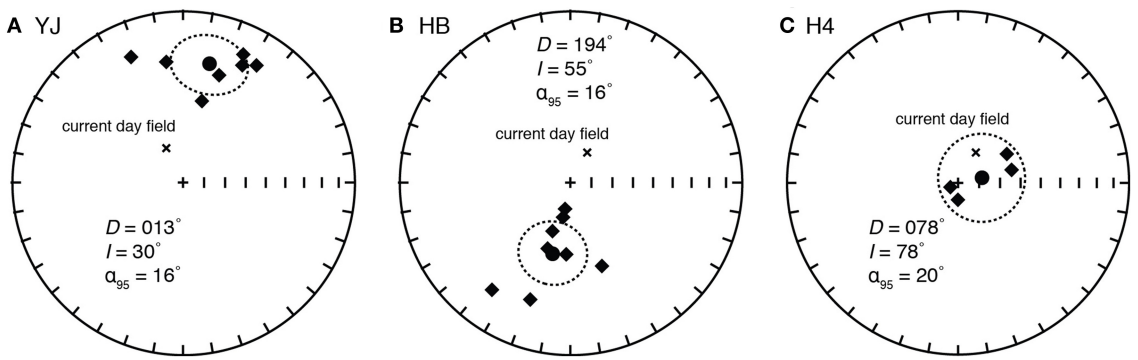

FIGURE 3 | Equal area projection plots for erratics. (A) YJ (Mýrdalssandur), **(B)** HB (Bonneville) and **(C)** H4 (Bonneville). Stereographic projections for erratics MB, BQ, YJ, and HB. All the points are solid filled squares, indicating they plot on the lower hemisphere. Mean directions are plotted (solid circles) and quoted, as are the α_{95} values. For reference, the current day field is also highlighted (cross); this is for 2009 when the samples were collected.

events. Older VRMs will be more affected by secular variation effects.

Some erratics, e.g., YJ and HB have clustered VRM directions (**Figure 3**), with north orientated components. Some erratics have poorly clustered VRM directions, or the mean direction was not in the correct hemisphere. The data from such erratics were rejected from further analysis. After directional analysis, a further 51 specimens were rejected, leaving 66 specimens for dating analysis (Section Age Estimations): 29 specimens (six erratics) from Bonneville, 28 specimens (four erratics) from Mýrdalssandur, and nine specimens from one erratic from Markarfljót (Supplementary Material Table S1).

HIGH-TEMPERATURE THERMOMAGNETIC ANALYSIS

Curie temperatures (technically maximum unblocking temperatures) were determined using the double derivative method of Tauxe (1998) (**Table 1**). Most, but not all, heating curves (**Figure 4**) for the Bonneville specimens had a single high-temperature T_C, e.g., HA3, whereas the Icelandic samples, e.g., YK3 and YJ4, displayed a gradual decay in their thermomagnetic curves, suggesting a broad range of unblocking spectra and mineralogies, making it difficult to accurately constrain T_C. As a general rule the Icelandic specimens had lower Curie temperatures ($\leq$500°C) than Bonneville specimens ($\leq$500°C) (Supplementary Material Table S1).

MAGNETIC HYSTERESIS

The magnetic hysteresis data is summarized on a "Day" plot in **Figure 5**. Most specimens plot within the pseudo-single-domain (PSD) grain region, with one sample plotting slightly to the left. There is no distinct grouping between samples that were accepted for dating analysis in Section Thermal Demagnetisation of NRM, and those that were rejected.

VISCOSITY MEASUREMENTS

The rate of acquisition of viscous magnetisation, i.e., the viscosity acquisition parameter S_A was determined and quantified using the first-order approximation (Street and Woolley, 1949):

$$M = S_A \log(t) \tag{5}$$

where M is the magnetisation. Generally the samples displayed a logarithmic dependency (**Figure 6**) over the measurement time ($\sim$10 min) in agreement with previous studies (Muxworthy and Williams, 2006b). The samples displayed a range of estimates for

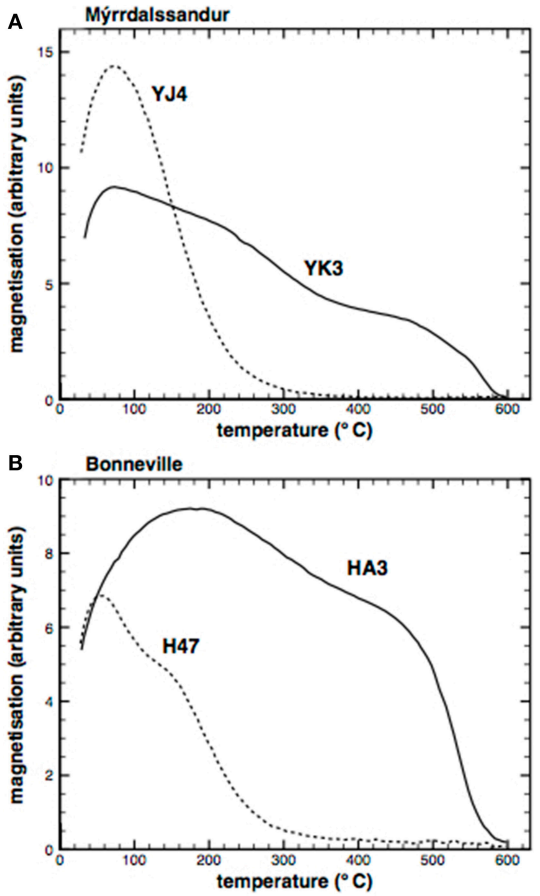

FIGURE 4 | Representative thermomagnetic curves for samples from (A) Mýrdalssandur, and (B) Bonneville. The samples were first alternating field (AF) demagnetised in a peak field of 200 mT, and heated in a field of 0.5 mT; the thermomagnetic curves are DC susceptibility curves.

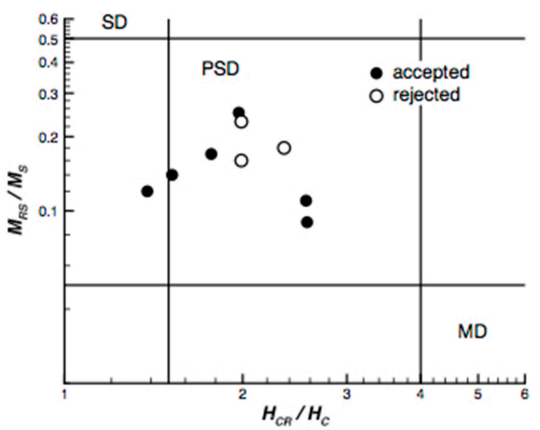

FIGURE 5 | A "Day" plot (Day et al., 1977) of the ratio of H_{CR}/H_C vs. M_{RS}/M_R for accepted samples. Whether a sample was accepted or rejected from the final dating calculation is highlighted. The standard SD, PSD, and MD fields are drawn.

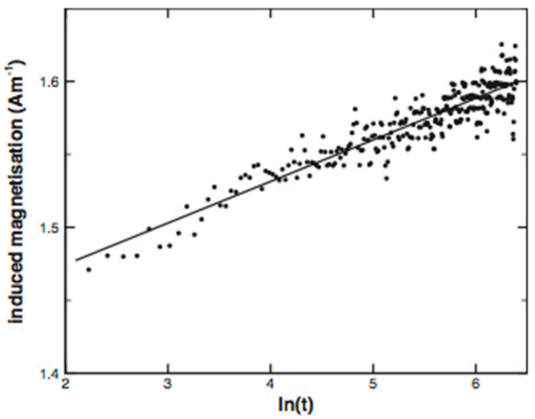

FIGURE 6 | Magnetisation versus time for a representative sample from erratic H3 (H35). The samples were AF demagnetised in peak fields of 200 mT, and then the magnetisation was measured as a function of time in an applied field of 126 μT. The viscosity acquisition parameter S_A (Equation 5) is determined directly from such plots.

Table 1 | Viscous acquisition parameter S_A, for 13 specimens.

Erratic	S_A(Am^{-1})
ACCEPTED	
BJ	0.016
BQ	0.014
BY	0.0044
H4	0.016
MB	0.037
YJ	0.0089
REJECTED	
BD	0.027
BH	0.046
HA	0.020
H3	0.029
MA	0.033
YL	0.051
YN	0.010

*S_A is determined from data like that shown in **Figure 6** for sample H3. Representative fresh samples from each erratic were used. "B" and "H" erratics are from Bonneville, "M" erratics from Markarfljót and "Y" erratics from Mýrdalssandur.*

S_A, as quantified in **Table 1**. Generally, samples that were accepted for VRM dating (**Table 1**), had lower S_A values. The means of the accepted and rejected samples were 0.016 and 0.030 Am^{-1}, respectively.

DISCUSSION

After analysis of the NRM data, 66 specimens out of 236 were deemed to be suitable for reliable estimates of T_L, having clear inflection points and "well-behaved" VRM directions (**Figures 2**, **3** and Supplementary Material Table S1).

AGE ESTIMATIONS

To make age estimations we apply Equation (4). All the parameters in Equation (4) were directly measured with the exception of the ambient temperature (T_A) and τ_0. We have determined the ages using the mean annual temperatures for T_A for Mýrdalssandur, Markarfljót and Bonneville (Supplementary Material Table S1), where the temperature ∼5.5°C for Mýrdalssandur was taken from the 1961–2013 record [available from the Icelandic Meteorological Office (http://en.vedur.is/)] for nearby Vík í Mýrda. For Markarfljót a mean annual temperature of ∼3.5°C was used, based on temperature records from Básar á Goðoalandi relative to Sámsstaðoir and Vík í Mýrda. For Bonneville the mean annual temperature (∼9°C) from the 1961–1990 record from Twin Falls, Idaho, was used (www.usclimatedata.com).

Each specimen yields a different t_A (Supplementary Material Table S1). It is immediately clear that the distribution of age estimates is not normally distributed; therefore we take the median to determine three representative VRM ages. Although there are several sources of error in the parameter estimates (see Section Uncertainties in input parameters for further analysis), to investigate the sensitivity of t_A on T_A, we plot t_A as function of T_A for median ages from Bonneville, Mýrdalssandur and Markarfljót (**Figure 7**). We have plotted two curves: (1) a mean annual temperature curve (24 h for 365 days), and (2) a mean summer maximum temperature curve. In the later calculation it is assumed that most of the VRM is acquired mostly at higher temperatures, and t_A is determined using VRM acquisition of only 6 h per day for 60 days of summer. To estimate the error on t_A we use a ± 1.0°C temperature window for the recent Mýrdalssandur flood, and for the older Bonneville and Markarfljót floods a ± 2.0°C window (**Table 2**). The ± 2.0°C window is a little arbitrary and should be seen as a guide rather than absolute measure of the error.

The age estimate (80 years) for the median Mýrdalssandur erratic is within 11 years of the known age of 91 years, and ± 1°C uncertainty in the mean annual temperature yields a range estimate of 61–105 years. The median estimate for the Markarfljót flood (∼15 ka) is older than the published value (∼2500 years, Tómmason, 2002), however, this is poorly constrained and is very likely younger or concurrent with the Younger Dryas, i.e., ≤12 ka. The Bonneville flood estimate (∼3.2 Ma) for the mean annual temperature is very old, however, the summer maximum temperature estimate is close to the expected value.

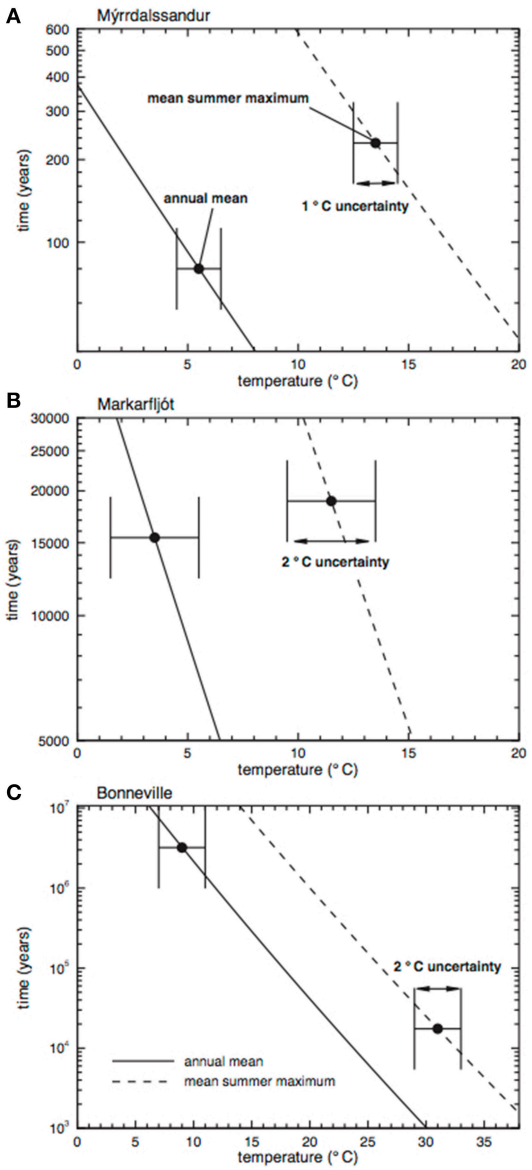

FIGURE 7 | VRM age estimates (t_A) as a function of the ambient temperature T_A for median ages from: (A) Mýrdalssandur, (B) Markarfljót and (C) Bonneville. On each diagram, two curves are plotted: (1) a annual mean temperature curve (24 h for 365 days), and (2) a mean summer maximum temperature curve. In the latter calculation it is assumed that the VRM is acquired mostly at higher temperatures, and t_A is determined using VRM acquisition of only 6 h per day for 60 days a year. To estimate the ages we use annual mean and mean summer maximum temperatures of: **(A)** 5.5 and 13.5°C, **(B)** 3.5 and 11.5°C, and **(C)** 9 and 31°C. To estimate the error on t_A we use a ± 1.0°C temperature window for the recent Mýrdalssandur flood, and for the older Bonneville and Markarfljót floods a ± 2.0°C window.

POSSIBLE REASONS FOR FAILURE

Potential errors in the age calculations can arise from a number of sources: (1) theoretical assumptions about the intrinsic magnetic properties of a specimen, (2) uncertainties in the input parameters into Equation (4), in particular in the ambient temperature T_A and τ_0, (3) variations in the geomagnetic field, and (4) sample handling. There was no obvious correlation between the time from collection to measurement, and rejection.

Domain state, mineralogy and viscous acquisition

The VRM dating method is based on the assumption that the magnetic remanence is carried by assemblages of non-interacting SD particles, dominated by uniaxial anisotropy imparted with a thermoremanence. The samples in this study display hysteresis properties typical for basalt, i.e., distributions of PSD particles (**Figure 4**). There is no real trend between the specimens accepted or rejected for VRM determination, based on their hysteresis properties; perhaps, the accepted specimens are slightly more

SD-like? However, hysteresis is an in-field measurement allowing for large MD particles, which are not thought to contribute significantly to VRM acquisition (Dunlop, 1983), to dominate, i.e., the SD particles, which contribute most to the VRM signal, might be masked. If MD particles are more abundant, then it might be expected that given the difference between blocking and unblocking temperatures for MD particles, that the MD contribution to VRM might lead to an overestimate for t_L.No such relationship was noticed in this study; however, this feature is likely to be quite subtle and easily dominated by other effects.

The viscosity acquisition parameter S_A (Equation 5) of the accepted erratics was roughly half that of the rejected erratics (**Table 1**). While the variation may be due to variation in magnetic mineral concentration, it suggests that erratics that are more efficient at acquiring a VRM component are less reliable. This initially seems counter intuitive; however, it may be because grains with high S_A values are more susceptible to short term paleosecular variation and are likely to acquire a contamination VRM signal subsequent to collection.

The theory used to determine the VRM date (Equation 4) is based on a magnetic thermal activation model. There are also non-magnetic effects, which can alter the magnetisation, e.g., disaccommodation (Moskowitz, 1985; Muxworthy and Williams, 2006b), which can lead to VRM acquisition behavior that is not explained by Equation (4) (Lowrie and Kent, 1978; Tivey and Johnson, 1984); it will likely lead to an overestimate of t_A. Such processes would be expected to have greater effects on older VRMs.

Ideally samples should be chosen which show no evidence of chemical alteration (oxidation); then the signal associated with the VRM should be thermal in origin.

Table 2 | Age estimates of the three flood events.

Flood event	Expected age (years)	Number of specimens	Annual age calculation (years)	Mean summer mean calculation (years)
Mýrdalssandur	91	28	80 (61–105)[a]	230 (178–389)[a]
Markarfljót	∼5k	9	15k (7–33k)[b]	19k (9–39k)[b]
Bonneville	14–18k	29	3.2M (0.6–7.4M)[b]	17k (9–36k)[b]

The annual age calculation is based on the mean annual temperature, whereas the mean summer calculation assumes that the VRM is only acquired in the summer at peak, daytime temperatures.

[a] *Range calculated using a* $\pm$ *1° C window.*

[b] *Range calculated using a* $\pm$ *2° C window.*

Uncertainties in input parameters

The age estimate t_A is sensitive to uncertainties in the input parameters in Equation (4), and is most likely the cause of the data scatter (Supplementary Material, Table S1). To assess these uncertainties we examine the partial derivatives of the five variables in Equation (4) in **Table 3**. It is clear that the biggest uncertainty comes from the uncertainty in τ_0, with uncertainties in T_A and T_L roughly equally important, whilst the uncertainties in the measured parameters T_C and t_L are less significant. For the Mýrdalssandur flood event, T_A is relatively well constrained from meteorological data from a nearby weather station; the calculation in **Table 3** uses an error of 5 K, but it is likely much smaller than this, i.e., ∼1–2 K. For the other two events, which are significantly older, we have made estimates for T_A based on recent temperature records; clearly, age estimates for older events will have greater uncertainties in T_A; 5 K is possibly an underestimate of the error in the mean temperature. The age estimates based on mean annual temperatures are clearly too old for Bonneville, and slightly too old for Markarfljót (**Table 2**). Because Equation (4) is very sensitive to temperature, i.e., a few hours at a higher temperature has a greater effect than many hours at a lower temperature, we have also calculated t_A based on mean summer maximum temperatures. For Markarfljót, the age estimate is similar to that for the mean annual temperature; for Bonneville the age estimate from the average summer maximum temperature is much lower and within the expected range. This

Table 3 | Estimation of the effect of errors/approximations for the parameters in Equation (4) on Equation (4) through analysis of partial derivatives.

Parameter	Partial derivatives	Maximum expected variation	Mýrdalssandur (years)	Markarfljót (kyrs)	Bonneville (kyrs)
τ_0	$\frac{\partial t_A}{\partial \tau_0} = (1-\lambda)\left(\frac{t_L}{\tau_0}\right)^{\lambda}$	5×10^{-9} s	380	92	23000
t_L	$\frac{\partial t_A}{\partial \tau_L} = \lambda\left(\frac{t_L}{\tau_0}\right)^{\lambda-1}$	0.2 s	12	27	637
T_C	$\frac{\partial t_A}{\partial T_C} = \frac{t_L^{\lambda}\tau_0^{1-\lambda}\ln\left(t_L/\tau_0\right)T_L\left(T_A-T_L\right)}{T_A\left(T_C-T_L\right)^2}$	5 K	21	11	2900
T_A	$\frac{\partial t_A}{\partial T_A} = \frac{-t_L^{\lambda}\tau_0^{1-\lambda}\ln\left(t_L/\tau_0\right)T_L T_C}{T^2\left(T_C-T_L\right)}$	5 K	110	30	6700
T_L	$\frac{\partial t_A}{\partial T_L} = \frac{t_L^{\lambda}\tau_0^{1-\lambda}\ln\left(t_L/\tau_0\right)T_C\left(T_C-T_A\right)}{T_A\left(T_C-T_L\right)^2}$	5 K	110	37	8755

The maximum expected variation values should be seen as guides in the error analysis.

difference in behavior is most likely due to the very large variation in mean temperatures in mid-latitude continental regions, in contrast, in maritime regions the temperature variation is significantly less, i.e., there is less variation and uncertainty in T_A. The temperatures used in the estimation of t_A are air temperatures; rock surfaces exposed to the sun can reach much higher temperatures, i.e., the temperatures used in this study might be too low or too high depending on average exposure to sunlight. The error in T_L, may not have been as large as quoted in **Table 3**, and depends on the shape of the inflection in the orthogonal projection plots (**Figure 2**): Care should be taken in identifying T_L.

Variations in the VRM directions

Several erratics had low-temperature magnetisations components that were south seeking; erratics displaying such behavior were not used in the age estimations. There are two possible causes of this behavior: (1) A remanence other than a VRM associated with the flood event had been measured, i.e., the VRM signal had been contaminated since collection (to reduce this effect the samples were placed directly in mu-metal boxes in the field). (2) The erratic had moved since the flood event, however, this must have happened relatively recently for the associated flood-event VRM not to be overprinted by a new north-seeking VRM direction. For erratics with mixed north- and south-seeking directions, the first scenario is more likely, and for erratics with only south seeking VRM directions, the second mechanism is more likely. Secular variation of the geomagnetic field will cause a variation in the inclination and declination that the VRM records, however, the variation is not large enough to cause a VRM to become south-seeking. It should also be noted that the directions of some VRM were poorly constrained, as the some VRMs demagnetisation data, e.g., **Figure 2**, were essentially curves rather than a straight line, making it difficult to determine an accurate VRM direction.

COMPARISONS WITH PREVIOUS STUDIES

Both previous VRM-dating studies of geological processes (Borradaile, 1998; Sato et al., 2014), relied on step-wise thermal demagnetisation rather than continuous thermal demagnetization as used in this study; this means that: (1) the temperature step sizes were larger purely for practical reasons, and (2) the heating rates are not identical, i.e., static versus continuous heating. Borradaile (1998) used a calibrated system based on archeological masonary to date rock slumps $<$1000 years in age; he primarily used the protocol to put events into chronological sequence. Sato et al. (2014) examined two large paleotsunami erratics. They used the same equation as us to determine the age of erratics, i.e., Equation (4). However, they did not conduct detailed error analysis, and essentially only used the VRM-dating technique to put events in chronological sequence.

On comparison, in this study we have conducted a significantly more extensive study by sampling many erratics, we have employed a more detailed temperature analysis of VRM demagnetisation through continuous demagnetisation and have conducted more rigorous error analysis. We believe that this study is a significant advancement on previous studies.

We also considered the VRM theory of Walton (1980) and Middleton and Schmidt (1982), which requires the same input data as Equation (4), though it is slightly modified. When we applied this approach to our data, all the ages for the erratics were less than a year. We therefore believe that Equation (4) is more appropriate.

FUTURE IMPROVEMENTS

This work is a preliminary study. We suggest a number of improvements for future studies:

- To better constrain T_A, collect cores from rock surfaces that are predominately in shadow or partially buried.
- Measure thermomagnetic curves for all the specimens or at one least per erratic, and use these thermomagnetic curves as input in the estimation calculation rather than using single Curie temperature estimations for each erratic.
- Determine τ_0 for a range of specimens, and assess whether it is necessary to determine τ_0 for each specimen/erratic.
- Determine the optimal heating rate for t_L.
- To reduce VRM decay rate and remove acquisition of new VRMs in the laboratory, store samples in mu-metal boxes in a refrigerator.
- Use of more detailed climate records for older events.

CONCLUSIONS

We have tested a VRM dating method on erratics associated with three flood events: (1) Mýrdalssandur (1918 AD), Markarfljót ($\sim$5 ka) and Bonneville (14–18 ka). We measured 236 specimens from 34 erratics, and based on various selection criteria only 66 were used in the final calculations (Supplementary Material Table S1). In summary the dating method is partially successful; inconsistency in age estimates increases dramatically for the older flood events. The results for the most recent event, worked reasonably well with an estimated age of 80 years (61–105 years) compared to the expected answer of 91 years. The ages of the other two events were over-estimated (**Table 2**). The estimates for Markarfljót were based on the results of just one erratic, whilst the uncertainty in the ambient temperature used in the age determination (Equation 4) was very large for Bonneville. From this it is concluded that the technique will work best for erratics associated with recent events, i.e., $<$2–3 ka, in locations that have constrained temperature histories. To further improve estimates, estimating τ_0 on a specimen/erratic/material level may be necessary.

Cosmogenic exposure analysis, arguably the most important technique for dating erratics (Phillips et al., 2006) is also dependent on rock type, variations in exposure, and changes in the geomagnetic field. ^{36}Cl dating can measure surface exposure time of young volcanic rocks and geomorphic features in the age range of 10^3–10^6 years (Phillips et al., 1986). Estimates for the youngest Mýrdalssandur flood on the scale of 10^2 years proved successful and therefore the VRM technique may be a more appropriate tool for dating recent erratics than cosmogenic dating.

ACKNOWLEDGMENTS

This work was funded by a Royal Society grant to Adrian R. Muxworthy. We thank Karin Strohecker for assistance during the fieldwork in Iceland.

REFERENCES

Borradaile, G. J. (1996). An 1800-year archeological experiment in remagnetization. *Geophys. Res. Lett.* 23, 1585–1588. doi: 10.1029/96GL01575

Borradaile, G. J. (1998). Rock magnetic constraints on long-term cliff-slump rates and coastal erosion. *Géotechnique* 48, 271–279. doi: 10.1680/geot.1998.48.2.271

Borradaile, G. J. (2003). Viscous magnetization, archaeology and Bayesian statistics of small samples from Israel and England. *Geophys. Res. Lett*. 30:1528 doi: 10.1029/2003GL016977

Borradaile, G. J., and Almqvist, B. S. (2006). Installation age of limestone masonry determined from its viscous remagnetization. *Geoarchaeology* 21, 29–60. doi: 10.1002/gea.20088

Borradaile, G. J., and Brann, M. (1997). Remagnetization dating of roman and mediaeval masonry. *J. Archaeol. Sci.* 24, 813–824. doi: 10.1006/jasc.1996.0162

Borradaile, G. J., Cameron, C., and Stewart, J. D. (1999). Magnetization dating at a medieval monastery (Tupholme, Lincolnshire). *Archaeometry* 41, 175–183. doi: 10.1111/j.1475-4754.1999.tb00859.x

Day, R., Fuller, M. D., and Schmidt, V. A. (1977). Hysteresis properties of titanomagnetites: grain-size and compositional dependence. *Phys. Earth Planet. Inter*. 13, 260–267. doi: 10.1016/0031-9201(77)90108-X

Duller, R. A., Mountney, N. P., Russell, A. J., and Cassidy, N. C. (2008). Architectural analysis of a volcaniclastic jokulhlaup deposit, southern Iceland: sedimentary evidence for supercritical flow. *Sedimentology* 55, 939–964. doi: 10.1111/j.1365-3091.2007.00931.x

Dunlop, D. J. (1973). Theory of magnetic viscosity of lunar and terrestrial rocks. *Rev. Geophys. Space Phys*. 11, 855–901. doi: 10.1029/RG011i004p00855

Dunlop, D. J. (1983). Viscous magnetization of 0.04-100 μm magnetites. *Geophys. J. R. Astron. Soc*. 74, 667–687.

Eliasson, J., Larsen, G., Gudmundsson, M. T., and Sigmundsson, F. (2006). Probabilistic model for eruptions and associated flood events in the Katla caldera, Iceland. *Comput. Geosci*. 10, 179–200. doi: 10.1007/s10596-005-9018-y

Heller, F., and Markert, H. (1973). The age of viscous remanent magnetization of Hadrian's Wall (northern England). *Geophys. J.* 31, 395–406. doi: 10.1111/j.1365-246X.1973.tb06510.x

Jarrett, R. D., and Malde, H. E. (1987). Paleodischarge of the late pleistocene bonneville flood, snake river, Idaho, computed from new evidence. *Geol. Soc. Am. Bull*. 99, 127–134.

Jiles, D. (1991). *Magnetism and Magnetic Materials.* London: Chapman and Hall.

Kent, D. V. (1985). Thermoviscous remagnetization in some Appalachian limestones. *Geophys. Res. Lett* 12, 805–808. doi: 10.1029/GL012i012p00805

Kirschvink, J. L. (1980). The least-squares line and plane and the analysis of paleomagnetic data. *Geophys. J. R. Astron. Soc*. 62, 699–718. doi: 10.1111/j.1365-246X.1980.tb02601.x

Liddicoat, J. C., and Coe, R. S. (1997). Paleomagnetic investigation of Lake Lahontan sediments and its application for dating pluvial events in the northwestern Great Basin. *Q. Res.* 47, 45–53. doi: 10.1006/qres.1996.1867

Lowrie, W., and Kent, D. V. (1978). Characteristics of VRM in Oceanic Basalts. *J. Geophys*. 44, 297–315.

Maher, L., Boarradaile, G., Stewart, J. D., and O'connor, M. (2000). The romanesque frieze at Lincoln Cathedral (England) - primary or secondary insertion? magnetic considerations. *Archaeometry* 42, 225–236. doi: 10.1111/j.1475-4754.2000.tb00878.x

Malde, H. E. (1968). The Catastrophic Late Pleistocene Bonneville Flood in the Snake River Plain, Idaho. *Geol. Surv. Prof. Pap.* 596, 1–69.

Middleton, M. F., and Schmidt, P. W. (1982). Paleothermometry of the Sydney basin. *J. Geophys. Res.* 87, 5351–5359. doi: 10.1029/JB087iB07p05351

Moskowitz, B. M. (1985). Magnetic viscosity, diffusion after-effect and disaccommodation in natural and synthetic samples. *Geophys. J. R. Astron. Soc.* 82, 143–161. doi: 10.1111/j.1365-246X.1985.tb05133.x

Moskowitz, B. M., Frankel, R. B., Walton, S. A., Dickson, D., Wong, K. K. W., Douglas, T., et al. (1997). Determination of the pre-exponential frequency factor for superparamagnetic maghemite particles in magnetoferritin. *J. Geophys. Res.* 102, 22671–22680.

Muxworthy, A. R., and Williams, W. (2006a). Critical single-domain/multidomain grain sizes in non-interacting and interacting elongated magnetite particles: implications for magnetosomes. *J. Geophys. Res.* 111:B12S12. doi: 10.1029/2006JB004588

Muxworthy, A. R., and Williams, W. (2006b). Low-temperature viscous magnetization of multidomain magnetite: evidence for disaccommodation contribution. *J. Magn. Magn. Mater*. 307, 113–119. doi: 10.1016/j.jmmm.2006.03.052

Nagata, T. (1961). *Rock Magnetism*. Tokyo: Maruzen.

Néel, L. (1949). Influence des fluctuations thermiques sur l'aimantation de grains ferromagnétiques très fins. *Comp. Ren. Heb. Séan. Acad. Sci*. 228, 664–666.

Oviatt, C. G., Currey, D. R., and Sack, D. (1992). Radiocarbon chronology of Lake Bonneville, Eastern Great Basin, USA. *Palaeogeogr. Palaeoclimatol. Palaeoecol*. 99, 225–241. doi: 10.1016/0031-0182(92)90017-Y

Oviatt, C. G., McCoy, W. D., and Nash, W. P. (1994). Sequence stratigraphy of lacustrine deposits: a quaternary example from the Bonneville basin. *Geol. Soc. Am. Bull.* 106, 133–144.

Phillips, F. M., Leavy, B. D., Jannik, N. O., Elmore, D., and Kubik, P. (1986). The accumulation of cosmogenic chlorine-36 in rocks: a method for surface exposure dating. *Science* 231, 41–43. doi: 10.1126/science.231.4733.41

Phillips, W. M., Hall, A. M., Mottram, R., Fifield, L. K., and Sugden, D. E. (2006). Cosmogenic 10Be and 26Al exposure ages of tors and erratics, cairngorm mountains, Scotland: timescales for the development of a classic landscape of selective linear glacial erosion. *Geomorphology* 73, 222–245. doi: 10.1016/j.geomorph.2005.06.009

Pullaiah, G., Irving, E., Buchan, K. L., and Dunlop, D. J. (1975). Magnetization changes caused by burial and uplift. *Earth Planet. Sci. Lett.* 28, 133–143. doi: 10.1016/0012-821X(75)90221-6

Sato, T., Nakamura, N., Goto, K., Kumagai, Y., Nagahama, H., and Minoura, K. (2014). Paleomagnetism reveals the emplacement age of tsunamigenic coral boulders on Ishigaki Island, Japan. *Geology*. 42, 603–606. doi: 10.1130/G35366.1

Smith, K. T., Dugmore, A. J., Larsen, G., Vilmundardottir, E. G., and Haraldsson, H. (2002). "New evidence for Holocene jökulhlaup routes west of Mýrdalsjökull," in *The 25 Nordic Geological Winter Meeting Abstracts*, ed S. S. Jonsson (Reykjavík: University of Iceland), 106.

Smith, R. T., and Verosub, K. L. (1994). Thermoviscous remanent magnetism of columbia river basalt blocks in the cascade landslide. *Geophys. Res. Lett.* 21, 2661–2664. doi: 10.1029/94GL02669

Street, R., and Woolley, J. C. (1949). A study of magnetic viscosity. *Proc. Phys. Soc. Lond. A* 62, 562–572. doi: 10.1088/0370-1298/62/9/303

Tauxe, L. (1998). *Paleomagnetic Principles and Practice*. Dordrecht: Kluwer Academic Publishers.

Tivey, M. A., and Johnson, H. P. (1984). The characterization of viscous remanent magnetization in large and small magnetite particles. *J. Geophys. Res.* 89, 543–552. doi: 10.1029/JB089iB01p00543

Tómmason, H. (2002). "Catastrophic floods in Iceland" in *The Extremes of Extremes: Extraordinary Floods* Vol. 271, eds A. Snorrason, H. P. Finnsdóttir and M. E. Moss (Wallingford: IAHS International Commission on Water Resources Systems), 121–126.

Walton, D. (1980). Time-temperature relations in the magnetisation of assemblies of single domain grains. *Nature* 286, 245–247. doi: 10.1038/286245a0

Williams, W., and Muxworthy, A. R. (2006). Understanding viscous magnetization of multidomain magnetite. *J. Geophys. Res.* 111:B02102. doi: 10.1029/2005JB003695

Conflict of Interest Statement: The authors declare that the research was conducted in the absence of any commercial or financial relationships that could be construed as a potential conflict of interest.

Received: 24 November 2014; paper pending published: 12 December 2014; accepted: 07 January 2015; published online: 23 January 2015.

*Citation: Muxworthy AR, Williams J and Heslop D (2015) Testing the use of viscous remanent magnetisation to date flood events. Front. Earth Sci. **3**:1. doi: 10.3389/feart.2015.00001*

This article was submitted to Geomagnetism and Paleomagnetism, a section of the journal Frontiers in Earth Science.

frontiers in Earth Science

ORIGINAL RESEARCH
published: 17 June 2015
doi: 10.3389/feart.2015.00031

Striped domains of coarse-grained magnetite observed by X-ray photoemission electron microscopy as a source of the high remanence of granites in the Vredefort dome

Hiroto Kubo[1], *Norihiro Nakamura*[1]*, *Masato Kotsugi*[2], *Takuo Ohkochi*[3], *Kentaro Terada*[4] *and Kohei Fukuda*[5]

[1] Division of Geo-Environmental Science, Department of Earth Science, Graduate School of Science and Faculty of Science, Tohoku University, Sendai, Japan, [2] Department of Materials Science and Technology, Tokyo University of Science, Tokyo, Japan, [3] Hard-X-ray Spectroscopy Group, Division of the Research and Utilization, SPring-8/Japan Synchrotron Radiation Institute, Hyogo, Japan, [4] Department of Earth and Space Science, Graduate School of Science, Osaka University, Toyonaka, Japan, [5] Department of Earth and Planetary Science, The University of Tokyo, Tokyo, Japan

OPEN ACCESS

Edited by:
Eric Font,
University of Lisbon, Portugal

Reviewed by:
Dario Bilardello,
University of Minnesota, USA
Melina Macouin,
Centre National de Recherche Scientifique, France

***Correspondence:**
Norihiro Nakamura,
Division of Geo-Environmental Science, Graduate School of Science and Faculty of Science, Tohoku University, 6-3 Aoba, Aramaki, Aoba-ku, Sendai 980-8578, Japan
norihironakamura21@gmail.com

Specialty section:
This article was submitted to Geomagnetism and Paleomagnetism, a section of the journal Frontiers in Earth Science

Received: 27 February 2015
Accepted: 02 June 2015
Published: 17 June 2015

Citation:
Kubo H, Nakamura N, Kotsugi M, Ohkochi T, Terada K and Fukuda K (2015) Striped domains of coarse-grained magnetite observed by X-ray photoemission electron microscopy as a source of the high remanence of granites in the Vredefort dome. Front. Earth Sci. 3:31. doi: 10.3389/feart.2015.00031

The characteristics of a coarse-grained high-remanence magnetite obtained from shocked Vredefort granite were investigated by X-ray magnetic circular dichroism (XMCD) analysis and X-ray absorption spectroscopy (XAS). The study utilized a spectroscopic photoelectron low-energy electron emission microscope (SPELEEM) and was conducted in the SPring-8 large-synchrotron radiation facility. It is generally believed that the strong and stable bulk remanence of Vredefort granites is due to the presence of minerals that have been strongly magnetized by either an impact-generated magnetic field or terrestrial lightning strikes. Although coarse-grained magnetite is traditionally characterized by weak coercivity and remanence, the specimen used in the present study exhibited high coercivity and an intense remanent magnetization. The presence of hematite lamellae observed on the partially oxidized magnetite specimen indicated an array of striped domains, intensifying a remanence and coercivity. We also conducted XAS and XMCD analyses on a natural lodestone permanent magnet produced by lightning strikes; while maghemite was found to be present, no magnetic domain structures were observed. Considering that the nucleation of hematite lamellae on magnetite/maghemite grains is due to oxidation, we attribute the intense remanent magnetization and magnetic hardening of Vredefort granites to post-impact hydrothermal activity.

Keywords: striped domain, corase-grained magnetite, XMCD, lodestone, post-impact hydorothermal activity, lightning, hematite lamellae

Introduction

The Vredefort dome is known as the largest and oldest (2023 ± 4 Ma) terrestrial impact structure. It is the deeply-exhumed remnant of the central uplift zone of a crater with an original diameter of ~250 km (Reimold and Gibson, 1996; Gibson and Reimold, 2008) and exhibits strong aeromagnetic anomalies (Hart et al., 1995). Shocked Archean granitic rocks in the crystalline core

of the Vredefort crater exhibit anomalously strong natural remanent magnetization (NRM), but with random centimeter-scale orientation (Hart et al., 1995; Carporzen et al., 2005; Salminen et al., 2009). Previous researchers have hypothesized that the origin of these unique magnetic remanence properties is associated with very intense impact-generated small-wavelength magnetic fields that not only produce strong remanence, but also randomize the directions of the remanence (e.g., Hart et al., 1995; Cloete et al., 1999; Carporzen et al., 2005). This hypothesis has been rejected based on the observation of terrestrial lightning remagnetization in studies that utilized 10-m borehole paleomagnetic measurements (Carporzen et al., 2012) and artificial lightning experiments (Salminen et al., 2013). Salminen et al. (2013) found that lightning-induced enhancement of remanence is due to the secondary production of partially oxidized magnetite, implying the presence of post-impact alteration. To understand these unusual remanence properties of Vredefort rocks, it might be necessary to consider the effect of impact-generated hydrothermal fluids that flow through fractures in the rocks (e.g., Osinski et al., 2013; Quesnel et al., 2013; Yokoyama et al., 2015). Such fluids enhance the remanence of primary low-coercivity coarse-grained magnetite by high-temperature oxidation.

Lightning-induced remanent magnetization (LIRM) is capable of remagnetizing grains with relatively low magnetic coercivities. Verrier and Rochette (2002) described alternating-field (AF) demagnetization and clearly distinguished secondary variably-oriented LIRM from primary remanence in a high AF (Graham, 1961). Vredefort granitic rocks contain magnetite with two different grain sizes. The first size is often on the order of microns to millimeters and grains of this size are formed at about 3.0 Ga (e.g., Cloete et al., 1999; Nakamura et al., 2010). The second size is less than 1 μm and grains of such size are formed within the interstices of the planar deformation features (PDFs) of quartz formed by impacts of 2.02 Ga (e.g., Cloete et al., 1999). Although it is generally believed that coarse-grained magnetites contain soft secondary components that are of "little geological interest" (Butler, 1992; Nakamura et al., 2010) showed that such magnetites embedded in biotite produce highly coercive and strong remanence, as determined by surface magnetic imaging using a scanning magneto-impedance magnetic microscope (**Figure 1A**). By Raman spectroscopy, they also found that a particular type of coarse-grained magnetite has lamellae of hematite. Salminen et al. (2013) succeeded in reproducing the unusual remanence properties by artificial lightning experiments, and showed that the source mineral was a coarse-grained partially oxidized magnetite with irregular magnetic microstructures and reduced grain size. They, however, undertook no further petrographic examination. Banfield et al. (1994) also proposed a relationship between the inter-grown nanometer-scale microstructure of massive-maghemite and the strong magnetic properties of the natural permanent magnet known as lodestone. It is well known that the magnetite-ilmenite intergrowths formed by the high-temperature oxidation of titanomagnetite, and not the multiple mineralogies, are what contribute to the highly stable remanence of a subdivision of minerals that include magnetite, maghemite, and non-magnetic ilmenite (e.g., Davis and Evans, 1976; Tucker and O'Reilly, 1980). Harrison et al. (2002) showed that magnetic susceptibility and remanence can be substantially enhanced by the formation of small amounts of magnetite and/or maghemite. However, there has been no report on the magnetic domain structure of highly magnetized natural rocks.

Almost all the Vredefort granitoid rocks with random and strong remanence that were examined by Carporzen et al. (2005) and Salminen et al. (2013) exhibited high-temperature metamorphism at >800°C during post-impact event (e.g., Gibson and Reimold, 2008). This mechanism is capable of nearly or completely remagnetizing any remanence by subsequent cooling and/or post-impact hydrothermal activity (Salminen et al., 2009). We therefore investigated the effect of post-impact high-temperature metamorphism on the microtexture of magnetic minerals that have been strained or modified by a shock event or post-shock process. The investigation, which was undertaken at the SPring-8 facility, utilized X-ray magnetic circular dichroism (XMCD) and X-ray absorption spectroscopy (XAS) using a spectroscopic photoelectron low-energy electron emission microscope (SPELEEM). We also determined the crystallographic orientation of the minerals by electron backscatter diffraction (EBSD). This study was undertaken to address the question of why coarse-grained types of magnetite found in Vredefort rocks possess strong and high coercive remanence.

Materials and Method

Sample Description

The utilized shocked granite of 2.5 cm in diameter was drilled from an exposed crystalline basement of the Vredefort crater near Parys, South Africa, at 26°52.615′S 27°25.277'E. The sample was provided by J. Salminen (University of Helsinki). The magnetic properties of the rock specimen had already been measured by J. Salminen, and comprised a density of 2599 kg/m^3, bulk NRM intensity of 9.1 A/m, Königsberger ratio (defined as the ratio of the NRM to the product of the magnetic susceptibility and geomagnetic field) of 75, and Curie temperature of 588°C (which is equal to that of magnetite). Nakamura et al. (2010) examined the Raman spectroscopy of tip samples of thickness 1.0 and 1.5 mm and found the NRM intensities to be 13.1 A/m. They confirmed the presence of hematite lamellae on the host magnetite, which was embedded in chloritized biotite.

A thin section was made from the same tip sample examined by Nakamura et al. (2010) to examine the magnetic properties of the same grain by SPELEEM. Before the present experiments, the surface of the thin section was carefully polished using 1-μm-diameter diamond paste. The specimen was then finished by buff polishing using colloidal silica slurry. The thin section was subjected to an impulse field of several hundred milli-Teslas in an out-of-plane orientation. We then rescanned the surface magnetic stray field on the thin section and detected the presence of highly coercive coarse-grained magnetites after 50-mT stepwise AF demagnetization using a scanning magneto-impedance (MI) magnetic microscopy (**Figure 1A**). The grain was also examined by reflected light microscopy (**Figure 1B**)

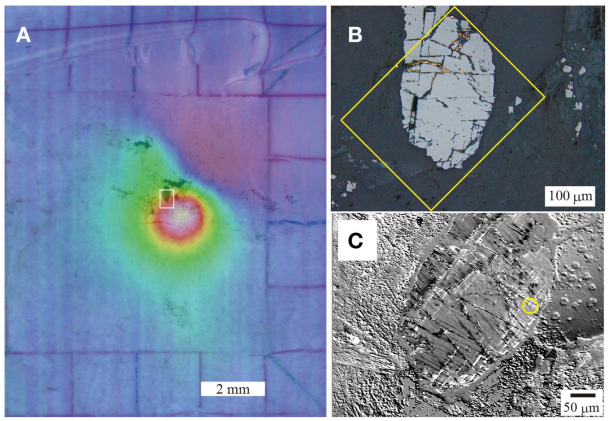

FIGURE 1 | Isothermally magnetized thin section of target magnetite obtained from Vredefort granite. (A) Microphotograph of superimposition of the thin section on a surface stray magnetic field obtained by a scanning MI magnetic microscope. Note that there are two coarse-grained magnetites beneath the magnetic anomaly. The warm color indicates a strong stray magnetic field, white the white rectangle indicates the region of the image enlarged in **(B)**. **(B)** Reflected-light optical image of the thin section. The surface was polished by ¼-μm diamond paste and finished by colloidal silica. The yellow rectangle indicates the area enlarged in **(C)**. **(C)** Magneto-optical Kerr-effect microscope image of target magnetite. Note the three different arrays of lamellae (white and black). The yellow circle indicates the target area analyzed by a SPELEEM.

and magnetic Kerr-effect microscopy (**Figure 1C**), and this revealed three different orientations of lamellae. No fine-grained magnetites were found in the PDFs of the shocked quartz grain of the thin section, and this suggested that our coarse-grained magnetite was a major paleomagnetic carrier. This type of magnetite is unique and can be used to investigate the unusual magnetic properties of Vredefort granite. This enhances the reliability of using only one sample for this study.

Spectroscopic Photoemission and low-energy electron microscope (SPELEEM)

The experiments were performed using a SPELEEM produced by ElmitecCreative Commons Attribution License (CC BY)and a soft X-ray beamline (BL17SU) at the SPring-8 facility. The SPELEEM achieved a high spatial resolving power by the use of magnetostatic lenses, with a spatial resolution of 22 nm. Three different excitation sources (highly brilliant circularly polarized soft X-ray, electron beam, and mercury lamp) were used to visualize the surface structure of the specimen. Circular-polarized soft X-rays were used to determine the spatially resolved chemical composition, the electronic states, and the magnetic domain structures of the specimen. The fine structure of the X-ray absorption spectrum (XAS) was used to analyze the mineral species and their spatial distribution. The XMCD effect was used to visualize the magnetic domain structures of the sample, and an electron beam was used to image the surface topological structure. The SPELEEM was used to simultaneously obtain information about the mineral species and their distribution as well as the magnetic domain structure and surface structure (Kotsugi et al., 2010, 2011).

We analyzed the X-ray absorption spectrum at the Fe L_3 absorption (706–712 eV) edge to determine the species of iron oxides, and used XMCD to visualize the magnetic domains. The XMCD-PEEM contrast was expressed as the intensity difference $I_\mu(+) - I_\mu(-)$, where $I_{\mu(+)}$ and $I_{\mu(-)}$ are respectively the image intensities determined by right-handed ($\mu(+)$) and left-handed ($\mu(-)$) circularly-polarized lights. This image treatment contrasts due to non-magnetic factors, namely, the topography and chemical composition. Because 3d transition metals (Fe, Co, and Ni) have $L_{3,2}$ absorption-edges that experience 2p→3d core electron transitions at 700–730 eV, magnetic information about the 3d electrons can be selectively obtained from the soft X-ray region. The Fe $L_{3,2}$-edge XMCD spectra of iron oxides such as magnetite exhibit three characteristic peaks with respect to the chemical environment (Pearce et al., 2006), namely, the Fe^{2+} octahedral peak (negative peak, ∼710.5 eV), Fe^{3+} tetrahedral peak (positive peak, ∼711.5 eV), and Fe^{3+} octahedral peak (negative peak, ∼712.5 eV).

Furthermore, to determine the differences between the crystallographic orientations of magnetite and those of hematite crystals, we employed EBSD using a scanning electron microscope (HITACHI S-3400N) equipped with HKL Flamenco for EBSD data acquisition.

Results

The SPELEEM was used to examine the remanence-carrying coarse-grained magnetite with lamellae, indicated by the yellow circle in **Figure 1C**. The chemical distribution of Fe on the Fe L_3 absorption edge was determined, and the local XAS spectra were extracted from areas 1–7 indicated by the colored lines in the XAS-PEEM image in **Figure 2A** ($I_\mu(+) - I_\mu(-)$). The green square (area 1), yellow square (area 2), and sky blue square (area 3) indicate regions within the host minerals; and the red triangle (area 4), blue square (area 5), violet triangle (area 6), and purple square (area 7) indicate portions of the lamellae. The corresponding X-ray absorption spectra of the host minerals are shown in **Figure 2C**, and those of the lamellae are shown in **Figure 2D**. **Figure 2B** shows the reference spectra of the Fe $L_{3,2}$ absorption edge of the iron oxides obtained from previous works (e.g., Kuiper et al., 1993; Pearce et al., 2006; Signorini et al., 2006; Kuzmin and Chaboy, 2014; Piquer et al., 2014). By comparing the spectral shapes of the data obtained from the present study with the references, the materials in areas 1–3 were determined to be magnetite, and those in areas 4–7 were determined to be hematite. The noticeable energy shift of ∼2 eV observed between the present and reference data is due to the differing oxidation states, and such is not uncommon in magnetite (Waychunas et al., 1983; Okudera et al., 2012).

Figure 3A shows a clear image of the structure of the striped magnetic domain. The striped domains in the target magnetite have a horizontally sinuous pattern that is cut by the hematite lamellae that run perpendicular to the domain walls. The magnetic contrast of the magnetic domain structure is proportional to the cosine of the angle between the atomic magnetic moment and the incident light. Hence, the absence of a change in the contrast of the XMCD image indicates

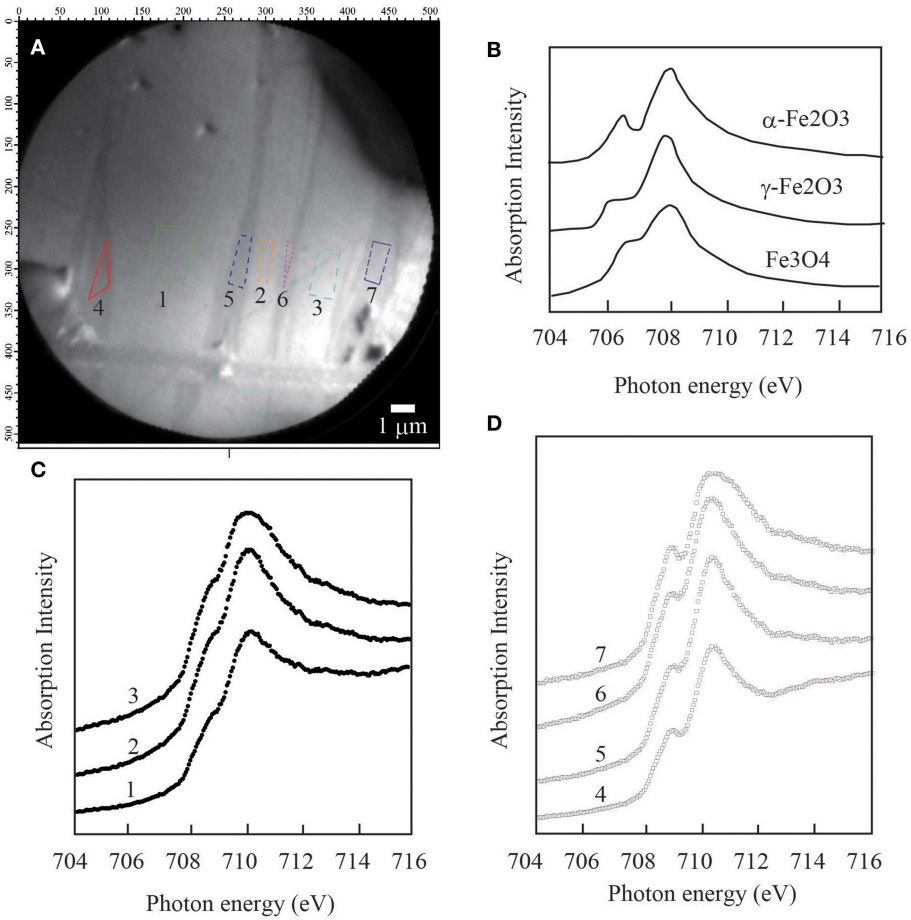

FIGURE 2 | X-ray Fe L_3 edge chemical analysis of the magnetite specimen. (A) X-ray absorption spectroscopy (XAS) image of areas 1–7. **(B)** XAS spectra of the reference bulk samples of hematite (α-Fe_2O_3), maghemite (γ-Fe_2O_3), and magnetite (Fe_3O_4). **(C)** XAS spectra of areas 1–3 on the host mineral, indicating the presence of magnetite by comparison with the reference spectra. **(D)** XAS spectra of areas 4–7 on the lamellae, indicating the presence of hematite by comparison with the reference spectra.

out-of-plane magnetization, while the observation of a change indicates in-plane magnetization. To further verify the out-of-plane orientation of the magnetization, the specimen was rotated by 70° about the vertical axis, while the same incident angle of the synchrotron radiation was maintained. As can be observed from **Figure 3B**, the brightness and contrast of the underlying striped magnetic domains revealed no change in the incident light of the synchrotron radiation, thereby indicating out-of-plane magnetization. The grayscale of the figure indicates the XMCD intensity. The dark portions of the image indicate upward-magnetization, and the white portions indicate downward-magnetization perpendicular to the surface. Owing to the difficulty of achieving saturated out-of-plane magnetization, it can be concluded that our magnetite possessed highly coercive and strong remanence.

Figure 3C shows the XAS and XMCD spectra of the magnetite region (white box) in **Figure 3A**. The XAS spectra of this region agree well with the reference spectra of the natural magnetite in **Figure 2C**. The XMCD was calculated as the difference between two different helicities (**Figure 3C**). The XMCD difference spectrum (**Figure 3C**, bottom) shows the well-defined peaks on the L_3 and L_2 edges, as characteristic of magnetite (Goering et al., 2006). The two negative peaks on the L_3 edge are mainly due to the octahedral Fe^{2+} and Fe^{3+} ions. The small positive peak in the middle is due to the tetrahedral Fe^{3+} ions. The opposite signs of the XMCD peaks produced by the Fe cations at the octahedral and tetrahedral sites indicate antiferromagnetic coupling. The magnetite crystals are thus ferrimagnetic. The cause of the little differences between the positive tetrahedral Fe^{3+} and negative octahedral Fe^{2+} is unknown. According to Piquer et al. (2014), the shift of the energies of the absorption peaks in the magnetite XAS spectra is due to a single-phase non-stoichiometric $Fe_{3-\delta}O_4$ oxide, and this modifies the structural arrangements at the Fe sites.

To compare the magnetic properties of the strongly magnetic Vredefort rocks with those of a lightning-created material (i.e., lodestone), we undertook the first ever XAS and XMCD analyses of natural lodestone (**Figure 4**), which has different

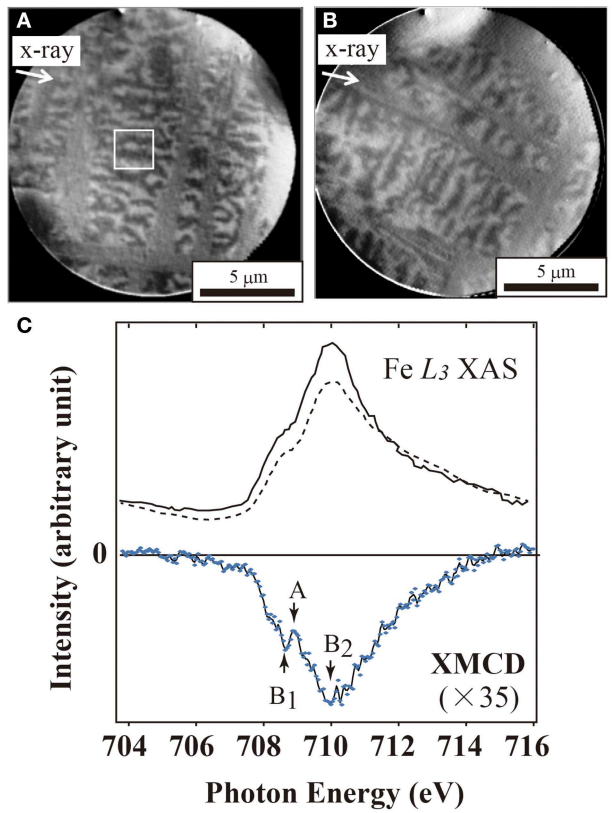

FIGURE 3 | Magnetic domain structure of the same area of the magnetite specimen in Figure 2. (A) XMCD images obtained using the difference between two different helicities acquired from the Fe L_3 absorption edge (708.4 eV). The host magnetite is cut by a biaxial array of hematite lamellae, and has striped magnetic domains measuring less than about $4 \times 0.8\,\mu m$. The white box indicates the acquisition area for XAS and XMCD. **(B)** Rotation of the image in **(A)** by 70° about an axis vertical to the specimen. No change was observed in the domain structure, suggesting that the magnetic moment was directed toward the out-of-plane component. **(C)** XAS and XMCD spectra of the X-ray Fe L_3 edge of the magnetite matrix. The solid and dashed lines are the XAS spectra of two different helicities, and the blue dots indicate the XMCD spectrum, which shows a positive peak (A) and two negative peaks (B_1 and B_2).

host mineralogy. Lodestone is a natural permanent magnet that attracts a paper clip (see **Figure 4A**), and the specimen used in this study was obtained from a magnetite ore, namely, a granitic pegmatites (Utah, USA, exact locality unknown). **Figures 4B,C** show a typical LEEM chemical component image and XMCD magnetic domain image of lodestone. Maghemite contained in a magnetite matrix cut by hematite lamellae was observed in the lodestone specimen (**Figure 4B**). The magnetite had a typical maze-like domain pattern (**Figure 4C**, bottom) and a characteristic disordered domain pattern (**Figure 4C**, upper). The XAS spectra of the L_3 and L_2 edges revealed the presence of maghemite (**Figures 4D,E**) (Brice-Profeta et al., 2005), and the XMCD spectra had two negative peaks (octahedral Fe^{2+} and Fe^{3+}) and one positive peak (tetrahedral Fe^{3+}). The XAS spectra of our Vredefort specimen were identical with those of the magnetite. However, the negative octahedral Fe^{2+} peak in the XMCD spectra was lower than that of lodestone, and the corresponding magnetic contribution was comparable to that of the octahedral Fe^{3+}. The lower octahedral Fe^{2+} peak indicates partial oxidation of magnetite, and this suggests the presence of trace maghemite in the L_3 spectrum of the host magnetite, as also observed by Salminen et al. (2013). The magnetic domain structure of our partially oxidized magnetites contained a striped domain cut by hematite lamellae. The domain structure differs from the maze-like domains of the host magnetites in lodestone.

The crystal orientations of the minerals (i.e., magnetite and hematite) were obtained by EBSD in the same region of the XMCD analysis. The observed Kikuchi patterns of the magnetite grain clearly indicated an inverse spinel pattern (**Figures 5A,B**), while the hematite lamellae were observed to have trigonal patterns (**Figures 5C,D**). **Figure 5E** is an equal-area diagram of the lower hemisphere, and it shows that the <0001> direction on the c-axis of the hematite is perpendicular to the {111} plane of the magnetite. Although magnetization can be easily achieved in the <111> direction of magnetite, the results of the XMCD analysis showed that the actual magnetization direction in the specimen was close to the hard <100> axis.

Discussion

By 10-m borehole paleomagnetic measurements, Carporzen et al. (2012) showed that terrestrial lightning strike was the cause of the unusual magnetic rock properties of Vredefort granites. They also found that the natural remanence directions and their 0.55-m magnetic anomaly vectors mostly lie along a great vertical circle and are consistent with the circular field expected for a current flowing horizontally in the northeastern direction. In addition, in the southeastern part of their study area, they observed a negative magnetic anomaly that extended concentrically around the center of the dome. This concentric magnetic anomaly has often been observed within an inner annular zone (e.g., Quesnel et al., 2013; Yokoyama et al., 2015), and it cannot be explained by only terrestrial lightning strike. Moreover, the inner annular zone might be a path for percolated post-hydrothermal fluids that flowed along fractures. Salminen et al. (2013) confirmed that the strong remanence of Vredefort granites was due to lightning strikes on the rocks, which previously contained partially oxidized magnetite within their microstructures. Our results also showed that coarse-grained magnetite in Vredefort granites contained an array of hematite lamellae, resulting from a partial oxidation. The presence of hematite lamellae might be prerequisite for the origin of high magnetization. It is therefore considered that preexisting partially oxidized magnetite in Vredefort granites intensify the remanence.

Our XMCD and XAS analyses showed that the hematite lamellae cut magnetic domains in the host magnetite. The opposite sense of the XMCD peaks produced by the Fe cations at the octahedral and tetrahedral sites indicated antiferromagnetic coupling of the cations (Monti et al., 2012). The grains of the host magnetite were divided into smaller grains measuring less than $5 \times 10\mu m$. These smaller parallel-piped grains correspond to a pseudo-single domain of magnetite in terms of size

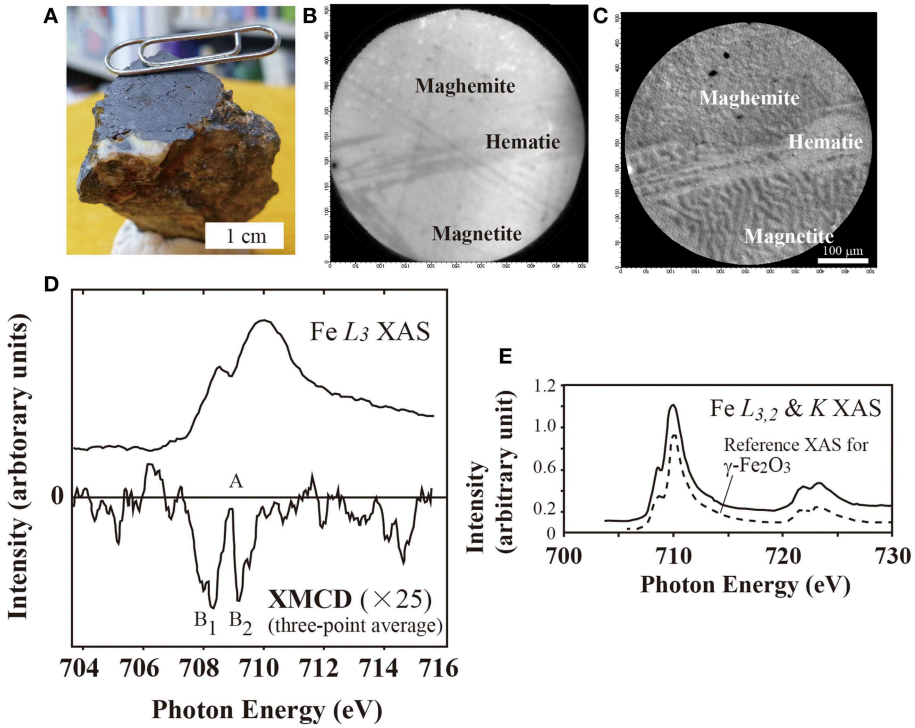

FIGURE 4 | Reference spectra of lodestone (natural permanent magnet). (A) Photograph of the sample lodestone attracting a clip. The bulk sample was obtained from the arbitrary surface shown in the photograph. The surface was polished by ¼-μm diamond paste and finished by colloidal silica. **(B)** X-ray Fe L_3 edge chemical analysis of the target area, showing oxidized magnetite (maghemite), hematite lamellae, and the host magnetite. **(C)** Magnetic domain structures of the corresponding area, showing the typical maze-like domain pattern of the magnetite cut by the hematite; no magnetic domain structure of the maghemite is discernible from the magnified image. **(D)** XAS and XMCD spectra of the X-ray Fe L_3 edge of the maghemite. The solid lines are the XAS and XMCD spectra, with the latter showing a positive peak (A) and two negative peaks (B_1 and B_2). **(E)** Comparison of the reference XAS spectrum of the X-ray Fe $L_{3,2}$ and K edge of maghemite with that of our sample.

and shape (Butler and Banerjee, 1975). EBSD showed that the {0001} planes of hematite contact the plane parallel to the {111} planes of magnetite (the easily magnetized axes of magnetite and hematite are in the <111> direction and {0001} plane). The subdivision of the host magnetite by a biaxial array of hematite yielded new and smaller striped domains with out-of-plane magnetizations. Kasama et al. (2006) reported that the out-of-plane magnetization of magnetite thin films are directly associated with the presence of structural defects and antiferromagnetic coupling. Incidentally, based on an annealing experiment performed on a magnetite thin film for 4 min in air at 250°C, Wei et al. (2006) showed that the appearance of striped domain structures was possibly caused by defect-related out-of-plane magnetization. Therefore, antiferromagnetically coupled hematite lamellae may immobilize the movement of striped domain walls. This suggests that the highly coercive and intense remanence of our coarse-grained magnetite is due to the presence of newly formed striped domains.

Yokoyama et al. (2015) reported the impact-induced hydrothermal alteration of the magnetic mineralogy of basalts obtained from an internal annular zone in the Vargeão impact structure in southern Brazil. This confirmed the formation of new secondary magnetic carriers such as magnetite and hematite along a highly hydrated and oxidized fracture. They proposed that the interaction of a hydrothermal fluid with brecciated basalts at higher than 200°C account for the occurrence of magnetite and hematite under no equilibrium with the atmosphere in an internal annular zone. This suggests that the observed concentric aeromagnetic anomalies were due to localized hydrothermal alteration along concentric faults, which acted as conduits for fluid circulation through the impact structure. Such a concentric and negative aeromagnetic anomaly has been observed in the Vredefort dome (Muundjua et al., 2007). The magnetite sample used in this study was taken from the region in which the anomaly was found, and this implies the occurrence of hydrothermal alteration in the impact structure.

Magnetite generally transforms to hematite by oxidation at high temperatures. Below 300°C, magnetite oxidizes to the metastable phase known as maghemite (γ-Fe_2O_3) by the migration of Fe cations (e.g., Gallagher et al., 1968). At higher temperatures (roughly above 600°C), the oxidation of magnetite always results in the formation of secondary hematite (Colombo et al., 1965). The granite used in this study must have experienced a reheating event due to the impact of a

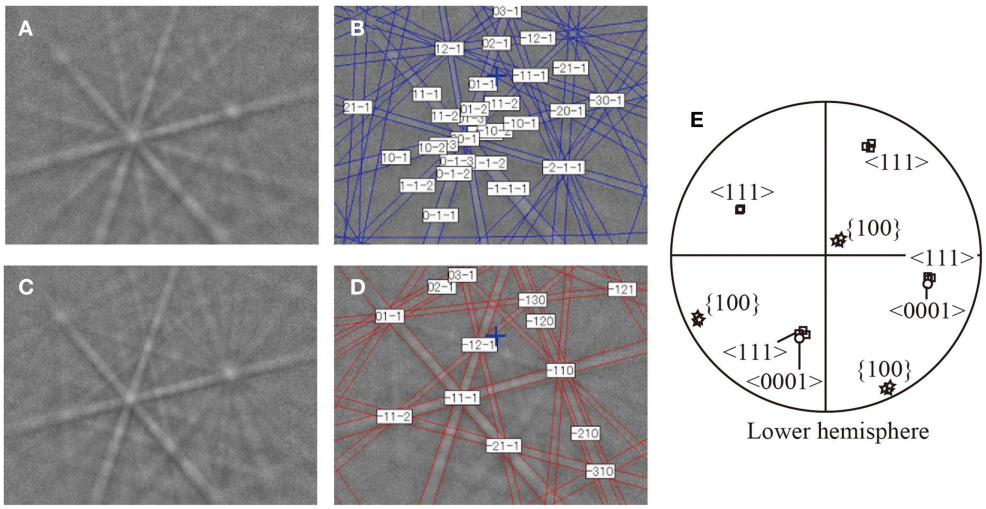

FIGURE 5 | EBSD Kikuchi patterns of (A,B) magnetite and (C,D) hematite. (E) Superposition of the crystal orientations of magnetite and hematite in the lower hemisphere. The <0001> directions of hematite indicated by the open circles correspond to the <111> directions of magnetite indicated by the open squares. The star symbols represent the {100} plane of magnetite.

meteorite. Based on the model of Ivanov (2005), the central part of the impact structure (of radius $\leq$15 km) would have been extensively heated above 700°C. Magnetites in the granite might have transformed into hematite by high-temperature oxidation induced by the impact of the meteorite (2.03 Ga). By *in situ* X-ray spectroscopy, McCarty et al. (2014) found a biaxial array of hematite lamellae in oxidized magnetite after heating to 600°C. We also found that our magnetite contained very dense hematite lamellae that run horizontally and vertically (see **Figures 2A**, **3A**), and this suggests the occurrence of secondary high-temperature metamorphism. Furthermore, the presence of maghemite might indicate that our magnetite also experienced low-temperature oxidation such as induced by lightning strikes. Our XMCD spectra and the domain examination of our magnetite revealed the conversion of Fe^{2+} ions to Fe^{3+} ions and the presence of characteristic striped magnetic domains cut by biaxial hematite lamellae. As previously proposed by Salminen et al. (2009), these evidences of high-temperature oxidation suggest that Vredefort rocks have experienced hydrothermal alteration induced by an impact event, and hence the occurrence of impact-generated hydrothermal activity beneath the crater. It is posited that latter terrestrial lightning strikes on the hydrothermally oxidized magnetites intensified their magnetization.

Conclusion

Using a SPELEEM, we observed striped magnetic domains subdivided by hematite lamellae in a high-coercivity coarse-grained magnetite obtained from Vredefort granite. In addition, X-ray absorption spectra showed that the coarse-grained magnetite had been partially oxidized into maghemite, and XMCD analysis clarified the magnetic contribution of the octahedral Fe^{3+} ions. The array of hematite lamellae within the partially oxidized magnetite suggests that the rock has been affected by post-impact hydrothermal activity beneath the Vredefort crater. Latter terrestrial lightning strikes on the partially oxidized magnetite intensified its remanence.

Acknowledgments

I sincerely thank Prof. Roger Gibson and Mr. Cristo Mayer for their kind field guides around the Vredefort dome. The synchrotron radiation experiments were performed at the BL17SU of SPring-8 with the approval of the Japan Synchrotron Radiation Research Institute (JASRI) (Proposal No. 2011A1194 and 2012A1323). Mr. Mandai helped our SPLEEM measurements. This work was supported by JSPS KAKENHI Grant Number 22340146.

References

Banfield, J. F., Wasilewski, P. J., and Veblen, D. R. (1994). TEM study of relationships between the microstructures and magnetic properties of strongly magnetized magnetite and maghemite. *Am. Mineral.* 79, 654–667.

Brice-Profeta, S., Arrio, M-.A., Tronc, E., Letard, I., dit Moulin, C. C., and Sainctavit, P. (2005). XMCD investigation of spin disorder in γ-Fe_2O_3 nanoparticles at the Fe $L_{2,3}$ edges. *Phys. Scr.* T115, 626–628. doi: 10.1238/Physica.Topical.115a00626

Butler, R. F. (1992). *Paleomagnetism: Magnetic Domains to Geologic Terranes.* Oxford: Blackwell Science.

Butler, R. F., and Banerjee, S. K. (1975). Theoretical single-domain grain size range in magnetite and titanomagnetite. *J. Geophys. Res.* 80, 4049–4058. doi: 10.1029/JB080i029p04049

Carporzen, L., Gilder, S. A., and Hart, R. J. (2005). Palemagnetism of the Vredefort meteorite crater and implications for craters on Mars. *Nature* 435, 198–201. doi: 10.1038/nature03560

Carporzen, L., Weiss, B. P., Gilder, S. A., Pommier, A., and Hart, R. J. (2012). Lightning remagnetization of the Vredefort impact crater: no evidence for impact-generated magnetic fields. *J. Geophys. Res.* 117, E01007. doi: 10.1029/2011JE003919

Cloete, M., Hart, R. J., Schmidt, H. K., Mdrury, M., Demanet, C. M., and Vijaya, S. K. (1999). Characterization of magnetic particles in shocked quartz by means of electron- and magnetic force microscopy: Vredefort, South Africa. *Contrib. Mineral. Petrol.* 137, 232–245. doi: 10.1007/s004100050548

Colombo, U., Gazzarini, F., Lanzavecchia, G., and Sironi, G. (1965). Magnetite oxidation: a proposed mechanism. *Science* 147:1033. doi: 10.1126/science.147.3661.1033

Davis, P. M., and Evans, M. E. (1976). Interacting single-domain properties of magnetite intergrowths. *J. Geophys. Res.* 81, 989–994. doi: 10.1029/JB081i005p00989

Gallagher, K., Feitknecht, W., and Mannweiler, U. (1968). Mechanism of oxidation of magnetite to gamma-Fe_2O_3. *Nature* 217, 1118–1121. doi: 10.1038/2171118a0

Gibson, R., and Reimold, W. U. (2008). *Geology of the Vredefort Impact Structure: A Guide to Sites of Interest.* Pretoria: Council for Geoscience.

Goering, E., Gold, S., Lafkioti, M., and Schutz, G. (2006). Vanishing Fe 3d orbital moments in single-crystalline magnetite. *Europhys. Lett.* 73, 97. doi: 10.1209/epl/i2005-10359-8

Graham, K. W. T. (1961). The re-magnetization of a surface outcrop by lightning currents. *Geophys. J. R. Astron. Soc.* 6, 85–102. doi: 10.1111/j.1365-246X.1961.tb02963.x

Harrison, R., Dunin-Borkowski, R. E., and Putnis, A. (2002). Direct imaging of nanoscale magnetic interactions in minerals. *Proc. Natl. Acad. Sci. U.S.A.* 99, 16556–16561. doi: 10.1073/pnas.262514499

Hart, R. J., Hargraves, R. B., Andreoli, M. A. G., Tredoux, M., and Doucourè, C. M. (1995). Magnetic anomaly near the center of the Vredefort structure: implications for impact-related magnetic signatures. *Geology* 23, 277–280.

Ivanov, B. A. (2005). Numerical modeling of the largest terrestrial meteorite craters. *Solar Syst. Res.* 39, 381–409 doi: 10.1007/s11208-005-0051-0

Kasama, T., Dunin-Borkowski, R. E., and Eerenstein, W. (2006). Off-axis electron holography observation of magnetic microstructure in a magnetite (001) thin film containing antiphase domains. *Phys. Rev. B* 73:104432. doi: 10.1103/PhysRevB.73.104432

Kotsugi, M., Mitsumata, C., Maruyama, H., Wakita, T., Taniuchi, T., Ono, K., et al. (2010). Novel magnetic domain structure in iron meteorite induced by the presence of $L1_0$-FeNi. *Appl. Phys. Exp.* 3:013001. doi: 10.1143/APEX.3.013001

Kotsugi, M., Mizuguchi, M., Sekiya, S., Ohkouchi, T., Kojima, T., Takanashi, K., et al. (2011). Determination of local magnetic moment in $L1_0$-FeNi using photoelectron emission microscopy (PEEM). *J. Phys.* 266:012095. doi: 10.1088/1742-6596/266/1/012095

Kuiper, P., Searle, B. G., Rudolf, P., Tjeng, L. H., and Chen, C. T. (1993). X-ray magnetic dichroism of antiferromagnet Fe_2O_3: the orientation of magnetic moments observed by Fe 2p X-ray absorption spectroscopy. *Phys. Rev. Lett.* 70, 1549–1552. doi: 10.1103/PhysRevLett.70.1549

Kuzmin, A., and Chaboy, J. (2014). EXAFS and XANES analysis of oxides at the nanoscale. *Inter. Union Crystallogr. J.* 1, 571–589. doi: 10.1107/S2052252514021101

McCarty, K. F., Monti, M., Nie, S., Siegel, D. A., Starodub, E., El Gabaly, F., et al. (2014). Oxidation of magnetite (100) to hematite observed by *in situ* spectroscopy and microscopy. *J. Phys. Chem. (C)* 118, 19768–19777. doi: 10.1021/jp5037603

Monti, M., Santos, B., Mascaraque, A., de la Fuente, O. R., Niño, M. A., Menteş, T. O., et al. (2012). Magnetism in nanometer-thick magnetite. *Phys. Rev. B* 85, 020404(R). doi: 10.1103/physrevb.85.020404

Muundjua, M., Hart, R. J., Gilder, S. A., Carporzen, L., and Galdeano, A. (2007). Magnetic imaging of the Vredefort impact crater, South Africa. *Earth Planet. Sci. Lett.* 261, 456–468. doi: 10.1016/j.epsl.2007.07.044

Nakamura, N., Okuno, K., Uehara, M., Ozawa, T., and Fuller, M. (2010). "Coarse-grained magnetites in biotite as a possible stable remanence-carrying phase in Vredefort granites," in *Large Meteorite Impacts and Planetary Evolution IV, The Geological Society of America Special Paper*, Vol. 465, eds R. L. Gibson and W. U. Reimold (Boulder, CO: The Geological Society of America, Inc.), 165–172.

Okudera, H., Yoshiasa, A., Murai, K., Okube, M., Takeda, T., and Kikkawa, S. (2012). Local structure of magnetite and maghemite and chemical shift in Fe K-edge XANES. *J. Mineral. Petrol. Sci.* 107, 127–132. doi: 10.2465/jmps.110624

Osinski, G. R., Tornabene, L. L., Banerjee, N. R., Cockell, C. S., Flemming, R., Izawa, M. R. M., et al. (2013). Impact-generated hydrothermal systems on Earth and Mars. *Icarus* 224 347–363. doi: 10.1016/j.icarus.2012.08.030

Pearce, C. I., Michael, C., Henderson, B., Pattrick, R. A. D., van der Laan, G., and Vaughan, D. J. (2006). Direct determination of cation site occupancies in natural ferrite spinels by $L_{2,3}$ X-ray absorption spectroscopy and X-ray magnetic circular dichroism. *Am. Mineral.* 91, 880–893. doi: 10.2138/am.2006.2048

Piquer, C., Laguna-Marco, M. A., Roca, A. G., Boada, R., Guglieri, C., and Chaboy, J. (2014). Fe K-edge X-ray absorption spectroscopy study of nanosized nominal magnetite. *J. Phys. Chem. (C)* 118, 1332–1346. doi: 10.1021/jp4104992

Quesnel, Y., Gattacceca, J., Osinski, G. R., and Rochette, P. (2013). Origin of the central magnetic anomaly at the Haughton impact structure, Canada. *Earth Planet. Sci. Lett.* 367, 116–122. doi: 10.1016/j.epsl.2013.02.032

Reimold, W. U., and Gibson, R. L. (1996). Geology and evolution of the Vredefort impact structure, South Africa. *J. Afr. Earth Sci.* 23, 125–162. doi: 10.1016/S0899-5362(96)00059-0

Salminen, J., Pesonen, L. J., Lahti, K., and Kannus, K. (2013). Lightning-induced remanent magnetization-the Vredefort impact structure, South Africa. *Geophys. J. Int.* 195, 117–129. doi: 10.1093/gji/ggt230

Salminen, J., Pesonen, L. J., Reimold, W. U., Donadini, F., and Gibson, R. L. (2009). Paleomagnetic and rock magnetic study of the Vredefort impact structure and the Johannesburg Dome, Kaapvaal Craton, South Africa – Implications for the apparent polar wander path of the Kaapvaal Craton during the Mesoproterozoic. *Precambrian Res.* 168, 167–184. doi: 10.1016/j.precamres.2008.09.005

Signorini, L., Pasquini, L., Boscherini, F., and Bonetti, E. (2006). Local magnetism in granular iron/iron oxide nanostructures by phase- and site-selective X-ray magnetic circular dichroism. *Phys. Rev. B* 74:014426. doi: 10.1103/PhysRevB.74.014426

Tucker, P., and O'Reilly, W. (1980). Reversed thermoremanent magnetization in synthetic titanomagnetites as a consequence of high temperature oxidation. *J. Geomagn. Geoelectr.* 32, 341–355.

Verrier, V., and Rochette, P. (2002). Estimating peak currents at ground lightning impacts using remanent magnetization. *Geophys. Res. Lett.* 29, 1867. doi: 10.1029/2002GL015207

Waychunas, G. A., Apted, M. J., and Brown, G. E. Jr. (1983). X-ray K-edge absorption spectra of Fe minerals and model compounds: near edge structure. *Phys. Chem. Min.* 10, 1–9. doi: 10.1007/BF01204319

Wei, J. D., Knittle, I., Hartmann, U., Zhou, Y., Murphy, S., Shvets, I., et al. (2006). Influence of the antiphase domain distribution on the magnetic structure of magnetite thin films. *Appl. Phys. Lett.* 89, 122517. doi: 10.1063/1.2356308

Yokoyama, E., Nedelec, A., Baratoux, D., Trindade, R. I. F., Fabre, S., and Berger, G. (2015). Hydrothermal alteration in basalts from Vargeão impact structure, south Brazil, and implications for recognition of impact-induced hydrothermalism on Mars. *Icarus* 252, 347–365. doi: 10.1016/j.icarus.2015.02.001

Conflict of Interest Statement: The authors declare that the research was conducted in the absence of any commercial or financial relationships that could be construed as a potential conflict of interest.

frontiers in
EARTH SCIENCE

MINI REVIEW ARTICLE
published: 25 September 2014
doi: 10.3389/feart.2014.00023

Paleoenvironmental signature of the Deccan Phase-2 eruptions

***Eric Font*[1]* and *Alexandra Abrajevitch*[2]**

[1] *Instituto Dom Luís, Faculdade de Ciências, Universidade de Lisboa, Lisboa, Portugal*
[2] *Institute of Tectonics and Geophysics, Russian Academy of Sciences, Khabarovsk, Russia*

Edited by:
Kenneth Philip Kodama, Lehigh University, USA

Reviewed by:
Oscar Pueyo Anchuela, Universidad de Zaragoza, Spain
Qingsong Liu, Chinese Academy of Sciences, China

***Correspondence:**
Eric Font, IDL-FCUL, Instituto Dom Luís, Faculdade de Ciências, Universidade de Lisboa, Edifício C8-8.3.22, Campo Grande, 1749-016 Lisboa, Portugal
e-mail: font_eric@hotmail.com

The environmental impact of the Deccan trap volcanism is poorly understood as yet. The paucity of geological markers that can unambiguously be attributed to the Deccan volcanism and the temporal coincidence of the volcanism with an asteroid impact make evaluation of volcanic contribution to the end Cretaceous mass extinction difficult. Here we briefly review environmental proxy records of two reference Cretaceous-Tertiary boundary (KTB) sections, Bidart (France) and Gubbio (Italy). In both sections, a change in color of sediments located just below the KTB is systematically associated with very low values of (low-field) magnetic susceptibility (MS). Rock magnetic characteristics suggest that the decrease in MS values results from the loss (dissolution) of ferrimagnetic mineral in this intervals. In addition to the characteristic change in magnetic assemblage, akaganeite (chlorine-bearing iron oxyhydroxide) is commonly observed under the scanning electron microscope in the low MS intervals at Bidart and Gubbio, but has never been detected in the remaining sedimentary successions. We suggest that the association of granular akaganeite and iron oxides dissolution features can be explained by an ocean acidification and aerosol deposition event linked to the Deccan Phase-2 volcanism.

Keywords: akaganeite, Deccan volcanism, mass extinction, acidification, rock magnetism

INTRODUCTION

The Deccan traps, the greatest episode of continental flood basalt volcanism in the Phanerozoic, released large volumes of greenhouse gasses into the atmosphere perturbing the Earth's carbon cycle and contributing to the end Cretaceous mass extinction (Courtillot et al., 1986; Keller et al., 2011, 2012). The full appreciation of the climatic effects of the Deccan volcanism has been hampered by difficulties in precise dating of the volcanic episodes and correlating them with biostratigraphically dated marine sections. Recently, three discrete Deccan volcanism phases with variable intensity have been dated based on magnetostratigraphy and ^{40}K-^{40}Ar age (Chenet et al., 2007): Phase-1 (~67.5 Ma, 6% in volume), Phase-2 (~65 Ma; 80% in volume) and Phase-3 (~64.5 Ma; 14% in volume). The timing of the largest Deccan volcanic phase (Phase-2) and the Chicxulub impact are thus not resolvable based on their ^{40}K-^{40}Ar ages. The nearly contemporaneous occurrence of these two catastrophic events limits our ability to evaluate their respective contribution to biotic changes at the end of the Cretaceous.

Environmental changes at the KT boundary are recorded in sedimentary archives. Several carbonate sections from the Bay of Biscay and Tethys realm show peculiar changes in the mineralogy, color and magnetic properties within the narrow stratigraphic interval located just below the KT boundary clays. This interval roughly corresponds to the CF1 and CF2 biozones that show dramatic changes in planktic foraminifera, nanno and macrofossils leading up to the KT boundary extinction and is roughly coincident with the timing of the Deccan Phase-2 eruptions (Thibault and Gardin, 2007; Gertsch et al., 2011; Keller et al., 2012). Conventionally, the changes in sediment properties are attributed to the asteroid impact (e.g., Lowrie et al., 1990). Here we argue instead that these characteristic changes record an ocean acidification event caused by the Deccan Phase-2 eruptions.

IRON OXIDE DISSOLUTION AND AKAGANEITE DEPOSITION: DIAGENESIS OR SYN-DEPOSITIONAL CHANGES LINKED TO DECCAN PHASE-2?

The latest Maastrichtian sediments just below the KT boundary at sections from the Bay of Biscay (Bidart) and the Tethys (Gubbio) show significant changes in color, mineralogy and magnetic properties within a narrow stratigraphic interval, thickness of which varies between the sections from several decimeters up to about one meter. The Bidart section consists of hemipelagic to pelagic sediments deposited in a deep basin, and is considered to be one of the most complete KTB sections in Europe (Alegret et al., 2004; Galbrun and Gardin, 2004; Gallala et al., 2009). The KT boundary, easily identifiable by the iridium anomaly (Bonté et al., 1984), is overlain by the typical thin dark clay layer containing the relics of the Chicxulub impact (Apellaniz et al., 1997). The change in color is systematically associated with very low values of magnetic susceptibility (MS) at Bidart and Gubbio (Lowrie et al., 1990; Ellwood et al., 2003; Font et al., 2011). Magnetic susceptibility data, however, is difficult to interpret in a unique way as it includes contributions (in proportion to their abundance) from all—diamagnetic, paramagnetic and

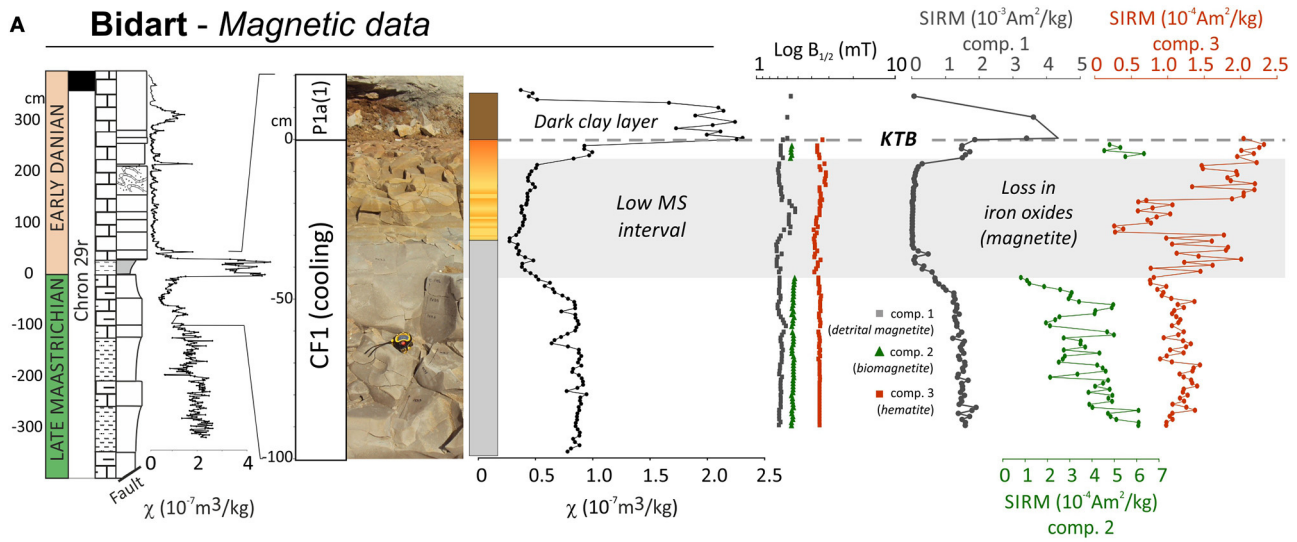

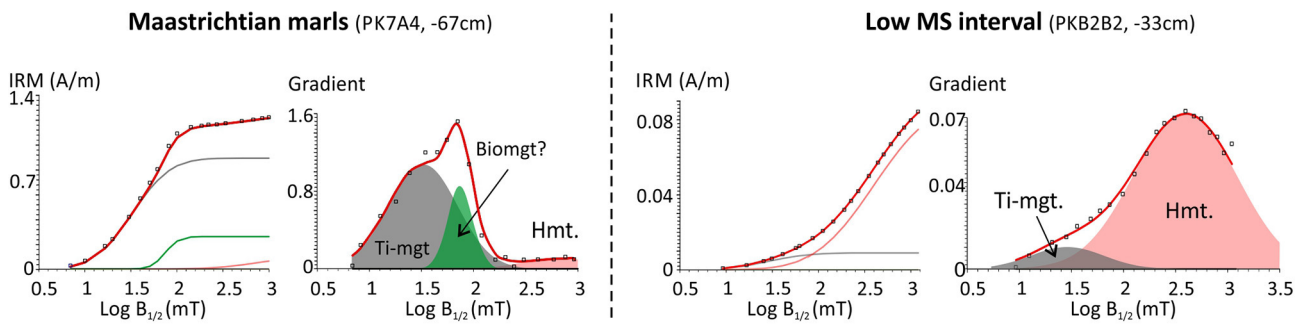

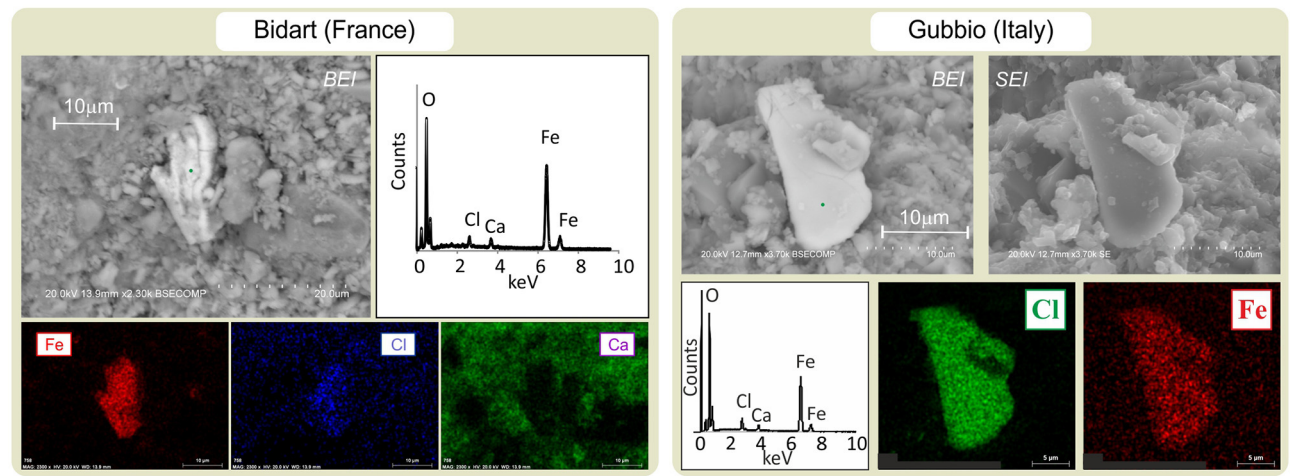

FIGURE 1 | (A) Magnetic data (mass magnetic susceptibility (*x*) and Isothermal Remanent Magnetization parameters) of the Bidart section [modified from Font et al. (2011, 2014)]. KTB is the Cretaceous-Tertiary boundary. Log $B_{1/2}$ (mT) is the mean coercivity of each magnetic component. SIRM corresponds to IRM values at saturation. Component 1 and 2 correspond to detrital and biogenic magnetite, respectively, whereas component 3 is probably hematite. The low MS interval is featured by a loss in detrital and biogenic magnetite. **(B)** Examples of Isothermal Remanent Magnetization (IRM) curves and corresponding

(Continued)

FIGURE 1 | Continued
Cumulative Log-Gaussian curves of one sample from the lower Maastrichtian marls (PKB7A4) and one sample from the low MS interval (PKB2B2); **(C)** Scanning Electron Microscopic photographs (SEM) and Energy Dispersive Spectra (EDS) of akaganeite crystals found at Bidart and Gubbio. BEI and SEI correspond to Back-scattered and Secondary Electron Image, respectively. Compositional mapping show that Fe and Cl are associated to the akaganeite crystal, whereas Ca is only observed in the matrix.

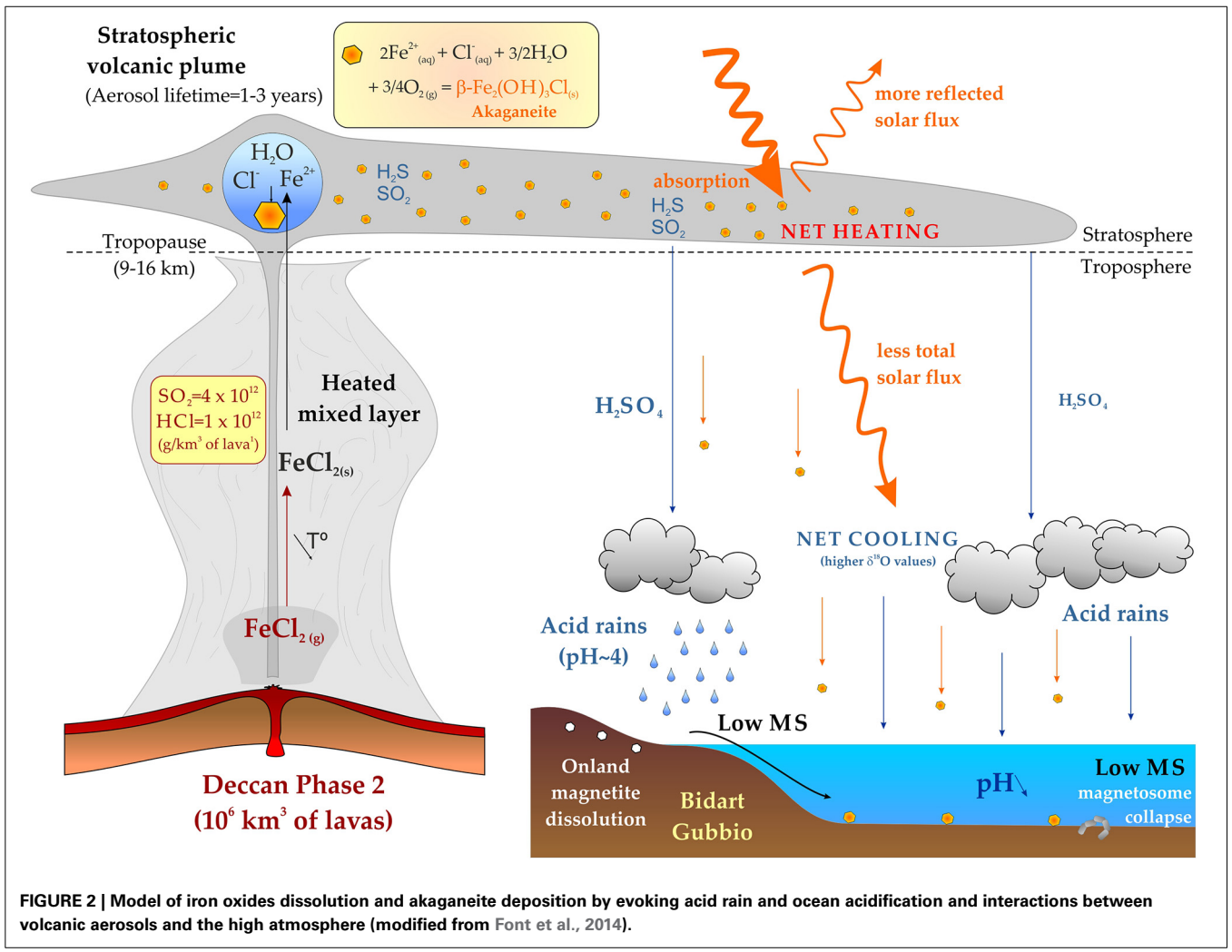

FIGURE 2 | Model of iron oxides dissolution and akaganeite deposition by evoking acid rain and ocean acidification and interactions between volcanic aerosols and the high atmosphere (modified from Font et al., 2014).

ferromagnetic—minerals present in the sediment. Statistical analysis of Isothermal Remanent Magnetization (IRM) acquisition curves (Robertson and France, 1994; Kruiver et al., 2001) provides more detailed information on composition, concentration and grain-size distribution of ferrimagnetic phases. IRM acquisition analyses combined with other rock magnetic techniques identified detrital and biogenic (magnetosomes of magnetotactic bacteria) magnetite, hematite and goethite in the studied sections (Font et al., 2014; **Figure 1**). When compared to background Cretaceous sediments, the low MS zone is characterized by an absence of biogenic magnetite, a decrease in total ferrimagnetic mineral content, and preferential loss of magnetite with respect to hematite (Galbrun and Gardin, 2004; Font et al., 2011; Abrajevitch et al., 2014). A similar style of ferrimagnetic assemblage modification is commonly observed in marine sediments during reductive diagenesis (Cornell and Schwertmann, 2003; Abrajevitch and Kodama, 2011). Reductive dissolution of detrital iron oxides by downward infiltration of reducing waters had previously been proposed by Lowrie et al. (1990) as an explanation for the low susceptibility of white limestones below the KT boundary at Gubbio. The reducing environment was thought to result from the decomposition of large quantity of organic matter produced by the extinctions after the asteroid impact at the KT boundary.

However, at Bidart section the presence of biogenic magnetite (which is particularly sensitive to reductive dissolution) in-between the impact clay and the low MS zone (Abrajevitch et al., 2014) and preservation of primary carbon isotopic signature (Font et al., 2014) are incompatible with the downward infiltration model of Lowrie et al. (1990). More likely, the loss of iron oxides in the low MS zone was due to unusual atmospheric and oceanic chemistry, probably related to high influx of CO_2

and sulfuric acid aerosols from the Deccan Traps (Chenet et al., 2005; Self et al., 2006). The decrease in the content of detrital magnetic minerals may reflect modification of source sediments due to acidic weathering. Modeling of on-land magnetite dissolution suggests that at rainwater pH value of 4.6 (lower than present day pH of ∼5.6) more than 90% of detrital magnetite could have been dissolved during transport from the source to deposition site (Font et al., 2014). The disappearance of biogenic magnetite in the low MS interval at Bidart and Gubbio (Abrajevitch et al., 2014) marks environmental change in marine environment, with the onset of conditions that were unfavorable either to magnetotactic bacteria or to preservation of their fossil magnetosomes.

In addition to the loss of detrital and biogenic magnetite, the low MS interval is characterized by the presence of an unusual mineral akaganeite—a chlorine-bearing iron oxyhyhydroxide (β -$Fe_2(OH)_3Cl$) that has hollandite-type (tunnel-like) structure with the Cl ions residing in the tunnels. Akaganeite has been only observed under SEM microscope in two samples located within the low MS interval, but has never been identified in samples from the underlying Maastrichtian marls, the KT boundary nor in the Danian limestones (Font et al., 2011). Akaganeite is rare in nature and is generally found in environments that are rich in Fe(II) and Cl (Reguer et al., 2007; Remazeilles and Refait, 2007, 2008; Yue et al., 2011), such as like hypersaline lakes (Emmerich et al., 2012), iron sulfide-rich environments (Bibi et al., 2011), fumaroles (Johnston, 1977), corroded steel (Li et al., 2008) and weathered meteorites (Bland et al., 1997). Synthetic and natural akaganeite precipitated from aqueous solutions usually forms as bundles of nanometer-scale particles with spindle- or cigar-shaped morphology (Cornell and Schwertmann, 2003; Yue et al., 2011; Zhang and Jia, 2014). In contrast, akaganeite identified by SEM in Bidart and Gubbio sections occurs as large (∼5–40 μm) isolated crystals with unusual plate-like, granular and semi-hexagonal morphologies. Chlorine-bearing particles of similar size range (2–20 μm) and morphology are presently observed in aerosols of the Masaya volcano in Nicaragua (Moune et al., 2010). Such similarity suggests that akaganeite particles of Gubbio and Bidart sections are also of volcanic origin, likely formed in the Deccan Traps volcanic plume. In the eruption plume that was expanding vertically into the atmosphere, highly soluble chlorine-rich gasses (NaCl, KCl, $FeCl_2$…) rapidly reacted with iron in the presence of water vapor to form akaganeite according to the following equation: $2Fe^{2+}_{(aq)} + 2Cl^{-}_{(aq)} + 3/2H_2O + 3/4O_2 = \beta\text{-}Fe_2(OH)_3Cl_{(s)}$ (Remazeilles and Refait, 2007). Volcanic ash, including akaganeite, was then transported through the stratosphere (Kaminski et al., 2011) and become incorporated into marine sediments (**Figure 2**).

SUMMARY

Rock magnetism is an efficient technique for detecting the variations in composition, concentration and grain-size of the mineral magnetic fraction in sedimentary sequences. Distribution patterns of environmentally sensitive biogenic magnetite in the Bidart section indicate that iron oxide dissolution event, identified by the characteristically low MS values of the latest Maastrichtian sediments, predates the deposition of the KT boundary clay, and thus is not causally related to the asteroid impact. The exclusive presence of akaganeite, a mineral known to form in volcanic plumes, within the low MS intervals suggests instead a causal link to the contemporaneous Deccan Phase-2 eruption episode. Acid rains and ocean acidification resulting from the release of large volumes of greenhouse gasses during the eruptions can account for the loss of magnetic phases. We hypothesize that the association of iron oxide dissolution features and the presence of akaganeite in marine sediments might represent valuable indicators of volcanism-related ocean acidification events in geologic records.

ACKNOWLEDGMENTS

Funding was provided by FCT (ref. PTDC/CTE_GIX/110205/2010). We thank Celia Lee and Ana Sousa for administrative supply, and Fabio Florindo for internal review. We are grateful to Quinsong Liu and Oscar Pueyo Anchuela for their constructive comments.

REFERENCES

Abrajevitch, A., Font, E., Florindo, F., and Roberts, A. (2014). "The origin of white beds below the cretaceous-tertiary boundary revisited," in *AGU Fall Meeting*, (San Francisco, CA).

Abrajevitch, A., and Kodama, K. (2011). Diagenetic sensitivity of paleoenvironmental proxies: A rock magnetic study of Australian continental margin sediments. *Geochem. Geophys. Geosyst.* 12, 1–18. doi: 10.1029/2010GC003481

Alegret, L., Kaminski, M. A., and Molina, E. (2004). Paleoenvironmental recovery after the Cretaceous/Paleogene boundary crisis: evidence from the marine bidart section (SW France). *Palaios* 19, 574–586. doi: 10.1669/0883-1351(2004)019<0574:PRATPB>2.0.CO;2

Apellaniz, E., Baceta, J. I., Bernaola-Bilbao, G., Núñez-Betelu, K., Orúe-Etxebarría, X., Payros, A., et al. (1997). Analysis of uppermost cretaceous–lowermost Tertiary hemipelagic successions in the Basque Country (western Pyrenees): evidence for a sudden extinction of more than half planktonic foraminifer species at the K/T boundary. *Bull. Soc. Géol. France* 168, 783–793.

Bibi, I., Singh, B., and Silvester, E. (2011). Akaganeite (beta-FeOOH) precipitation in inland acid sulfate soils of south-western New South Wales (NSW), Australia. *Geochim. Cosmochim. Acta* 75, 6429–6438. doi: 10.1016/j.gca.2011.08.019

Bland, P. A., Kelley, S. P., Berry, F. J., Cadogan, J. M., and Pillinger, C. T. (1997). Artificial weathering of the ordinary chondrite Allegan: implications for the presence of Cl- as a structural component in akaganeite. *Am. Mineral.* 82, 1187–1197.

Bonté, P., Delacotte, O., Renard, M., Laj, C., Boclet, D., Jehanno, C., et al. (1984). An iridium rich layer at the cretaceous tertiary boundary in the bidart section (southern france). *Geophys. Res. Lett.* 11, 473–476. doi: 10.1029/GL011i005p00473

Chenet, A. L., Fluteau, F., and Courtillot, V. (2005). Modelling massive sulphate aerosol pollution, following the large 1783 Laki basaltic eruption. *Earth Planet Sci. Lett.* 236, 721–731. doi: 10.1016/j.epsl.2005.04.046

Chenet, A. L., Quidelleur, X., Fluteau, F., Courtillot, V., and Bajpai, S. (2007). K-40-Ar-40 dating of the main Deccan large igneous province: further evidence of KTB age and short duration. *Earth Planet Sci. Lett.* 263, 1–15. doi: 10.1016/j.epsl.2007.07.011

Cornell, R. M., and Schwertmann, U. (2003). *The Iron Oxides: Structure, Properties, Reactions, Occurrences, and Uses.* Weinheim: Wiley-VCH. doi: 10.1002/3527602097

Courtillot, V., Besse, J., Vandamme, D., Montigny, R., Jaeger, J. J., and Cappetta, H. (1986). Deccan flood basalts at the cretaceous tertiary boundary. *Earth Planet Sci. Lett.* 80, 361–374. doi: 10.1016/0012-821X(86)90118-4

Ellwood, B. B., MacDonald, W. D., Wheeler, C., and Benoist, S. L. (2003). The K-T boundary in oman: identified using magnetic susceptibility field measurements with geochemical confirmation. *Earth Planet Sci. Lett.* 206, 529–540. doi: 10.1016/S0012-821X(02)01124-X

Emmerich, M., Bhansali, A., Losekann-Behrens, T., Schroder, C., Kappler, A., and Behrens, S. (2012). Abundance, distribution, and activity of fe(II)-oxidizing and

fe(III)-reducing microorganisms in hypersaline sediments of lake kasin, southern russia. *Appl. Environ. Microb.* 78, 4386–4399. doi: 10.1128/AEM.07637-11

Font, E., Fabre, S., Nédélec, A., Adatte, T., Keller, G., Veiga-Pires, C., et al. (2014). "Atmospheric halogen and acid rains during the main phase of Deccan eruptions: magnetic and mineral evidence," in *Volcanism, Impacts, and Mass Extinctions: Causes and Effects: Geological Society of America Special Paper 505,* eds G. Keller and A. C. Kerr, 353–368. doi: 10.1130/2014.2505(18)

Font, E., Nédélec, A., Ellwood, B. B., Mirão, J., and Silva, P. F. (2011). A new sedimentary benchmark for the Deccan Traps volcanism? *Geophys. Res. Lett.* 38:L24309. doi: 10.1029/2011GL049824

Galbrun, B., and Gardin, S. (2004). New chronostratigraphy of the cretaceous-paleogene boundary interval at bidart (France). *Earth Planet Sci. Lett.* 224, 19–32. doi: 10.1016/j.epsl.2004.04.043

Gallala, N., Zaghbib-Turki, D., Arenillas, I., Arz, J. A., and Molina, E. (2009). Catastrophic mass extinction and assemblage evolution in planktic foraminifera across the cretaceous/paleogene (K/Pg) boundary at bidart (SW France). *Mar. Micropaleontol.* 72, 196–209. doi: 10.1016/j.marmicro.2009.05.001

Gertsch, B., Keller, G., Adatte, T., Garg, R., Prasad, V., Berner, Z., et al. (2011). Environmental effects of Deccan volcanism across the cretaceous-tertiary transition in meghalaya, india. *Earth Planet Sci. Lett.* 310, 272–285. doi: 10.1016/j.epsl.2011.08.015

Johnston, J. H. (1977). Jarosite and akaganeite from white island volcano, newzealand - an x-ray and mossbauer study. *Geochim. Cosmochim. Acta* 41, 539–544. doi: 10.1016/0016-7037(77)90291-5

Kaminski, E., Chenet, A. L., Jaupart, C., and Courtillot, V. (2011). Rise of volcanic plumes to the stratosphere aided by penetrative convection above large lava flows. *Earth Planet Sci. Lett.* 301, 171–178. doi: 10.1016/j.epsl.2010.10.037

Keller, G., Adatte, T., Bhowmick, P. K., Upadhyay, H., Dave, A., Reddy, A. N., et al. (2012). Nature and timing of extinctions in cretaceous-tertiary planktic foraminifera preserved in Deccan intertrappean sediments of the krishna-godavari basin, india. *Earth Planet Sci. Lett.* 341, 211–221. doi: 10.1016/j.epsl.2012.06.021

Keller, G., Bhowmick, P. K., Upadhyay, H., Dave, A., Reddy, A. N., Jaiprakash, B. C., et al. (2011). Deccan volcanism linked to the cretaceous-tertiary boundary mass extinction: new evidence from ongc wells in the krishna-godavari basin. *J. Geol. Soc. India* 78, 399–428. doi: 10.1007/s12594-011-0107-3

Kruiver, P. P., Dekkers, M. J., and Heslop, D. (2001). Quantification of magnetic coercivity components by the analysis of acquisition curves of isothermal remanent magnetisation. *Earth Planet Sci. Lett.* 189, 269–276. doi: 10.1016/S0012-821X(01)00367-3

Li, Q. X., Wang, Z. Y., Han, W., and Han, E. H. (2008). Characterization of the rust formed on weathering steel exposed to qinghai salt lake atmosphere. *Corros. Sci.* 50, 365–371. doi: 10.1016/j.corsci.2007.06.020

Lowrie, W., Alvarez, W., and Asaro, F. (1990). The origin of the white beds below the cretaceous tertiary boundary in the gubbio section, italy. *Earth Planet Sci. Lett.* 98, 303–312. doi: 10.1016/0012-821X(90)90032-S

Moune, S., Gauthier, P. J., and Delmelle, P. (2010). Trace elements in the particulate phase of the plume of masaya volcano, nicaragua. *J. Volcanol. Geoth. Res.* 193, 232–244. doi: 10.1016/j.jvolgeores.2010.04.004

Reguer, S., Dillmann, P., and Mirambet, F. (2007). Buried iron archaeological artefacts: corrosion mechanisms related to the presence of Cl-containing phases. *Corros. Sci.* 49, 2726–2744. doi: 10.1016/j.corsci.2006.11.009

Remazeilles, C., and Refait, P. (2007). On the formation of beta-FeOOH (akaganeite) in chloride-containing environments. *Corros. Sci.* 49, 844–857. doi: 10.1016/j.corsci.2006.06.003

Remazeilles, C., and Refait, P. (2008). Formation, fast oxidation and thermodynamic data of Fe(II) hydroxychlorides. *Corros. Sci.* 50, 856–864. doi: 10.1016/j.corsci.2007.08.017

Robertson, D. J., and France, D. E. (1994). Discrimination of remanence-carrying minerals in mixtures, using isothermal remanent magnetization acquisition curves. *Phys. Earth Planet. Int.* 82, 223–234. doi: 10.1016/0031-9201(94)90074-4

Self, S., Widdowson, M., Thordarson, T., and Jay, A. E. (2006). Volatile fluxes during flood basalt eruptions and potential effects on the global environment: a Deccan perspective. *Earth Planet Sci. Lett.* 248, 518–532. doi: 10.1016/j.epsl.2006.05.041

Thibault, N., and Gardin, S. (2007). The late Maastrichtian nannofossil record of climate change in the south atlantic DSDP Hole 525A. *Mar. Micropaleontol.* 65, 163–184. doi: 10.1016/j.marmicro.2007.07.004

Yue, J., Jiang, X. C., and Yu, A. B. (2011). Experimental and theoretical study on the beta-FeOOH nanorods: growth and conversion. *J. Nanopart. Res.* 13, 3961–3974. doi: 10.1007/s11051-011-0320-4

Zhang, Y. X., and Jia, Y. (2014). A facile solution approach for the synthesis of akaganeite (beta-FeOOH) nanorods and their ion-exchange mechanism toward As(V) ions. *Appl. Surf. Sci.* 290, 102–106. doi: 10.1016/j.apsusc.2013.11.007

Conflict of Interest Statement: The authors declare that the research was conducted in the absence of any commercial or financial relationships that could be construed as a potential conflict of interest.

Received: 18 August 2014; paper pending published: 05 September 2014; accepted: 09 September 2014; published online: 25 September 2014.

*Citation: Font E and Abrajevitch A (2014) Paleoenvironmental signature of the Deccan Phase-2 eruptions. Front. Earth Sci. **2**:23. doi: 10.3389/feart.2014.00023*

This article was submitted to Geomagnetism and Paleomagnetism, a section of the journal Frontiers in Earth Science.

frontiers in Earth Science

ORIGINAL RESEARCH
published: 20 April 2015
doi: 10.3389/feart.2015.00011

A detailed paleomagnetic and rock-magnetic investigation of the Matuyama-Brunhes geomagnetic reversal recorded in the tephra-paleosol sequence of Tlaxcala (Central Mexico)

Ana M. Soler-Arechalde[1], Avto Goguitchaichvili[2], Ángel Carrancho[3], Sergey Sedov[4], Cecilia I. Caballero-Miranda[1], Beatriz Ortega[1], Berenice Solis[5], Juan J. Morales Contreras[2], Jaime Urrutia-Fucugauchi[1] and Francisco Bautista[5]*

[1] *Laboratorio de Paleomagnetismo del Instituto de Geofísica, Universidad Nacional Autónoma de México, Mexico City, Mexico,* [2] *Laboratorio Interinstitucional de Magnetismo Natural, Instituto de Geofísica, Unidad Michoacán, Morelia, Mexico,* [3] *Área de Prehistoria, Departamento de Ciencias Históricas y Geografía, Universidad de Burgos, España, Burgos, Spain,* [4] *Departamento de Edafología del Instituto de Geología, Universidad Nacional Autónoma de México, Mexico City, Mexico,* [5] *Centro de Investigaciones en Geografía Ambiental, Universidad Nacional Autónoma de México, Morelia, Mexico*

Geomagnetic reversals are global phenomena that require several stratigraphic correlation and dating methods for their firm identifications. For about 50 years the paleomagnetists attempted to acquire as many detailed records as possible using the magnetic memory of sediments and lava flows. Yet, transitional field behavior remains poorly characterized largely because of sporadic aspect of volcanic eruptions. In some specific cases, paleosols such as those developed from alluvial or aeolian sediments, may also record the variations of the Earth's Magnetic Field across the polarity changes. Here, we report a detailed paleomagnetic and rock-magnetic investigation on some radiometrically dated chromic Luvisols located in Central Mexico carrying detrital or chemical remanent magnetization. The research was developed in order (i) to demonstrate the primary origin of the recorded magnetic remanence and (ii) to show that paleosols are good candidates to provide a high resolution record of the behavior of Earth magnetic field during geomagnetic reversals. The lower part of the paleosol sequence shows a clearly defined reverse polarity magnetization followed by geomagnetically unstable transitional field and ended by normal polarity remanence. Considering the K-Ar datings available at the bottom of the sequence, observed polarity changes most probably correspond to the Matuyama-Brunhes transition. Our AMS and rock magnetic data suggest that the magnetization is acquired during the initial stage of soil formation in context of active volcanic activity since the magnetic fabric is essentially sedimentary and reverse and normal polarity paleodirections are almost antipodal. Moreover, titanomagnetites are identified as main magnetic carriers of rock-magnetic measurements including thermomagnetics and hysteresis cycles. We propose that the transition recorded in this study correspond to the Brunhes-Matuyama boundary and

OPEN ACCESS

Edited by:
Fabio Florindo, Istituto Nazionale di Geofisica e Vulcanologia, UK

Reviewed by:
Eric Font, University of Lisbon, Portugal
Leonardo Sagnotti, Istituto Nazionale di Geofisica e Vulcanologia, Italy

***Correspondence:**
Ana M. Soler-Arechalde, Instituto de Geofisica, Universidad Nacional Autónoma de México, Circuito Institutos s/n, Ciudad Universitaria, Coyoacán, Mexico City, ZC 04510 DF, Mexico
anesoler@geofisica.unam.mx

Specialty section:
This article was submitted to Geomagnetism and Paleomagnetism, a section of the journal Frontiers in Earth Science

Received: *22 December 2014*
Accepted: *04 March 2015*
Published: *20 April 2015*

Citation:
Soler-Arechalde AM, Goguitchaichvili A, Carrancho Á, Sedov S, Caballero-Miranda CI, Ortega B, Solis B, Morales Contreras JJ, Urrutia-Fucugauchi J and Bautista F (2015) A detailed paleomagnetic and rock-magnetic investigation of the Matuyama-Brunhes geomagnetic reversal recorded in the tephra-paleosol sequence of Tlaxcala (Central Mexico). Front. Earth Sci. 3:11. doi: 10.3389/feart.2015.00011

that the chromic Luvisols are potentially good recorders of the paleosecular variation. The identification of the Brunhes-Matuyama boundary within the studied sequence has fundamental significance for improving the chronological scale of Tlaxcala paleosol-sedimentary sequence and its correlation with the global proxies.

Keywords: paleomagnetism, rock-magnetism, geomagnetic reversal, paleosols, central Mexico

Introduction

Several geomagnetic reversals have been documented from geological records. However, we still have limited evidence from paleomagnetic measurements about the patterns of change in the magnetic field during a polarity transition. A still debated question is whether reversals and secular variation are different features, or whether the polarity changes may be considered as an extreme expression of the secular variation. Because a polarity reversal is a global event, the geomagnetic reversals provide an effective mean of stratigraphic correlation and dating. Recognition of polarity changes and excursions as a part of the Earth's paleomagnetic field behavior has developed during the last five decades together with absolute age (astrochronological) calibration of the polarity timescale (Singer et al., 2002).

Brunhes (1907) and later Mercanton (1926) demonstrated first that volcanic rocks may record reverse polarity remanent magnetization. Later, Opdyke et al. (1966) found a reversal record in marine sediments. During a polarity transition, the virtual geomagnetic poles (VGP) follow different paths for different reversals (Prévot and Camps, 1993). Moreover, Earth's magnetic field has often departed for brief periods from its usual axial configuration without establishing a reversed direction. This fundamental property, which has been reported in lava flows and sediments worldwide, is known as geomagnetic excursion. The relatively short periods ($10^3 - 8 \times 10^3$ after Gubbins, 1999) during which the geomagnetic field changes polarity are of considerable interest in our understanding of the physical processes in the Earth's liquid core that generate the geomagnetic field (see also Petronille et al., 2005).

Numerous geomagnetic events have been discovered in the previously believed stable Brunhes and Matuyama chrons (Laj and Channell, 2007) and the Matuyama-Brunhes transition was revisited by several authors because of its particularity to show a kind of precursor prior to the polarity change (Tauxe et al., 1996; Quidelleur et al., 2002; Singer et al., 2005 among others).

The last geomagnetic polarity reversal took place about 790 ka ago (Singer et al., 2002; Coe et al., 2004), marking the beginning of the present period of normal polarity—the Brunhes chron. Channell et al. (2010) recently reported that the mean age for the midpoint of M-B reversal is about 773.1 ka ($SD = 0.4$ ka), ~7 ka younger than the presently accepted astrochronological age for this polarity reversal (780–781 ka). Valet et al. (2012) analyzed seven most detailed geomagnetic transitions worldwide since 180 Ma including two B-M reversals recorded at Hawaii and Tahiti. They propose that reversing field is characterized by a precursor event, a full polarity change and rebound. The polarity "switch" seems to occur during in less than 1000 years which is too brief to be accurately recorded by the sedimentary rocks.

There is now a general agreement that volcanic rocks are the best recorders of geomagnetic transitions and reversals. However, sub-aerial volcanism is mainly characterized by sporadic eruptions with some periods of intense eruptions alternating with quiet intervals. This is well illustrated investigating several parallel sections in Hawaii (Herrero-Bervera and Valet, 1999, 2005). They all recorded the same reversal but do not show the same successions of transitional directions. Incremental $^{40}Ar/^{39}Ar$ heating techniques reports ages for Hawaiian lavas from 783 ± 11 ka (Baksi and Farrar, 1990; Baksi et al., 1992) to 780. A mean unweighted value of 787 ± 1.9 ka was reported by Singer and Pringle (1996) from lavas of Maui, Chile, La Palma and Tahiti. A younger value of 783 ± 11 ka was obtained by Spell and McDougall (1992) from Valles lava by $^{40}Ar/^{39}Ar$. Thus, due their sporadic character volcanic rocks are unable to deliver the complete picture of geomagnetic transition. Sediments can provide continuous records of magnetic field variation, while data from lavas, due to the sporadic nature of volcanic activity, yield rather discontinuous records of geomagnetic field variation.

Some rapidly deposited sedimentary rocks offered relatively continuous records of reversal transitions available. Certain lake sediments have also permitted to reveal important information to study the secular variation of the Earth's magnetic field over geological time. It is also true that the natural remanent magnetization in sediments is frequently post-DRM (depositional remanent magnetization) and secondary overprints are common (Barton et al., 1980). As underlined by Channell and Lehman (1997) the remanence is locked in over a depth that varies significantly from one to another sediment, depending on how the sediments are compacted, how benthic organisms mix them, differences in remanence acquisition or real differences in the timing record (Channell and Kleiven, 2000).

Soil magnetism emerged during the last two decades, it initially was used to detect the presence of pedogenic ferrimagnetic minerals (Thompson and Oldfield, 1986), particularly in loess-palaeosol sequences where measurements are used as proxy indicators of climatic change. The magnetic properties of soils are currently used for identifying soil-forming processes and to identify their possible links with paleoclimate (Maher and Thompson, 1995; Han et al., 1996). Recently, rock-magnetism was also applied to Quaternary and older paleosols, in order to identify their soil-forming processes and environments. The magnetic properties of paleosols of Permian age appear to record glacial-interglacial fluctuations in low-latitude Pangea (e.g., Tramp et al., 2004).

This study is aimed to investigate whether a multilayer quaternary paleosol formed essentially in volcanic context, and thus providing high magnetic signal, may be used in terms of

recording the paleosecular variation and polarity transition. "La Barranca de Tlalpan" sequence was first investigated for paleoenvironmental purpose (Ortega-Guerrero et al., 2004; Sedov et al., 2009; Solis-Castillo et al., 2012), but some few oriented hand samples at the lower part yielded stable, reverse polarity magnetization. This fact was the main motivation to revisit and sample the whole sequence in greater details. We determine the characteristic magnetizations by AF demagnetization and employ AMS and rock magnetic studies to determine if the origin of these remanences is primary.

Geological Settings and Sampling

The Trans-Mexican Volcanic Belt (TMVB) is a major continental volcanic arc which spans about 1000 km across central Mexico from the Pacific to the Atlantic coast (**Figure 1**). The TMVB began to form in middle Miocene as a result of subduction of the Cocos and Rivera plates and covers the Eocene to early Miocene Sierra Madre Occidental volcanic province (Ferrari et al., 1999). The initial stage of the TMVB is marked by a widespread basaltic volcanism, occurring from the Pacific coast to Mexico City, to the north of the modern volcanic arc. This volcanism is characterized by plateau-like structures which have an aggregate volume estimated between 3200 and 6800 km^3 (Ferrari et al., 2000). Geologic and stratigraphic studies have shown that these basaltic lavas were emplaced in a well defined period between 11 and 8 Ma (Ferrari et al., 1994, 2000; Moore et al., 1994; Righter et al., 1995). However, the volcanic activities continued during the Plio-Quaternary.

The "Barranca de Tlalpan" is a paleosol sequence near the city of Tlaxcala in the central part of the Trans Mexican Volcanic Belt (**Figure 1**). The studied sequence consists of seven pedostratigraphic units separated by ash layers. It is subdivided in four main layers based on morphologic characteristics: a modern soil, the Gray, the Brown and the Red Units, from top to bottom with a total depth of 1528 cm (**Figure 2**) (for more details see Rivas et al., 2006; Sedov et al., 2009; Solis-Castillo et al., 2012).

The 30 cm thick modern soil horizon shows evidence of numerous prehispanic artifacts like obsidian and ceramic fragments including colonial ones. A well marked erosion horizon defines a clear boundary with the underlying unit.

The Gray unit from 30 to 303 cm consists of two gray paleosols (P1 and P2), separated by a *tepetate* (Central American term for a kind of brittle volcanic rock) layer. The P1 (of 178 cm thickness) shows Ah, Bt and Cx horizons, the P2 (60 cm thickness) is partly truncated and only exhibits the Bt horizon (Sedov et al., 2009).

The Brown unit from 303 to 1168 cm has three brown paleosols (P3, P4, and P5), Fragic Luvisol, with well developed Bt horizons, underlying by *tepetates* consolidated subsoil tephtous horizons, (Sedov et al., 2009) now identified as Fragipan (IUSS Working Group WRB, 2006).

The Red unit from 1168 to 1528 cm includes two paleosols (P6 and P7) with reddish-brown Bt horizons. These paleosols are classified as Chromic Luvisols (Sedov et al., 2009). The P1

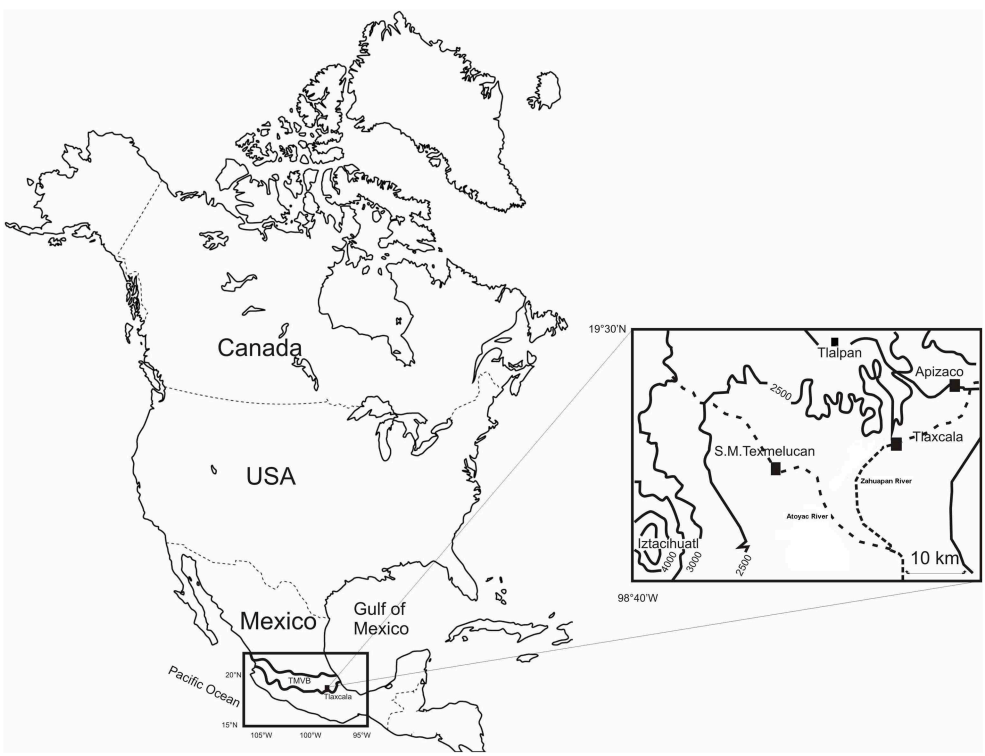

FIGURE 1 | Location of Barranca de Tlalpan in the central sector of the Trans Mexican Volcanic Belt.

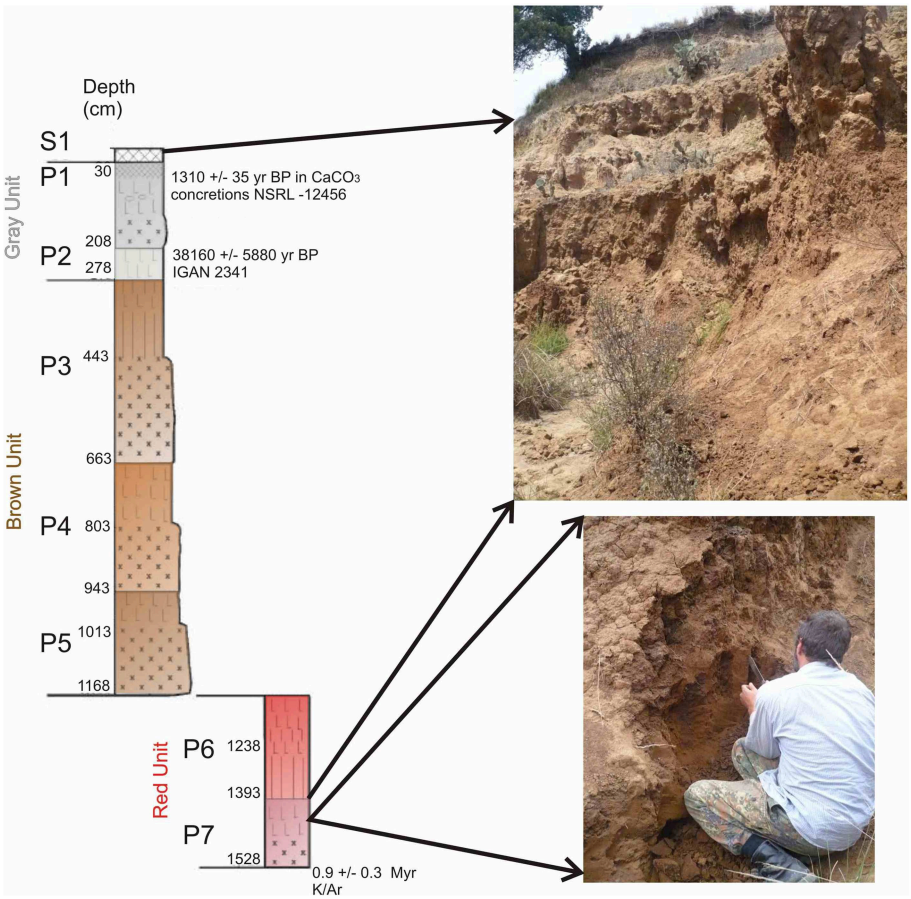

FIGURE 2 | Paleosol sequence with the different units: Gray (30–278 cm), Brown (278–1168 cm) and Red (1168–1528 cm). Please see text for more details.

paleosol was dated by ^{14}C on $CaCO_3$ concretions with 1310 ± 35 year BP and calibrated age of 656–772 AD, a very young age produced by pedogenic carbonates (Sedov et al., 2009). The ^{14}C dates of P2 paleosol on humus gave 38,160 ± 5880 and >33,595 year BP (Sedov et al., 2009). Finally, a 0.9 Ma date by K/Ar was obtained from the lowest layer, underlying P7 (Sedov et al., 2009). This date corresponds to very upper part of Matuyama reversed polarity chron.

Our sampling campaign was motivated to obtain oriented samples from P7 trough P5 profiles hoping to catch the last Matuyama-Brunhes reversal. The sampled section consists of two segments, one that corresponds to 1153–1439 cm (P5, P6, and part of P7, **Figure 2** upper right side) and one from 1417 to 1528 cm (P7, **Figure 2** lower right side).

The pedostratigraphic units surfaces were cleaned and later cutted with non-magnetic tools following pedologycal techniques to get rectangular blocks. These blocks were oriented with a Brunton compass (**Figure 3**). At laboratory the blocks were consolidated with a solution of vinil poliacetic resine and water. The consolidated blocks were cut with a non-magnetic tool to get standard cubes of 8 cm^3 and introduced in plastic cubic sample boxes (**Figure 3**). A total of 125 samples were prepared and kept about 1 month in free magnetic field in order to diminish the effect of viscous remanent magnetization.

Methods

Representative samples from the studied palaeosols were analyzed in order to identify the main magnetic carriers, their domain state and thermomagnetic stability. With the aid of a Variable field Translation Balance (MM_MFTV) we measured progressive isothermal remanent (IRM) acquisition curves, hysteresis loops (±1 T), backfield coercivity curves and thermomagnetic curves up to 700°C in air. All these analyses were performed on bulk sample (∼400 mg) extracted from 16 representative specimens at the laboratory of Palaeomagnetism of Burgos University (Spain). Curie temperatures were determined using the two-tangent method of Grommé et al. (1969).

The remanent magnetization of the samples were measured in a JR6 in a field free environment and demagnetized by alternating fields using 7–12 steps up to a maximum fields of 100 mT with Molspin demagnetizer. A detailed AMS analysis was performed on 117 samples from P5, P6 and P7 paleosols employing a KLY2

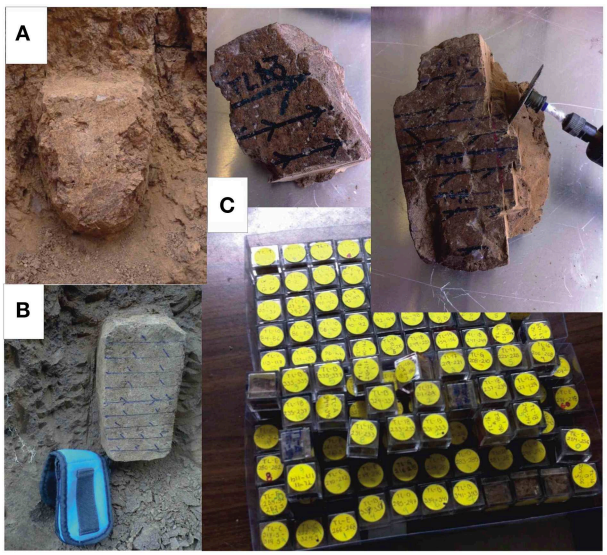

FIGURE 3 | (A) In situ block **(B)** In situ block oriented **(C)** Sample preparation and cutting using a non-magnetic moto tool.

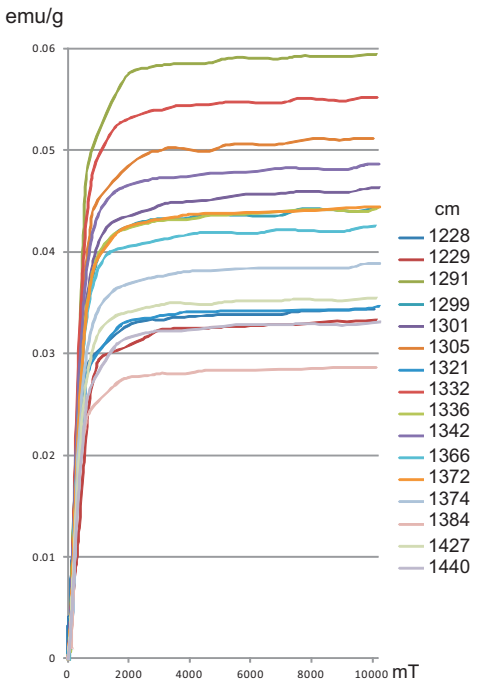

FIGURE 4 | Representative Isothermal Remanent Magnetization (IRM) acquisition curves.

instrument and *anisoft* software for obtaining principal AMS directions and AMS parameters of shape T, anisotropy degree Pj and main susceptibility Km in SI units.

Results

IRM acquisition curves are almost saturated between 150 and 300 mT, indicating that the remanent magnetization is dominated by low coercivity minerals (i.e.,: magnetite/maghaemite). A small fraction of high coercivity minerals seems to be also present because the curves are not fully saturated at 1 T. However, its contribution to the total remanent magnetization do not exceeds 5%. Thus, it cannot be considered really significant (**Figure 4**).

Some representative thermomagnetic curves (saturation magnetization vs. temperature) are shown in **Figure 5**. In the heating cycles of the studied samples several slope changes at ∼150–200°C, ∼510°C and ∼580°C were observed. The ferromagnetic phase with a Curie point of ∼150—200°C is characteristic of Ti-rich Titanomagnetite and is particularly evident in samples TLG 212–214 5b (1396 cm depth) and TL-F 256.5–258.5 (1438 cm depth, **Figures 5A,B**). The second slope change observed around 510°C in the heating curves most probably corresponds to a slightly substituted magnetite and the phase with a Tc around 580°C is magnetite. Occasionally, this latter phase displays higher Curie temperatures up to 600–610°C (e.g.,: **Figure 5C**) which is interpreted as magnetite partially maghaemitized due to oxidation (TL 13 148.5–150.5, 1334 cm depth). Finally, three samples exhibit also a subtle inflection on the heating curve around 320°C, which is absent in their respective cooling cycles (e.g.,: **Figure 5D**, TL 18 243–245, 1425 cm depth). We do not have evidences of ferromagnetic sulphurs (e.g.,: pyrrothite or greigite) in these sediments, so this inflection might be attributable to maghaemite which partially inverts to (titano) haematite. The magnetite *Tc* appears in all cooling curves and in most cases also reproduces the inflection around 150–200°C. Within their variability, the cooling cycles exhibit a relatively high thermal stability and all samples except one (**Figure 5D**) display cooling cycles of lower intensity than heating ones. On the basis of these results, remanent magnetization prove to reside in Titanomagnetites (with variable Ti-content), as one may expect considering the volcanoclastic origin of the deposit.

The **Figure 6A** show hysteresis cycles of some selected samples belonging to P5, P6, and P7. Considering that these samples are dominated by titano-magnetites, the hysteresis parameters (saturation magnetisation, Ms; remanence saturation magnetisation, Mrs; and coercive field, Hc) together with remanence coercivity (Bcr -determined separately from the back field curves-) were plotted in the so-called Day plot (Day et al., 1977) to estimate the domain state of the sample set (**Figure 6B**). Bc and Bcr ranges between 5.02–8.83 mT and 22.89–27.65 mT, respectively, in general accordance with IRM acquisition curves. The hysteresis ratios range from $0.09 < Mrs/Ms < 0.14$ and $2.90 < Bcr/Bc < 4.68$, indicative of (Ti) magnetite in pseudo- single domain state (Day et al., 1977; Dunlop, 2002). It is striking how the hysteresis parameters of these samples are rather uniform, suggesting small granulometric variations among paleosols. Interestingly, the presence of ultrafine (∼10–30 nm) magnetite particles is significant when compared with the mixing theoretical lines of Dunlop (2002) and this agrees well with the results already observed by Ortega-Guerrero et al. (2004) specifically in these paleosols (P5, P6, and P7).

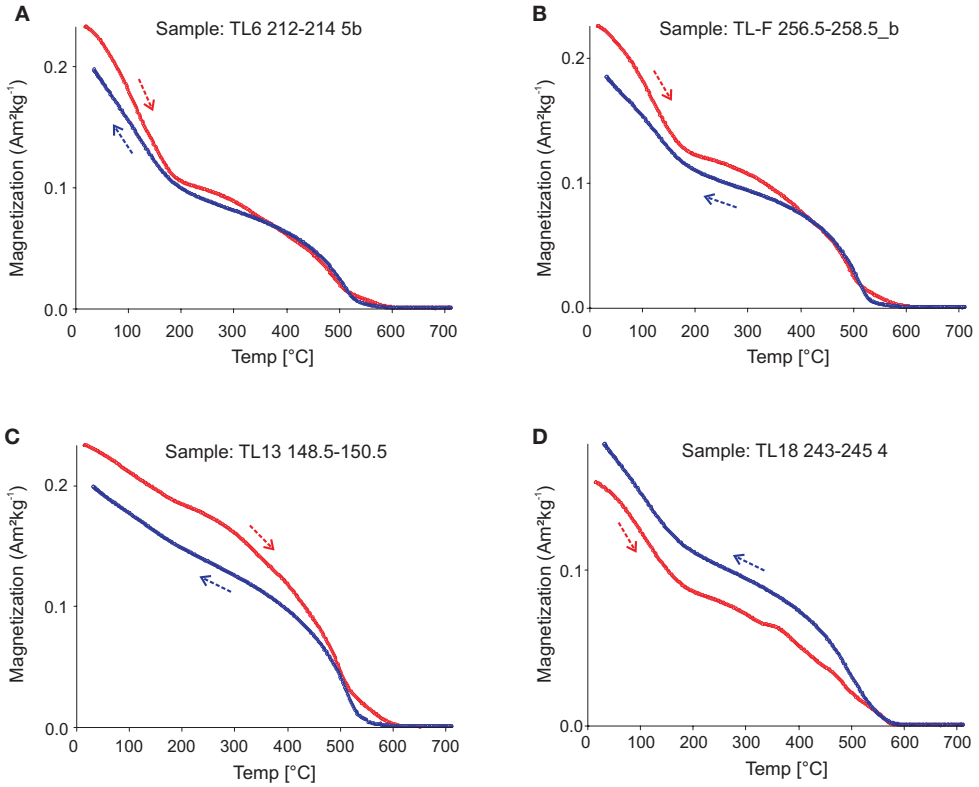

FIGURE 5 | (A–D) Representative thermomagnetic curves from the Tlalpan Paleosols. The sample code and magnetization values are indicated for each specimen. Heating (red) and cooling (blue) cycles are shown with their respective arrows.

The characteristic magnetization directions were obtained by principal component analysis on stepwise demagnetization data with remasoft 3.0 software (Chadima and Hrouda, 2006). Some representative orthogonal vector plots (so-called Zijdervel diagrams) are shown on **Figure 7**. A characteristic magnetization was determined by the least squares method (Kirschvink, 1980), with 4–9 points used for this determination. A secondary component, probably of viscous origin was present in an important number of samples, but was removed after applying an alternative peak field of 10 mT (**Figure 7**). Moreover, some few samples show slight deviation from the origin mainly at high alternating peak fields. However in any case, the maximum angular deviation to calculate the characteristic directions was less than 3°C. The median destructive fields (MDF) range mostly from 20 to 40 mT, suggesting pseudo-single domain grains as remanent magnetization carriers (Dunlop and Özdemir, 1996).

The susceptibility of magnetic anisotropy (AMS) analysis is not common practice for paleosols. However, the objective of employing it was to estimate whether magnetic fabric is sedimentary. A detailed AMS analysis was performed with 117 samples from P5, P6, and P7 paleosols employing a KLY2 instrument and anisoft software. Since the Brunhes-Matuyama reversal was observed along the P6 paleosol profile, special attention was focused along this profile in order to detect possible AMS changes that could give some insight about soil formation processes that could support or reject the reliability of observed reversal (**Figure 8**).

AMS results suggest sedimentary magnetic fabric all along P5, P7, and most of P6, in which the k3 mean directions are around vertical positions with narrow error ellipsoids, meanwhile the k1 and k2 directions are around sub-horizontal and scattered positions. Only along a short interval in P6 profile (1235–1215), the AMS shows a most disorganized fabric on which it seems to have a tendency of subvertical k1 and subhorizontal k3 directions.

AMS results above and below the turn point of the Brunhes Matuyama reversal in P6, as well as AMS results from most of the studied profiles, suggest that paleosols are from an alluvial origin, as would be expected in Luvisols (P6 and P7); and that pedogenic process did not change the original magnetic fabric in most part of paleosol profiles. Only along the 1235–1215 interval, which correspond to a middle part of the P6 paleosol, apparently to a Bt paleo-horizon, the illuvial processes seem to have been strong enough to alter the original sedimentary fabric and produce the magnetic fabric observed.

The **Figure 9** shows the evolution of magnetic declination (blue diamonds), inclination (red diamonds) and intensity (green diamonds) vs. depth. Lowest layer studied (between 1505 and 1434 cm) show mean inclination of −44.4° (orange square, **Figure 9**) and declination fluctuating around 175° yielding the

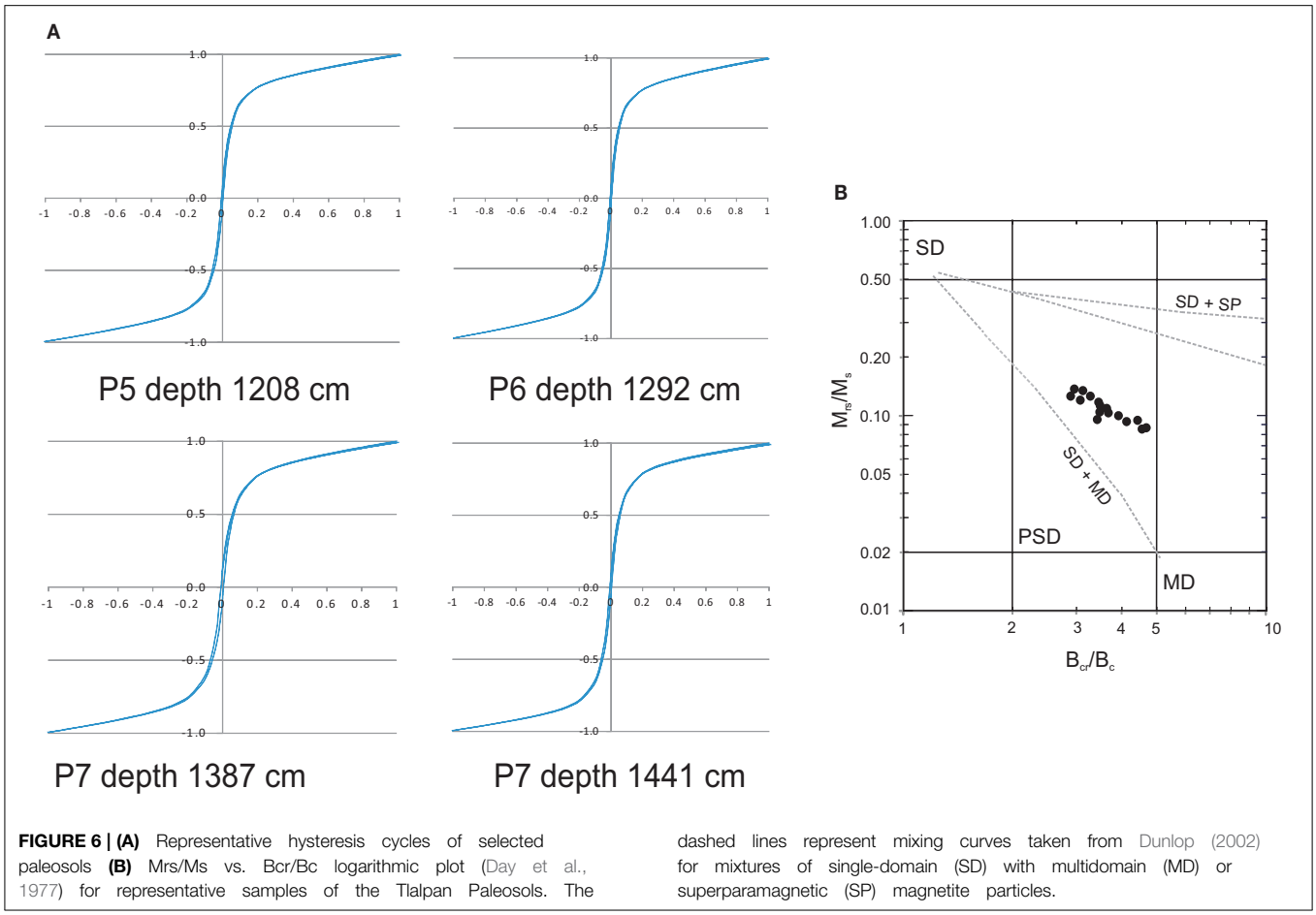

FIGURE 6 | (A) Representative hysteresis cycles of selected paleosols **(B)** Mrs/Ms vs. Bcr/Bc logarithmic plot (Day et al., 1977) for representative samples of the Tlalpan Paleosols. The dashed lines represent mixing curves taken from Dunlop (2002) for mixtures of single-domain (SD) with multidomain (MD) or superparamagnetic (SP) magnetite particles.

evidence of clear reversed polarity paleodirections as may be expected for the Matuyama chron. Then, inclinations become shallower with the mean value of −34°. Between 1319 and 1436 cm (red square, **Figure 9**) the inclination swings from positive to negative defining a transitional zone of clear intermediate polarity. This phenomenon seems to be a common event prior to the Matuyama-Brunhes reversal. The upper layers (green zone on **Figure 9** and beyond) yielded a mean paleoinclination of 44.3° and paleodeclination of 344°. A single sample belonging to P5 shows the negative inclination which we attribute to some measurement artifact rather than true feature of the Earth's Magnetic Field just after the reversal.

The intensity (green diamonds, **Figure 9**) shows a clear decrease in the section of the green zone followed by large fluctuations in the red zone and finally recovering the same pre-transitional mean value.

The mean magnetic direction of the normal component ($N = 53$) has an Inclination: 54.7°, Declination: 324.8°, the reverse component ($N = 73$) has an inclination: 21.4°, Declination: 336.0°. Using 60° of paleolatitude as cut of angle to separate the transitional field and stable geomagnetic (normal or reversed) directions because it is widely used in literature, we have 29 normal and 41 reverse polarity (full and open circles respectively, **Figure 10**) with critical angle $\gamma = 5.76°$ which corresponds to positive type B reversal test following McFadden and McElhinny's (1990) classification. Interestingly, the cut of angle given by Vandamme's iterative method Vandamme (1994) is 61°, very similar to our preferred cut of angle pointing to $\gamma = 5.76°$ It should be also noted that the cut of angle of Vandamme guaranty the Fisherian distribution of data. We also estimated the "antipodality" through reversal test using 45° obtaining the critical angle above 10° (11.65°) pointing still positive, but Type B reversal test. The **Figure 10** showing exclusively data selected using a 60° paleolatitude cut of angle, also shown mean directions and α_{95} values for normal (Dec:350.9°, Inc:43.0°, α_{95}:3.8°) and reverse components (Dec:347.2°, Inc:26.7°, α_{95}:4.1°), the fact that these α_{95}'s do not overlap may be interpreted as the asymmetry between the pre and post-transitional record and the difficulties to accurate remanence acquisition, as already shown in previous works analyzing sediments and soils (Kong et al., 2014 among others).

Discussion and Concluding Remarks

The type of remanent magnetization carried by these paleosols may be a matter of debate. It is well known that the NRM in sedimentary rocks is often a DRM or post-DRM and secondary

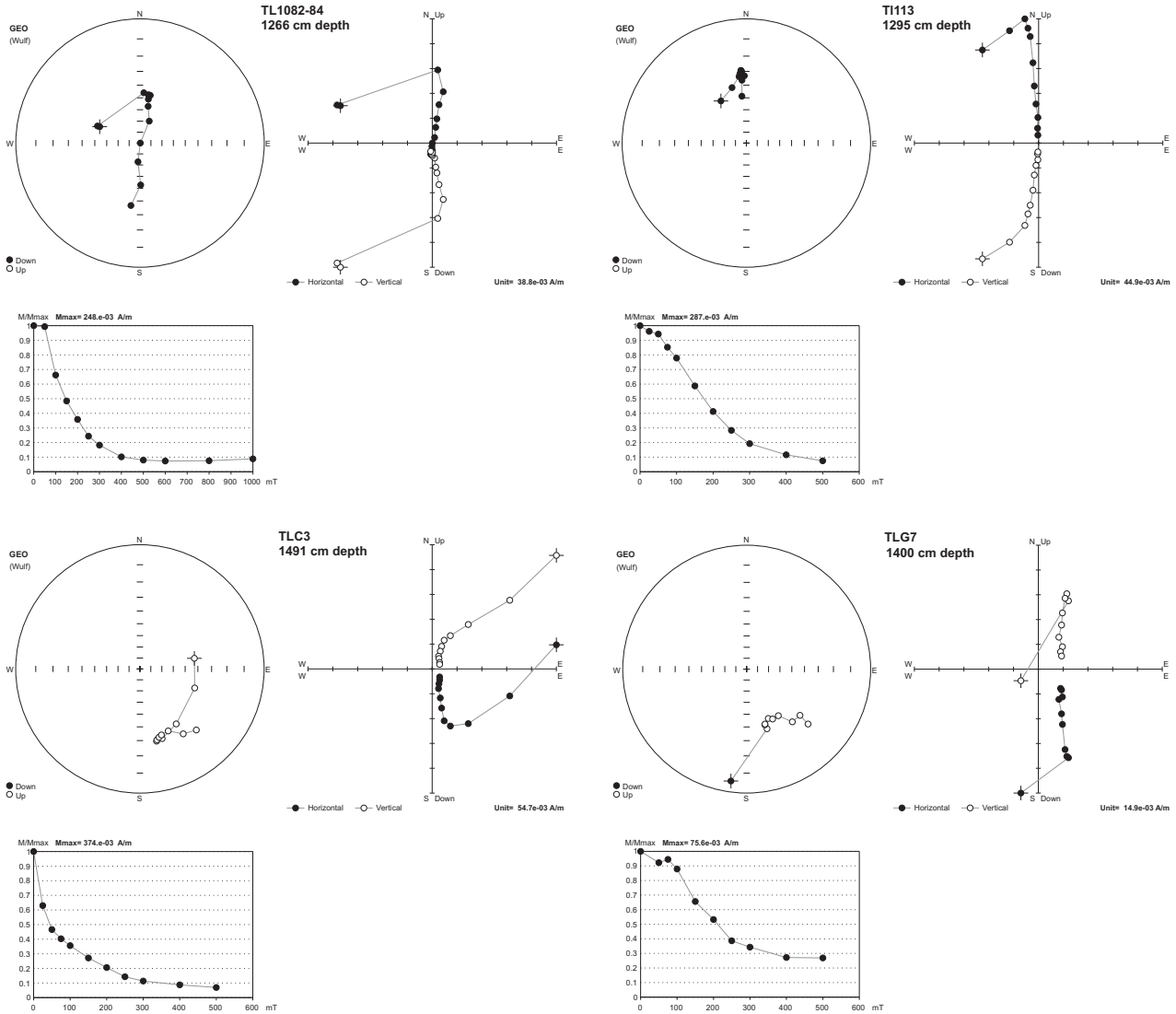

FIGURE 7 | Equal area projection, Orthogonal diagram and Demagnetization spectra for some representative samples: TL10-82-84, TL11-3, TIC3, andTLG7.

overprints are not uncommon (e.g., Dunlop and Özdemir, 1996). Nevertheless, a few marine and terrestrial sedimentary cores (particularly for rapidly deposited sediments) have produced some of the best continuous records of reversal transitions available. Liu and Zhang (2013) showed that the chemical remanent magnetization (CRM) is the main mode of remanence due to pedogenesis. Thus, an extreme caution is required to interpret the paleomagnetic signal in paleosol as true geomagnetic characteristics. This is probably the main reason to explain why loess paleosol sequence yield distinct magnetic record during the M–B transition than records from marine sediments (Kong et al., 2014). In case of Tlalpan paleosols, our preferred interpretation is detrital or post-detrital remanence since the magnetic fabric is essentially sedimentary and reverse and normal polarity paleodirections are almost antipodal. As underlined by Suganuma et al. (2011), the lock-in of post-detrital remanent magnetization may be delayed but with relatively little distortion of the geomagnetic signal. We obviously admit the possibility of chemical remanence but their direction should be recorded parallel to the original DRM.

The identification of the BM boundary within the Red Unit has fundamental significance for improving the chronological scale of Tlaxcala paleosol-sedimentary sequence and its correlation with the global proxies. Before of this finding, the only instrumental time marker available for the lower part of the exposure was the K-Ar date obtained from the basal *tepetate* of the Red Unit. Establishing precise and confinable position of BM boundary provides an independent chronological marker, consistent with previous datings. Furthermore this finding facilitates correlation of the Tlaxcalan sequence with the Marine Oxygen Isotope curve and loess-paleosol sequences where BM boundary is well established (Hambach, 2012). The BM magnetic reversal

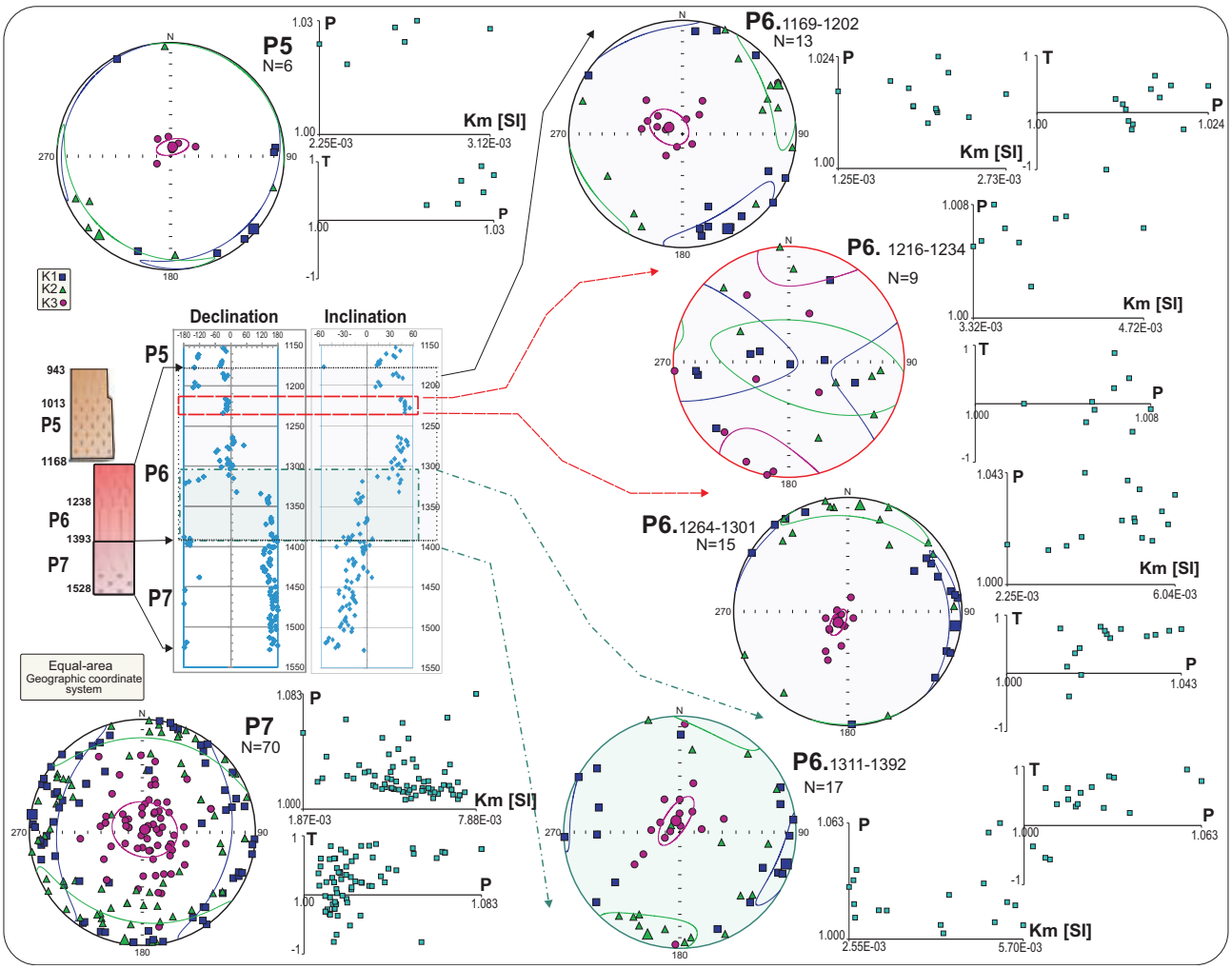

FIGURE 8 | AMS directional results in equal-area equatorial diagrams and corresponding graphs of AMS parameters, referred to characteristic magnetization results of soil profile. P5 and P7 are shown in one set of graphs each. P6 results are shown in 4 sections, depth of each is labeled in centimeters next to the P6 label; N is the number of samples. The lower P6 (1311–1392) section corresponds to the section of polarity switching which shows a typical primary fabric. P6 transect in red shows a disordered AMS results corresponding apparently to illuvial process in a B horizon.

is now accepted as the limit between low and middle Pleistocene. Its presence in Tlaxcala sequence allows considering it as the unique record of the Mid-Pleistocene Climate Transition period (MPT) (Mudelsee and Stattegger, 1997), known for the territory of Mexico.

The occurrence of intermediate directions just before transition is also evidenced by Quidelleur et al. (2002) (see also Quidelleur and Valet, 1996) who reported first volcanic evidence of a geomagnetic excursion occurring some 40 ka prior to the Matuyama-Brunhes transition. An age of 821 ± 13 ka was obtained using the Cassignol K-Ar technique for a transitionally magnetized flow. In other hand, Singer et al. (2002) obtained the mean age of 822.2 ± 8.7 ka on three intermediate polarity lava flows (again from Canaries) using ^{40}Ar-^{39}Ar systematics. Their absolute paleointensity gave relatively low values as commonly accepted for transitions and large departures from the geomagnetic axial dipole (Goguitchaichvili et al., 1999). Petronille et al. (2005) reported same evidence studying Ceboruco lava flows at the Western Trans-Mexican Volcanic Belt. More evidences for a geomagnetic event just prior to M-B reversal comes from the sedimentary records (Kent and Schneider, 1995; Hartl and Tauxe, 1996; Carcaillet et al., 2004). These authors detected shallow inclinations and relatively low paleointensity prior to M-B transition.

Sagnotti et al. (2014) demonstrated that unusually rapid directional change may be occurred in some lake sediments at an extremely fast rate, estimated to be less than 2° per year, with no intermediate paleodirections documented during the polarity change. This is supported by the fact that a mean sediment accumulation rate is of about 0.2 mm year^{-1} during the transition. We should however note that in our particular case it is extremely

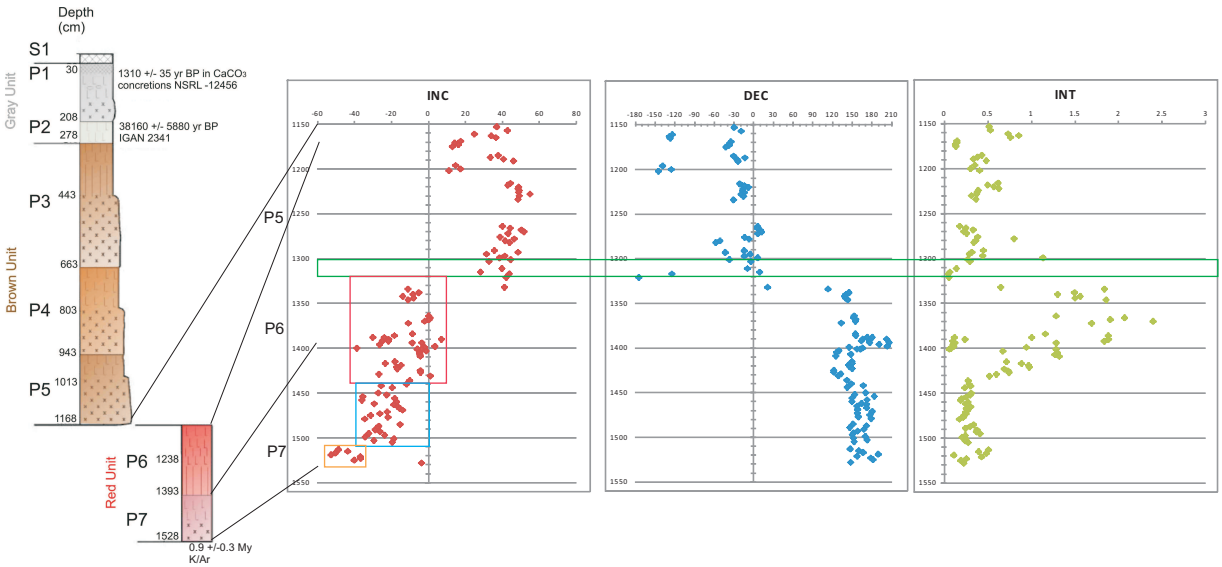

FIGURE 9 | Paleosols sequence with depths in cm. Inclination, Declination of characteristic magnetization and NRM Intensity. Four sections have been recognized: the green rectangle (1300–1319 cm) when the inversion starts, the red rectangle (1318–1438 cm) where the inclination swings from positive to negative and vice versa, the blue rectangle (1438–1505 cm) with a mean negative inclination of 34.4° and finally the orange rectangle where the inversion ends with a mean inclination of 44.4°. The full data appears at the **Supplementary Table 1**.

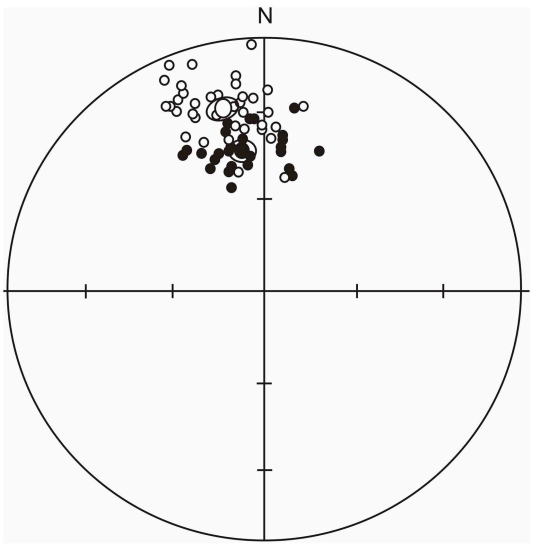

FIGURE 10 | Mean magnetic directions of normal and reverse components with a_{95} of a data selected using a 60° paleolatitude cut of angle. The mean Normal direction of 29 samples has 43.0° of Inclination, 350.9° of Declination and an $\alpha_{95} = 3.8°$. The mean Reverse direction of 41 samples has 26.8° of Inclination, 347.2° of Declination and an $\alpha_{95} = 4.1°$. Normal (full circles) and Reverse (empty circles) magnetic directions show a positive reversal test type B.

difficult to estimate the deposition rate in soils because of obvious difference with the lacustrine sediments. An abrupt directional change occurs at about 1330 cm depth (characteristic mean inclination jumps from ca. −20° to ca. 40° while declination from ca. 120° to ca. 0°).

In summary, we propose that Tlalpan paleosol records Matuyama-Brunhes reversal at the lower part of sequence. This opens new opportunities to study the fine characteristics of the Earth's Magnetic Field on chromic Luvisols worldwide.

Acknowledgments

AG acknowledges the financial support provided by UNAM - PAPIIT n° IN105214 and CONACYT n° 129653 and 169915. We also thanks the financial support of the project CGL2012-32149, MINECO.

Supplementary Material

The Supplementary Material for this article can be found online at: http://www.frontiersin.org/journal/10.3389/feart.2015.00011/abstract

Supplementary Table 1 | Characteristic magnetisation declination (CHRMdec), inclination (CHRMinc) and Maximum Angular Deviation (MAD), demagnetization steps (demag steps), number of steps (# steps) and NRM intensity of Paleosol Tlalpan obtained per sample.

References

Baksi, A. K., and Farrar, E. (1990). Evidence for errors in the geomagnetic polarity time-scale at 17–15 Ma: $^{40}Ar/^{39}Ar$ dating of basalts from the Pacific Northwest, USA. *Geophys. Res. Lett.* 17, 1117–1120. doi: 10.1029/GL017i008p01117

Baksi, A. K., Hsu, V., McWilliamsm, M. O., and Farrar, E. (1992). $^{40}Ar/^{39}Ar$ dating of the Brunhes-Matuyama geomagnetic reversal. *Science* 256, 356–357.

Barton, C., McElhinny, M., and Edwards, D. (1980). Laboratory studies of depositional DRM. *Geophys. J. R. Astron. Soc.* 61, 355–377.

Brunhes, D. (1907). Recherches sur les directions d'aimantation des roches volcaniques, *J. Phys.* 5, 705–724.

Carcaillet, J. T., Bourles, D., and Thouveny, N. (2004). Geomagnetic dipole moment and ^{10}Be production rate intercalibration from authigenic $^{10}Be/^{9}Be$ for the last 1.3 Ma. *Geochem. Geophys. Geosys.* 5, 1–13. doi: 10.1029/2003GC000641

Chadima, M., and Hrouda, F. (2006). Remasoft 3.0 a user-friendly paleomagnetic data browser and analyzer. *Trav. Géophys.* XXVII, 20–21.

Channell, J. E. T., Hodell, D. A., Singer, B. S., and Xuan, C. (2010). Reconciling astrochronological and 40Ar/39Ar ages for the Matuyama-Brunhes boundary and late Matuyama Chron. *Geochem. Geophys. Geosys.* 11, Q0AA12. doi: 10.1029/2010GCG003203.

Channell, J. E. T., and Kleiven, H. F. (2000). Geomagnetic Paleointensities and astrochronological ages for the Matuyama-Brunhes boundary and the boundaries of the Jaramillo Subchron: palaeomagnetic and oxygen isotope records from ODP Site 983, *Phylos. Trans. R. Soc. Lond. Ser. A* 358, 1027–1047. doi: 10.1098/rsta.2000.0572

Channell, J. E. T., and Lehman, B. (1997). The last two geomagnetic polarity reversals recorded in high-deposition-rate sediment drifts. *Nature* 389, 712–715.

Coe, R. S., Singer, B. S., Pringle, M., and Zhao, X. (2004). Matuyama-Brunhes reversal and Kamikatsura event on Maui: paleomagnetic directions, $^{40}Ar/^{39}Ar$ ages and implications. *Earth Planet. Sci. Lett.* 222, 667–684. doi: 10.1016/j.epsl.2004.03.003

Day, R., Fuller, M. D., and Schmidt, V. A. (1977). Hysteresis properties of titanomagnetites grain size and composition dependence. *Phys. Earth Planet. Inter.* 13, 260–266.

Dunlop, D. J. (2002). Theory and application of the Day plot (Mrs/Ms versus Hcr/Hc) 2. Application to data for rocks, sediments, and soils. *J. Geophys. Res.* 107, 1–15. doi: 10.1029/2001JB000487

Dunlop, D. J., and Özdemir, O. (1996). *Rock Magnetism: Fundamentals and Frontiers*. Cambridge; New York, NY: Cambridge University Press.

Ferrari, L., Conticelli, S., Vaggelli, C., Petrone, C., and Manetti, P. (2000). Late miocene mafic volcanism and intra-arc tectonics during the early development of the Trans-Mexican Volcanic Belt. *Tectonophysics* 318, 161–185. doi: 10.1016/S0040-1951(99)00310-8

Ferrari, L., Garduño, V. H., Innocenti, F., Manetti, P., Pasquarè, G., and Vaggelli, G. (1994). A widespread mafic volcanic unit at the base of the Mexican Volcanic Belt between Guadalajara and Queretaro. *Geofísica Int.* 33, 107–124.

Ferrari, L., Lopez-Martinez, M., Aguirre-Diaz, G., and Carrasco-Nuñez, G. (1999). Space-time patterns of Cenozoic arc volcanism in central Mexico: from the Sierra Madre Occidental to the Mexican Volcanic Belt. *Geology* 27, 303–306.

Goguitchaichvili, A., Prévot, M., and Camps, P. (1999). No evidence for strong fields during the R3-N3 Icelandic geomagnetic reversals. *Earth Planet. Sci. Lett.* 167, 15–34.

Gromm,é, C. S., Wright, T. L., and Peck, D. L. (1969). Magnetic properties and oxidation of iron-titanium oxide minerals in Alae and Makaopuhi lava lakes, Hawaii. *J. Geophys. Res.* 74, 5277–5294.

Gubbins, D. (1999). The distinction between geomagnetic excursions and reversals, *Geophys. J. Int.* 137, F1–F3.

Hambach, U. (2012). The Matuyama-Brunhes Boundary in the Stari Slankamen loess section (Vojvodina, Serbia): its detailed record and its stratigraphic position. *Q. Int.* 279–280, 186. doi: 10.1016/j.quaint.2012.08.302

Han, J., Lu, H., Wu,. N., and Guo, Z. (1996). Magnetic susceptibility of modern soils in China and climate conditions. *Stud. Geophys. Geodaetica* 40, 262–275.

Hartl, P., and Tauxe, L. (1996). A precursor to the Matuyama/Brunhes transition–field instability as recorded in pelagic sediments. *Earth Planet. Sci. Lett.* 138, 121–135.

Herrero-Berrvera, E., and Valet, J. P. (2005). Absolute paleointensity from the Waianae volcanics (Oahu, Hawaii) between the Gilbert-Gauss and the upper Mammoth reversals. *Earth Planet. Sci. Lett.* 234, 279–296. doi: 10.1016/j.epsl.2005.02.032

Herrero-Bervera, E., and Valet, J. P. (1999). Paleosecular variation during sequential geomagnetic reversals from Hawaii. *Earth Planet. Sci. Lett.* 171, 139–148.

IUSS Working Group WRB. (2006). *World reference base for soil resources 2006: Rome, Food and Agriculture Organization of the United Nations (FAO), World Soil Resources Reports No.103, 2nd Edn.* (Rome), 128.

Kent, D. V., and Schneider, D. A. (1995). Correlation of paleointensity variation records in the Brunhes/Matuyama polarity transition interval, *Earth Planet. Sci. Lett.* 129, 135–142.

Kirschvink, J. L. (1980). The least-squares line and plane and the analysis of palaeomagnetic data. *Geophys. J. Int.* 62, 699–718.

Kong, X., Zhou, W., Beck, J. W., Xian, F., and Wu, Z. (2014). Asynchronous records of Brunhes/Matuyama reversal in marine sediments and Chinese loess: review and discussion. *Q. Int.* 319, 137–142. doi: 10.1016/j.quaint.2013.08.001

Laj, C., and Channell, J. E. T. (2007). "Geomagnetic excursions. C," in *Treatise in Geophysics: Vol. 5 Geomagnetism,* ed M. Kono (Amsterdam: Elservier), 373–416.

Liu, W., and Zhang, L. (2013). Chemical magnetization in Chinese loess. *Phys. Earth Planet. Inter.* 218, 14–18. doi: 10.1016/j.pepi.2013.02.005

Maher, B. A., and Thompson, R. (1995). *Quaternary Climates, Environments and Magnetism.* Cambridge: Cambridge University Press.

McFadden, P. L., and McElhinny, M. W. (1990). Classification of reversal test in palaeomagnetism. *Geophys. J. Int.* 103, 725–729.

Mercanton, P. L. (1926). Inversion de l'inclinaison magnétique terrestres aux ages géologiques. *Terr. Magn. Atmosph. Elec.* 31, 187–190.

Moore, G., Marone, C., Carmichael, I. S. E., and Renne, P. (1994). Basaltic volcanism and extension near the intersection of the Sierra Madre volcanic province and the Mexican Volcanic Belt. *Geol. Soc. Am. Bull.* 106, 383–394.

Mudelsee, M., and Stattegger, K. (1997). Exploring the structure of the mid-Pleistocene revolution with the advanced methods of time-series analysis. *Geol. Rundsch.* 86, 499–511.

Opdyke, N. D., Glass, B., Hays, J. D., and Foster, J. H. (1966). Palaeomagnetic study of Antarctic deep sea cores *Science* 154, 349.

Ortega-Guerrero, B., Sedov, S., Solleiro-Rebolledo, E., and Soler, A. (2004), Magnetic mineralogy in Barranca Tlalpan exposure paleosols, Tlaxcala, Mexico. *Rev. Mex. Cienc. Geol.* 21, 120–132.

Petronille, M., Goguitchaichvili, A., Henry, B., Alva-Valdivia, L. M., Rosas-Elguera, J., Urrutia-Fucugauchi, J., et al. (2005). Paleomagnetism of Ar-Ar dated lava flows from the Ceboruco-San Pedro volcanic field (western Mexico): evidence for the Matuyama-Brunhes transition precursor and a fully reversed geomagnetic event in the Brunhes chron. *J. Geophysical Res.* 110, 1–11. doi: 10.1029/2004JB003321

Prévot, M., and Camps, P. (1993). Absence of preferred longitude sectors for poles from volcanic records of geomagnetic reversals. *Nature* 366, 53–57.

Quidelleur, X., Carlut, J., Gillot, P. Y., and Soler, V. (2002). Evolution of the geomagnetic field prior to the Matuyama-Brunhes transition: radiometric dating of a 820 ka excursion at La Palma. *Geophys. J. Int.* 151, F6–F10. doi: 10.1046/j.1365-246X.2002.01841.x

Quidelleur, X., and Valet, J. P. (1996), Geomagnetic changes across the last reversal recorded in lava flows from La Palma (Canary Islands). *J. Geophys. Res.* 101, 13755–13773.

Righter, K., Carmichael, I. S. E., and Becker, T. (1995). Pliocene-Quaternary volcanism and faulting at the intersection of the Gulf of California and the Mexican Volcanic Belt. *Geol. Soc. Am. Bull.* 107, 612–626.

Rivas, J., Ortega, B., Sedov, S., Solleiro, E., and Sycheva, S. (2006). Rock magnetism and pedogenetic processes in Luvisol profiles: examples from Central Russia and Central Mexico. *Q. Int.* 156/157, 212–223. doi: 10.1016/j.quaint.2006.05.007

Sagnotti, L., Scardia, G., Giaccio, B., Liddicoat, J. C., Nomade, S., Renne, P. R., et al. (2014). Extremely rapid directional change during Matuyama-Brunhes geomagnetic polarity reversal. *Geophys. J. Int.* 199, 1110–1124. doi: 10.1093/gji/ggu287

Sedov, S., Solleiro-Rebolledo, E., Terhorst, B., Solé, J., Flores-Delgadillo, M. L., Werner, G., et al. (2009). The Tlaxcala basin paleosol sequence: a multiscale

proxy of middle to late Quaternary environmental change in central Mexico. *Rev. Mex. Cienc. Geol.* 26, 448–465.

Singer, B. S., Hoffman, K. A., Coe, R. S., Brown, L. L., Jicha, B. R., Pringle, M. S., et al. (2005). Structural and temporal requirements for geomagnetic reversal deduced from lava flows. *Nature* 434, 633–636. doi: 10.1038/nature 03431

Singer, B. S., and Pringle, M. S. (1996). Age and duration of the Matuyama-Brunhes geomagnetic polarity reversal from 40Ar/39Ar incremental heating analyses of lavas. *Earth Planet. Sci. Lett.* 139, 47–61.

Singer, B. S., Relle, M. K., Hoffman, K. A., Battle, A., Laj, C., Guillou, H., et al. (2002). Ar/Ar ages from transitionally magnetized lavas on La Palma, Canary Island, and the geomagnetic instability timescale. *J. Geophys. Res.* 107, EPM 7-1–EPM 7-20. doi: 10.1029/2001JB001613

Solis-Castillo, B., Sedov, S., Solleiro-Rebolledo, E., and Salcido-Berkovich, C. (2012). Paleosuelos en secuencias coluvio-aluviales del Pleistoceno –Holoceno en Tlaxcala: registros paleoambientales del poblamiento temprano en el centro de México. *Bol. Soc. Geol. Mexi.* 64, 91–108.

Spell, T. L., and McDougall, I. (1992). Revisions to the age of the Brunhes-Matuyama boundary and the pleistocene geomagnetic polarity timescale. *Geophys. Res. Lett.* 19, 1181–1184. doi: 10.1029/92GL01125. issn: 0094-8276

Suganuma, Y., Okuno, J., Heslop, D., Roberts, A. P., Yamazaki, T., and Yokoyama, Y. (2011). Post-depositional remanent magnetization lock-in for marine sediments deduced from 10Be and paleomagnetic records through the Matuyama–Brunhes boundary. *Earth Planet. Sci. Lett.* 311, 39–52. doi: 10.1016/j.epsl.2011.08.038

Tauxe, L., Herbert, T., Shackleton, N. J., and Kok, Y. S. (1996). Astronomical calibration of the Matuyama-Brunhes boundary consequences for magnetic remanence acquisition in marine carbonates and the Asian loess sequences. *Earth Planet. Sci. Lett.* 140, 133–146.

Thompson, R., and Oldfield, F. (1986). "Environmental Magnetism," in eds Allen and Unwin (London: Springer), 227.

Tramp, K. L., Soreghan, G. S. L., and Elmore, R. D. (2004). Paleoclimatic inferences from paleopedology and magnetism of the Permian Maroon Formation loessite, Colorado, USA. *Geol. Soc. Am. Bull.* 116, 671–686. doi: 10.1130/B25354.1

Valet, J. P., Fournier, A., Courtillot, V., and Herrero-Bervera, E. (2012). Dynamical similarity of geomagnetic field reversals. *Nature* 490, 89–94. doi: 10.1038/nature11491

Vandamme, D. (1994). A new method to determine paleosecular variation. *Phys. Earth Planet. Int.* 85, 131–142. doi: 10.1016/0031-9201(94)90012-4

Conflict of Interest Statement: The authors declare that the research was conducted in the absence of any commercial or financial relationships that could be construed as a potential conflict of interest.

frontiers in Earth Science

PERSPECTIVE
published: 09 April 2015
doi: 10.3389/feart.2015.00014

Possible relationship between the Earth's rotation variations and geomagnetic field reversals over the past 510 Myr

Igor G. Pacca[1]*, *Everton Frigo*[2] *and Gelvam A. Hartmann*[3]

[1] Departamento de Geofísica, Instituto de Astronomia, Geofísica e Ciências Atmosféricas, Universidade de São Paulo, São Paulo, Brazil, [2] Universidade Federal do Pampa, Campus Caçapava do Sul, Caçapava do Sul, Brazil, [3] Coordenação de Geofísica, Observatório Nacional, Rio de Janeiro, Brazil

The Earth's rotation can change as a result of several internal and external processes, each of which is at a different timescale. Here, we present some possible connections between the Earth's rotation variations and the geomagnetic reversal frequency rates over the past 120 Myr. In addition, we show the possible relationship between the geomagnetic field reversal frequency and the $\delta^{18}O$ oscillations. Because the latter reflects the glacial and interglacial periods, we hypothesize that it can be used as a possible indicator to explain the length of day (LOD) variations and consequently the reversal field frequency over the past 510 Myr. Therefore, our analysis suggests that the relationships between the geomagnetic reversal frequency rates and the Earth's rotation changes during the Phanerozoic. However, more reversal data are required for periods before the Kiaman Reverse Superchon (KRS) to strengthen the perspective of using the geomagnetic reversal data as a marker for the LOD variations through geological times.

Keywords: geomagnetic field reversals, Earth's rotation variation, length of day, Earth's temperature variation, Phanerozoic

OPEN ACCESS

Edited by:
Eric Font,
University of Lisbon, Portugal

Reviewed by:
Oscar Pueyo Anchuela,
Universidad de Zaragoza, Spain
Ramon Egli,
Central Institute for Meteorology and Geodynamics, Australia

***Correspondence:**
Igor G. Pacca,
Departamento de Geofísica, Instituto de Astronomia, Geofísica e Ciências Atmosféricas, Universidade de São Paulo, Rua do Matão, 1226, Cidade Universitária, São Paulo 05508-090, Brazil
igpacca@usp.br

Specialty section:
This article was submitted to Geomagnetism and Paleomagnetism, a section of the journal Frontiers in Earth Science

Received: *18 December 2014*
Accepted: *23 March 2015*
Published: *09 April 2015*

Citation:
Pacca IG, Frigo E and Hartmann GA (2015) Possible relationship between the Earth's rotation variations and geomagnetic field reversals over the past 510 Myr. Front. Earth Sci. 3:14. doi: 10.3389/feart.2015.00014

Introduction

The Earth's rotation can be understood through internal and external processes that act upon the planet. External processes include: gravitational interactions with the Moon, the Sun and the planets; orbital and rotation axis variations; and position of the solar system relative to the galactic spiral arms. Internal processes include: the redistribution of densities in the mantle because of the lithospheric plate subduction and mantle convection; distribution of continents; variations caused by glacial and interglacial periods (e.g., Lambeck, 1980; Hide and Dickey, 1991; Gross, 2007).

The variations in Earth's rotation can be studied using the principle of conservation of angular momentum for the Earth system. The solid Earth rotation varies as a result of the applied external torques, internal mass redistribution and transfer of angular momentum between the solid Earth and its fluids (Gross, 2007). Regarding the fluids, hydrodynamic and magneto hydrodynamic torques strongly act at the solid and fluid parts of planet Earth (e.g., Hide et al., 2000). Rotation variations are often expressed as length of day (LOD) variations, which have been observed at decadal timescale and are considered a result of the angular momentum transfer from the outer core zonal flow to the mantle (e.g., Holme and De Viron, 2005, 2013; Holme, 2007). Large LOD variations

over decadal time scales arise from the exchange of angular momentum between the solid mantle and the fluid core (Holme, 1998).

The main geomagnetic field is generated in the Earth's liquid metallic outer core. Driven by buoyancy forces from the action of gravity on density heterogeneities, the core motions are strongly affected by Coriolis forces because of the Earth's rotation and geometry of the coupling surfaces (e.g., Lambeck, 1980; Hide and Dickey, 1991; Hide et al., 2000; Miyagoshi and Hamano, 2013). A link between the decadal geomagnetic field and LOD variations has been treated (e.g., Yoshida and Hamano, 1995; Dumberry and Bloxham, 2006); however, the relationship between the geomagnetic field and LOD variations has not been explored for the geological timescale. Geomagnetic field reversals are the most important field features that have been observed throughout the geological timescales. The Earth's magnetic field irregularly reverses, and the reversal frequencies are highly variable: there are periods with high reversal frequencies and periods of remarkable stability, i.e., the superchrons (e.g., Merrill et al., 1998). The reason for this apparent discrepancy in reversal frequencies remains in debate, and the variations in Earth's rotation can play an important role during the geological times.

Here, we present some possible connections between the Earth's rotation variations and the geomagnetic reversal frequency rates over the past 120 Myr. In addition, we show the possible relationship between the geomagnetic field reversal frequency and $\delta^{18}O$ oscillations. Because the latter reflects the glacial and interglacial periods, we hypothesize that it can be used as a possible indicator to explain LOD variations and consequently the reversal field frequency over the past 510 Myr. In this case, we suggest that the superchrons can be the Earth's internal markers for LOD oscillations through the Phanerozoic.

Magnetic Field Reversal Frequency and the Earth's Rotation Variations

The field reversal rate changes can be obtained based on the geomagnetic polarity time scale (GPTS), which is well constrained for the 0–160 Ma period using high-resolution sea-floor magnetic anomalies. For the period prior to 160 Ma, the GPTS is obtained from lower-resolution, paleomagnetic measurements in sedimentary and igneous rock records (Ogg, 1995). The current GPTS database spans approximately the past 540 Ma and indicates periods of high and low reversal rates according to Pavlov and Gallet (2005) (see **Figures 1**, **2**). For the past 540 Ma, three periods without reversals are observed at approximately 125-83 Ma (the Cretaceous Normal Superchron—CNS), at approximately 314-267 Ma (the Kiaman Reverse Superchon—KRS) and at approximately 482-463 Ma (the Moyero Reversal Superchron—MRS), although some reversals may have occurred within these intervals (e.g., Ogg, 1995; Granot et al., 2012). High-frequency reversal periods have been determined before and after the CNS and KRS.

Each external or internal cause for rotation change acts at a certain timescale (Lambeck, 1980). Creer (1975) suggested that there might be a connection between changes in the predominant geomagnetic polarity reversals and Earth rotation variations, which were obtained from coral growth data. Greff-Lefftz (2011) constructed a 120 Ma model for the length of day (LOD) variations, where the change components are attributed to mantle

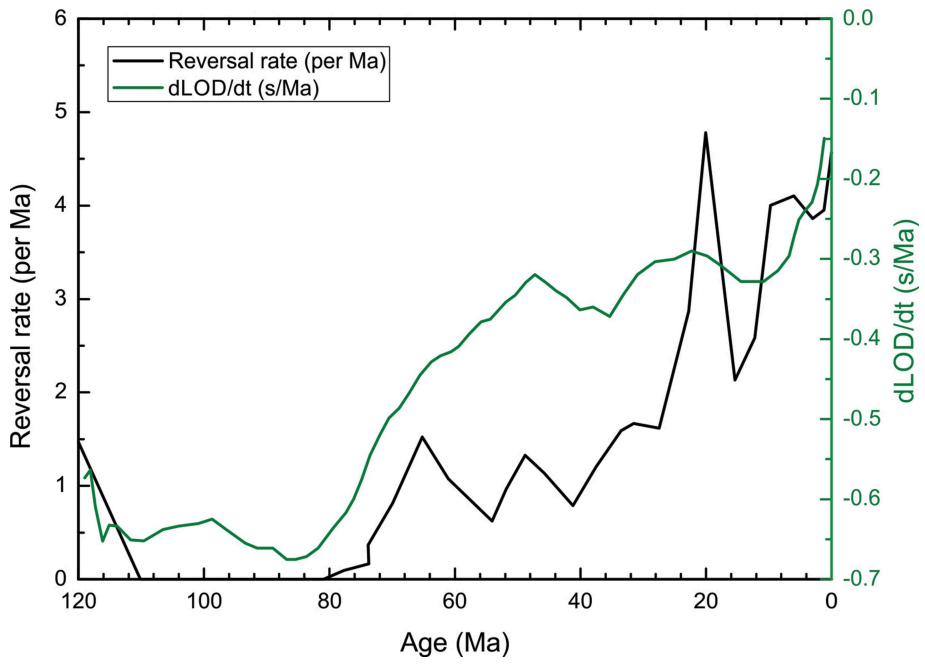

FIGURE 1 | Geomagnetic reversal rates over the past 120 Ma period, which were calculated according to Pavlov and Gallet (2005) and compared with the LOD time derivative variations from Greff-Lefftz (2011).

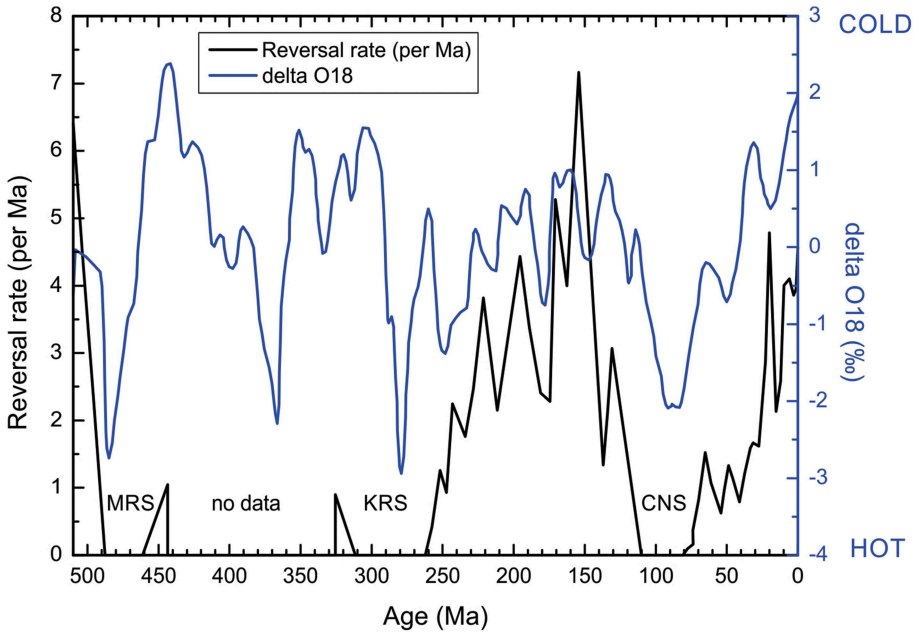

FIGURE 2 | Geomagnetic field reversal rates over the past 510 Myr from Pavlov and Gallet (2005) compared with the $\delta^{18}O$ (delta O18) variations from Veizer et al. (2000) and Price et al. (2013).

density heterogeneities (i.e., upwelling domes and sinking plates) and viscoelasto-gravitational deformations according to Ricard et al. (1993) and Rouby et al. (2010). In that work, the LOD perturbation was estimated as 0.4 μs per year, which is an order of magnitude smaller than the effects of the last glaciation. **Figure 1** shows the LOD time derivative from Greff-Lefftz (2011) and the geomagnetic reversal rates for the past 120 Ma. The two curves are similar from ∼80 Ma until the present, although between approximately 115 and 80 Ma, which coincides with the CNS, the LOD variation and reversal rates (**Figure 1**) are approximately constant. Prior to approximately 115 Ma, both the LOD and reversal rate variations show a similar trend, which can be ascertained by the strong correlation ($r = +0.82$) between both curves (**Figure 1**). In addition, both phenomena vary at the identical timescale (i.e., at Ma), which indicates that the geomagnetic field reversals "instantaneously respond" to the LOD changes. These observations clearly suggest a possible direct connection between the LOD variations and an internal process in the Earth's core (geodynamo).

Comparison with $\delta^{18}O$ data

At a Phanerozoic time scale, the variations of the Earth's rotation can be a result of glacial isostatic adjustment (GIA) (e.g., Wu and Peltier, 1984; Nakada and Okuno, 2003; Martinec and Hagedoorn, 2014). The glacial-interglacial transitions induce variations in sea level and temperature. The $\delta^{18}O$ values for the Phanerozoic calcitic and phosphatic shells from all continents (Veizer et al., 1999, 2000) have been used as a proxy for sea level and temperature variations (Miller et al., 2005; Shaviv, 2005; Müller et al., 2008; Price et al., 2013; Shaviv et al., 2014). A correlation between the sea level and the rotation caused by glacial-interglacial transitions can follow from the Earth's angular momentum conservation, when large displaced water masses induce changes in the inertia tensor, which consequently causes variations in rotation. The geomagnetic field responds to the rotation changes because one of the main forces in the geodynamo dynamical equation (Navier-Stokes) is the Coriolis force.

Figure 2 shows a comparison between the Phanerozoic geomagnetic reversal frequency variation and $\delta^{18}O$ values. The $\delta^{18}O$ curve is adapted from Veizer et al. (2000) and Price et al. (2013). The curve shows detrended running averages with steps of 10 Myr and windows of 20 Myr. The reversal frequency curve was linearly interpolated with an interval of 10 Myr. The data were divided into three time intervals: 0–120 Ma, 120–270 Ma and 270–510 Ma. The first time interval is shown in **Figure 1**. The second interval is a continuation of the first interval, for which many reversal frequency data are available. The third interval has little available geomagnetic reversal data. The computed correlation coefficients between the reversal frequency rate and $\delta^{18}O$ variations are +0.79 and +0.72 for the 0–120 Ma and 120–270 Ma intervals, respectively. In these cases, the correlations between both curves indicate a similar trend, and both CNS and KRS superchrons coincide with temperature maxima values from $\delta^{18}O$ values. These temperature maxima correspond to the inertia momentum maxima and rotation minima during the Phanerozoic. For both intervals (0–120 and 120–270 Ma), the statistical significance of the calculated correlation coefficients was tested using Student's test. The results indicate that the calculated correlation coefficients are reliable considering the 95% confidence level. For the 270–510 Ma interval, the correlation coefficient is −0.26, and the significance test indicates that the

95% confidence level has not been reached. This result may have been strongly affected by the lack of reversals data. This is not an evident clue for the relation between the geomagnetic field reversal rate (consequently, LOD variations) and $\delta^{18}O$ oscillations for this time interval.

Final Remarks

The LOD variations over the past 120 Myr show a close relationship with the geomagnetic field reversal frequency. This relationship is ascertained by strong similarities between both curves with a correlation coefficient of +0.82. Because geomagnetic field variations can be an "instantaneous direct response" of the LOD oscillations, they can be used as a marker for other phenomena. According to the LOD modeling, it causes perturbations in the Earth's rotation that are approximately one order of magnitude smaller than those caused by the last glaciation. If this assumption is correct, the glacial-interglacial transitions directly affect the LOD variations. In this case, the reversal frequency rate can be used to compare with climatic proxies such as $\delta^{18}O$ data.

The comparison between $\delta^{18}O$ and the geomagnetic reversal frequency presents similar trends during 0–120 Ma and 120–270 Ma. For these two periods, the CNS and KRS superchrons coincide with the temperature maxima, which correspond to the inertia momentum maxima and rotation minima. The MRS superchron also corresponds to a temperature maxima, although the correlation between the two curves is low due to scarcity of data. These rotation variations (LOD) can occur because of the hydrodynamic changes (water and ice mass displacements) on the Earth's surface. These hydrodynamic variations consequently reflect the observed glacial and interglacial transitions during the 510 Ma period. There is a fourth Phanerozoic temperature maximum, where reversal data are scarce, that could correspond to a Devonian Superchron.

Therefore, our analysis suggests relationships between the geomagnetic reversal frequency rates and the Earth's rotation changes during the Phanerozoic. However, more reversal data are required for periods before the KRS to strengthen the perspective of using geomagnetic reversal data as a marker for LOD variations through geological times.

Acknowledgments

IP is thankful for a CNPq Research Fellowship; GH is thankful for CNPq (454609/2014-0) and CAPES (AUXPE 2043/2014) grants. We would like to thank the Instituto de Astronomia, Geofísica e Ciências Atmosféricas of the Universidade de São Paulo (IAG/USP) the Universidade Federal do Pampa and the Coordenação de Geofísica of the Observatório Nacional (COGE/ON) for the institutional support.

References

Creer, K. M. (1975). "On a tentative correlation between changes in geomagnetic polarity bias and reversal frequency and the earth's rotation through Phanerozoic time" in *Growth Rhythms and the History of the Earth's Rotation*, eds G. D. Rosenbeg and S. K. Runcorn (London: John Wiley and Sons), 559.

Dumberry, M., and Bloxham, J. (2006). Azimuthal flows in the Earth's core and changes in length of day at millennial timescales. *Geophys. J. Int*. 165, 32–46. doi: 10.1111/j.1365-246X.2006.02903.x

Granot, R., Dyment, J., and Gallet, Y. (2012). Geomagnetic field variability during the Cretaceous Normal Superchron. *Nat. Geosci*. 5, 220–223. doi: 10.1038/ngeo1404

Greff-Lefftz, M. (2011). Length of day variations due to mantle dynamics at geological timescale. *Geophys. J. Int*. 187, 595–612. doi: 10.1111/j.1365-246X.2011.05169.x

Gross, R.S. (2007). "Earth rotation variations—long period," in *Treatise on Geophysics*, Vol. 3, Geodesy, eds G. Schubert and T. Herring (Amsterdam: Elsevier), 239–294.

Hide, R., Boggs, D.H., and Dickey, J.O. (2000). Angular momentum fluctuations within the Earth's liquid core and torsional oscillations of the core–mantle system. *Geophys. J. Int*. 143, 777–786. doi: 10.1046/j.0956-540X.2000.01283.x

Hide, R., and Dickey, J.O. (1991). Earth's variable rotation. *Science* 253, 629–637. doi: 10.1126/science.253.5020.629

Holme, R. (1998). Electromagnetic core–mantle coupling—I. Explaining decadal changes in the length of day. *Geophys. J. Int*. 132, 167–180. doi: 10.1046/j.1365-246x.1998.00424.x

Holme, R. (2007). "Large-scale flow in the Core," in *Treatise on Geophysics*, Vol. 8, Core Dynamics, eds G. Schubert and P. Olson (Amsterdam: Elsevier), 107–131.

Holme, R., and De Viron, O. (2005). Geomagnetic jerks and a high-resolution length-of-day profile for core studies. *Geophys. J. Int*. 160, 435–439. doi: 10.1111/j.1365-246X.2004.02510.x

Holme, R., and De Viron, O. (2013).Characterization and implications of intradecadal variations in length of day. *Nature* 499, 202–204. doi: 10.1038/nature12282

Lambeck, K. (1980). *The Earth's Variable Rotation*. Cambridge: Cambridge University Press.

Martinec, Z., and Hagedoorn, J. (2014). The rotational feedback on linear momentum balance in glacial isostatic adjustment. *Geophys. J. Int*. 199, 1823–1846. doi: 10.1093/gji/ggu369

Merrill, R.T., McElhinny, M.W., and McFadden, P.L. (1998). *The Magnetic Field of the Earth: Paleomagnetism, the Core, and the Deep Mantle,* Vol. 63 *(International Geophysics Series.)*. Amsterdam: Elsevier; Academic Press.

Miller, K. G., Kominz, M. A., Browning, J. V., Wright, J. D., Mountain, G. S., Katz, M. E., et al. (2005). The phanerozoic record of global sea-level change. *Science* 310, 1293–1298. doi: 10.1126/science.1116412

Miyagoshi, T., and Hamano, Y. (2013). Magnetic field variation caused by rotational speed change in a magnetohydrodynamic dynamo. *Phys. Rev. Lett*. 111, 124501. doi: 10.1103/PhysRevLett.111.124501

Müller, R. D., Sdrolias, M, Gaina, C., Steinberger, B., and Heihe, B. (2008). Long-term sea-level fluctuations driven by ocean basin dynamics. *Science* 319, 1357–1362. doi: 10.1126/science.1151540

Nakada, M., and Okuno, J. (2003). Perturbations on the Earth's rotation and their implications for the present day mass balance of both polar ice caps. *Geophys. J. Int*. 152, 124–138. doi: 10.1046/j.1365-246X.2003.01831.x

Ogg, J. (1995). "Magnetic polarity time scale of the Phanerozoic," in *AGU Reference Shelf,* Vol. 1, *Global Earth Physics: A Handbook of Physical Constants*, ed T. J. Ahrens (Washington, DC: AGU), 240–270.

Pavlov, V., and Gallet, Y. (2005). A third superchron during the Early Paleozoic. *Episodes* 28, 78–84.

Price, G.D., Twitchett, R.J., Wheeley, J.R., and Buono, G. (2013). Isotopic evidence for long term warmth in the Mesozoic. *Nat. Sci. Rep*. 3, 1438. doi: 10.1038/srep01438

Ricard, Y., Richards, M., Lithgow-Bertelloni, C., and Le Stunff, Y. (1993). A geodynamic model of mantle density heterogeneity. *J. Geophys. Res.* B98, 21895–21909. doi: 10.1029/93JB02216

Rouby, H., Greff-Lefftz, M., and Besse, J. (2010). Mantle dynamics, geoid, inertia and TPW since 120 Myr. *Earth Planet. Sci. Lett*. 292, 301–311. doi: 10.1016/j.epsl.2010.01.033

Shaviv, N. J. (2005). On climate response to changes in the cosmic ray flux and radiative budget. *J. Geophys. Res.* 110, A08105. doi: 10.1029/2004JA010866

Shaviv, N. J., Prokoph, A., and Veizer, J. (2014). Is the solar system's galactic motion imprinted in the phanerozoic climate? *Sci. Rep*. 4, 6150. doi: 10.1038/srep06150

Veizer, J., Ala, D., Azmy, K., Bruckschen, P., Buhl, D., Bruhn, F., et al. (1999). ^{87}Sr, ^{86}Sr, $d^{13}C$ and $d^{18}O$ evolution of Phanerozoic seawater. *Chem. Geol*. 161, 59–88. doi: 10.1016/S0009-2541(99)00081-9

Veizer, J., Godderis, Y., and François, L.M. (2000). Evidence for decoupling of atmospheric CO_2 and global climate during the Phanerozoic eon. *Nature* 408, 698–701. doi: 10.1038/35047044

Wu, P., and Peltier, W.R. (1984). Pleistocence deglaciation and the Earth's rotation: a new analysis. *Geophys. J. R. Astr. Soc*. 76, 753–791. doi: 10.1111/j.1365-246X.1984.tb01920.x

Yoshida, S., and Hamano, Y. (1995). Geomagnetic decadal variations caused by length-of-day variation. *Phys. Earth Planet. Int*. 91, 117–129. doi: 10.1016/0031-9201(95)03038-X

Conflict of Interest Statement: The authors declare that the research was conducted in the absence of any commercial or financial relationships that could be construed as a potential conflict of interest.

frontiers in Earth Science

ORIGINAL RESEARCH
published: 18 May 2015
doi: 10.3389/feart.2015.00018

Low temperature magnetic properties of the Late Archean Boolgeeda iron formation (Hamersley Group, Western Australia): environmental implications

Julie Carlut[1]*, *Aude Isambert*[1], *Hélène Bouquerel*[1], *Ernesto Pecoits*[1], *Pascal Philippot*[1], *Emmanuelle Vennin*[2], *Magali Ader*[1], *Christophe Thomazo*[2], *Jean-François Buoncristiani*[2], *Frank Baton*[1], *Elodie Muller*[1] and *Damien Deldicque*[3]

[1] Institut de Physique du Globe de Paris, Universite Paris Diderot, Sorbonne Paris Cite, UMR 7154 Centre National de la Recherche Scientifique, Paris, France, [2] UMR, Centre National de la Recherche Scientifique 6282 Biogéosciences, Université de Bourgogne, Dijon, France, [3] Ecole Normale Supérieure - Géologie, UMR8538, Paris, France

OPEN ACCESS

Edited by:
Eric Font,
University of Lisbon, Portugal

Reviewed by:
Juan Cruz Larrasoaña,
Instituto Geológico y Minero de España, Spain
Pedro Silva,
Instituto Superior de Engenharia de Lisboa, Portugal

***Correspondence:**
Julie Carlut,
Institut de Physique du Globe de Paris, Universite Paris Diderot, Sorbonne Paris Cite, UMR 7154 Centre National de la Recherche Scientifique, 1 rue Jussieu, F-75238 Paris Cedex 05, France
jcarlut@yahoo.fr

Specialty section:
This article was submitted to Geomagnetism and Paleomagnetism, a section of the journal Frontiers in Earth Science

Received: 25 February 2015
Accepted: 23 April 2015
Published: 18 May 2015

Citation:
Carlut J, Isambert A, Bouquerel H, Pecoits E, Philippot P, Vennin E, Ader M, Thomazo C, Buoncristiani J-F, Baton F, Muller E and Deldicque D (2015) Low temperature magnetic properties of the Late Archean Boolgeeda iron formation (Hamersley Group, Western Australia): environmental implications. Front. Earth Sci. 3:18. doi: 10.3389/feart.2015.00018

The origin of the iron oxides in Archean and Paleoproterozoic Banded Iron Formations (BIFs) is still a debated question. We report low and high temperature magnetic properties, susceptibility and saturation magnetization results joined with scanning microscope observations within a 35 m section of the Late Archean Boolgeeda Iron Formation of the Hamersley Group, Western Australia. With the exception of two volcanoclastic intervals characterized by low susceptibility and magnetization, nearly pure magnetite is identified as the main magnetic carrier in all iron-rich layers including hematite-rich jasper beds. Two populations of magnetically distinct magnetites are reported from a 2 m-thick interval within the section. Each population shows a specific Verwey transition temperature: one around 120–124 K and the other in the range of 105–110 K. This temperature difference is interpreted to reflect two distinct stoichiometry and likely two episodes of crystallization. The 120–124K transition is attributed to nearly pure stoichiometric magnetite, SEM and microprobe observations suggest that the lower temperature transition is related to chemically impure silician magnetite. Microbial-induced partial substitution of iron by silicon is suggested here. This is supported by an increase in Total Organic Carbon (TOC) in the same interval.

Keywords: rock magnetism, Verwey transition, banded iron formation, Archean, great oxidation event, Hamersley group, magnetite

Introduction

Banded Iron Formations (BIFs) are massive to layered chemical sedimentary rocks composed of silica, at least 15% iron oxides (hematite, Fe_2O_3 and magnetite, Fe_3O_4) and minor Fe-bearing carbonate and chlorite. These rocks are emblematic of the Archean and Paleoproterozoic eons (Trendall and Blockey, 1970; Ewers and Morris, 1981; Bekker et al., 2010). The association between BIFs and free oxygen derived from oxygenic photosynthesis has long been recognized (Cloud, 1973). More recent models have considered oxidation under anoxic conditions via anoxygenic Fe(II)-oxidizing photosynthesis (Konhauser et al., 2002; Kappler et al., 2005), UV photo-oxidation

(Braterman et al., 1983; Konhauser et al., 2007) and atmospherically produced hydrogen peroxide (Pecoits et al., 2015). The former is regarded as the most likely mechanism responsible for Archean BIFs, before the Great Oxidation Event (GOE), i.e., at a time when the Earth's atmosphere and oceans remained essentially anoxic.

The crystallization process of iron oxides in these sedimentary rocks is still debated. It is generally accepted that iron oxides in BIFs derived from the oxidation of solubilized Fe(II) into iron hydroxide precursors ($Fe(OH)_3$) (e.g., Ewers and Morris, 1981). Ahn and Buseck (1990) provided evidences that some of the nano hematites present in a 2.5 Ga BIF section of the Marra Mamba Iron Formation were most likely the result of direct dehydration of colloidal iron hydroxide particles. This suggests that colloidal transport and deposition may be involved in BIFs formation. However, such observations have not been duplicated. The crystallization of magnetite is even less clear, so that magnetite is generally regarded as non-primary and driven by post-depositional, likely biologically generated, ferric iron reduction (Li et al., 2011, 2013).

Few paleomagnetic studies have been dedicated to BIFs (but see Chamalaun and Dempsey, 1978; Schmidt and Clark, 1994; Sumita et al., 2001; Tompkins and Cowan, 2001). Most of these studies are focused on remanence analysis and measurements of the anisotropy of magnetic susceptibility. Rock magnetic property variations linked to changes in concentration and composition of iron oxides in BIFs remained largely unexplored. The Hamersley Basin in Western Australia contains large deposits of BIFs that encompasse the Archean-Proterozoic transition. This basin, therefore, is an ideal location to unravel the paleoenvironmental conditions attending one of the most critical periods in Earth history, namely the rise of atmospheric oxygen. In this study, we present rock-magnetic measurements performed on a 35 m thick section of the Boolgeeda Iron Formation of the Hamersley Group, Western Australia. The content in magnetite was constrained using susceptibility and saturation magnetization. In addition, low temperature magnetic properties allowed detecting small changes in the stoichiometry and composition of magnetite. This in turn was used to constrain the environmental conditions associated with deposition of the Boolgeeda Iron Formation. Specifically, magnetite undergoes a low-temperature transformation, called the Verwey transition, at a given temperature (T_v) and transforms from cubic ($T > T_v$) to monoclinic ($T < T_v$) symmetry. This transformation, related to changes in crystal symmetry and cation ordering, is accompanied by changes in magnetic properties. When magnetite is heated through T_v its magnetic remanence decreases while its susceptibility increases, both sharply (e.g., Verwey et al., 1947; Özdemir et al, 1993; Muxworthy and McClelland, 2000; Novák et al., 2000). The T_v temperature depends on variables of interest including stoichiometry, cation substitution or grain size. Increasing amounts of cation vacancy or substitution decrease the Verwey temperature from ∼122 K until a threshold around 80 K (Moskowitz, 1993; Jackson et al., 2011). Low temperature properties are thus an interesting way to derive bulk properties from a population of magnetite and T_v is widely used for identification of magnetite in natural samples. Low temperature analyses performed here allowed to report the coexistence of two distinct Verwey transitions within a 2 m thick sedimentary section of the Boolgeeda Iron Formation. The possible causes and environmental significance of this specific occurrence are discussed.

Geological Setting and Sampling Strategy

The Boolgeeda Iron Formation consists of deep to shallow iron-rich marine sedimentary successions deposited at the top of the Hamersley Group in the southern Pilbara Craton, Western Australia (**Figure 1**; Trendall, 1979; Hickman and Van Kranendonk, 2012). The formation overlies the Woongarra Rhyolite (Barley et al., 1997) and is conformably overlain by the Kungarra Formation, which constitues the base of the Turee Creek Group. The age of deposition is not well constrained and lies between 2450 ± 3 Ma, obtained for the Woongarra Rhyolite, and 2209 ± 15 Ma obtained on the unconformably overlying Cheela Spring's basalts (Barley et al., 1997; Martin et al., 1998; Trendall et al., 2004; Müller et al., 2005). The samples investigated in this study come from TCDP-1, one of the three drill cores of the Turee Creek Drilling Project collected in May 2013. TCDP-1 intersects the transition between the Boolgeeda Iron Formation and the overlying Kungarra Formation. Our study focuses on the upper part of the Boolgeeda Iron Formation, near the transition with the Kungarra Formation. The samples were collected at regular intervals between 163.25 and 130.4 m depth. This sedimentary section is composed mainly of dark, iron-rich strata (typical BIFs), interlayered with red, silica-rich, jasper layers (**Figure 1**). It is cut by volcanoclastic layers around 153 and 146 m depth. The jasper layers occur mostly in the intervals 165–156, 152–149, and 132–130 m depth (**Figure 1**).

Methods

Susceptibility and saturation magnetization were measured on small sub samples using an AGICO™ KLY-3 and a Princeton Measurements™ micromag Vibrating Sample Magnetometer (VSM) at IPGP. Thermomagnetic measurements of low-field magnetic susceptibility (κ) at low and high temperature were performed on powdered bulk samples at the IPGP using the AGICO™ KLY-3 coupled to a CS-3 apparatus. In the low-temperature experiments, samples were cooled until ∼ 77 K using liquid nitrogen, then κ was monitored during warming up to room temperature. In the high-temperature experiments κ was measured during a heating-cooling cycle from room temperature up to 620°C in air.

Field Cooled (FC) and Zero Field Cooled (ZFC) remanence measurements were carried out on $\sim 3 \times 3 \times 3\,mm^3$ bulk rock fragments using a Quantum Designs™ superconducting device Magnetic Properties Measurement System (SQUID MPMS) at IPGP. In both cases, the moment was measured as the sample was progressively warmed from 10 to 300 K in a 0 T field. ZFC data were obtained after the samples were previously cooled from 300 to 10 K in a 0 T field, at 10K a 2.5 T field is rapidly applied then quenched. FC data were obtained after the samples were cooled in a 2.5 T field. Warming to 300 K was proceeded in 5 K steps. In

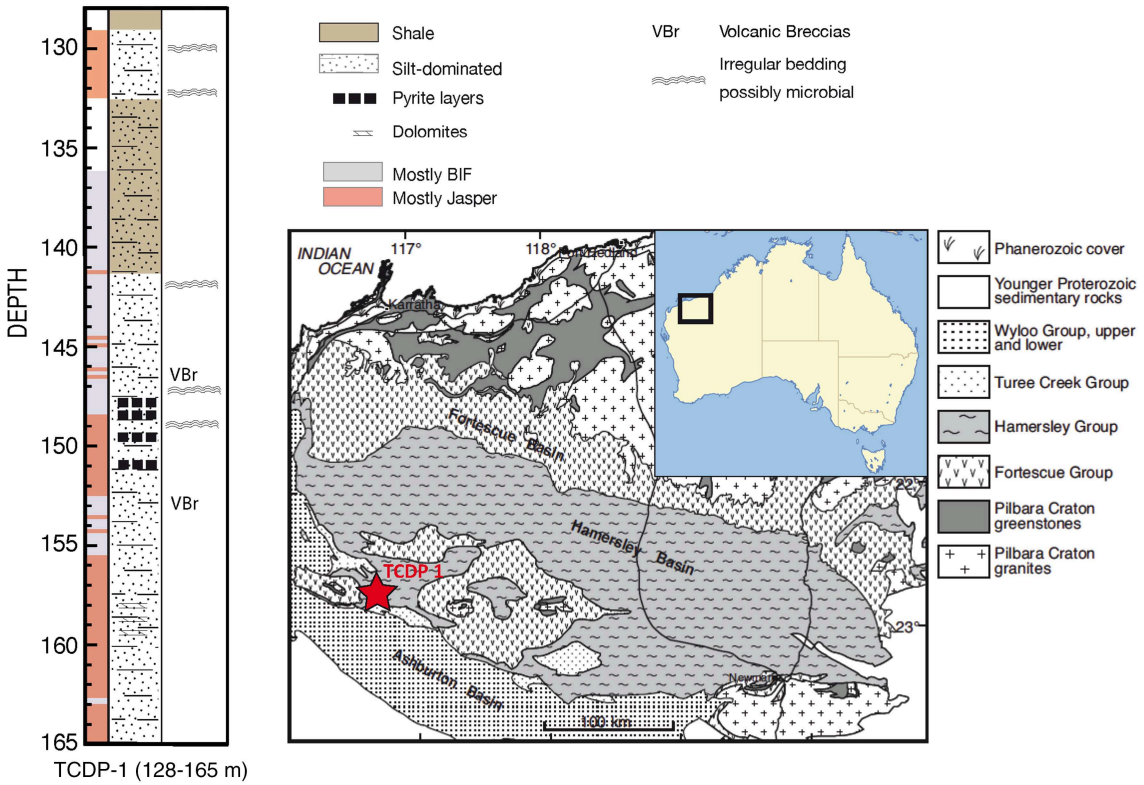

FIGURE 1 | Regional geological map of the Pilbara area in Northwest Australia (after van Kranendonk et al., 2015) and simplified lithology of the TCDP-1 core between 128 and 165 m depth. The red star localizes the drilling.

a few cases a 1 K step was used in the 80–140 K range for the ZFC in order to have a detailed curve around T_v. Then during Room-Temperature Saturation Isothermal Remanent Magnetization (RT-SIRM) cycle, a 2.5 T SIRM was given at room temperature, the samples was then cooled in a zero field down to 10 K, and warmed back to room temperature.

The first derivative of the susceptibility data (for KLY-3 measurements) and the ZFC curves (for MPMS measurements) were calculated. T_v was defined as the maximum of the derivative curve of susceptibility (κ) or moment (M) with respect to temperature (T). For each sample measured using the MPMS apparatus, we calculated the normalized decrease in magnetization (δ_{zfc}) at the Verwey transition defined as $\delta_{zfc} = (M_{80K} - M_{150K})/M_{80K}$, with M the magnetic moment during ZFC cycle at 80 or 150 K (following Moskowitz, 1993 and Carporzen et al., 2006). In the case of two Verwey transitions the relative percentage of each fraction is defined by $fv1 = (M_{80K} - M_{(Tv1+Tv2)/2})/(M_{80K} - M_{150K})$ and $fv2 = (M_{(Tv1+Tv2)/2} - M_{150K})/(M_{80K} - M_{150K})$.

Microscopic observations and semi-quantitative chemical data were collected on 9 thin sections using 2 field emission scanning electronic microscope (Fe-SEM, Zeiss Sigma and Zeiss Auriga) equipped with EDS detectors (Oxford instrument) at École Normale Supérieure de Paris (ENS, Paris) and IPGP, respectively. Observations were made in Back Scattered mode (BSE).

More than 50 analyses were performed on selected magnetite crystals from one of the thin section using a CAMECA SX100 electron microprobe at CAMPARIS, CNRS, Paris, France. Mineral standards used for calibration were diopside (for Mg, Si, and Ca), manganese titanate (for Mn and Ti), hematite (for Fe) and chromium oxide (for Cr). A 15 keV energy, 20 nA current, and 2 μm spot size was used. Acquisition time was 10 s per element.

A total of 31 samples were powdered to a size smaller than 60 μm using a ring and puck mill at the Biogéosciences Laboratory of the Université de Bourgogne in Dijon, France. They were decarbonated using HCl, rinsed until neutral and dried at 60°C. Aliquots of dried decarbonated samples (27–333 mg) were weighed in tin capsules. TOC content and $\delta^{13}C_{org}$ measurements were performed on the capsules using a flash elemental analyser (Thermo Scientific™) coupled in continuous flow mode to a Finnigan DELTA plus XP stable isotope ratio mass spectrometer at the stable isotope geochemistry lab of the Institut de Physique du Globe de Paris, France. The TOC content is expressed as a dry weight percentage of the total fraction; external reproducibility based on triplicate analyses of dried decarbonated samples is better than ± 0.0043 wt.% (1σ).

The carbon isotopic composition is expressed in delta notation and reported in parts per thousand (‰) relative to the Vienna Pee Dee Belemnite (VPDB) standard; external reproducibility is better than ± 0.25‰ (1s).

Results

SEM Observations and Oxides Characterization

Two polished thin sections of jasper located at 130.45 and 159.30 m depth were investigated in detail. The jasper is characterized by alternating red and gray microscopic layers, darker blackish layers are sometimes noticeable (**Figure 2A**). SEM observations show that the matrix is mostly composed of quartz. Carbonate (ankerite) is locally present (**Figures 2B,D**). Within the red layers, aggregates of euhedral to rounded hematite grains around 1 μm in size occur as randomly dispersed patches of a few tens of microns (**Figures 2B,D,E,F**). These hematite patches occur in association with cubic magnetite grains around 5–10 μm, and thin needles of Fe-carbonate identified as siderite (see **Figure 2E**). The organization of the hematite patches is compatible with phenocryst ghosts of a few μm and could be the result of the replacement of a primary phase by microcrystalline quartz and iron oxides. The darker blackish layers (**Figures 2A,C**) are characterized by a quartz matrix with a dense population of large cubic iron oxides grains a few tens to several hundreds microns in size. The gray sub layers are mostly composed of quartz with occasional iron oxides and ankerite (**Figures 2A,B**).

Three thin sections of a more cherty material collected at 146.70, 150.17, and 152.86 m depth were investigated using SEM technique (**Figure 3**). The chert layers are mainly composed of quartz, phyllosilicate and ankerite. Occasional rutile associated with ilmenite and zircon of possible volcanic origin were observed in samples 146.70 and 152.86 (**Figures 3A,B**). Ilmenite locally displays visible stages of growth probably linked to their volcanic origin (**Figure 3A** arrows). Sample 150.17 (**Figures 3C,D**) shows a marked layered structure characterized by iron oxide- and/or pyrite-rich layers alternating with quartz-rich layers. Ankerite is observed often in close association with pyrite and iron oxide.

BIF layers were observed at 148.02, 148.08, 148.15 (**Figure 4**) and 159.29 m depth. In all thin sections we observed a millimeter-scale layering structure composed of alternating quartz and ankerite rich layer and iron oxides rich layers (**Figure 4A**). The iron-rich layers show densely packed euhedral magnetites, often larger than 100 μm in size (**Figures 4B,C**). Cherty carbonate and silicate rich zones are observed surrounding the BIF layers. These zones contain also titanium-rich oxides, apatite, zircon, pyrite and occasional metallic alloys. Titanium rich oxides sometimes present a core with exsolved ilmenite and magnetite lamellae (**Figure 4D**). These observations are typical of subaerial volcanism and probably attest for the transport of volcanic particles at the deposition site. Different tuning in the BSE mode with brightness and contrast distributed on magnetite revealed that samples 148.02 and 148.15 contained magnetite displaying density contrasts (**Figures 4E**). These were not observed in sample 159.29. Semi-quantitative compositional analysis revealed that the brighter magnetite domains of samples

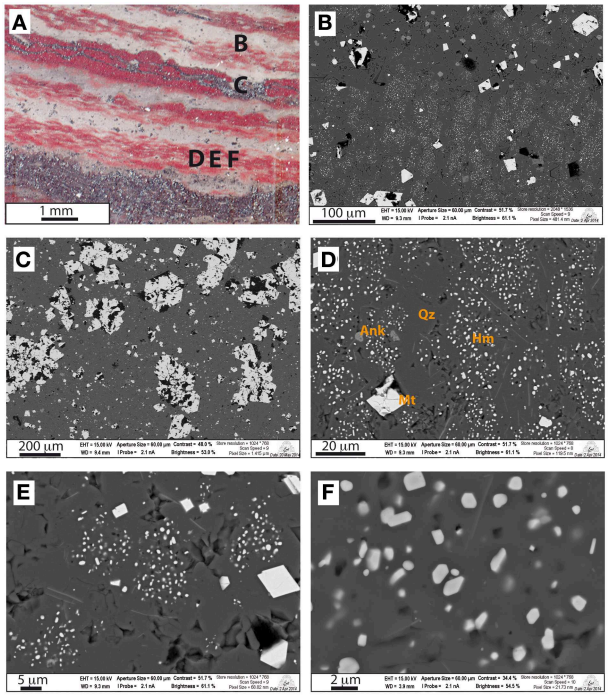

FIGURE 2 | Optical and SEM representative images of iron oxides for sample 130.45. (A) optical microscope image with indications of the area observed with the SEM; **(B)** SEM image at the transition between gray and red areas; **(C)** bulky iron oxides within the white gray area interpreted as being magnetite; **(D)** patches of small euhedral to rounded iron oxide grains interpreted as hematite in the red layers, Qz, quartz; Ank, ankerite; Mt, magnetite; Hm, hematite; **(E)** small iron oxide grains, interpreted as hematite with bigger grains population interpreted as magnetite and **(F)** high magnification image of small hematite grains.

148.02 and 148.15 correspond to low Si content (Si less than 0.5% in atom%), whereas the darker domains are associated with high Si content (with Si around 2% in atom%). Compositional maps made in different parts of the samples confirm the role of Si in the density contrasts (**Figure 4F**).

Electron Microprobe Analysis

Chemical analyses performed on more than 50 oxides within the BIF layers of sample 148.02 yielded a stoichiometry compatible with magnetite with the addition of minor silicon (**Figure 5**). The FeO content varies between 91 and 94 wt% (Fe_3O_4 between 98 and 100.5 wt%) and the SiO_2 content between 0.5 and 2 wt%. Owing to the relatively large interaction volume of the electron beam, we failed to distinguish the two magnetite populations identified with the SEM. However, the systematic detection of Si in magnetite suggests that silicon is intrinsic of the mineral structure and not due to a contamination by microquartz inclusions. This is inferred following two lines of evidence, first, none of the other phases that were analyzed (pyrite, ilmenite, carbonate) show Si, and ultra high magnification investigations using the SEM confirmed that the magnetites are devoid of SiO_2 inclusions. Although nano-inclusions cannot be completely ruled out we believe that silicon is a part of the crystalline structure

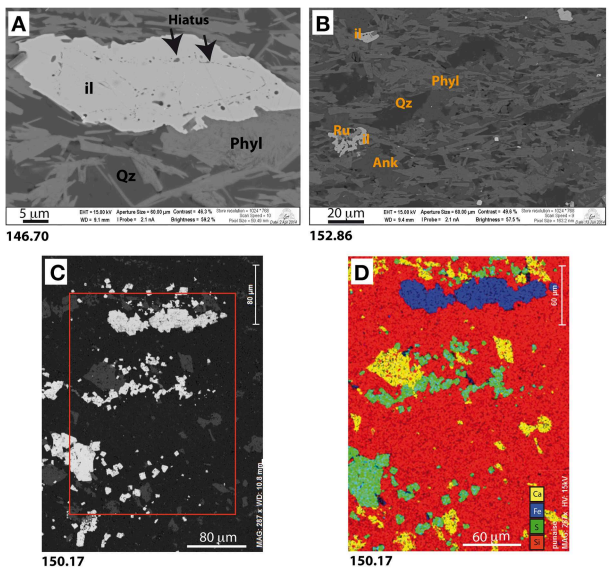

FIGURE 3 | SEM images and Si, S, Fe, Ca elements mapping of textures observed in sample (A) 146.70, (B) 152.86, and (C) 150.17; (D) mapping of the area delimited by the red rectangle in (C). Iron oxides and/or pyrites-rich alternating with quartz-rich layers are observed.

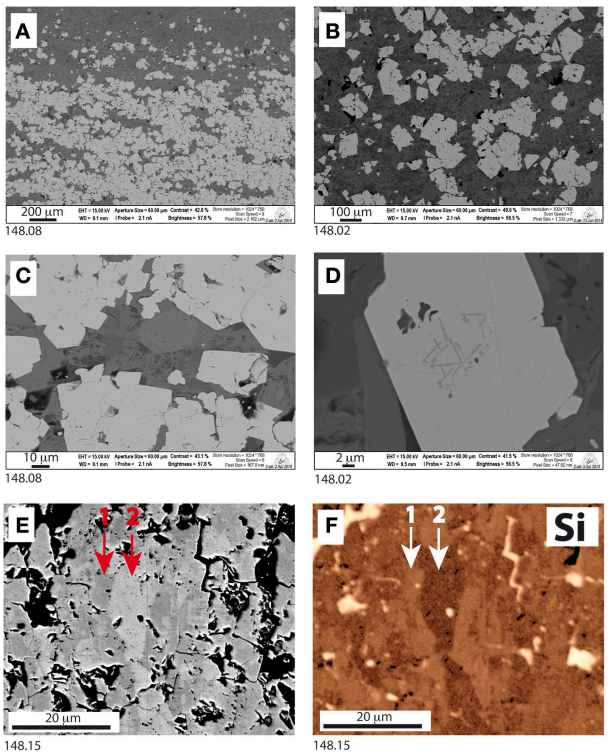

FIGURE 4 | SEM images and elements mapping in samples 148.08 (A,C), 148.02 (B,D) and 148.15 (E,F). (A,B): low magnification images of BIF layers in 148.08 and 148.02. (C) BIF layers in 148.08 at high magnification showing close packed magnetite crystals. **(D)**: high magnification image of an iron oxide crystal in the cherty part of 148.02 showing lamellar exsolutions in an iron-titanium oxide. **(E)** Back-scattered electron image of a magnetite crystal in 148.15 with tuned brightness and contrast and **(F)** corresponding EDX Si elemental mapping. The arrows indicate 2 areas of different compositions (1: Si-rich magnetite and 2: Si-low magnetite).

of magnetite as a substitute for iron. This observation is in agreement with previous studies reporting the occurrecne of silician magnetite in BIFs from the Hamersley group (Huberty et al., 2012).

Organic Carbon Content and Isotopic Composition

With the exception of one sample displaying 720 ppm of Total Organic Carbon (TOC) all samples show TOC values between 30 and 346 ppm (**Table 1**). Such low contents fall within the low range of Precambrian sedimentary rocks, but are typical, although on the high end, of BIFs (Yamaguchi, 2002). The $\delta^{13}C_{org}$ values range from −22.4 to −30‰, which is typical for organic matter derived from photosynthetic organisms (Thomazo et al., 2009) (**Table 1**). The sample with a TOC level of 720 ppm presents one of the most negative $\delta^{13}C_{org}$ value (−29.6‰). Neither TOC nor $\delta^{13}C_{org}$ values show increasing or decreasing trends along the section, indicating an overall stable depositional environment over the time scale covered by the section. However, both TOC and $\delta^{13}C_{org}$ present apparently noisy small-scale variations and show a rough trend of decreasing $\delta^{13}C_{org}$ with increasing TOC. This trend is typical of Precambrian sedimentary rocks and commonly explained as indicating a higher proportion of organic matter with more negative $\delta^{13}C_{org}$ values issued from secondary productivity [chemosynthesis or methanotrophy e.g., Thomazo et al., 2009 and ref therein; Figures 2–20 in Yamaguchi (2002)].

Susceptibility and Saturation Magnetization

Mass normalized susceptibility (χ) ranges from 1×10^{-8} to 5.7×10^{-4} m^3/kg. Saturation magnetization (Ms) ranges from 4×10^{-3} to 74 Am^2/kg (**Table 2**). Variations in χ and Ms are closely inter-correlated and show a strong dependence with lithology. Specifically, jasper layers have a mean Ms around 5.5 Am^2/kg and BIFs around 40 Am^2/kg (**Table 2**). The lower values are found for samples at 146.7 and 152.86 m depth, corresponding to volcanic breccias rich in ilmenite.

Low Temperature Remanence

Low temperature remanence analyses were performed on 20 powdered sub-samples of a few tens of mg for 10 bulk samples (130.45, 146.70, 148.02, 148.08, 151.59, 152.86, 156.52, 159.29, 159.30, and 159.80) using the SQUID MPMS. In all cases, except for samples 146.70 and 152.86, which both have a low and noisy signal without clear transition, data show a strong Verwey transition around 110–120 K indicative of magnetite (**Figure 6**). In all samples the ZFC magnetization is always larger than the FC magnetization, the R_{LT} value define as M_{fc}(20 K)/M_{zfc}(20 K) (Smirnov, 2009) is between 0.62 and 0.73. These are characteristics of large multi domain magnetite (Brachfeld et al., 2002; Smirnov, 2009). The Morin transition, around 262 K (Morrish, 1994), is characteristic of hematite and is only faintly detected in the RT-SIRM cycle in sample 130.45 and

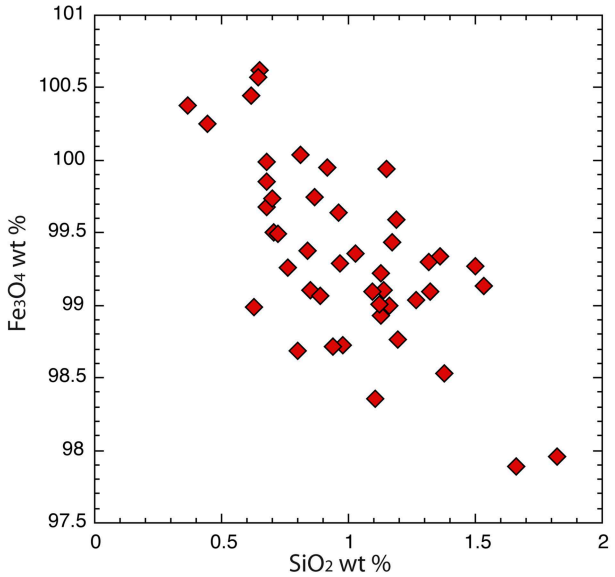

FIGURE 5 | Fe_3O_4 and SiO_2 concentrations (in wt%) from microprobe analyses performed on more than 50 magnetite crystals in the BIF layers of sample 148.02.

159.30 (**Figure 6A**). This is likely due to the weak remanence signal of hematite compared to magnetite. Experiments were often noisy due to electrical instability, but in most cases, the first derivative of ZFC curves could be calculated and the T_v temperature derived (defined as the temperature corresponding to the peak in the derivative; **Figures 6B,D**). One peak of variable thickness is determined around 120 K in all samples with sufficient signal except for samples 148.02 and 148.08, where two distinct peaks are observable. This feature leads to the determination of two distinct T_v: a low T_v around 105–110 K and a high T_v around 122–124 K (**Figure 6D**). These two temperatures reflect two different magnetite populations coexisting in these samples. The δ_{zfc} parameter allows an estimation of the loss of remanence between 80 K and 150 K: all samples display high values, between 0.93 and 0.99. The δ_{fc}/δ_{zfc} ratio clusters around 1 for all samples (between 0.99 and 1.03) and again indicates large grain sizes. For the samples showing two Verwey transitions, the relative contribution of each population to the loss of remanence can be roughly established by calculating fv1 and fv2 as described in the method section. Samples 148.02 and 148.08 show a loss of signal of about 70% and 55 to 75% respectively, carried by the low temperature fraction (**Figure 6C**).

Low Temperature Susceptibility Curves

To extend the range of samples characterization at low temperature we performed series of low temperature, low field susceptibility measurements on more than 25 samples. A comparison between Verwey temperature derived from the MPMS ZFC curves and κ(t) measurements is shown in **Figure 7**. Results are quite similar and no systematic offset is observed giving confidence in T_v determined using susceptibility. Typical

TABLE 1 | $\delta^{13}C_{org}$ and Total Organic Carbon (TOC) data for TCDP-1 from 130.39 to 161.35 m depth.

Depth in m	$\delta^{13}C_{org}$ in ‰	TOC in ppm
130.39	−26.64	112
132.31	−29.52	212
132.32	−28.98	88
135.80	−27.78	120
136.50	−27.29	58
139.20	−28.04	144
139.76	−29.41	316
139.80	−28.13	272
142.18	−28.60	346
144.13	−28.20	65
145.40	−27.61	53
145.50	−29.13	98
146.36	−28.27	86
147.05	−29.60	720
147.79	−26.59	277
147.80	−22.41	102
150.61	−29.04	182
150.62	−28.38	170
151.40	−27.00	209
155.50	−26.41	46
155.51	−29.93	233
155.60	−27.70	75
156.50	−25.36	46
156.69	−24.67	29
156.70	−25.97	30
158.98	−28.55	161
159.00	−27.56	140
159.12	−29.71	132
159.54	−28.45	118
159.55	−29.58	133
161.35	−28.31	139

selected results of low temperature susceptibilities are shown in **Figure 8**. As for the remanence measurements, most samples show a strong Verwey transition characterized by a sharp increase in susceptibility starting around 115–120 K. However, samples belonging to the interval 146.08–148.17 m depth have two distinct Verwey temperatures. For all the samples outside this range only one peak with varying width can be clearly identified (see **Figure 8**).

In order to check the stability of the two Verwey transitions toward heating, the magnetic susceptibility of three samples (148.02, 148.08, and 148.15) was monitored during a four steps cycle including: low temperature measurements, heating and cooling from 20 until 630°C in air (samples 148.02 and 148.08) or argon atmosphere (sample 148.15), followed by a new low temperature measurement step (**Figures 9A–C**). No significant difference was found between the low temperature measurements before and after heating, the two T_v show the same characteristics (**Figures 9D–F**). This indicates that the double transition is resistant to heating at least at the time scale of our experiment.

TABLE 2 | Saturation magnetization Ms and susceptibility χ data for TCDP-1 from 130.45 to 163.25 m depth, susceptibility results are obtained using the KLY-3 except data with * obtained using the VSM.

Sample #	Depth (in m)	Ms (in A.m^2/kg)	χ (in 10^{-6} m^3/kg)
130-45-a	130.45	3.097	18.77
130-45-b1	130.45	5.071	37.47
130-45-b2	130.45	4.889	35.26*
130-45-c1	130.45	9.067	91.20
130-45-c2	130.45	45.14	304.72
130-98	130.98		300.33
131-7	131.70	24.73	310.62
134-46	134.46	21.27	138.44
136-46	136.46	16.80	285.76
138-7	138.70	30.15	179.21
142-7-a1	142.70		206.63
142-7-a2	142.70	27.17	221.96
142-7-b	142.70	34.72	247.81
142-7-c	142.70	34.35	144.57
144-9	144.90	61.95	268.65
146-08-c	146.08	39.16	227.63
146-7-a	146.70	0.006	0.014*
146-7-b	146.70	0.006	0.018*
146-7-c	146.70	0.006	0.017*
147-96-a	147.96	42.33	343.00
148-02-a	148.02	8.024	206.98
148-02-b	148.02	48.52	300.25
148-02-c	148.02	47.61	310.09
148-05-a	148.05	22.87	239.80
148-05-e	148.05		267.15
148-08-a	148.08	4.681	29.34
148-08-b	148.08	49.01	398.60
] 148-08-c	148.08	73.90	368.60*
148-08-d	148.08	13.44	106.12*
148-15-a	148.15		47.610
148-15-b	148.15	69.48	310.62
148-15-c	148.15		45.97
] 148-17-b	148.17		145.47
149-48	149.48		3.91
151-59-a	151.59	3.276	22.08*
151-59-b	151.59	2.547	19.06*
151-59-c	151.59	2.018	13.74*
151-59-d	151.59		22.36
151-59-e	151.59		20.76
151-59-f	151.59		16.09
152-86-a	152.86	0.004	0.013*
152-86-b1	152.86	0.006	0.34
152-86-b2	152.86	0.006	0.34
152-86-c	152.86	0.006	0.44
156-52-a	156.52	16.82	130.59*
156-52-b	156.52	17.15	571.11
156-52-c	156.52	14.94	118.56*
159-29-a	159.29	66.86	365.73
159-29-b	159.29	56.88	528.80
159-29-c	159.29	27.44	275.48
159-30-a	159.3	7.33	63.75
159-30-b	159.3	5.48	48.62
159-30-c	159.3	4.60	36.23
159-30-d	159.3	6.09	50.82
159-30-e	159.3	8.50	136.49
159-47-a1	159.47	39.67	330.16
159-47-a2	159.47	53.73	250.21
159-47-b	159.47	31.92	255.40
159-47-c	159.47	52.18	434.57
159-47-d	159.47	37.39	180.09
159-80-a	159.8	3.075	22.95*
159-80-b	159.8	61.59	346.82
159-80-c	159.8	31.39	254.09
159-80-d	159.8	54.85	364.84
163-25-a	163.25	28.04	191.89
163-25-b	163.25		81.07
163-25-c	163.25		113.06

(Continued)

Discussion

Iron Oxides Composition

Except for samples 146.70 and 152.86, the strong Verwey transition found in all samples attests to the ubiquitous presence of magnetite throughout the studied stratigraphic section. To investigate this further, the relation between Ms and the concentration and type of iron oxides (magnetite vs hematite) is used. Pure magnetite has Ms = 92 A.m^2/kg whereas pure hematite has Ms = 0.4 Am^2/kg (e.g., O'Reilly, 1984). Thus, all values above 0.4 Am^2/kg clearly indicate that magnetite is present (in addition to possible hematite). The Ms results (**Table 2** and **Figure 10A**) show that magnetite is widespread in all samples, including jasper layers, as attested by values in the 3–10 Am^2/kg range. Unsurprisingly, the highest Ms values were recorded in BIF layers (Ms between 9 and 74 Am^2/kg, **Table 2**). Such high values indicate that in some ssamples magnetite can represent up to 80% of the sample mass.

The two samples 146.70 and 152.86 displaying the lowest Ms and χ values are associated with the absence of Verwey transition and correspond to volcanoclastic layers (**Figures 10B,C**). SEM observations indicate that iron oxides within these layers have a high titanium content. No magnetite is reported in these layers.

The Two Verwey Transitions

The high temperature (∼120K) Verwey transition is characteristic of a pure, nearly stoichiometric population of magnetite, while the low temperature (∼105K) Verwey transition is attributed to non-stoichiometric magnetite (Moskowitz, 1993). Non-stoichiometry can be due to partial oxidation and/or partial substitution within crystals. The 146.08–148.17 m depth interval is characterized by two populations of both stoichiometric and -non-stoichiometric magnetite (**Figures 8**, **10D**). This unique

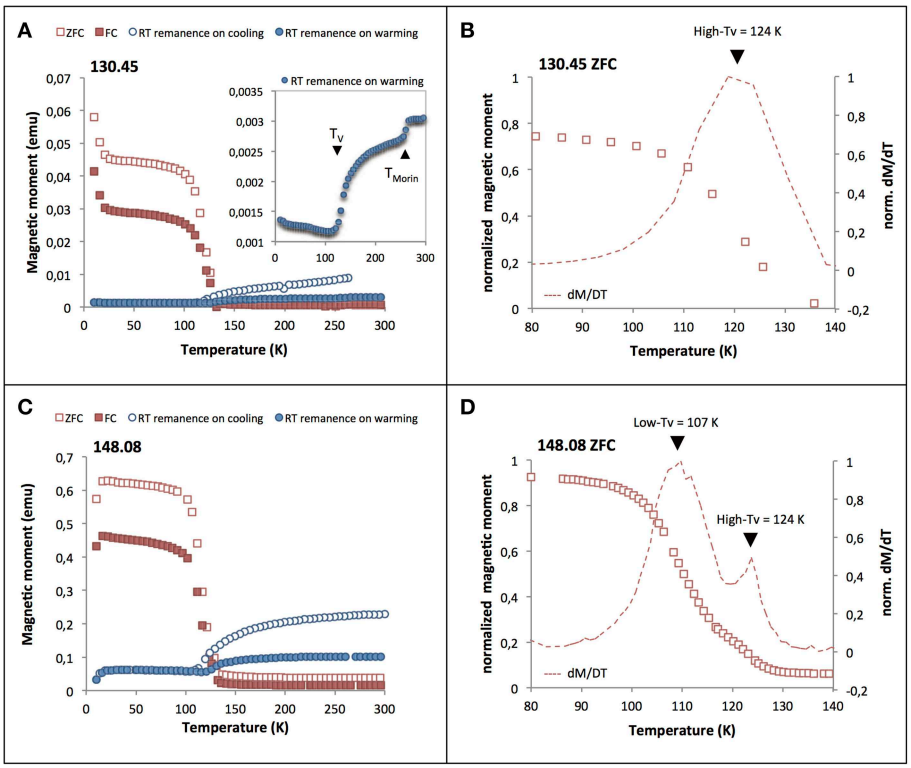

FIGURE 6 | Low-temperature remanence cycles of 130.45 (A) and 148.08 (C) samples. The inset in **(A)** shows the RT remanence measurement with the Morin transition of hematite around 260 K. **(B,D)**: ZFC curves and corresponding first derivative normalized to maximum value. ZFC measurement has been performed with a 1 K step for 148.08. Arrows show peaks in derivative curve corresponding to T_V(130.45: 1 peak corresponding to 1 T_V (High-T_V), 148.08: 2 peaks corresponding to 2 T_V (Low-T_V and High-T_V)).

and specific interval will be referred as the "2 T_v interval" in the following. Such observation is seldom reported in the literature (Liu et al., 2004; Carporzen et al., 2006; Mang and Kontny, 2013) and was interpreted so far as the magnetic signature of two populations with rather different distributions of grain sizes. The favored mechanism proposed for producing the two T_v was a differential oxidation state, the smaller magnetite populations being more prone to oxidation than the larger one (e.g., Mang and Kontny, 2013). Under oxidative conditions magnetite transforms gradually to its oxidized form maghemite. The presence of non-stoichiometric maghemite induces a decrease in Verwey temperature. However, this scenario is unlikely in our samples. Indeed, upon heating in air, maghemite reverses to magnetite (Dunlop and Özdemir, 1997). Thus if a part of the magnetite population in our samples is maghemitized, heating the sample in air or in argon will result in changes in the oxidation state and hence changes in the low-T_v transition. As shown in **Figure 9**, the high temperature susceptibility curves do not reveal significant maghemitization phenomenon (usually characterized by non-reversibility) and more importantly, the two Verwey transitions remained unchanged after heating. The partial oxidation of a part of the magnetite population is thus not our favored hypothesis for the low T_v.

Both low temperature remanence and low temperature susceptibility measurements were performed on two samples showing the double transition. The two selected samples 148.02 and 148.08 show a loss of remanence signal of about 70% and 55 to 75%, respectively (**Figure 6C**), while the increase in susceptibility is on the order of 90% for both samples. Both remanence and susceptibility show an important transition around the 105–110 K. This indicates that the non-stoichiometric magnetite represents a significant amount of the total population in these samples, as shown by the amplitude of the corresponding peak (**Figures 6–9**). The magnetite grain population responsible for the low-T_v is therefore likely to be rather common. Even at the highest magnification (e.g., as in **Figure 2E** or **Figure 4D**) the SEM images did not reveal systematic population of fine grain oxides except in the jasper layers where it is attributed to hematite. Hence, even if sometimes spotted, the smaller oxide grains (typically around 1 μm and less) represent a marginal volume compared to the ubiquitous bulky sub-millimeter magnetite grain and can hardly be responsible for the low-T_v.

Verwey Transitions and Lithology

Different lithologies are represented in the 2 T_v interval (**Figures 10C,D**), suggesting that the double Verwey transition does not depend on lithology. This interval includes indeed laminated cherts (in 146.08, 147.98, 148.08, 148.15, and 148.17), jasper layers (in 148.05 and 148.15) and typical BIF layers, (in 147.96, 147.98, 148.02, and 148.08). Assuming that a specific lithology represents a period during which conditions of

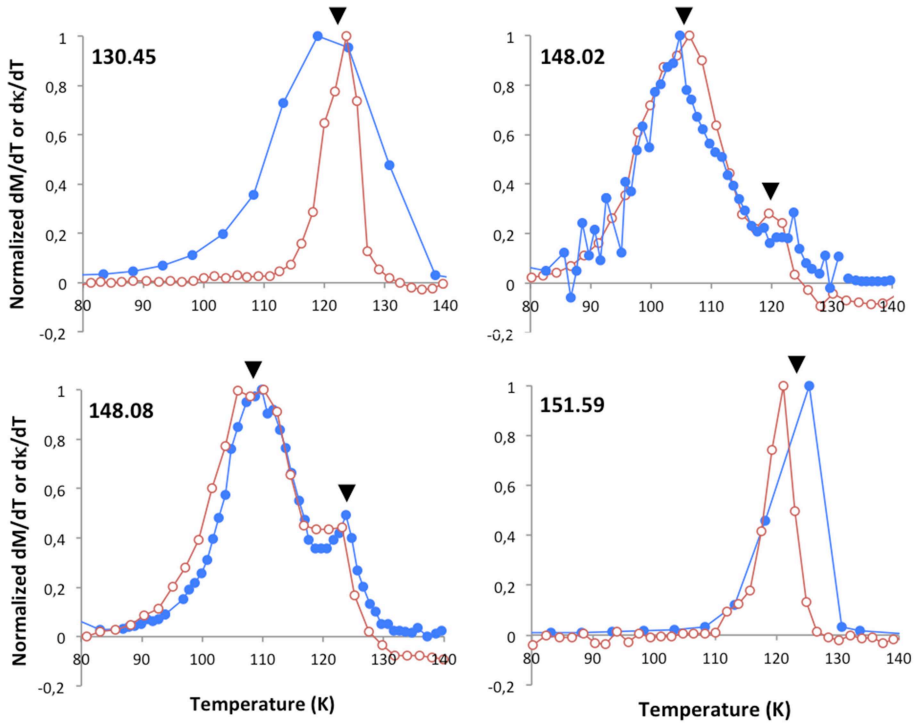

FIGURE 7 | Comparison of normalized derivative curves of low-temperature thermomagnetic measurements for samples 130.45, 148.02, 148.08, and 151.59 (plain circles: ZFC-derivative, empty circles: susceptibility-derivative). Arrows correspond to temperature of Verwey transition: 1 T_V for samples 130.45 and 151.59, 2 T_V for samples 148.02 and 148.08. The noise in 148.02 data is due to electrical problems during MPMS measurements.

precipitation were reasonably stable (Ewers and Morris, 1981) our results indicate that the occurrence of the two magnetite populations is largely independent of precipitation conditions. This phenomenon must then be related to a post-deposition process, pervasive through 2 m of sedimentary stratigraphic interval and having a strong influence on the crystallization of magnetite.

The Effect of Substitution

As we discarded oxidation as the main cause for the lower T_v we must turn to partial subsitution. The effect of cation substitution occurring in octahedral sites in magnetite ($Fe_{3-x}X_xO_4$where X = Ti, Al, Zn,..) has already been studied by several authors (Miyahara, 1972; Kozłowski et al., 1996a,b). A decrease in the Verwey temperature is reported, by about 1° per tenth of a percent metal cation. During SEM observations volcanic particles were reported in some thin, centimeter scale, layers. Titanomagnetite ($Fe_{3-x}Ti_xO_4$) is detected in these layers but always with a broad range of titanium content, clustering around $x = 0.6$. Such high titanium concentration is quite enough to totally suppress the Verwey transition (Kakol et al., 1992; Kozłowski et al., 1996a). The high titanium content and very localized layers where these iron oxides are observed make this phase a poor candidate for the low T_v. Silicon was faintly detected within most magnetite analyzed by EDX during our SEM observations. With brightness and contrast distributed specifically on magnetite, zonation patterns were highlighted in some bulky magnetites. An associated contrast in silicon content is evidenced using EDX elemental mapping. This feature was observed only in samples within the 2 T_v interval (**Figures 4E,F**). Microprobe measurements performed on a thin section at 148.02 m depth confirmed this finding (**Figure 5**) and up to 2% of SiO_2 was measured at some site, silicon was the only cation detected in magnetite in addition to iron. This result is consistent with previous studies showing the presence of silician magnetite in BIFs, in particular from the Dales Gorge Member of the Hamersley Group (Huberty et al., 2012). Using very detailed microprobe analysis but also TEM observations Huberty et al. (2012) reported silician magnetite overgrowths containing up to 3% wt SiO_2 over low-Si magnetite (less than 1 wt% SiO_2). Our microprobe data did not allow the observation of such a marked compositional difference but SEM element map (**Figure 4F**) show textures compatible with Huberty et al. (2012) observations. Silicon represents thus a serious candidate for substitution and could explain the low Verwey transition. An underlying question appears now: why is silician magnetite restricted to a 2 m interval at the top of the Boolgeeda Iron formation?

Environmental Implications

Samples with two Verwey temperatures were reported in the Vredefort impact crater (South Africa) by Carporzen et al. (2006 and 2012) and within the Chesapeake Bay impact structure, (USA) by Mang and Kontny (2013). The authors

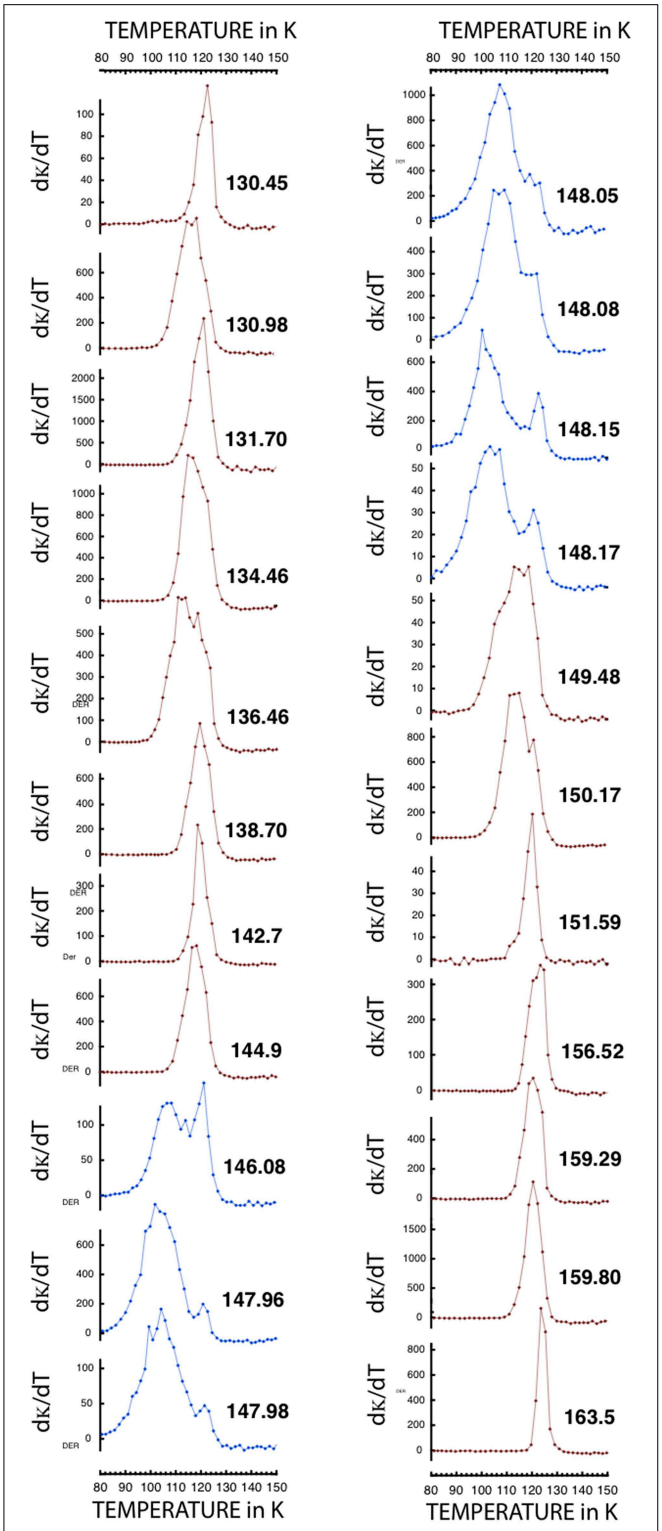

FIGURE 8 | Comparison of derivative curves of representative low-temperature susceptibility curves between 130.45 and 163.5 m depth. Red curves: 1 T_V, blue curves: '2 T_V interval' between 146.08 and 148.17 where 2 peaks are clearly observed.

attributed the low temperature T_v to a post impact population of magnetite with different stoechiometry that crystallized from melt pocket within planar deformation features and alteration halos during the impact event at 2.02 Ga. Vredefort is the oldest documented impact craters on Earth. The impact record for older times is largely incomplete. However, seven spherule layers, attesting for very large impacts on Earth, were found in distinct locations around the Archean-Proterozoic boundary (Simonson et al., 2009). No evidence of impact related features was found in our samples such as planar deformation features or amorphization phenomenon (Stöffler and Langenhorst, 1994; Koeberl, 2006), microfractures or increasing concentrations of siderophile platinum-group elements (Ru, Rh, Pd, Os, Ir, and Pt). Thus, TCDP-1 samples do not support the interpretation of a shock related origin of the two magnetite populations. Alternatively, lightning-induced partial melting and recrystallization of magnetite has been advocated as a potential mechanism for the unusual rock magnetic properties recorded in the Vredefort rocks (Carporzen et al., 2012). As the Boolgeeda section was formed below the storm-wave base and shows no sign of subaerial exposure, it is difficult to envision a 2.4 Ga lightning strike as a possible cause of our peculiar rock magnetite property. More recent lightning strikes are not considered plausible either as the section was buried and samples are taken from cored material.

In modern environments the occurrence of high organic matter intervals (as the sapropels in the Mediterranean area) induces dramatic changes in iron oxides bearing sediments during post depositional processes. Intense bacterial activity fueled by organic matter causes downward migration of reducing fronts, which change the redox state of previously deposited layers. Dissolution of iron oxides is a common phenomenon but in some cases population of small magnetites can also be formed at depth at paleo-oxidation fronts after re-oxygenation of the overlying layers (e.g., Larrasoaña et al., 2003; Drab et al., 2015). In these layers the occurrence of magnetite is thus in relation with microbiological cycles.

A biological origin of magnetite in BIFs is strongly suggested based on modeling of the iron cycle (Konhauser et al., 2005; Koehler et al., 2010), iron isotope composition (Johnson et al., 2003) and experimental data (Li et al., 2013). Following Huberty et al. (2012) the occurrence of silician magnetite is linked to excess in organic carbon. Silician magnetite may thus be an interesting potential biomarker. Within the 2 T_v layer, and immediately below, irregular peloids organized in dome-shaped structures and locally recrystallized are observed (**Figure 10C**). These sedimentary structures are interpreted as hallmark of microbial activities. In addition we observed some small scale variability in TOC and $\delta^{13}C_{org}$ along the section (**Figures 10E,F**), these variations are probably related to depositional conditions. However, within the 2 m interval where the two populations of magnetite are found, a higher bulk TOC value, which clearly stands out from the range of other data, is measured as well as rather low $\delta^{13}C_{org}$ values (**Figures 10E,F**). These observations

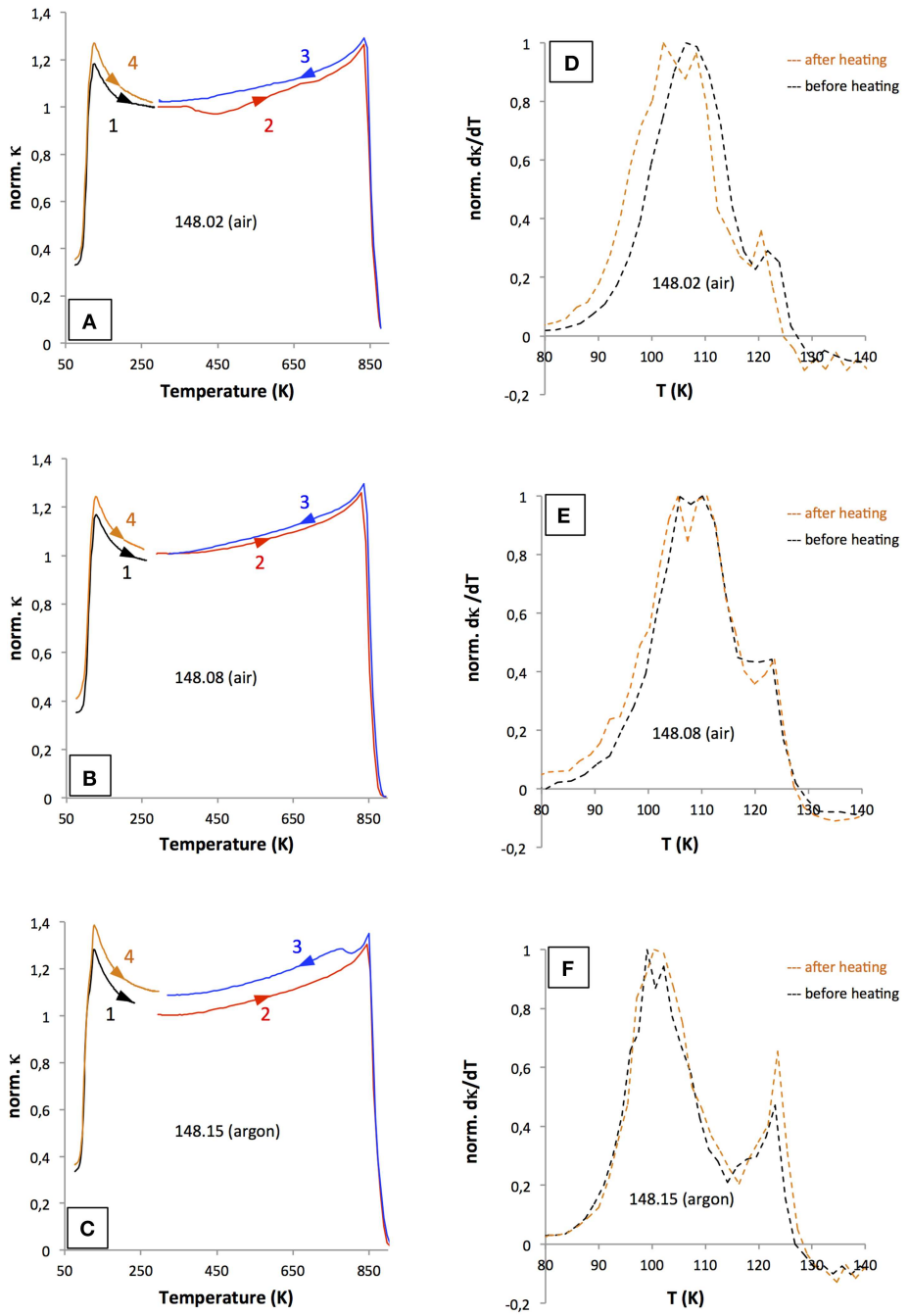

FIGURE 9 | Temperature dependent susceptibility for 148.02 (A), 148.08 (B), and (C) 148.15 experiments performed in air or in argon (data normalized to the room temperature value before heating). Step 1: low temperature measurement from 77 K to RT, step 2: heating from RT to 900 K, step 3: cooling from 900 K to RT and step 4: repeated low temperature measurement, **(D–F)** are the corresponding derivative curves for steps 1 and 4.

can be interpreted as indicating both a more productive and hence reducing depositional environments. Despite the absence of a large scale trend the small-scale extreme variations observed in TOC and $\delta^{13}C_{org}$ in the 2 T_v interval as well as the observation of dome-shaped peloids are interpreted as indicators of an enhancement in microbial activity in the depositional environment around 148 m depth. Our results suggest that crystallization of silician magnetite, whether it occurs immediately post deposition or at a latter stage, is controlled by organic carbon.

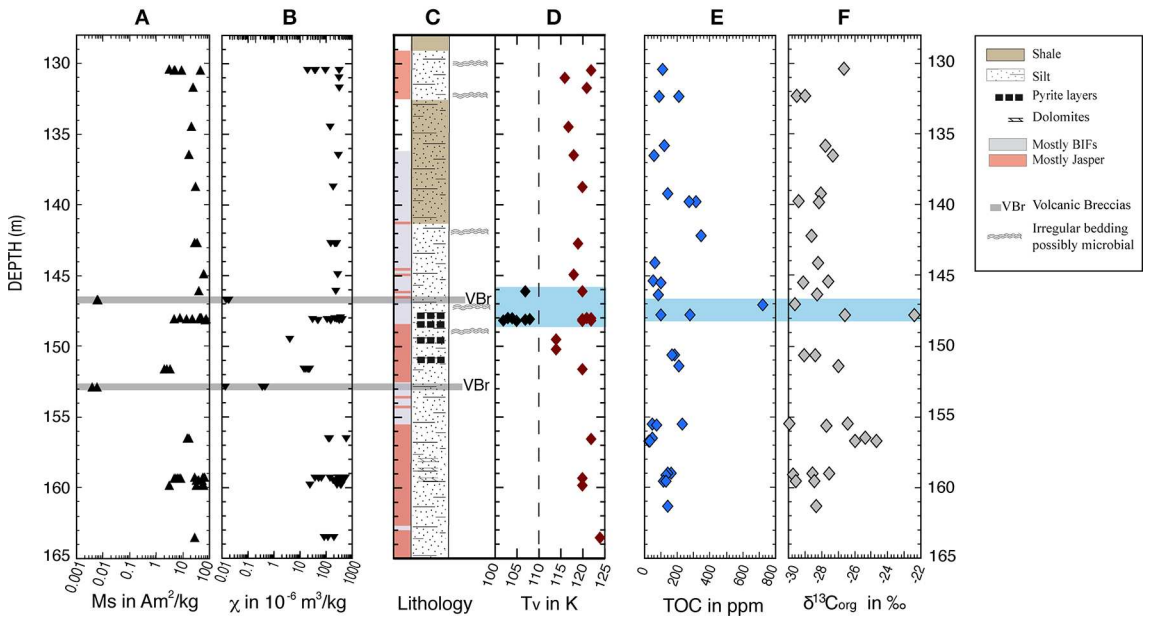

FIGURE 10 | Magnetic parameters, simplified lithology, TOC and $\delta^{13}C_{org}$ results and as a function of depth: (A) saturation magnetization Ms; (B) Mass normalized susceptibility; (C) lithology; (D) Verwey Temperature; (E) Total Organic Carbon (TOC) and (F) $\delta^{13}C_{org}$. Gray area in (A–C) indicates volcanic breccias; blue area in (D) underlines the two T_V interval and anomalous TOC and $\delta^{13}C_{org}$ in (E,F).

Conclusions

The magnetic mineralogy of a 35 m section composed mainly of BIF and jasper layers at the top of the Boolgeeda Iron Formation and onset of the GOE was studied. Magnetite is ubiquitous in the section, even in the hematite-rich jasper layers. The occurrence of two Verwey temperatures, within a 2 m high interval, indicates that two distinct magnetite populations with different stoichiometry coexist. Silician magnetite is clearly observed by SEM and confirmed by microprobe analyses. Peculiar sedimentary structures and higher TOC values suggest more important organic matter deposition and intense microbial activity at the same location. On the basis of these observations we propose that the occurrence of a secondary silicon-rich magnetite population is responsible for the low Verwey transition temperature and that the crystallization of this phase could be linked to biological activity. Although additional experimental studies under controlled conditions are required to test this hypothesis, at this stage, however, low temperature magnetic measurements appear to be a valuable tool to unravel the occurrence of microbial activity in banded iron formations.

Acknowledgments

We are grateful for the detailed and constructive comments provided by the two reviewers and fast handling of the paper by the editors. We thank Mike Jackson and France Lagroix for interesting discussions about the "double Verwey transition," Stephan Borensztajn for help with the SEM analyses, Marc Quintin for making the thin sections and the Institut de Physique du Globe de Paris (IPGP), the Geological Survey of Western Australia (GSWA), for supporting the Turee Creek Drilling Project. This work was supported by the Labex UnivEarths program of Sorbonne Paris Cité (ANR-10-LABX-0023 and ANR-11-IDEX-0005-02). This is IPGP contribution 3624.

References

Ahn, J. H., and Buseck, P. R. (1990). Hematite nanospheres of possible colloidal origin from a Precambrian banded iron formation. *Science* 250, 111–113. doi: 10.1126/science.250.4977.111

Barley, M. E., Pickard, A. L., and Sylvester, P. J. (1997). Emplacement of a large igneous province as a possible cause of banded iron formation 2.45 billion years ago. *Nature* 385, 55–58. doi: 10.1038/385055a0

Bekker, A., Slack, J. F., Planavsky, N., KrapeŽ, B., Hofmann, A., Konhauser, K. O., et al. (2010). Iron formation: the sedimentary product of a complex interplay among mantle, tectonic, oceanic, and biospheric processes. *Econ. Geol.* 105, 467–508. doi: 10.2113/gsecongeo.105.3.467

Brachfeld, S. A., Banerjee, S. K., Guyodo, Y., and Acton, G. D. (2002). A 13 200 year history of century to millennial-scale paleoenvironmental change magnetically recorded in the Palmer Deep, western Antarctic Peninsula. *Earth Planet. Sci. Lett.* 194, 311–326. doi: 10.1016/S0012-821X(01)00567-2

Braterman, P. S., Cairns-Smith, A. G., and Sloper, R. W. (1983). Photo-oxidation of hydrated Fe^{2+}; significance for banded iron formations. *Nature* 303, 163–164. doi: 10.1038/303163a0

Carporzen, L., Gilder, S. A., and Hart, R. J. (2006). Origin and implications of two Verwey transitions in the basement rocks of the Vredefort meteorite crater, South Africa. *Earth Planet. Sci. Lett.* 251, 305–317. doi: 10.1016/j.epsl.2006.09.013

Carporzen, L., Weiss, B. P., Gilder, S. A., Pommier, A., and Hart, R. J. (2012). Lightning remagnetization of the Vredefort impact crater: no evidence for impact-generated magnetic fields. *J. Geophys. Res. Planets* 117:E01007. doi: 10.1029/2011JE003919

Chamalaun, F. H., and Dempsey, C. E. (1978). Palaeomagnetism of the Gawler Range Volcanics and implications for the genesis of the middleback hematite orebodies. *J. Geol. Soc. Aust.* 25, 255–265. doi: 10.1080/00167617808729034

Cloud, P. (1973). Paleoecological Significance of the Banded Iron-Formation. *Econ. Geol.* 68, 1135–1143. doi: 10.2113/gsecongeo.68.7.1135

Drab, L., Carlut, J., Hubert-Ferrari, A., Martinez, P., LePoint, G., and El Ouahabi, M. (2015). Paleomagnetic and geochemical record from cores from the Sea of Marmara, Turkey: age constraints and implications of sapropelic deposition on early diagenesis. *Mar. Geol.* 360, 40–54. doi: 10.1016/j.margeo.2014.12.002

Dunlop, D., and Özdemir, Ö. (1997). *Rock Magnetism Fundamentals and Frontiers* (New York, London, Cambridge: Cambridge University Press), 573p.

Ewers, W. E., and Morris, R. C. (1981). Studies of the Dales Gorge Member of the Brockman Iron Formation, Western Australia. *Econ. Geol.* 76, 1929–1953. doi: 10.2113/gsecongeo.76.7.1929

Hickman, A. H., and Van Kranendonk, M. J. (2012). Early Earth evolution: evidence from the 3.5-1.8 Ga geological history of the Pilbara region of Western Australia. *Episodes* 35, 283.

Huberty, J. M., Konishi, H., Heck, P. R., Fournelle, J. H., Valley, J. W., and Xu, H. (2012). Silician magnetite from the Dales Gorge Member of the Brockman Iron Formation, Hamersley Group, Western Australia. *Am. Mineral.* 97, 26–37. doi: 10.2138/am.2012.3864

Jackson, M., Moskowitz, B., and Bowles, J. (2011). The magnetite Verwey transition. *IRM Q.* 20, 1–11.

Johnson, C. M., Beard, B. L., Beukes, N. J., Klein, C., and O'Leary, J. M. (2003). Ancient geochemical cycling in the Earth as inferred from Fe isotope studies of banded iron formations from the Transvaal Craton. *Contrib. Mineral. Petrol.* 144, 523–547. doi: 10.1007/s00410-002-0418-x

Ka,kol, Z., Sabol, J., Stickler, J., and Honig, J. M. (1992). Effect of low-level titanium(IV) doping on the resistivity of magnetite near the Verwey transition. *Phys. Rev. B* 46, 1975–1978. doi: 10.1103/PhysRevB.46.1975

Kappler, A., Pasquero, C., Konhauser, K. O., and Newman, D. K. (2005). Deposition of banded iron formations by anoxygenic phototrophic Fe(II)-oxidizing bacteria. *Geology* 33, 865–868. doi: 10.1130/G21658.1

Koeberl, C. (2006). The record of impact processes on the early Earth: a review of the first 2.5 billion years. *Geol. Soc. Am. Spec. Pap.* 405, 1–22. doi: 10.1130/2006.2405(01)

Koehler, I., Konhauser, K., and Kappler, A. (2010). "Role of microorganisms in banded iron formations," in *Geomicrobiology: Molecular and Environmental Perspective*, eds L. L. Barton, M. Mandl, and A. Loy (Springer), 309–324. Available online at: http://dx.doi.org/10.1007/978-90-481-9204-5_14

Konhauser, K., Newman, D., and Kappler, A. (2005). The potential significance of microbial Fe (III) reduction during deposition of Precambrian banded iron formations. *Geobiology* 3, 167–177. doi: 10.1111/j.1472-4669.2005.00055.x

Konhauser, K. O., Amskold, L., Lalonde, S. V., Posth, N. R., Kappler, A., and Anbar, A. (2007). Decoupling photochemical Fe(II) oxidation from shallow-water BIF deposition. *Earth Planet. Sci. Lett.* 258, 87–100. doi: 10.1016/j.epsl.2007.03.026

Konhauser, K. O., Hamade, T., Raiswell, R., Morris, R. C., Ferris, F. G., Southam, G., et al. (2002). Could bacteria have formed the Precambrian banded iron formations? *Geology* 30, 1079–1082. doi: 10.1130/0091-7613(2002)030<1079:CBHFTP>2.0.CO;2

Kozłowski, A., Metcalf, P., Kąkol, Z., and Honig, J. M. (1996a). Electrical and magnetic properties of Fe3-zAlzO4(z <0.06). *Phys. Rev. B* 53, 15113–15118. doi: 10.1103/PhysRevB.53.15113

Kozłowski, A., Metcalf, P., Kakol, Z., and Honig, J. M. (1996b). Electrical transport and magnetization measurements of Fe3-zAlzO4, z < 0.06. *J. Magn. Magn. Mater.* 157–158, 415–416. doi: 10.1016/0304-8853(95)01217-6

Larrasoaña, J. C., Roberts, A. P., Stoner, J. S., Richter, C., and Wehausen, R. (2003). A new proxy for bottom-water ventilation in the eastern Mediterranean based on diagenetically controlled magnetic properties of sapropel-bearing sediments. *Palaeogeogr. Palaeoclimatol. Palaeoecol.* 190, 221–242. doi: 10.1016/S0031-0182(02)00607-7

Li, Y.-L., Konhauser, K. O., Cole, D. R., and Phelps, T. J. (2011). Mineral ecophysiological data provide growing evidence for microbial activity in banded-iron formations. *Geology* 39, 707–710. doi: 10.1130/G32003.1

Li, Y.-L., Konhauser, K. O., Kappler, A., and Hao, X.-L. (2013). Experimental low-grade alteration of biogenic magnetite indicates microbial involvement in generation of banded iron formations. *Earth Planet. Sci. Lett.* 361, 229–237. doi: 10.1016/j.epsl.2012.10.025

Liu, Q., Banerjee, S. K., Jackson, M. J., Chen, F., Pan, Y., and Zhu, R. (2004). Determining the climatic boundary between the Chinese loess and palaeosol: evidence from aeolian coarse-grained magnetite. *Geophys. J. Int.* 156, 267–274. doi: 10.1111/j.1365-246X.2003.02148.x

Mang, C., and Kontny, A. (2013). Origin of two Verwey transitions in different generations of magnetite from the Chesapeake Bay impact structure, USA. *J. Geophys. Res. Solid Earth* 118, 2012JB009973. doi: 10.1002/jgrb.50291

Martin, D. M., Li, Z. X., Nemchin, A. A., and Powell, C. M. (1998). A pre-2.2 Ga age for giant hematite ores of the Hamersley Province, Australia? *Econ. Geol.* 93, 1084–1090. doi: 10.2113/gsecongeo.93.7.1084

Miyahara, Y. (1972). Impurity effects on the transition temperature of magnetite. *J. Phys. Soc. Jpn.* 32, 629–634. doi: 10.1143/JPSJ.32.629

Morrish, A. H. (1994). *Canted Antiferromagnetism: Hematite.* Singapore: World Scientific. Available online at: http://www.worldscientific.com/doi/pdf/10.1142/9789812831569_fmatter (Accessed March 3, 2015).

Moskowitz, B. M. (1993). Micromagnetic study of the influence of crystal defects on coercivity in magnetite. *J. Geophys. Res. Solid Earth* 98, 18011–18026. doi: 10.1029/93JB01719

Müller, S. G., KrapeŽ, B., Barley, M. E., and Fletcher, I. R. (2005). Giant iron-ore deposits of the Hamersley province related to the breakup of Paleoproterozoic Australia: New insights from in situ SHRIMP dating of baddeleyite from mafic intrusions. *Geology* 33, 577–580. doi: 10.1130/G21482.1

Muxworthy, A. R., and McClelland, E. (2000). Review of the low-temperature magnetic properties of magnetite from a rock magnetic perspective. *Geophys. J. Int.* 140, 101–114. doi: 10.1046/j.1365-246x.2000.00999.x

Novák, P., Štipánková, H., Englich, J., Kohout, J., and Brabers, V. A. M. (2000). NMR in magnetite below and around the Verwey transition. *Phys. Rev. B* 61, 1256–1260. doi: 10.1103/PhysRevB.61.1256

O'Reilly, W. (1984). *Rock and Mineral Magnetism*. Glasgow: Blackie.

Özdemir, Ö., Dunlop, D. J., and Moskowitz, B. M. (1993). The effect of oxidation on the Verwey transition in magnetite. *Geophys. Res. Lett.* 20, 1671–1674. doi: 10.1029/93GL01483

Pecoits, E., Smith, M. L., Catling, D. C., Philippot, P., Kappler, A., and Konhauser, K. O. (2015). Atmospheric hydrogen peroxide and Eoarchean iron formations. *Geobiology* 13, 1–14. doi: 10.1111/gbi.12116

Schmidt, P. W., and Clark, D. A. (1994). Palaeomagnetism and magnetic anisotropy of Proterozoic banded-iron formations and iron ores of the Hamersley Basin, Western Australia. *Precambrian Res.* 69, 133–155. doi: 10.1016/0301-9268(94)90083-3

Simonson, B. M., McDonald, I., Shukolyukov, A., Koeberl, C., Reimold, W. U., and Lugmair, G. W. (2009). Geochemistry of 2.63–2.49 Ga impact spherule layers and implications for stratigraphic correlations and impact processes. *Precambrian Res.* 175, 51–76. doi: 10.1016/j.precamres.2009.08.004

Smirnov, A. V. (2009). Grain size dependence of low-temperature remanent magnetization in natural and synthetic magnetite: experimental study. *Earth Planets Space* 61, 119–124. doi: 10.1186/BF03352891

Stöffler, D., and Langenhorst, F. (1994). Shock metamorphism of quartz in nature and experiment: I. Basic observation and theory. *Meteoritics* 29, 155–181. doi: 10.1111/j.1945-5100.1994.tb00670.x

Sumita, I., Hatakeyama, T., Yoshihara, A., and Hamano, Y. (2001). Paleomagnetism of late Archean rocks of Hamersley basin, Western Australia and the paleointensity at early Proterozoic. *Phys. Earth Planet. Inter.* 128, 223–241. doi: 10.1016/S0031-9201(01)00288-6

Thomazo, C., Pinti, D. L., Busigny, V., Ader, M., Hashizume, K., and Philippot, P. (2009). Biological activity and the Earth's surface evolution: insights from carbon, sulfur, nitrogen and iron stable isotopes in the rock record. *C. R. Palevol* 8, 665–678. doi: 10.1016/j.crpv.2009.02.003

Tompkins, L. A., and Cowan, D. R. (2001). Opaque mineralogy and magnetic properties of selected banded iron-formations, Hamersley Basin, Western Australia. *Aust. J. Earth Sci.* 48, 427–437. doi: 10.1046/j.1440-0952.2001.00869.x

Trendall, A. (1979). A revision of the Mount Bruce Supergroup. *Geol. Surv. West. Aust. Annu. Rep.* 1978, 63–71.

Trendall, A. F., and Blockey, J. (1970). *The Iron Formations of the Precambrian Hamersley Group, Western Australia with Special Reference to the Associated Crocidolite*. Perth, WA: Geological Survey of Western Australia.

Trendall, A. F., Compston, W., Nelson, D. R., De Laeter, J. R., and Bennett, V. C. (2004). SHRIMP zircon ages constraining the depositional chronology of the Hamersley Group, Western Australia. *Aust. J. Earth Sci.* 51, 621–644. doi: 10.1111/j.1400-0952.2004.01082.x

van Kranendonk, M. J., Mazumder, R., Yamaguchi, K. E., Yamada, K., and Ikehara, M. (2015). Sedimentology of the Paleoproterozoic Kungarra Formation, Turee Creek Group, Western Australia: a conformable record of the transition from early to modern Earth. *Precambrian Res.* 256, 314–343. doi: 10.1016/j.precamres.2014.09.015

Verwey, E. J., Haayman, P. W., and Romeijn, F. C. (1947). Physical properties and cation arrangement of oxides with spinel Structures II. *Electron. Conductivity. J. Chem. Phys.* 15, 181–187. doi: 10.1063/1.1746466

Yamaguchi, K. (2002). *Geochemistry of Archean–Paleoproterozoic Black Shales: The Early Evolution of the Atmosphere, Oceans, and Biosphere*. Available online at: https://etda.libraries.psu.edu/paper/5920/1187(Accessed April 11, 2015).

Conflict of Interest Statement: The authors declare that the research was conducted in the absence of any commercial or financial relationships that could be construed as a potential conflict of interest.

frontiers in Earth Science

ORIGINAL RESEARCH
published: 01 September 2015
doi: 10.3389/feart.2015.00044

Is the Neoproterozoic oxygen burst a supercontinent legacy?

Melina Macouin[1]*, *Damien Roques*[1], *Sonia Rousse*[1], *Jérôme Ganne*[1], *Yoann Denèle*[1] *and Ricardo I. F. Trindade*[2]

[1] *Géosciences Environnement Toulouse, Centre National de Recherche Scientifique, UMR 5563, UR234, Université de Toulouse, Toulouse, France,* [2] *Departamento de Geofísica, Instituto de Astronomia, Geofísica e Ciências Atmosféricas, Universidade de São Paulo, São Paulo, Brazil*

The Neoproterozoic (1000–542 mol.yr ago) witnessed the dawn of Earth as we know it with modern-style plate tectonics, high levels of O_2 in atmosphere and oceans and a thriving fauna. Yet, the processes leading to the fully oxygenation of the external envelopes, its exact timing and its link with the inner workings of the planet remain poorly understood. In some ways, it is a "chicken and egg" question: did the Neoproterozoic Oxygenation Event (NOE) cause life blooming, low-latitudes glaciations, and perturbations in geochemical cycles or is it a consequence of these phenomena? Here, we suggest that the NOE may have been triggered by multi-million years oxic volcanic emissions along a protracted period at the end of the Neoproterozoic when continents were assembled in the Rodinia supercontinent. We report a very oxidized magma source at the upper mantle beneath a ring of subducting margins around Rodinia, and detail here the evidence at the margin of the Arabian shield. We investigate the 780 Ma Biotite and Pink granites and associated rocks of the Socotra Island with rock magnetic and petrographic methods. Magnetic susceptibility and isothermal remanent magnetization acquisitions show that, in these granites, both magnetite and hematite are present. Hematite subdivides magnetite grains into small grains. Magnetite and hematite are found to be primary, and formed at the early magmatic evolution of the granite at very high oxygen fugacity. Massive degassing of these oxidized magmas would reduce the sink for oxygen, and consequently contribute to its rise in the atmosphere with a net O_2 flux of at least 2.25×10^7 Tmol. Our conceptual model provides a deep Earth link to the NOE and implies the oxygenation burst has occurred earlier than previously envisaged, paving the way for later changes in the outer envelopes of the planet epitomized on the extreme Neoproterozoic glaciations and the appearance of the first animals.

Keywords: rock magnetism, Neoproterozoic oxygenation event, hematite-magnetite buffer, Rodinia, Socotra

OPEN ACCESS

Edited by:
Eric Font,
University of Lisbon, Portugal

Reviewed by:
Alexandra Abrajevitch,
Institute of Tectonics and Geophysics, Russia
Qingsong Liu,
Chinese Academy of Sciences, China

***Correspondence:**
Melina Macouin,
Géosciences Environnement Toulouse, Centre National de Recherche Scientifique, UMR 5563, Université de Toulouse, 14 avenue E. Belin 31400 Toulouse, France
melina.macouin@get.obs-mip.fr

Specialty section:
This article was submitted to Geomagnetism and Paleomagnetism, a section of the journal Frontiers in Earth Science

Received: *27 January 2015*
Accepted: *24 July 2015*
Published: *01 September 2015*

Citation:
Macouin M, Roques D, Rousse S, Ganne J, Denèle Y and Trindade RIF (2015) Is the Neoproterozoic oxygen burst a supercontinent legacy? Front. Earth Sci. 3:44. doi: 10.3389/feart.2015.00044

Introduction

The Neoproterozoic Oxygenation Event (NOE) (Och and Shields-Zhou, 2012) (**Figure 1A**) marks a turning point in the early Earth's history after which atmospheric free oxygen has reached the Present Atmospheric Level (PAL) as indicated by several different geochemical proxies (e.g., Canfield et al., 2007; Och and Shields-Zhou, 2012; Sahoo et al., 2012; Reinhard et al., 2013; Lyons et al., 2014). But the mechanism leading to the full oxygenation of Earth's external envelopes, its exact timing (Baldwin et al., 2013) and its link with the inner workings of the planet remain poorly

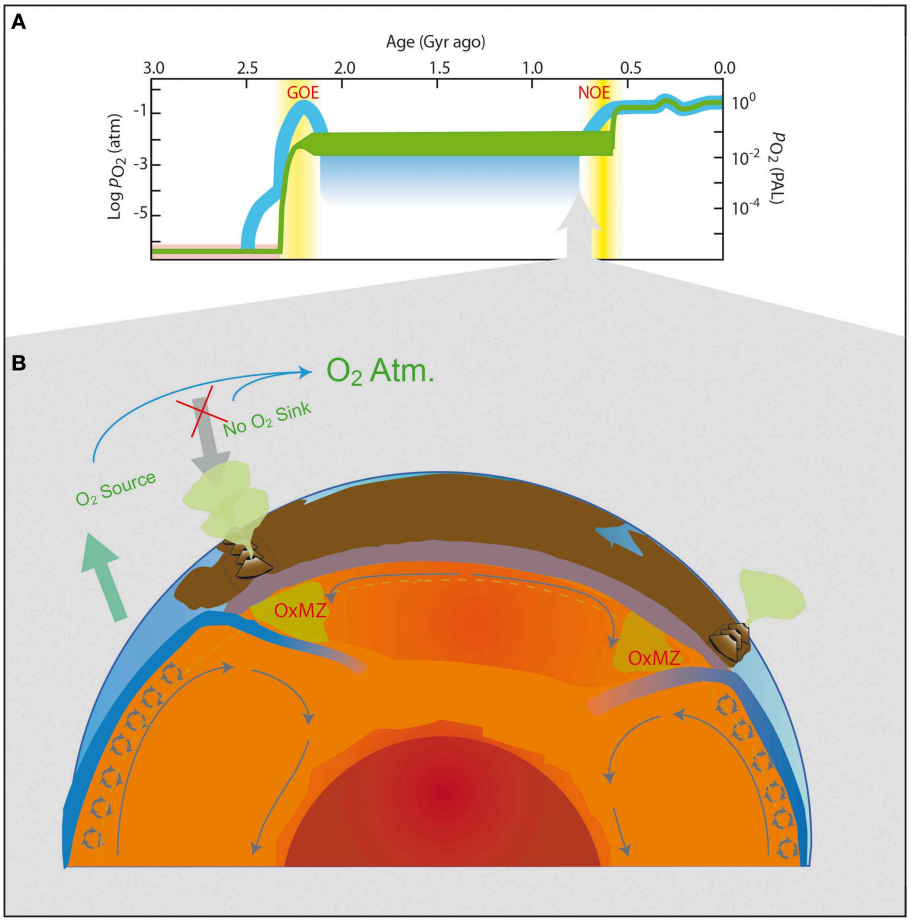

FIGURE 1 | (A) Evolution of Earth's atmospheric oxygen content between 3.5 Ga and present (from Lyons et al., 2014). PO_2 is the atmospheric partial pressure of O_2 and PAL is the present atmospheric level. The green and blue curves depict a two-step evolution of atmospheric evolution (Kump, 2008) and a recent model (Lyons et al., 2014), respectively. In yellow are the classical time windows for the GOE (Great Oxydation Event) and NOE (Neoproterozoic Oxydation Event). **(B)** Model of Cryogenian Oxygen cycle and subduction zones in the frame of Rodinia. Green zones highlight the suspected hot and oxidized magma zone (OxMZ) under subductions.

understood. In some ways, it is a "chicken and egg" problem: did the NOE cause life blooming (Och and Shields-Zhou, 2012), low-latitude glaciations and perturbations in geochemical cycles or is it a consequence of these phenomena (Lenton et al., 2014)? But what if the Neoproterozoic oxygen burst was in fact a supercontinent legacy? Some authors have evoked the possible role of changes in global geodynamics on the increase of the oxygen content in atmosphere and oceans (Kump et al., 2001; Gaillard et al., 2011 and see a review in Kasting, 2013) but the topic remains poorly explored.

Special geodynamical conditions prevailed during most of the Neoproterozoic. By the time the continents were assembled for the first time into a supercontinent the size of Pangea (Hawkesworth et al., 2013). The Rodinia supercontinent (1000–720 Ma) was the most long-lived supercontinent in Earth's history (Ernst et al., 2013; Li et al., 2013) (**Figure 2**). It was surrounded by subduction zones (Li et al., 2013) whose relics are now sparsely dispersed around the world as fossil magmatic arcs and ophiolites. Subduction-related magmatism likely surpassed in volume the large magmatic activity of collision and dispersal of continental fragments, well-preserved in the zircon record for this time period (Hawkesworth et al., 2013), thus corresponding to a peak in volcanic degassing between 850 and 750 millions of years ago.

Here, we explore the role of subductions and associated volcanic degassing on the redox state of the upper mantle, atmosphere and oceans at Rodinian times by investigating rock magnetic properties of the 840–780 Ma old rocks of the Socotra Island.

A New Model for the Oxygenation of the Neoproterozoic Atmosphere?

Nowadays, and probably, since the Archean, the redox state of the mantle is considered to be around the Fayalite–Magnetite–Quartz (FMQ) buffer as exemplified by modern MORB's fO_2-values (Δ FMQ +0.5) (Frost and McCammon, 2008). Deeper into the mantle, spinel peridotites display a larger range

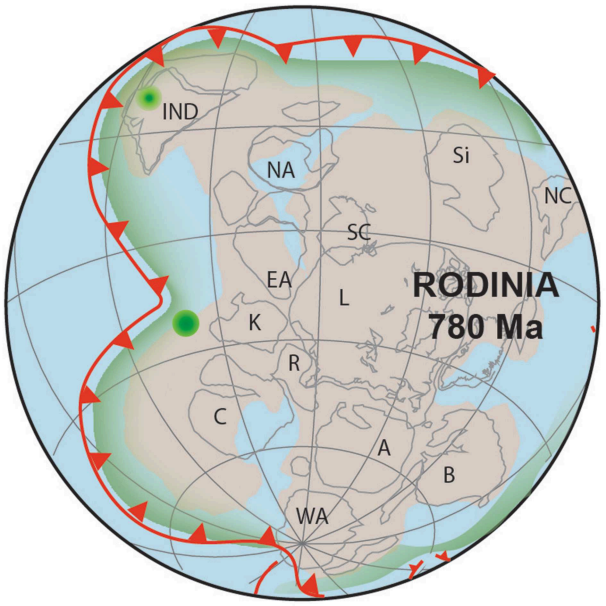

FIGURE 2 | Rodinia paleogeography model around 780 Ma (adapted and modified from Li et al. 2013 and using Paleomac software, Cogne, 2003). In red is the extension of presumed subductions around the supercontinent. Green zones highlight the suspected hot and oxidized magma zone under subductions. Green dots represent indian (ind) and arabic (soc) highly oxidized rocks related to subductions. Craton/terrane names abbreviations: IND, India; A, Amazonia; Si, Siberia; SC, South China; NA, Northern Australia; EA, East Antarctica; L, Laurentia; K, Kalahari; R, Rio de Plata; C, Congo; B, Baltica; WA, West-Africa; NC, North China.

of fO_2-values between ΔFMQ −2 and +2. Given the long lifetime of Rodinia, the insulation effect due to the presence of a supercontinent must have been important (Grigne and Labrosse, 2001), increasing the temperature of the mantle beneath the continent (Lenardic et al., 2011). Furthermore, when a supercontinent is surrounded by subduction margins, this heating effect is enhanced since subducting plates prevent lateral thermal mixing of the mantle as shown by numerical and analogical experiments (Lenardic et al., 2011). Another consequence of the global temperature increase below the supercontinent is a possible enhancement of the large-scale convection by the reduced viscosity of the mantle, while small-scale convection will be almost absent preventing efficient mixing (Samuel and King, 2014). This would result in a hot and poorly mixed mantle beneath Rodinia. For the subduction zones, this would mean an increase in the melting of the oxidized rocks of the slab, resulting in a large zone of oxidized magmas, possibly further enhanced by thick arcs (Chiaradia, 2014), around the edges of Rodinia.

A large reservoir of oxidized magma beneath the fringe of Rodinia probably resulted in large emissions of oxidized volcanic gases (Burgisser and Scaillet, 2007) into the ocean-atmosphere system with an impact on the balance between sources and sinks for the free oxygen in the atmosphere. Indeed, the oxidation of reduced volcanic gases is one of the major sinks for various atmospheric oxidants, notably oxygen (Kump et al., 2001; Catling and Claire, 2005; Kasting, 2013) (**Figure 1B**). Today, with a total emission of 1.5 $Tmol.yr^{-1}$, the volcanic sink for O_2 is estimated to consume around 25% of the O_2 generated by photosynthesis and subsequent organic carbon burial (Kump et al., 2001).

Below we detail the petrographic and magnetic evidence for these Neoproterozoic highly oxidized magma in Socotra Island (Yemen).

Geological Setting

In order to test for the oxidation state of magmas across subduction zones surrounding Rodinia, and investigate their eventual role on the rise of atmospheric oxygen, we studied the Neoproterozoic basement outcropping at the Socotra Island (Yemen) in the Arabic peninsula. The Socotra Island belongs to the southern rifted margin of the Gulf of Aden (**Figure 3**), extending the tip of Somalia to the ENE (**Figure 3**). The island is about 135 km from east to west and 45 km wide from north to south and lies about 250 km of Somalian coast (longitude: 53′19° and 54′33° E; latitude: 12′18° and 12′42° N). Most of the island is covered by Mesozoic to Cenozoic pre- to syn-rift sedimentary rock successions affected by tilted-block tectonics linked to the Gulf of Aden opening (Leroy et al., 2012; Ahmed et al., 2014). Three main basement outcrops can be observed in the island (Denéle et al., 2012) (**Figure 3**), which corresponds to three basement highs located at the head of tilted blocks. To the west the Qalansya and Sherubrub areas represents respectively, 65 and 50 km^2 of basement outcrop and to the east the Mont-Haggier basement outcrop represents 580 km^2.

The basement of the Socotra Island displays a variety of plutonic, volcanic and metamorphic rocks formed in an active margin between 840 and 780 Ma (Denéle et al., 2012). A voluminous highly potassic calc-alkaline granitic magmatism, comprising the Biotite granite and the Pink Haggier granite plutons, were emplaced in an Andean-type arc setting at 790 Ma (Denéle et al., 2012). Slightly before, mafic to intermediate intrusions as vertical sheets, a kilometer-scale gabbro laccolith, mafic dike swarms and lavas with a depleted arc signature were emplaced in the upper crust of the arc. Together, this assemblage represents a long-lived subduction-associated magmatism spanning up to 50 Ma.

Methods

Neoproterozoic basement rocks of Socotra were sampled with a gasoline-powered drill during a field trip realized in 2009–2010. The Biotite and Pink granites and the Haggier layered gabbro were sampled in the Haggier Mount domain. The geological map of Socotra shows the location of the analyzed samples.

Forty-nine samples were selected for magnetic mineralogy studies, 25 from the Biotite granite and others from the Pink Haggier granite, the Layered Gabbros and from Mafic to Intermediate Plutonic Sheets. Eight thin sections were analyzed with scanning electron microscope (SEM) and reflected light microscopy (Nikon Eclipse LV100POL). SEM observations were performed with a JEOL instrument (JSM-6360LV) at the GET laboratory (Toulouse, France) operating at 20 kV with

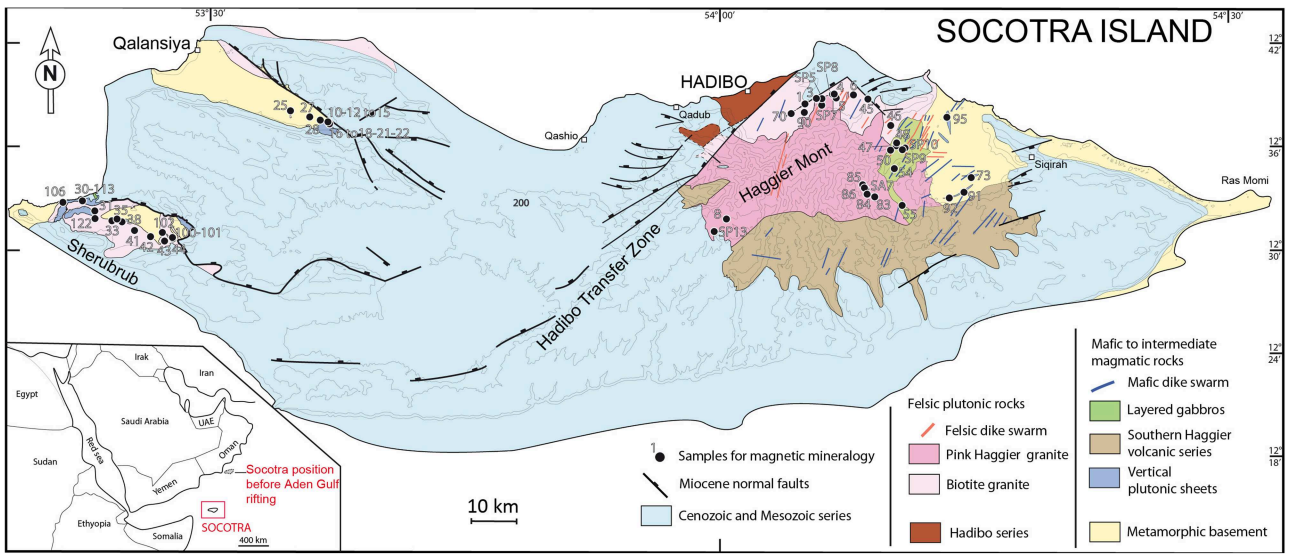

FIGURE 3 | Geological map of Socotra (modified from Denéle et al., 2012), locating the different samples accross the Neoproterozoic basement.

an Electron Dispersive System (EDS) that allows a punctual qualitative characterization of the chemical composition.

Magnetic measurements consisted of thermomagnetic curves, isothermal remanent magnetization (IRM) acquisition curves, hysteresis loops, and first-order reversal curves (FORC) diagrams. Temperature dependent magnetic susceptibility curves from room temperature up to 700°C were obtained with a KLY2-CS2 (AGICO) at the GET laboratory on 12 powdered samples. IRM acquisitions (Kruiver et al., 2001; Heslop et al., 2002), hysteresis loops and first-order reversal curves (FORC) diagrams (Roberts et al., 2000; Harrison and Feinberg, 2008) were made using a Princeton Measurements Corporation Vibrating Sample Magnetometer (VSM: Micromag Model 3900) at the IPGP laboratory. IRM acquisition curves were performed non-linearly (with 150 points) up to +1.5 T. IRM acquisition curves were analyzed using the excel spreadsheet of Kruiver et al. (2001) based on cumulative log Gaussian analysis (see also Heslop et al., 2002). The magnetic components are characterized by saturation isothermal remanent magnetization (SIRM), a parameter that is proportional to the content of the mineral in a sample, the peak field ($B_{1/2}$) at which half of the SIRM is reached, and the dispersion (DP) of its corresponding cumulative log-normal distribution (Kruiver et al., 2001). Magnetic hysteresis loops were measured on small size rectangular samples (<5 mm in length; max. field = 1.0 T). Hysteresis loops are corrected for the dia/paramagnetic effect and normalized by mass. There are four major parameters obtained: Ms, saturation magnetization; Mrs, saturation remanent magnetization; Hc, coercive force or coercivity; Hcr, remanent coercivity (which is determined by operating back-field DC demagnetization up to -1.0 T after IRM acquisitions had been imparted up to +1.0 T). FORC diagrams were realized to model magnetic mixtures and magnetostatic interactions. FORC diagrams were realized to better constrain mixtures and magnetostatic interactions. For each formation, 80–100 FORCs were measured with an averaging time of 100 ms and a waiting time before successive measurements of 1 s. FORC diagrams were processed using the FORCinel software (Harrison and Feinberg, 2008) with an average smoothing factor (SF) of four (see Roberts et al., 2000) after correction of the paramagnetic slope. Paleogeographic map was drawn with paleomac software (Cogne, 2003).

Results

Determination of Magnetic Mineralogy

Magnetite and hematite are the main magnetic minerals in the samples as revealed by temperature dependent magnetic susceptibility curves (**Figure 4**) ($n = 12$). However, the presence and relative contribution of hematite are difficult to define on these experiments (they are represented by a second slight susceptibility decay above 580°C) because magnetite has a much higher intrinsic magnetic susceptibility (Kletetschka et al., 2000).

Magnetite also dominates the IRM acquisition curves (more than 80% of total magnetization) (**Figure 5C**). Magnetite can be divided into two populations, with variable proportions from one sample to another, identified by a statistical analysis (Kruiver et al., 2001). The more abundant magnetite population (called high coercivity magnetite component = C_{HMag}) represents between 43 and 97% of the magnetization (**Table S1** in Supplementary Material). This population is characterized by a medium coercivity (mean $B_{1/2}$ = 63.2 mT) and a mean SIRM between 4.4×10^{-4} and 1.23×10^{-1} A/m (mostly between 10^{-3} and 5×10^{-2} A/m). The second magnetite-like population (medium coercivity magnetite component = C_{MMag}) has a lower mean coercivity (mean $B_{1/2}$ = 25.9 mT; **Table S1** in Supplementary Material). It can represent up to 47% of the

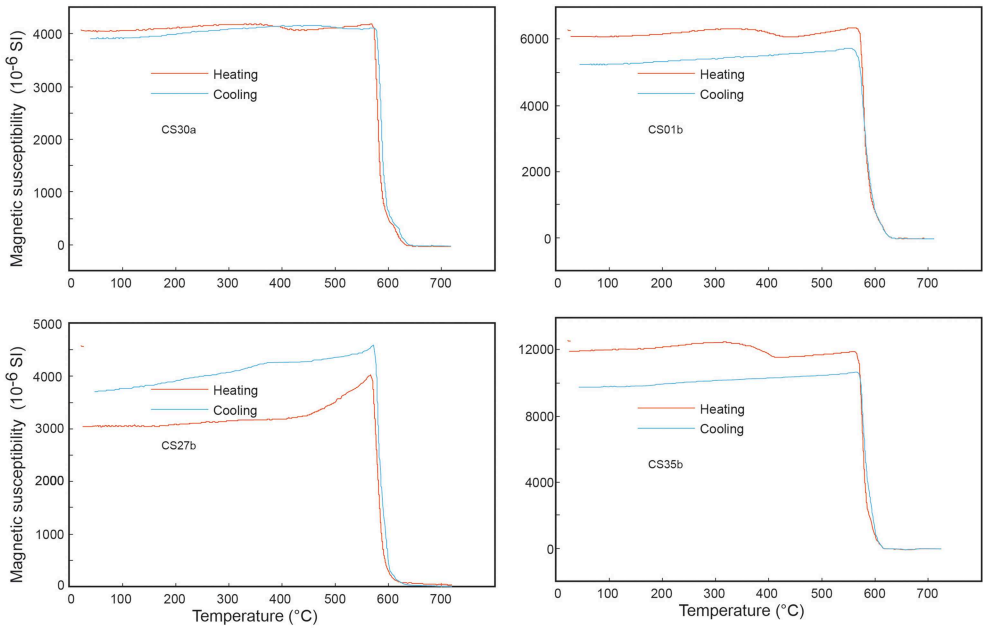

FIGURE 4 | Variation of low-field magnetic susceptibility during a heating-cooling cycle (red and blue lines, respectively).

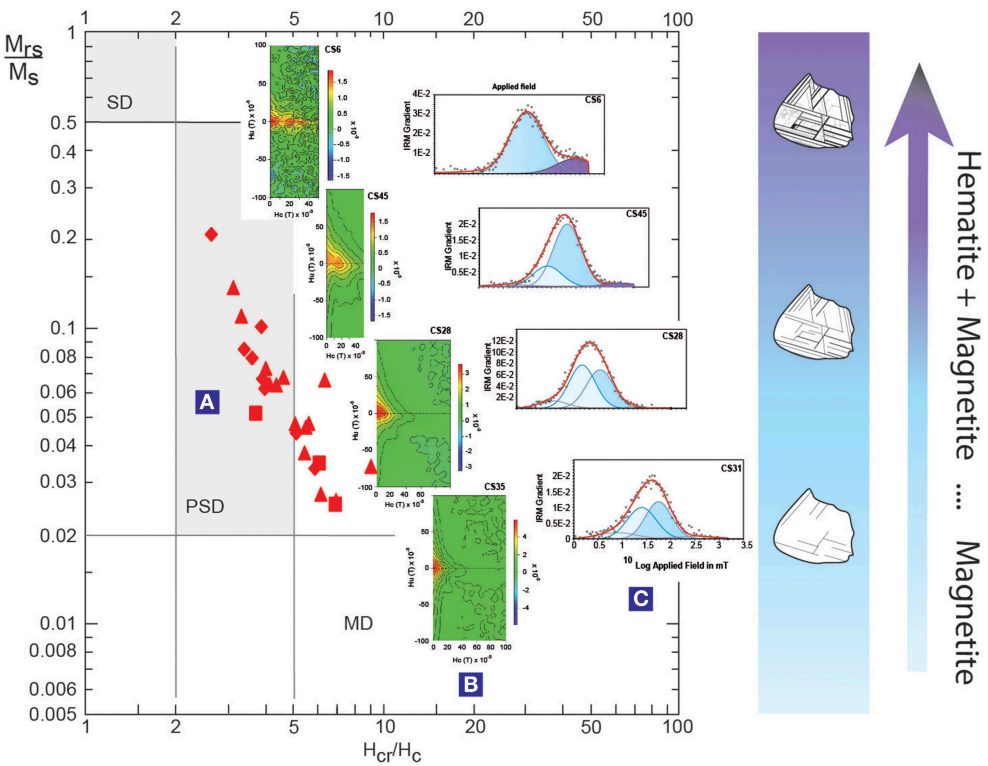

FIGURE 5 | Magnetic properties of the Biotite granite of Socotra. (A) Linear trend and PSD behavior on a Day-plot of Biotite granite samples. The diamonds, squares, and triangles, respectively correspond to the localization in Haggier Mont, Qalansya, and Sherebrub zones (see **Figure 3**) **(B)** IRM acquisition curves (linear and Gaussian cumulative treatment, respectively, showing magnetite dominance and hematite appearance with decreasing magnetic grain size. **(C)** FORC diagrams showing SD and PSD behavior disappearance to a MD-like behavior and increasing magnetic interactions with increasing magnetic grain size.

magnetization with SIRM varying between 7×10^{-4} and 5.3×10^{-2} A/m.

Hematite component (called high coercivity hematite = C_{hem}) is represented by a higher coercivity, with a mean $B_{1/2}$ = 490 mT (**Table S1** in Supplementary Material). This component represents on average only 4% of the total magnetization, but it is not evenly distributed. In fact, hematite-like pattern corresponds to 1–2% of magnetization in the majority of samples, but for some samples, like CS6, it represents more than 20% of magnetization (**Table S1** in Supplementary Material).

A low coercivity component (called low coercivity magnetite component = C_{LMag} – mean $B_{1/2}$ = 6.4 mT) represents 7% of the total magnetization on average (**Table S1** in Supplementary Material). This component could be maghemite or coarse-grained magnetite.

Grain Sizes and Magnetic Interactions

Hysteresis parameters (**Table S2** in Supplementary Material) and their classical representation on a Day plot (where the ratio M_{rs}/M_s is plotted against the ratio H_{cr}/H_c) are used to determine magnetic grain size or to compare relative proportions of two or three populations (Carter-Stiglitz et al., 2001; Dunlop, 2002a,b; Heslop and Roberts, 2012). Here, we observed that magnetic parameters display a trend parallel to SD-MD mixing curves (**Figure 5A**), corresponding to a magnetic grain size ranging between 1 and 10 μm. Hysteresis loops (n = 27) are not distorted. We observed a thinning of loops with the branch that straightens up before saturation from high to lower M_{rs}/M_s ratio.

Inherent ambiguities in interpretation of the Day plot such as those induced by magnetostatic interactions (Muxworthy et al., 2003) and by mixtures could be deciphered using first-order reversal curve (FORC) diagrams (Pike et al., 1999; Carvallo et al., 2006). FORC diagrams (n = 14) (**Figure 5B**) obtained for the Biotite granite display the variability from PSD grain size to more MD grain size. They also clearly show the presence of two components for samples lying close to the SD region in the Day plot. An example is given by CS6 sample that presents a mixture between two components of relatively low to medium coercivity. The first component have a PSD-like pattern with a coercivity peak close to the vertical axis and the second component have a coercivity peak at about 20 mT, and it corresponds to a SD-like pattern with contours closing on the diagram. From the highest to the lower M_{rs}/M_s ratio, the SD-like component evolves from sample CS6 (coercivity peak = 20 mT) to sample CS45 (coercivity peak = 15 mT) and then disappear from sample CS46 (**Figure 5**). The PSD-like pattern tends to migrate to a MD-like pattern (from samples CS46 to CS31). We notice a negligible spreading parallel to the vertical axis of FORC diagram from sample CS5 to sample CS31 that indicates that no interactions occurred between magnetic grains. Moreover, in all FORC diagrams, we notice that coercivity peaks are slightly displaced above the horizontal axis that confirms the hypothesis of relative non-interactions between grains.

What is striking in the log–log Day Plot is the linear distribution of hysteresis parameters for both Biotite Granites and Vertical Plutonic Sheets formation. This trend is parallel to the SD-MD mixing curves as proposed by Dunlop (2002a) but has higher H_{cr}/H_c ratio. This strongly suggests a binary mixing solution between two magnetite populations that belongs to the SD domain for the small one and lies at the base of the PSD domain and near the MD domain for the larger one. Magnetostatic interactions can strongly affect the hysteresis parameters, shifting them toward the SD behavior for large grains (see Sprowl, 1990; Muxworthy et al., 2003) and therefore change the trend of a binary mixing solution. However, here we can discard this effect since few interactions are detected with the FORC measurements.

The trend on the Day plot (**Figure 5A**) can be interpreted in two ways: a mixing between two end-members (SD and MD grains) or a variability from PSD grains to more MD grains. We argue here that the hematite and ilmenite lamellae define subdivisions into magnetite grains, which result in smaller-domain magnetite (<5 μm in average), explaining the PSD behavior observed. We discuss that the abundance and the increasing thickness of ilmenite–hematite lamellae result in tightening of the exsolution treillis. So, this treillis tightening is consistent with the decreasing of domain size in magnetic grains from a MD-behavior to a PSD-behavior.

Hematite was detected both by microscopic observations and by IRM analyses. The presence of hematite has an effect on hysteresis parameters. Indeed, hematite, even in quite large grain sizes, has M_{rs}/M_s-values of 0.5–0.6 and H_{cr}/H_c-values of 1.5–2 that mimic those of SD magnetite (Dunlop, 1971; Dankers, 1977). This corresponds to values of granitic samples with higher M_{rs}/M_s. Nevertheless, hematite is known to display "square" hysteresis curves (Tauxe et al., 1996; Brownlee et al., 2011). This type of shape and its influence on hysteresis curves, are not detected in our results. As well, no shapes characteristic of mixtures like potbellied or wasp-waisted curves are identified in our samples. The occurrence of hematite in magnetic parameters (hysteresis curves and FORC diagram in particular) is observable only from 88% of hematite (Carvallo et al., 2006) recorded in the total magnetization in magnetic mixtures with magnetite. However, according to microscopic observations, content of hematite in the Socotra samples never reach more than about 20% of the samples. Thus, there is no surprise that the presence of hematite is not detectable with these methods in the Socotra samples. Nevertheless, comparison between the IRM data and the Day-plot help to demonstrate that the increase in hematite proportion in the total magnetization is associated with decreasing magnetic grain size of samples. In addition, it also applies to the lamellae of ilmenite. According to our microscopic observations, ilmenite having a paramagnetic behavior, their thickness and their number increases in concert with the decrease of magnetite grain size.

SEM-light Reflected Microscopy

To establish the relationship between magnetic oxide populations and their relation to magnetic parameters of the Biotite granite, we performed microscopic observations on eight thin sections (**Figures 6**, **7**). Magnetic oxides present in the Biotite granite of Socotra were found to be associated with two mineral assemblages: (1) ferromagnesian minerals (biotite and amphibole) that represent the most common association and

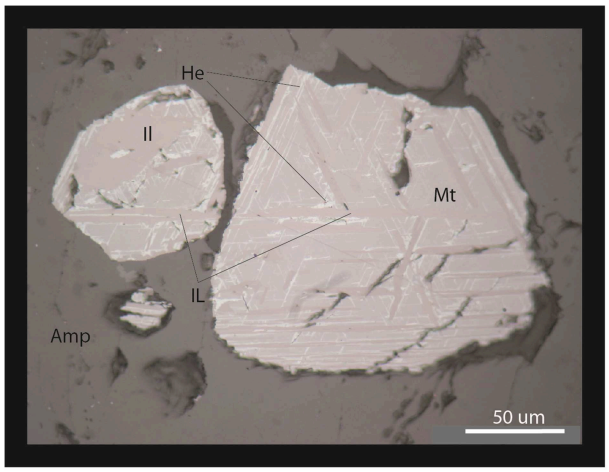

FIGURE 6 | Photomicrographs under reflected light microscopy of subhedral crystals of magnetite (Mt) with hematite (He) and ilmenite (Il) from the Neoproterozoic terrains of Socotra (Oman).

(2) feldspars (perthite and zoned plagioclase). Both associations are marked by magnetite with both ilmenite and hematite exsolutions representing the Fe–Ti oxides (sometimes with some amount of Mn) that dominate the Biotite granite oxide mineralogy.

Magnetites with exsolutions associated with ferromagnesian minerals are subhedral to anhedral crystals of large size ($>100\,\mu m$). They are disseminated into biotite and amphibole zones either in isolated grains or in the form of grain clusters or in the form of large zone of oxides in close association to the ferromagnesian minerals. Magnetites associated to feldspars are finer (mean size about $30\,\mu m$). Their crystal's shapes range from euhedral to subhedral and seldom anhedral. They are disseminated into zonated plagioclase and perthites. Individual ilmenite grains with variable Mn content, mainly associated with feldspar grains, can be found in few samples.

Microtextures of Fe–Ti oxide minerals in Biotite granite were observed closely with SEM and light-reflected microscopy. According to Buddington and Lindsley (1964) and Haggerty (1991), degrees of oxidation and diffusion result in series of exsolutions in titanomagnetite varying in morphology, size and in abundance. Using their terminology, ilmenite–hematite intergrowths occur as Treillis, Sandwich and Composite types exsolution lamellae in the host Ti-poor magnetite from the Biotite granite. Following this classification, oxide grains observed in Biotite granite samples can be classified between C2 stage and C4 stage of oxidation. It should be noted that C1 stage, which corresponds to homogeneous Ti-rich magnetite has not been identified in our samples of the Biotite granite. The oxidation index of all samples always reaches the C4 stage, which corresponds to the beginning of titanomagnetite-ilmenite intergrowths oxidation. It is superimposed most often into C2 and C3 stages previously formed. This stage results in formation of hematite in Ti-poor magnetite host and normally in formation of rutile in ilmenite lamellae. Textural forms of hematite are characterized by Trellis types (lamellae between <1 and $2\,\mu m$) and by internal or external Composites types (Haggerty, 1991). Rutile lenses and indistinct mottling in ilmenite lamellae (Haggerty, 1991) were not observed in the Biotite granite. These elements denote the very high oxidation state of the Biotite granite.

Discussion

Coexistence of Magnetite and Hematite

The crystallization of magnetic minerals (iron oxides and sulfides) is strongly dependent on the oxygen fugacity of the host magma (Haggerty, 1991). Moderate to high oxidation states correspond to the Fayalite–Magnetite–Quartz (FMQ) buffer of the present-day mantle. A very high oxidation state would correspond to the Magnetite-Hematite (MH) buffer, and would imply the synchronous crystallization of these two iron oxides. But the coexistence of primary hematite and magnetite in magmatic rocks is rare; extremely oxidized magmatic rocks being only found in some Phanerozoic copper porphyries–granitoids (Sun et al., 2013; Zhang et al., 2013). In Socotra, magnetite and hematite coexist, and are intertwined in trellis, sandwich, and composite textures (**Figures 6**, **7**). In this configuration, hematite divides the large oxide grains ($>10\,\mu m$) into smaller ones producing a pseudo-single domain (PSD) behavior for magnetite (**Figure 5**). Hematite and magnetite were formed at the beginning of magma crystallization and ilmenite appeared after all of them, occurring as inclusions in magmatic biotite (**Figure 7**). Both petrographic and magnetic parameters indicate that hematite is primary, and formed at the early magmatic evolution of the granite at very high oxygen fugacity and does not result from hydrothermalism or subsequent alteration.

Implications for the NOE

The intergrowth of hematite and magnetite observed in the Socotra granites indicates a very high oxygen fugacity (fO_2) for the magmas at this margin of Rodinia, around the MH buffer (ΔFMQ between $+4$ and $+5$). Rocks in subduction settings are known to be oxidized (Parkinson and Arculus, 1999; Evans et al., 2012), with fO_2-values of most subduction-related igneous rocks at ΔFMQ $+2$. The mechanisms invoked to explain their high oxidation are H_2O incorporation from the subducting plate and subduction of oxidized materials like carbonates, aseismic ridges (Sun et al., 2013) among others. Yet, these values remain well below the values found for Socotra Island granites. Interestingly, even if the database remains up to now too sparse and more detailed investigations on the fO_2 for other Neoproterozoic magmatic rocks are needed, other examples of highly oxidized igneous rocks of similar age have been reported for the Eastern Desert of Egypt (Ahmed, 2013; Khedr and Arai, 2013), and the Indian craton granites of Malani suites (Ashwal et al., 2013), all of them emplaced across the margin of Rodinia (**Figure 2**). Another occurrence may be suspected in South China (Liu et al., 2012; Zhang et al., 2013). The high apparent fO_2 at the Arabian–Nubian shield in Egypt and Socotra, NW Indian, and perhaps in South China, imply a significant reservoir of oxidized magma in the upper mantle between at least between 800 and 750 Ma on the magmatic arcs at the western hinge of Rodinia.

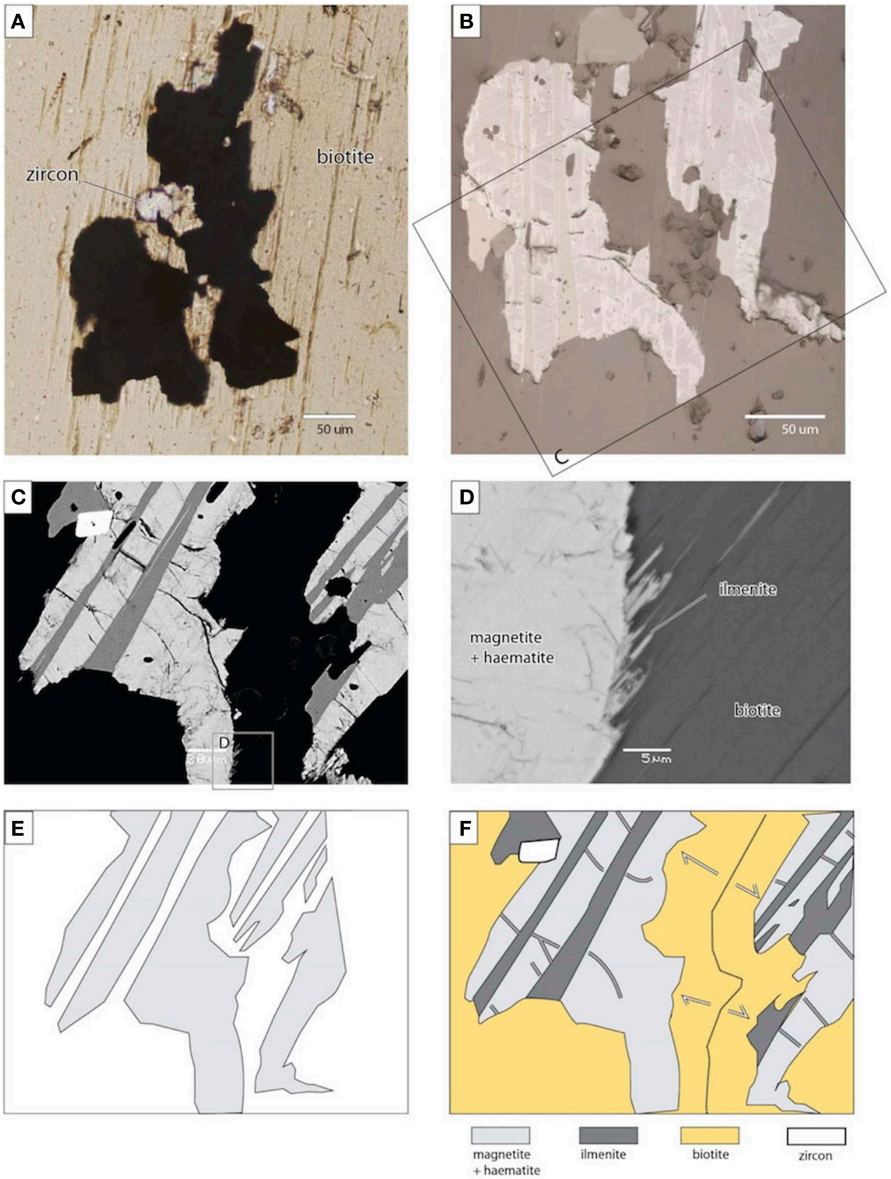

FIGURE 7 | Photomicrographs of magnetite. (A) Photomicrographs of subhedral crystals of magnetite (black minerals) trapped in a poikiloblast crystal of biotite (brown mineral) from the Neoproterozoic terrains of Socotra (Oman). **(B)** Recognition of treillis-like shaped hematite within the crystal of magnetite under reflected light microscopy. **(C)** Back-scattered electron imaging on the internal structure of oxide, using a scanning electron microscope (SEM), reveals multiple grains of magnetite-hematite separated by elongated crystals of ilmenite. **(D)** Oriented needles or patches of ilmenite outline the contact with biotite. **(E,F)** Interpreted chronology of magmatic events depicted from microscopic and SEM observations: (1) treillis-like shaped hematite developed early along cleavage planes of magnetite, due to magmatic oxy-exsolution processes; (2) magnetite was further fractured and divided into several grains; (3) Cracks were subsequently filled with ilmenite growing in equilibrium with the large magmatic biotite.

Now we can estimate the impact of volcanic oxidized gases from Rodinian magmatic arcs on the atmospheric composition. In steady state, the O_2 budget can be described following Catling and Claire (2005) and Claire et al. (2006) (Equation 1):

$$F_e + F_b = F_v + F_m + F_w, \quad (1)$$

where source fluxes correspond, respectively, to the escape of hydrogen to the space (Fe) and the total O_2 released from organic matter and pyrite burial (Fb). The sink fluxes are the O_2 consumed by reaction with reduced volcanic gases (Fv), reduced metamorphic gases (Fm), and reduced material on the continents Fw (Catling and Claire, 2005). Following Claire et al. (2006), we consider Fv and Fm to be around 1.5 Tmol.yr^{-1} of equivalent O_2 consumption each. In this way, a first estimation on the impact of oxidized to very oxidized emissions to Fv can be provided. For that, we used the estimation given by Gerlach (2011) where the proportion of emitted gases (CO_2) from arc volcanoes nowadays is at 30–34% of the total amount

of gases on Earth. Using the conservative estimate of 30%, that would represent 0.45 Tmol.yr^{-1} of the 1.5 Tmol.yr^{-1} emitted by volcanic fluxes and considering a minimum time of 50 Ma for the duration of oxidized emissions in subduction zones, this would correspond to a net flux of O_2 of at least 2.25×10^7 Tmol.

The rough estimation obtained above corresponds to oxygen concentrations of at around 0.5 PAL (Lasaga and Ohmoto, 2002). Such a burst of oxygen, due to a decrease in one of the most important sinks of O_2 during the lifetime of Rodinia (of at least 50 mol.yr) would be large enough to increase significantly the oxygen content of the atmosphere (Laakso and Schrag, 2014). Our findings have two additional implications. First, they imply that the NOE may have started earlier than generally thought (Sahoo et al., 2012), and before the Neoproterozoic low-latitude glaciations, in line with most recent findings (Sahoo et al., 2012; Baldwin et al., 2013; Ader et al., 2014). Second, by starting atmospheric oxygenation earlier (**Figure 1A**), our conceptual model also provides an explanation for the Neoproterozoic glaciations themselves. If the NOE occurred prior to the first glaciation, it would have likely resulted from the oxidation of a methane-rich atmosphere (Pavlov et al., 2003) as previously evocated by Claire et al. (2006). In this case, the drop in methane and ethane (which are both greenhouse gases) would have caused the drop in surface temperature promoting the onset of severe glacial episodes at the end of the Proterozoic.

Acknowledgments

The study is supported by the Syster and Marges programs of the INSU-CNRS and by the OMP-AO1 program. MM benefited from three months of invitation to stay at IAG, Brazil supported by grant 2013/08862-1, São Paulo Research Foundation (FAPESP).

Supplementary Material

The Supplementary Material for this article can be found online at: http://journal.frontiersin.org/article/10.3389/feart.2015.00044

Table S1 | Isothermal remanent magnetization (IRM) acquisition data showing the repartition of magnetic components for each rock formation of Socotra.

Table S2 | Hysteresis parameters, susceptibility and remanent magnetization of each selected rocks of Socotra basement. Hcr is the coercivity of remanence, Hc the coercive force, Mr the saturation remanence, and Ms the saturation magnetization.

References

Ader, M., Sansjofre, P., Halverson, G. P., Busigny, V., Trindade, R. I. F., Kunzmann, M., et al. (2014). Ocean redox structure across the late Neoproterozoic oxygenation event: a nitrogen isotope perspective. *Earth Planet. Sci. Lett.* 396, 1–13. doi: 10.1016/j.epsl.2014.03.042

Ahmed, A. H. (2013). Highly depleted harzburgite-dunite-chromitite complexes from the Neoproterozoic ophiolite, south Eastern Desert, Egypt: a possible recycled upper mantle lithosphere. *Precambrian Res.* 233, 173–192. doi: 10.1016/j.precamres.2013.05.001

Ahmed, A. S., Leroy, D., Keir, F., Korostelev, K., Khanbari, F., et al. Obrebski (2014). Crustal structure of the Gulf of Aden southern margin: evidence from receiver functions on Socotra Island (Yemen). *Tectonophysics* 637, 251–267. doi: 10.1016/j.tecto.2014.10.014

Ashwal, L. D., Solanki, A. M., Pandit, M. K., Corfu, F., Hendriks, B. W. H., Burke, K., et al. (2013). Geochronology and geochemistry of Neoproterozoic Mt. Abu granitoids, NW India: regional correlation and implications for Rodinia paleogeography. *Precambrian Res.* 236, 265–281. doi: 10.1016/j.precamres.2013.07.018

Baldwin, G. J., Nagler, T. F., Greber, N. D., Turner, E. C., and Kamber, B. S. (2013). Mo isotopic composition of the mid-Neoproterozoic ocean: an iron formation perspective. *Precambrian Res.* 230, 168–178. doi: 10.1016/j.precamres.2013.02.011

Brownlee, S. J., Feinberg, J. M., Kasama, T., Harrison, R. J., Scott, G. R., and Renne, P. R. (2011). Magnetic properties of ilmenite-hematite single crystals from the Ecstall pluton near Prince Rupert, British Columbia. *Geochem. Geophys. Geosyst.* 12. doi: 10.1029/2011GC003622

Buddington, A. F., and Lindsley, D. H. (1964). Iron-titanium oxide minerals and synthetic equivalents. *J. Petrol.* 5, 310–357. doi: 10.1093/petrology/5.2.310

Burgisser, A., and Scaillet, B. (2007). Redox evolution of a degassing magma rising to the surface. *Nature* 445, 194–197. doi: 10.1038/nature05509

Canfield, D. E., Poulton, S. W., and Narbonne, G. M. (2007). Late-Neoproterozoic deep-ocean oxygenation and the rise of animal life. *Science* 315, 92–95. doi: 10.1126/science.1135013

Carter-Stiglitz, B., Moskowitz, B., and Jackson, M. (2001). Unmixing magnetic assemblages and the magnetic behavior of bimodal mixtures. *J. Geophys. Res. Solid Earth* 106, 26397–26411. doi: 10.1029/2001JB000417

Carvallo, C., Roberts, A. P., Leonhardt, R., Laj, C., Kissel, C., Perrin, M., et al. (2006). Increasing the efficiency of paleointensity analyses by selection of samples using first-order reversal curve diagrams. *J. Geophys. Res. Solid Earth* 111. doi: 10.1029/2005JB004126

Catling, D. C., and Claire, M. W. (2005). How Earth's atmosphere evolved to an oxic state: a status report. *Earth Planet. Sci. Lett.* 237, 1–20. doi: 10.1016/j.epsl.2005.06.013

Chiaradia, M. (2014). Copper enrichment in arc magmas controlled by overriding plate thickness. *Nat. Geosci.* 7, 43–46. doi: 10.1038/ngeo2028

Claire, M. W., Catling, D. C., and Zahnle, K. J. (2006). Biogeochemical modelling of the rise in atmospheric oxygen. *Geobiology* 4, 239–269. doi: 10.1111/j.1472-4669.2006.00084.x

Cogne, J. P. (2003). PaleoMac: a Macintosh (TM) application for treating paleomagnetic data and making plate reconstructions. *Geochem. Geophys. Geosyst.* 4. doi: 10.1029/2001GC000227

Dankers, P. (1977). Grain-size dependence of some magnetic parameters for different magnetites and hematites. *Trans. Am. Geophys. Union* 58, 897–897.

Denéle, Y., Leroy, S., Pelleter, E., Pik, R., Talbot, J. Y., and Khanbari, K. (2012). The Cryogenian arc formation and successive high-K calc-alkaline plutons of Socotra Island (Yemen). *Arabian J. Geosci.* 5, 903–924. doi: 10.1007/s12517-011-0476-3

Dunlop, D. J. (1971). Magnetic properties of fine-particle hematite. *Ann. Geophys.* 27, 269–293.

Dunlop, D. J. (2002a). Theory and application of the Day plot (M_{rs}/M_s versus H_{cr}/H_c) 1. theoretical curves and tests using titanomagnetite data. *J. Geophys. Res. Solid Earth* 107, EPM 4-1. doi: 10.1029/2001JB000486

Dunlop, D. J. (2002b). Theory and application of the Day plot (M-rs/M-s versus H-cr/H-c) 2. Application to data for rocks, sediments, and soils. *J. Geophys. Res. Solid Earth* 107, 15. doi: 10.1029/2001JB000487

Ernst, R. E., Bleeker, W., Soderlund, U., and Kerr, A. C. (2013). Large igneous provinces and supercontinents: toward completing the plate tectonic revolution. *Lithos* 174, 1–14. doi: 10.1016/j.lithos.2013.02.017

Evans, K. A., Elburg, M. A., and Kamenetsky, V. S. (2012). Oxidation state of subarc mantle. *Geology* 40, 783–786. doi: 10.1130/G33037.1

Frost, D. J., and McCammon, C. A. (2008). The redox state of Earth's mantle. *Annu. Rev. Earth Planet. Sci.* 36, 389–420. doi: 10.1146/annurev.earth.36.031207.124322

Gaillard, F., Scaillet, B., and Arndt, N. T. (2011). Atmospheric oxygenation caused by a change in volcanic degassing pressure. *Nature* 478, 229–232. doi: 10.1038/nature10460

Gerlach, T. (2011). Volcanic versus anthropogenic carbon dioxide. *Eos Trans. AGU* 92, 201. doi: 10.1029/2011EO240001

Grigne, C., and Labrosse, S. (2001). Effects of continents on Earth cooling: thermal blanketing and depletion in radioactive elements. *Geophys. Res. Lett.* 28, 2707–2710. doi: 10.1029/2000GL012475

Haggerty, S. E. (1991). Oxide textures-A mini-atlas, in *Oxide Minerals: Petrologic and Magnetic Significance*, Vol. 25, ed D. H. Lindsley (Washington: Mineralogical Society of America Reviews in Mineralogy), 129–219.

Harrison, R. J., and Feinberg, J. M. (2008). FORCinel: an improved algorithm for calculating first-order reversal curve distributions using locally weighted regression smoothing. *Geochem. Geophys. Geosyst.* 9:Q05016. doi: 10.1029/2008GC001987

Hawkesworth, C., Cawood, P., and Dhuime, B. (2013). Continental growth and the crustal record. *Tectonophysics* 609, 651–660. doi: 10.1016/j.tecto.2013.08.013

Heslop, D., Dekkers, M. J., Kruiver, P. P., and Van Oorschot, I. H. M. (2002). Analysis of isothermal remanent magnetization acquisition curves using the expectation-maximization algorithm. *Geophys. J. Int.* 148, 58–64. doi: 10.1046/j.0956-540x.2001.01558.x

Heslop, D., and Roberts, A. P. (2012). A method for unmixing magnetic hysteresis loops. *J. Geophys. Res. Solid Earth* 117:B03103. doi: 10.1029/2011JB008859

Kasting, J. F. (2013). What caused the rise of atmospheric O-2? *Chem. Geol.* 362, 13–25. doi: 10.1016/j.chemgeo.2013.05.039

Khedr, M. Z., and Arai, S. (2013). Origin of Neoproterozoic ophiolitic peridotites in south Eastern Desert, Egypt, constrained from primary mantle mineral chemistry. *Mineral. Petrol.* 107, 807–828. doi: 10.1007/s00710-012-0213-y

Kletetschka, G., Wasilewski, P. J., and Taylor, P. T. (2000). Hematite vs. magnetite as the signature for planetary magnetic anomalies? *Phys. Earth Planet. Inter.* 119, 259–267. doi: 10.1016/S0031-9201(00)00141-2

Kruiver, P. P., Dekkers, M. J., and Heslop, D. (2001). Quantification of magnetic coercivity components by the analysis of acquisition curves of isothermal remanent magnetisation. *Earth Planet. Sci. Lett.* 189, 269–276. doi: 10.1016/S0012-821X(01)00367-3

Kump, L. R., Kasting, J. F., and Barley, M. E. (2001). Rise of atmospheric oxygen and the "upside-down" Archean mantle. *Geochem. Geophys. Geosyst.* 2, 1525–2027. doi: 10.1029/2000GC000114

Kump, L. R. (2008). The rise of atmospheric oxygen. *Nature* 451, 277–278. doi: 10.1038/nature06587

Laakso, T. A., and Schrag, D. P. (2014). Regulation of atmospheric oxygen during the Proterozoic. *Earth Planet. Sci. Lett.* 388, 81–91. doi: 10.1016/j.epsl.2013.11.049

Lasaga, A. C., and Ohmoto, H. (2002). The oxygen geochemical cycle: dynamics and stability. *Geochim. Cosmochim. Acta* 66, 361–381. doi: 10.1016/S0016-7037(01)00685-8

Lenardic, A., Moresi, L., Jellinek, A. M., O'neill, C. J., Cooper, C. M., and Lee, C. T. (2011). Continents, supercontinents, mantle thermal mixing, and mantle thermal isolation: theory, numerical simulations, and laboratory experiments. *Geochem. Geophys. Geosyst.* 12:Q10016. doi: 10.1029/2011GC003663

Lenton, T. M., Boyle, R. A., Poulton, S. W., Shields-Zhou, G. A., and Butterfield, N. J. (2014). Co-evolution of eukaryotes and ocean oxygenation in the Neoproterozoic era. *Nat. Geosci.* 7, 257–265. doi: 10.1038/ngeo2108

Leroy, S., Razin, P., Autin, J., Bache, F., D'acremont, E., Watremez, L., et al. (2012). From rifting to oceanic spreading in the Gulf of Aden: a synthesis. *Arabian J. Geosci.* 5, 859–901. doi: 10.1007/s12517-011-0475-4

Li, Z. X., Evans, D. A. D., and Halverson, G. P. (2013). Neoproterozoic glaciations in a revised global palaeogeography from the breakup of Rodinia to the assembly of Gondwanaland. *Sediment. Geol.* 294, 219–232. doi: 10.1016/j.sedgeo.2013.05.016

Liu, X., Fan, H. R., Santosh, M., Hu, F. F., Yang, K. F., Li, Q. L., et al. (2012). Remelting of Neoproterozoic relict volcanic arcs in the Middle Jurassic: implication for the formation of the Dexing porphyry copper deposit, Southeastern China. *Lithos* 150, 85–100. doi: 10.1016/j.lithos.2012.05.018

Lyons, T. W., Reinhard, C. T., and Planavsky, N. J. (2014). The rise of oxygen in Earth's early ocean and atmosphere. *Nature* 506, 307–315. doi: 10.1038/nature13068

Muxworthy, A., Williams, W., and Virdee, D. (2003). Effect of magnetostatic interactions on the hysteresis parameters of single-domain and pseudo-single-domain grains. *J. Geophys. Res. Solid Earth* 108. doi: 10.1029/2003JB002588

Och, L. M., and Shields-Zhou, G. A. (2012). The Neoproterozoic oxygenation event: environmental perturbations and biogeochemical cycling. *Earth Sci. Rev.* 110, 26–57. doi: 10.1016/j.earscirev.2011.09.004

Parkinson, I. J., and Arculus, R. J. (1999). The redox state of subduction zones: insights from arc-peridotites. *Chem. Geol.* 160, 409–423. doi: 10.1016/S0009-2541(99)00110-2

Pavlov, A. A., Hurtgen, M. T., Kasting, J. F., and Arthur, M. A. (2003). Methane-rich Proterozoic atmosphere? *Geology* 31, 87–90. doi: 10.1130/0091-7613(2003)031<0087:MRPA>2.0.CO;2

Pike, C. R., Roberts, A. P., and Verosub, K. L. (1999). Characterizing interactions in fine magnetic particle systems using first order reversal curves. *J. Appl. Phys.* 85, 6660–6667. doi: 10.1063/1.370176

Reinhard, C. T., Planavsky, N. J., Robbins, L. J., Partin, C. A., Gill, B. C., Lalonde, S. V., et al. (2013). Proterozoic ocean redox and biogeochemical stasis. *Proc. Natl. Acad. Sci. U.S.A.* 110, 5357–5362. doi: 10.1073/pnas.1208622110

Roberts, A. P., Pike, C. R., and Verosub, K. L. (2000). First-order reversal curve diagrams: a new tool for characterizing the magnetic properties of natural samples. *J. Geophys. Res. Solid Earth* 105, 28461–28475. doi: 10.1029/2000JB900326

Sahoo, S. K., Planavsky, N. J., Kendall, B., Wang, X. Q., Shi, X. Y., Scott, C., et al. (2012). Ocean oxygenation in the wake of the Marinoan glaciation. *Nature* 489, 546–549. doi: 10.1038/nature11445

Samuel, H., and King, S. D. (2014). Mixing at mid-ocean ridges controlled by small-scale convection and plate motion. *Nat. Geosci.* 7, 602–605. doi: 10.1038/ngeo2208

Sprowl, D. R. (1990). Numerical estimation of interactive effects in single-domain magnetite. *Geophys. Res. Lett.* 17, 2009–2012. doi: 10.1029/GL017i011p02009

Sun, W. D., Liang, H. Y., Ling, M. X., Zhan, M. Z., Ding, X., Zhang, H., et al. (2013). The link between reduced porphyry copper deposits and oxidized magmas. *Geochim. Cosmochim. Acta* 103, 263–275. doi: 10.1016/j.gca.2012.10.054

Tauxe, L., Mullender, T. A. T., and Pick, T. (1996). Potbellies, wasp-waists, and superparamagnetism in magnetic hysteresis. *J. Geophys. Res. Solid Earth* 101, 571–583. doi: 10.1029/95JB03041

Zhang, H., Ling, M. X., Liu, Y. L., Tu, X. L., Wang, F. Y., Li, C. Y., et al. (2013). High oxygen fugacity and slab melting linked to cu mineralization: evidence from dexing porphyry copper deposits, Southeastern China. *J. Geol.* 121, 289–305. doi: 10.1086/669975

Conflict of Interest Statement: The authors declare that the research was conducted in the absence of any commercial or financial relationships that could be construed as a potential conflict of interest.

frontiers in Earth Science

GENERAL COMMENTARY
published: 09 December 2015
doi: 10.3389/feart.2015.00080

Commentary: Is the Neoproterozoic oxygen burst a supercontinent legacy?

Anne Nédélec[1]* *and Anastassia Y. Borisova*[1, 2]

[1] Géosciences Environnement Toulouse, Université de Toulouse, Observatoire Midi-Pyrénées, Toulouse, France, [2] Geological Department, Lomonosov Moscow State University, Moscow, Russia

Keywords: magnetite, hematite, exsolution, granite, neoproterozoic oxidation event

A commentary on

Is the Neoproterozoic oxygen burst a supercontinent legacy?
by Macouin, M., Roques, D., Rousse, S., Ganne, J., Denèle, Y., and Trindade, R. I. F. (2015). Front. Earth Sci. 3:44. doi: 10.3389/feart.2015.00044

The oxygen content of the atmosphere is thought to have increased in two steps: the Paleoproterozoic Great Oxidation Event and the Neoproterozoic Oxidation Event. The younger event is still a matter of debate (Och and Shields-Zhou, 2012). Macouin et al. (2015) suggest that it may have been triggered by volcanic degassing from unusually oxidized magmas occurring in a subduction ring surrounding the Rodinia supercontinent. Evidence for subduction-related oxidized magmas is supported by the study of 780 Ma biotite and pink granites of high K-calc-alkaline affinities and associated gabbros from Socotra Island (Denèle et al., 2012). Magnetite and subordinate hematite are revealed by magnetic properties, reflected-light microscopy, and scanning electron microscopy. Macouin et al. (2015) suggest that hematite is a primary phase witnessing a very high oxygen fugacity at magmatic conditions.

In igneous rocks, Ti-rich titanohematite (ilmenite) is a primary phase, whereas stoichiometric hematite represents a common secondary mineral due to post-magmatic alteration processes. Indeed, hematite was uniquely found to be a liquidus phase in an experimental peralkaline residua Na_2O - Al_2O_3 - Fe_2O_3 - SiO_2 system (Edgar, 1974), but the investigated system had no ferrous (Fe^{2+}) iron, hence it has no terrestrial equivalent in common tectonic settings.

The microphotographs of iron oxides presented as evidences of primary hematite by Macouin et al. (2015) in their Figures 6, 7 show subhedral magnetite crystals with typical subsolidus exsolution features such as fine trellis-lamellae of ilmenite and minor hematite parallel to (111) planes, or larger (sandwich) ilmenite lamellae in only one (111) plane. The petrographic nature (biotite granite, pink granite, or gabbro) of the relevant samples is not provided. Macouin et al. (2015) infer that some primary magnetite grains were fractured and subsequently filled by ilmenite (see caption of their Figure 7). We argue that sandwich ilmenite lamellae in Fe-Ti oxide grains do not arise from a reaction with biotite, unlike the small ilmenite needles at the contact between magnetite and biotite (Figure 7d of Macouin et al., 2015).

Indeed, primary igneous magnetite is generally titanomagnetite containing a percentage of ulvöspinel (Fe_2TiO_4) in solution. During slow cooling, subsolidus oxidative exsolution takes place from ~650°C to 450°C yielding ilmenite + magnetite (**Figure 1A**). Temperature and oxidation conditions control the exsolved phase proportions, hence the width of ilmenite lamellae. This is the common interpretation of Fe-Ti oxide intergrowths supported by experimental evidence (Buddington and Lindsley, 1964). Haggerty (1976) defined a seven-fold classification of the titanomagnetite oxidation stages from C1 (homogeneous titanomagnetite) to C7 (abundant pseudobrookite and hematite). It is worth noting that Macouin et al. (2015) argue that the biotite granites reached C4 oxidation stage superimposed on previously formed C2 and C3 stages, thus

OPEN ACCESS

Edited by:
Eric Font,
University of Lisbon, Portugal

Reviewed by:
Nicholas L. Swanson-Hysell,
University of California, Berkeley, USA
Juan Cruz Larrasoaña,
Instituto Geológico y Minero de España, Spain

***Correspondence:**
Anne Nédélec
anne.nedelec@get.obs-mip.fr

Specialty section:
This article was submitted to Geomagnetism and Paleomagnetism, a section of the journal Frontiers in Earth Science

Received: *09 October 2015*
Accepted: *23 November 2015*
Published: *09 December 2015*

Citation:
Nédélec A and Borisova AY (2015) Commentary: Is the Neoproterozoic oxygen burst a supercontinent legacy? Front. Earth Sci. 3:80. doi: 10.3389/feart.2015.00080

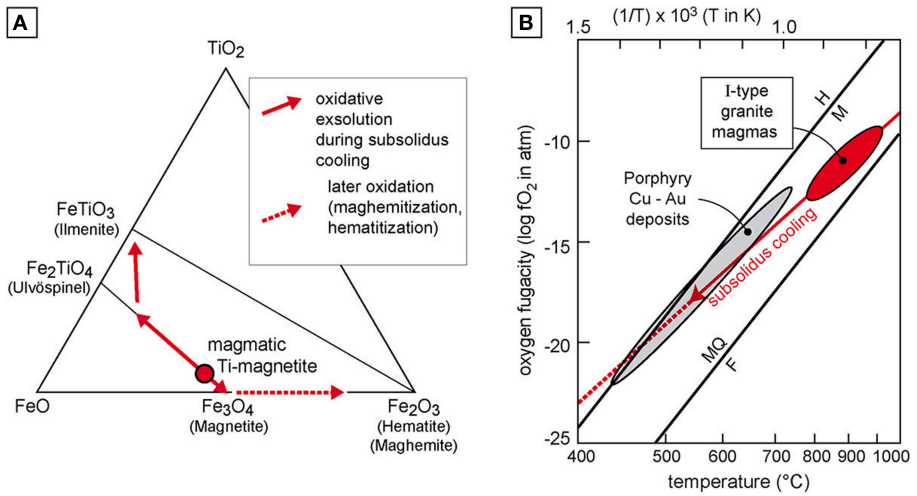

FIGURE 1 | (A) Solid solution series of Fe-Ti oxides; arrows indicate the subsolidus evolution of a magmatic titanomagnetite. **(B)** (fO_2, T) diagram showing the usual conditions of I-type granitic magmas and related porphyry Cu-Au deposits with respect to the FMQ (fayalite-magnetite-quartz) and H-M (hematite-magnetite) buffers, modified after Richards (2015).

suggesting a secondary evolution of the Fe-Ti oxides. The C4 stage would imply that the ilmenite lamellae were subsequently altered, a point that is not supported by the observation as stated by the authors themselves. Therefore, we claim that the presented samples mainly correspond to the C2-C3 oxidation stages, a common situation in granitic rocks.

Besides, natural magnetite may also contain a small excess of Fe_2O_3 due to the presence of cationic vacancies within the octahedral site (O'Reilly, 1984), that will yield maghemite (γFe_2O_3) lamellae, thereafter inverting to hematite. Indeed, minor hematite lamellae in magnetite crystals are commonly regarded as the result of late oxidation (e.g., Broska and Petrik, 2011).

The oxygen fugacity (fO_2) of a granitic magma is related to its source material (Ishihara, 1977). I-type granites, the most common granites in subduction-related settings, are relatively oxidized and generally contain magnetite (Nédélec and Bouchez, 2015). Nevertheless, the mineral assemblage alone is not sufficient to determine oxidizing or reducing conditions. Values of fO_2 and temperature must be considered together with respect to the usual redox buffers (e.g., FMQ: fayalite-magnetite-quartz). Arc magmas are characterized by oxidizing conditions slightly above the FMQ buffer (**Figure 1B**), typically at ΔFMQ $\sim +2$ i.e., 2 log units above the FMQ buffer (Gaillard et al., 2015).

During magmatic and post-magmatic cooling, fO_2 decreases together with T, following the lines of the usual mineral buffers. A hydrothermal fluid phase, either of magmatic or external (non-magmatic) origin, is able to modify fO_2 through the dissociation of H_2O ($H_2O = H_2 + \frac{1}{2}O_2$) as indicated by the equation:

$$fO_2 = (fH_2O/fH_2 \cdot K^{P,T})^2 \quad (1)$$

where K is the equilibrium thermodynamic constant.

However, the increase of fO_2 related to fluid degassing remains small in oxidized magmas, typically less than 1 log unit (Gaillard et al., 2001). Impact of a late external fluid may trigger more oxidizing conditions during subsolidus cooling, up to the magnetite-hematite buffer as shown by some ore deposits (Zhang et al., 2013). Nevertheless, most porphyry deposits related to arc magmas contain magnetite (Richards, 2015).

Formation of secondary hematite by hydrothermal alteration has been extensively studied and monitored by magnetic properties in some granites (Meller et al., 2014; Nédélec et al., 2015). None of these observations are related to unusually oxidized magmas. Secondary hematite in alkali feldspar grains is well known to be responsible for the pink to red color of A-type granites. For instance, SEM images of the Tana A-type granite in Corsica reveal that tiny hematite grains crystallized in vugs in the alkali feldspar grains, thus being related to water-rock interactions (Nédélec et al., 2015). Red rhyolites from the ~760 Ma Malani igneous suite of India also contain secondary hematite disseminated throughout the rocks (Torsvik et al., 2001), because these rhyolites suffered extensive hydrothermal alteration. Such a pronounced oxidation is not uncommon in rhyolites that usually suffered more hydrothermal alteration, than their deeper granitic equivalents.

It is worth noting that Macouin et al. (2015) did not explore the existence of primary hematite as idiomorphic inclusions in silicate minerals in their studied rocks. As Macouin et al. (2015) do not show any evidence of primary magmatic hematite crystals in the Socotra granites, we conclude that the presented magnetite-hematite assemblage is secondary. Therefore, the hypothesis of a contribution of these magmas to the Neoproterozoic Oxidation Event through unusually oxidizing degassing must be regarded with extreme caution.

AUTHOR CONTRIBUTIONS

AN: Petrology of granites, AB: Geochemistry of volcanic gases.

REFERENCES

Broska, I., and Petrik, I. (2011). Accessory Fe-Ti oxides in the West-Carpathian I-type granitoids: witnesses of the granite mixing and late oxidation processes. *Mineral. Petrol.* 102, 87–97. doi: 10.1007/s00710-011-0158-6

Buddington, A. F., and Lindslay, D. H. (1964). Iron-titanium oxide minerals and synthetic equivalents. *J. Petrol.* 5, 310–357. doi: 10.1093/petrology/5.2.310

Denèle, Y., Leroy, S., Pelleter, E., Pik, R., Talbot, J. Y., and Khanban, K. (2012). The Cryogenian arc formation and successive high-K calc-alkaline plutons of Socotra Island (Yemen). *Arabian J. Geosci.* 5, 903–924. doi: 10.1007/s12517-011-0476-3

Edgar, A. D. (1974). "Experimental studies," in *The Alkaline Rocks,* ed H. Sorensen (London: John Wiley and sons), 355–389.

Gaillard, F., Scaillet, B., Pichavant, M., and Bény, N. (2001). The effect of water and fO2 on the ferric-ferrous ration of silicic melts. *Chem. Geol.* 174, 255–273. doi: 10.1016/S0009-2541(00)00319-3

Gaillard, F., Scaillet, B., Pichavant, M., and Iacono-Marziano, G. (2015). The redox geodynamics linking basalts and their mantle sources through space and time. *Chem. Geol.* [Epub ahead of print].

Haggerty, S. E. (1976). "Opaque minerals oxides in terrestrial igneous rocks," in *Oxide Minerals,* Vol. 3, ed D. Rumble III (Washington, DC: Mineralogical Society of America short course notes), Hg101-Hg277.

Ishihara, S. (1977). The magnetite-series and ilmenite-series granitic rocks. *Mining Geol.* 27, 293–305.

Macouin, M., Roques, D., Rousse, S., Ganne, J., Denèle, Y., and Trindade, R. I. F. (2015). Is the Neoproterozoic|oxygen burst a supercontinent legacy? *Front. Earth Sci.* 3:44. doi: 10.3389/feart.2015.00044

Meller, C., Kontny, A., and Kohl, T. (2014). Identification and characterization of hydrothermally altered zones in granite by combining synthetic clay content logs with magnetic mineralogical investigations of drilled rock cuttings. *Geophys. J. Int.* 199, 465–479. doi: 10.1093/gji/ggu278

Nédélec, A., and Bouchez, J. L. (2015). *Granites: Petrology, Structure, Geological Setting, and Metallogeny*. Oxford: Oxford University Press.

Nédélec, A., Trindade, R. I. F., Peschler, A., Archanjo, C., Macouin, M., Poitrasson, F. et al. (2015). Hydrothermally-induced changes in mineralogy and magnetic properties of oxidized A-type granites. *Lithos* 212–215, 145–157. doi: 10.1016/j.lithos.2014.11.007

Och, L. M., and Shields-Zhou, G. A. (2012). The Neoproterozoic oxygenation event: environmental perturbations and biogeochemical cycling. *Earth Sci. Rev.* 110, 26–57. doi: 10.1016/j.earscirev.2011.09.004

O'Reilly, W. (1984). *Rock and Mineral Magnetism*. New York, NY: Chapman and Hall.

Richards, J. P. (2015). The oxidation state, and sulfur and Cu contents of arc magmas: implications for metallogeny. *Lithos* 233, 27–45. doi: 10.1016/j.lithos.2014.12.011

Torsvik, T. H., Carter, L. M., Ashwal, L. D., Bhushan, S. K., Pandit, M. K., and Jamtveit, B. (2001). Rodinia refined or obscured: palaeomagnetism of the Malani igneous suite (NW India). *Precambrian Res.* 108, 319–333. doi: 10.1016/S0301-9268(01)00139-5

Zhang, H., Ling, M. X., Liu, Y. L., Tu, X. L., Wang, F. Y., Li, C. Y. et al. (2013). High oxygen fugacity and slab melting linked to Cu mineralization: evidence from Dexing porphyry copper deposits, southeastern China. *J. Geol.* 121, 289–305. doi: 10.1086/669975

Conflict of Interest Statement: The authors declare that the research was conducted in the absence of any commercial or financial relationships that could be construed as a potential conflict of interest.

frontiers in Earth Science

GENERAL COMMENTARY
published: 31 August 2016
doi: 10.3389/feart.2016.00083

Response: Commentary: Is the Neoproterozoic oxygen burst a supercontinent legacy?

Melina Macouin[1], Sonia Rousse[1], Jérôme Ganne[1], Yoann Denèle[1], Damien Roques[1] and Ricardo I. F. Trindade[2]*

[1] *Géosciences Environnement Toulouse, UMR 5563 Centre National de la Recherche Scientifique, UR234 IRD, Université de Toulouse, Toulouse, France,* [2] *Departamento de Geofísica, Instituto de Astronomia, Geofísica e Ciências Atmosféricas, Universidade de São Paulo, São Paulo, Brazil*

Keywords: rock magnetism, Neoproterozoic Oxygenation Event, hematite-magnetite buffer, Rodinia, Socotra, subductions

A commentary on

Commentary: Is the Neoproterozoic oxygen burst a supercontinent legacy?
by Nédélec, A., and Borisova, A.Y. (2015). Front. Earth Sci. 3:80. doi: 10.3389/feart.2015.00080

OPEN ACCESS

Edited by:
Eric Font,
University of Lisbon, Portugal

Reviewed by:
Dario Bilardello,
University of Minnesota, USA
Nicholas L. Swanson-Hysell,
University of California, Berkeley, USA
Juan Cruz Larrasoaña,
Instituto Geológico y Minero de España, Spain

****Correspondence:***
Melina Macouin
melina.macouin@get.omp.eu

Specialty section:
This article was submitted to Geomagnetism and Paleomagnetism, a section of the journal Frontiers in Earth Science

Received: *25 April 2016*
Accepted: *19 August 2016*
Published: *31 August 2016*

Citation:
Macouin M, Rousse S, Ganne J, Denèle Y, Roques D and Trindade RIF (2016) Response: Commentary: Is the Neoproterozoic oxygen burst a supercontinent legacy? Front. Earth Sci. 4:83. doi: 10.3389/feart.2016.00083

We thank Nedelec and Borisova (2015) for giving us the opportunity to clarify our data and (derived) conceptual model. The purpose of Macouin et al. (2015) was to propose a new approach to explain the Neoproterozoic Oxygenation Event. It should be recalled that among the recent and abandoned hypotheses for the oxidation of the atmosphere, rise of less reduced gases (or more oxidized) remains one of the most frequently invoked (i.e., Kasting, 2013).

We illustrate our model with data acquired on the Neoproterozoic Socotra biotite granite (SBG) thought to be related to one of the subduction zones that surrounded Rodinia around 780 Ma. The main question raised by Nedelec and Borisova (2015) concerns the primary origin of hematite and ilmenite in this granite and the oxidized character of the emitted gases.

Before discussing the oxide assemblage, we answer on the use of the hematite-magnetite buffer, for which we refer to Sun et al. (2015) and Botcharnikov et al. (2008). Indeed, the magnetite-hematite assemblage does not permit to give a precise value of ΔFMQ, but as stated by these authors, the assemblage is a classical indicator of high oxygen fugacities and hence of an oxidized magma. As mentioned in the comment, it is true that, recently, fO_2 from gas has been shown to possibly diverge from the source magma contrary to what was commonly thought previously (i.e., Burgisser and Scaillet, 2007). Nevertheless, these authors have estimated the deviation from the redox state of the magma source by no more than 1.5 log unit at maximum. In our case, we can still invoke oxidized gases since our estimated fO_2 from sources is significantly higher (ΔFMQ + 4/5).

Concerning the oxide assemblage found in the SBG, we first state that magmatic or late magmatic origin of (titano-poor) hematite has already been reported. For example, Carvalho and Janasi (2012) found hematite in the 610 Ma Pedra Branca syenite (from a magmatic arc) in Brazil. These authors described a primary assemblage of hematite, ilmenite and magnetite. They conclude that this coexistence implies oxidized conditions and probably high oxygen fugacities. One of the authors herself reports an example of magmatic hematite in the unaltered Washita granite (Nedelec et al., 2015). In this publication, the hematite, in the unaltered granite, is interpreted as due to a change in oxygen fugacity in the magma "*without any influence of a hydrous fluid*." Also, contrary to what Nedelec and Borisova (2015) advance in their comment, Broska and Petrik (2011) do not state that hematite is always post magmatic but that the reactions could begin in the magmatic stage.

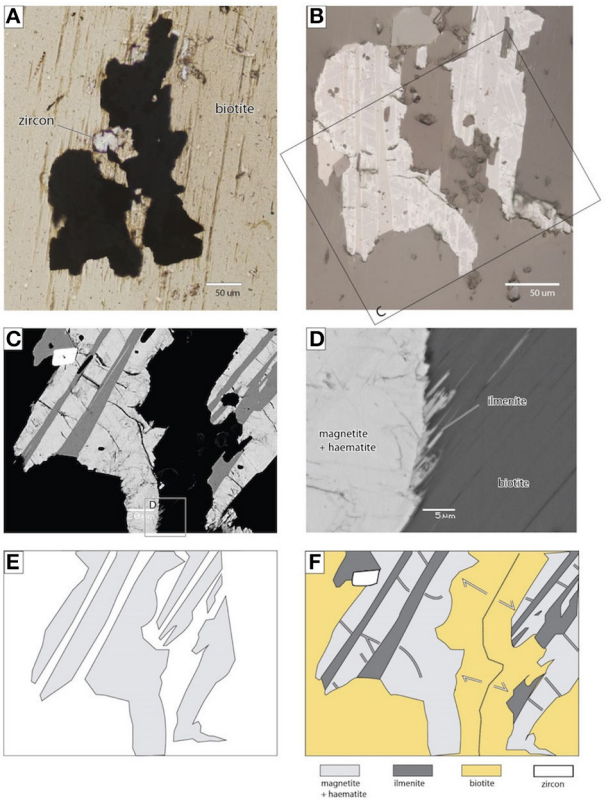

FIGURE 1 | Corrected caption of Figure 7 of Macouin et al. (2015). Photomicrographs of magnetite from CS46 sample (Socotra Biotite Granite, Neoproterozoic terrains, Oman) **(A)** Photomicrographs of subhedral crystals of magnetite (black minerals) trapped in a poikiloblast crystal of biotite (brown mineral). **(B)** Recognition of treillis-like shaped hematite within the crystal of magnetite under reflected light microscopy. Note that hematite is present in the ilmenite and at the fringe of the ilmenite lamellae **(C)** Back-scattered electron imaging on the internal structure of oxide, using a scanning electron microscope (SEM), reveals multiple grains of magnetite-hematite separated by elongated crystals of ilmenite. **(D)** Oriented needles or patches of ilmenite outline the contact with biotite. **(E,F)** Interpreted magmatic events depicted from microscopic and SEM observations. Ilmenite and hematite lamellae developed along cleavage planes of magnetite, due to magmatic oxy-exsolution processes. Magnetite was fractured and divided.

Nedelec and Borisova (2015) affirm that liquidus phase hematite was uniquely found in an experimental peralkaline residual (Edgar, 1974), and therefore not possible with natural samples. More recent literature reports formation of liquidus phase hematite on both, for example, I-type Chinese granite, remelted and recrystallized (Liaw et al., 2006) and a synthetic analog of a ferrobasaltic melt of the Skaergaard intrusion (Botcharnikov et al., 2008). These authors even demonstrate that they produce hematite in their experiments only at high oxygen fugacities ($fO_2 > 2.5$). Both these experiments involve formation of titano-poor hematite (and not of stoichiometric hematite) as it is interpreted in the SBG. This interpretation is strongly suggested by the reversible behavior of the thermomagnetic curves with Néel temperatures on the order of 620°-630°C (see samples CS27-CS30 from Figure 4, Macouin et al., 2015) combined with the petrological observations.

We are aware that hematite can be secondary in granites due to oxygenated fluids. Such secondary hematite has been described in different forms described in Nedelec et al. (2015), or associated with chloritized biotite (Just and Kontny, 2012). A typical mark of hematitization (maghemitization) of titano-magnetite is to display a progression from rims toward core center (often with the core untouched) or along the fractures (Figure 4H of Broska and Petrik, 2011). Curved cracks are also a typical feature of maghemitization (Figure 15 of Haggerty, 1991; Figure 3C of McEnroe and Brown, 2000). It is worth noting that in the SBG, the hematite does not appear into any of these forms and marks of alteration are absent (**Figure 1**).

In the SBG, as described by Haggerty (1991), the C4 stage is probably reached in the samples presenting the assemblage of magnetite-ilmenite-hematite. It is difficult to assess whether the hematite lamellae replaced previous thin ilmenite lamellae (as expected for C4 stage) or are secondary as Nedelec and Borisova (2015) argue. Nevertheless, in **Figure 1B**, thick ilmenite lamellae are seen to both contain hematite and be fringed by hematite, indicating the C4 stage. While we think that this stage was attained during the formation of the granite, late magmatic deuteric oxidation (above 600°C) could not completely be excluded. In this case, such a high temperature alteration would indicate high fugacity of oxygen at least in the fluids that were involved during the end or just after the crystallization as likely occured in the Malani red rhyolites described by Torsvik et al. (2001).

Furthermore, contrary to what Nedelec and Borisova (2015) claim, porphyries generally present hematite-magnetite assemblages and their primary origin has recently been evoked by Sun et al. (2013, 2015). As stated by Sun et al. (2013), intergrowths of magnetite-hematite, such as the ones we exposed in our paper (Macouin et al., 2015), are not often studied and may represent a challenge. It appears clearly that their occurrences are rare and therefore represent an unusual feature. The fact that hematite is ignored or systematically referred as secondary might be a bias in the studies.

Finally, the hematite in the SBG seems to be likely primary and our model remains a possible valid explanation for the NOE. This interesting discussion emphasizes the need to scrutinize this type of mineralogical assemblage in further studies. Additional methods could be used for that, such as paleomagnetic direction to decipher the synchronicity in hematite and magnetite formation or in-situ geochemistry.

AUTHOR CONTRIBUTIONS

All authors listed, have made substantial, direct and intellectual contribution to the work, and approved it for publication.

FUNDING

The study was supported by the Tellus-Syster, PNP and Marges programs of the INSU-CNRS and by the OMP-AO1 program.

REFERENCES

Botcharnikov, R. E., Almeev, R. R., Koepke, J., and Holtz, F. (2008). Phase relations and liquid lines of descent in hydrous ferrobasalt - Implications for the Skaergaard intrusion and Columbia River flood basalts. *J. Petrol.* 49, 1687–1727. doi: 10.1093/petrology/egn043

Broska, I., and Petrik, I. (2011). Accessory Fe-Ti oxides in the West-Carpathian I-type granitoids: witnesses of the granite mixing and late oxidation processes. *Mineral. Petrol.* 102, 87–97. doi: 10.1007/s00710-011-0158-6

Burgisser, A., and Scaillet, B. (2007). Redox evolution of a degassing magma rising to the surface. *Nature* 445, 194–197. doi: 10.1038/nature05509

Carvalho, B. B., and Janasi, V. D. A. (2012). Crystallization conditions and controls on trace element residence in the main minerals from the Pedra Branca Syenite, Brazil: an electron microprobe and LA-ICPMS study. *Lithos* 153, 208–223. doi: 10.1016/j.lithos.2012.05.003

Edgar,A.D. (1974). "Experimental studies," in *The Alkaline Rocks*, ed H. Sorensen (London: John Wiley and sons), 355–389.

Haggerty, S. E. (1991). "Oxide textures: a mini atlas," in *Oxide Minerals: Petrologic and Magnetic Significance*, Vol. 25, ed D. H. Lindsley (Washington, DC: Mineralogical Society of America), 129–219.

Just, J., and Kontny, A. (2012). Thermally induced alterations of minerals during measurements of the temperature dependence of magnetic susceptibility: a case study from the hydrothermally altered Soultz-sous-Forets granite, France. *Int. J. Earth Sci.* 101, 819–839. doi: 10.1007/s00531-011-0668-9

Kasting, J. F. (2013). What caused the rise of atmospheric O-2? *Chem. Geol.* 362, 13–25. doi: 10.1016/j.chemgeo.2013.05.039

Liaw, C. W., Liu, T. C., Iizuka, Y., and Yang, H. Y. (2006). Anhydrous melting and crystallization of granite from the transition zone of the Qilian orogenic belt, NW China: an experimental study at atmospheric pressure. *Terrestrial Atmos. Oceanic Sci.* 17, 233–251.

Macouin, M., Roques, D., Rousse, S., Ganne, J., Denèle, Y., and Trindade, R.I. F. (2015). Is the Neoproterozoic oxygen burst a supercontinent legacy? *Front. Earth Sci.* 3:44. doi: 10.3389/feart.2015.00044

McEnroe, S. A., and Brown, L. L. (2000). Palaeomagnetism, rock magnetism and geochemistry of Jurassic dykes and correlative redbeds, Massachusetts, USA. *Geophys. J. Int.* 143, 22–38. doi: 10.1046/j.1365-246x.2000.00193.x

Nedelec, A., and Borisova, A. Y. (2015). Commentary "Is the Neoproterozoic oxygen burst a supercontinent legacy?" *Front. Earth Sci.* 3:80. doi: 10.3389/feart.2015.00080

Nedelec, A., Trindade, R., Peschler, A., Archanjo, C., Macouin, M., Poitrasson, F., et al. (2015). Hydrothermally-induced changes in mineralogy and magnetic properties of oxidized A-type granites. *Lithos* 212, 145–157. doi: 10.1016/j.lithos.2014.11.007

Sun, W. D., Liang, H. Y., Ling, M. X., Zhan, M. Z., Ding, X., Zhang, H., et al. (2013). The link between reduced porphyry copper deposits and oxidized magmas. *Geochim. Cosmochim. Acta* 103, 263–275. doi: 10.1016/j.gca.2012.10.054

Sun, W., Huang, R.-F., Li, H., Hu, Y.-B., Zhang, C.-C., Sun, S.-J., et al. (2015). Porphyry deposits and oxidized magmas. *Ore Geol. Rev.* 65, 97–131. doi: 10.1016/j.oregeorev.2014.09.004

Torsvik, T. H., Carter, L. M., Ashwal, L. D., Bhushan, S. K., Pandit, M. K., and Jamtveit, B. (2001). Rodinia refined or obscured: palaeomagnetism of the Malani igneous suite (NW India). *Precambrian Res.* 108, 319–333. doi: 10.1016/S0301-9268(01)00139-5

Conflict of Interest Statement: The authors declare that the research was conducted in the absence of any commercial or financial relationships that could be construed as a potential conflict of interest.

Advantages of publishing in Frontiers

OPEN ACCESS
Articles are free to read, for greatest visibility

COLLABORATIVE PEER-REVIEW
Designed to be rigorous – yet also collaborative, fair and constructive

FAST PUBLICATION
Average 85 days from submission to publication (across all journals)

COPYRIGHT TO AUTHORS
No limit to article distribution and re-use

TRANSPARENT
Editors and reviewers acknowledged by name on published articles

SUPPORT
By our Swiss-based editorial team

IMPACT METRICS
Advanced metrics track your article's impact

GLOBAL SPREAD
5'100'000+ monthly article views and downloads

LOOP RESEARCH NETWORK
Our network increases readership for your article

Frontiers
EPFL Innovation Park, Building I • 1015 Lausanne • Switzerland
Tel +41 21 510 17 00 • Fax +41 21 510 17 01 • info@frontiersin.org
www.frontiersin.org

Find us on